UNIVERSITA' DEGLI STUDI DI PARMA

Dottorato di ricerca in Ingegneria Industriale

Ciclo XXVIII

A NUMERICAL AND EXPERIMENTAL STUDY ON ENERGY SAVING SOLUTIONS FOR MOBILE HYDRAULIC MACHINERY

STUDIO NUMERICO E SPERIMENTALE DI SOLUZIONI PER IL RISPARMIO ENERGETICO IN MACCHINE IDRAULICHE MOBILI

Coordinatore:
Chiar.mo Prof. Ing. Marco Spiga

Tutor:
Chiar.mo Prof. Ing. Paolo Casoli

Dottorando:

Dott. Ing. Luca Riccò

Table of Contents

Table of Contents i

Abstract v

Acknowledgments vi

Contents of Figures vii

Contents of Tables xv

Abbreviations xvi

Chapter 1: **Energy Saving in Mobile Hydraulic Machinery** 1

1.1 Mobile Hydraulic Machinery 3

1.1.1 Hydraulic Excavator 4

1.1.2 Valve Controlled Systems 5

Constant Flow Systems 6

Negative Flow Control 7

Positive Flow Control 9

Load Sensing Systems 11

1.2 Emission Regulation for Non-Road Vehicles 13

1.3 Energy Saving Solutions in MHM 14

1.3.1 Optimize Individual Components 14

1.3.2 New System Control Strategy Definition 14

1.3.3 New Efficient Hydraulic System Architectures 15

1.3.4 Optimize the Matching between ICE and Hydraulic System 20

1.3.5 Hybrid Systems and Energy Recovery Solutions 20

1.4 Discussion 26

References 27

Chapter 2: **Excavator Mathematical Modelling** 33

2.1 Eurocomach® ES85ZT Excavator 35

2.2 Mathematical Modelling 37

2.2.1 Diesel ICE 38

2.2.2 Flow Generation Unit 40

Main Pump 41

Pilot Pump 49

2.2.3 Directional Flow Control Valve 50

2.2.4 Hydraulic Linear Actuator 56

2.2.5 Hydraulic Rotary Actuator 57

2.2.6 Hydraulic Line Resistance 59

2.2.7 Hydraulic Chamber ... 59
2.2.8 Operator ... 60
2.2.9 Excavator Kinematics ... 61
Front Equipment ... 62
Turret and Travels ... 63
2.3 Discussion ... 64
Symbols ... 64
References ... 67
Chapter 3: **Experimental Activity on the Standard Excavator** ... 70
3.1 Test Bench Experimental Activities ... 72
3.1.1 Flow Generation Unit ... 72
Efficiency Tests ... 72
Swash Plate Actuation Pressure ... 75
Main Pump Dynamic Tests ... 76
Main Pump Regulators Calibration ... 79
3.1.2 Directional Flow Control Valve ... 81
3.2 Machinery Experimental Activities ... 84
3.2.1 Internal Combustion Engine ... 84
3.2.2 Excavator Experimental Setup ... 88
3.2.3 Excavator Characterization Tests ... 91
3.2.4 Excavator Fuel Consumption Tests ... 94
3.2.5 Reference Working Cycles ... 98
Symbols ... 101
References ... 101
Chapter 4: **Standard Excavator Model Validation** ... 103
4.1 Flow Generation Unit ... 105
4.2 Directional Flow Control Valve ... 108
4.3 Complete Standard Excavator ... 110
Chapter 5: **Energy Saving Solutions for LS Hydraulic Systems** ... 114
5.1 Energy Analysis of the Standard Excavator Hydraulic System ... 116
5.1.1 Trench Digging Cycle ... 116
Users Energy Analysis on Trench Digging Cycle ... 119
5.1.2 Grading Cycle ... 127
5.2 Proposed Energy Saving Solutions ... 129
5.2.1 Dual Pump LS System ... 129
5.2.2 Reduced Pump Margin LS System ... 133

5.2.3 Optimization of the outlet flow areas 134
5.2.4 Boom Energy Recovery System 138
5.3 Discussion 141
References 141
Chapter 6: **Energy Recovery System Optimal Dimensioning** 143
6.1 Optimal Energy Management Strategies 145
6.1.1 Dynamic Programming Optimization Method 146
6.2 Excavator Inverse Causality Model 147
6.2.1 Hydraulic Linear Actuator 148
6.2.2 Turret Hydraulic Rotary Actuator 149
6.2.3 Hydraulic User Lines Losses 150
6.2.4 Directional Flow Control Valve 151
6.2.5 Flow Generation Unit 153
Main Pump 153
Pilot Pump 154
6.2.6 Main Pump Torque Limiter 155
6.2.7 Internal Combustion Engine 156
6.2.8 Hydraulic Accumulator 156
6.2.9 Inverse Causality Model Validation 157
6.3 Optimization of the Excavator Boom ERS 162
6.3.1 Inverse Causality Model with the ERS 162
6.3.2 Optimization Problem Definition 164
6.3.3 Optimization Results 166
6.4 Discussion 169
Symbols 169
References 171
Chapter 7: **Energy Recovery System Mathematical Modelling** 173
7.1 Prototype of the Hybrid Control Valve 175
7.2 ERS Modelling 177
7.2.1 Valve X 177
7.2.2 Valve Y 178
7.2.3 Valve 3 179
7.2.4 Pressure Relief Valve 5 and Valve 4 180
7.3 Discussion 181
Symbols 181
Chapter 8: **Hybrid Excavator -Experimental Activity and Model Validation** 183

8.1 Test Bench Experimental Activities 185
8.1.1 Valve X Characterization 185
P → C Orifice 185
P → Y Orifice 187
8.1.2 Valve 3 Characterization 188
8.1.3 Valve Y Characterization 190
8.1.4 Recovery – Reuse Test Simulation 192
8.2 Hybrid Excavator Experimental Activities 197
8.3 Discussion 200
Chapter 9: **Proposed Energy Saving Solutions Comparison** 202
9.1 Energy Analysis of the Proposed Energy Saving Solutions 204
9.1.1 Dual Pump LS System 204
9.1.2 Reduced Pump Margin LS System 208
9.1.3 Optimized Flow Areas System 210
9.1.4 Boom Energy Recovery System 211
9.2 Hydraulic Hybrid Excavator 213
Conclusions 217
Appendix 220

Abstract

Energy saving in mobile hydraulic machinery, aimed to fuel consumption reduction, has been one of the principal interests of many researchers and OEMs in the last years.

Many different solutions have been proposed and investigated in the literature in order to improve the fuel efficiency, from novel system architectures and strategies to control the system to hybrid solutions.

This thesis deals with the energy analysis of a hydraulic system of a middle size excavator through mathematical tools. In order to conduct the analyses the multibody mathematical model of the hydraulic excavator under investigation will be developed and validated on the basis of experimental activities, both on test bench and on the field.

The analyses will be carried out considering the typical working cycles of the excavators defined by the JCMAS standard.

The simulations results will be analysed and discussed in detail in order to define different solutions for the energy saving in LS hydraulic systems.

Among the proposed energy saving solutions, energy recovery systems seem to be very promising for fuel consumption reduction in mobile machinery.

In this thesis a novel energy recovery system architecture will be proposed and described in detail. Its dimensioning procedure takes advantage of the dynamic programming algorithm and a prototype will be realized and tested on the excavator under investigation.

Finally the energy saving proposed solutions will be compared referring to the standard machinery architecture and a novel hybrid excavator with an energy saving up to 11% will be presented.

Acknowledgments

The author would like to express his gratitude to Prof. Eng. Paolo Casoli for the fantastic opportunity and experience granted to him in the last three years of the Ph.D. degree, for the guidance, advice and encouragement throughout the research project.

Additionally, a particular gratitude is also owed to Casappa S.p.A. and Walvoil S.p.A. for the firm of a scholarship and the substantial assistance in the activities, especially to Eng. Marco Guidetti, Eng. Andrea Fornaciari, Eng. Antonio Lettini, Eng. Cesare Dolcin, Eng. Pietro Dardani and Eng. Gianluca Ganassi.

A friendly thanks to all the colleagues and friends old and new: Nicola Pompini, Federico Campanini, Manuel Rigosi, Giulio Pietropaolo, Andrea Pedroni, Mirko Morini, Andrea Bedotti, Luca Cattani, Luca Calabrese, Carlo Corradi, Marco Mordacci, Enrico Campanini, Alessandro Faniulo and many others.

Thanks to all the master students for the given help in the research activity and their sympathy: Giulio Bellanova, Luca Guidetti, Marcos Sebastian Stirn, Antonello Cristalli, Sara Bonati, Marco Ivaldi, Alessandro Volante, Andrea Segala and Alessandro Sivelli.

A great debt of gratitude is owed to my family, for their support and love during all of these years.

Finally, a deeply and lovely thank to my life partner Irene for taking care of me and being always by my side in these last years.

Contents of Figures

Figure 1.1: Power Conversion in Mobile Hydraulic Machinery.

Figure 1.2: Hydraulic Excavator.

Figure 1.3: Open Center Constant Flow Rate Hydraulic System.

Figure 1.4: CFS Power Diagrams: A – Single User Operation, B – Parallel User Operation.

Figure 1.5: Open Center NFC Hydraulic System.

Figure 1.6: NFC Power Diagrams: A – Single User Operation, B – Parallel User Operation.

Figure 1.7: Open Center PFC Hydraulic System.

Figure 1.8: PFC Power Diagrams: A – Single User Operation, B – Parallel User Operation.

Figure 1.9: Closed Center LS Hydraulic System.

Figure 1.10: LS Power Diagrams: A – Single User Operation, B – Parallel User Operation.

Figure 1.11: EU and EPA Emission Standards for Non-Road Engines [*1.17*].

Figure 1.12: Electro-Hydraulic Dual-Circuit System [*1.5*].

Figure 1.13: DC Hydraulic Circuit Architecture [*1.6*].

Figure 1.14: HT to Control a Linear Actuator using a Directional Valve [*1.6*].

Figure 1.15: HT Circuit Architecture [*1.6*].

Figure 1.16: FS Hydraulic System.

Figure 1.17: SMISMO Hydraulic System [*1.31*].

Figure 1.18: DFP Hydraulic System [*1.33*].

Figure 1.19: Series Hybrid System Architecture.

Figure 1.20: Parallel Hybrid System Architecture.

Figure 1.21: Example of ICE Operating Points in Conventional and Hybrid Excavator [*1.36*].

Figure 1.22: Configuration of Hybrid Hydraulic Excavator with PERS [*1.43*].

Figure 1.23: Electric Hybrid System Architecture of a Hydraulic Excavator [*1.44*].

Figure 1.24: Hydraulic Hybrid System Architecture with Boom Energy Recovery [*1.45*].

Figure 1.25: Liebherr Pactronic® System [*1.46*].

Figure 1.26: Hydraulic Hybrid Excavator - Caterpillar 336EH.

Figure 1.27: Hydraulic Hybrid Excavator - Komatsu PC200-8 Hybrid.

Figure 1.28: Hydraulic Hybrid Excavator – Hitachi ZH210LC Hybrid.

Figure 2.1: Eurocomach® ES85ZT Excavator.

Figure 2.2: ES85ZT Simplified ISO Scheme.

Figure 2.3: Diesel ICE Causality.

Figure 2.4: Diesel ICE Block Diagram.

Figure 2.5: ISO Scheme of the FGU.

Figure 2.6: Main Pump Power Diagram.

Figure 2.7: Main Pump and Regulators Causality.

Figure 2.8: Pump Normalized Overall Efficiency η_g/η_{gMAX} at $\alpha/\alpha_{MAX}=1$.

Figure 2.9: Pump Swash Plate Free Body Diagram.

Figure 2.10: $p_{ACT}(p_D, \omega_{ICE}, \alpha)$ Experimental Correlation.

Figure 2.11: Schematic Drawing of the FC and PC Regulator Assembly.

Figure 2.12: Fluid Dynamic Model of the FC and PC Regulator Assembly.

Figure 2.13: Schematic Drawing of the TL Regulator.

Figure 2.14: Fluid Dynamic Model of the TL Regulator.

Figure 2.15: Pilot Pump Causality.

Figure 2.16: ISO Scheme of a Valve Section.

Figure 2.17: Valve Section Causality.

Figure 2.18: Schematic Drawing of a Valve Section.

Figure 2.19: Fluid Dynamic Model of a Valve Section.

Figure 2.20: Generic Example of a Valve Section Orifices Areas.

Figure 2.21: Hydraulic Cylinder Causality.

Figure 2.22: Hydraulic Cylinder Modelling Scheme.

Figure 2.23: Hydraulic Motor Causality.

Figure 2.24: Hydraulic Motor Modelling Scheme.

Figure 2.25: Hydraulic Line Causality.

Figure 2.26: Hydraulic Chamber Causality.

Figure 2.27: Operator Causality.

Figure 2.28: Operator Modelling Scheme.

Figure 2.29: Excavator Kinematics Causality.

Figure 2.30: Front Equipment of the Excavator.

Figure 3.1: FGU Efficiency Tests ISO Scheme.

Figure 3.2: Photograph of the Test Bench during the FGU Efficiency Tests.

Figure 3.3: Main Pump Overall Efficiency at different Pump Displacement.

Figure 3.4: FGU Drag Torque.

Figure 3.5: Swash Plate Actuation Pressure Characterization ISO Scheme.

Figure 3.6: Swash Plate Actuation Pressure Acquired Points.

Figure 3.7 Main Pump Dynamic Tests Setup ISO Scheme.

Figure 3.8: Dynamic Test Input/Output.

Figure 3.9: Dynamic Test Pressures Variations.

Figure 3.10: Main Pump Regulator Calibration Test ISO Scheme.

Figure 3.11: Main Pump Torque and Flow Rate During Regulator Calibration Test.

Figure 3.12: DFCV Test Bench ISO Scheme.

Figure 3.13: Photograph of the Test Bench Configuration during DFCV Test.

Figure 3.14: DFCV Sections Experimental Main Spool Positions.

Figure 3.15: DFCV Sections Experimental Load Pressures.

Figure 3.16: ISO Scheme of the ICE Experimental Tests.

Figure 3.17: Excavator Diesel Tank Deviation System Scheme.

Figure 3.18: Excavator Diesel Tank Deviation System Photograph.

Figure 3.19: ICE Tests Configuration Photograph.

Figure 3.20: ICE BSFC Map at Different Speeds.

Figure 3.21: ICE Speed Variation with Torque.

Figure 3.22: Standard Hydraulic Excavator System Experimental Setup ISO Scheme.

Figure 3.23: FGU and DFCV Instrumented.

Figure 3.24: Data Acquisition System Configuration.

Figure 3.25: Data Acquisition System Photograph.

Figure 3.26: Single Movement Test Limit Positions: Bucket.

Figure 3.27: Bucket Slow Single Movement Cycle.

Figure 3.28: Bucket Fast Single Movement Cycle.

Figure 3.29: Pressure Drop Characteristic of the Bucket Hydraulic Lines.

Figure 3.30: Turret Fiction Torque.

Figure 3.31: Trench Digging Limit Positions.

Figure 3.32: Grading Limit Positions.

Figure 3.33: Trench Digging Sequential Positions.

Figure 3.34: Excavator Photograph on Testing Field.

Figure 3.35: Boom Reference Actuator Position – Trench Digging Cycle.

Figure 3.36: Arm Reference Actuator Position – Trench Digging Cycle.

Figure 3.37: Bucket Reference Actuator Position – Trench Digging Cycle.

Figure 3.38: Boom Reference Actuator Position – Grading Cycle.

Figure 3.39: Arm Reference Actuator Position – Grading Cycle.

Figure 4.1: FGU Main Pump Swash Plate Actuation Pressure.

Figure 4.2: Main Pump Swash Plate Response - p_D=125 bar ,.n = 1500 r/min.

Figure 4.3: Main Pump Swash Plate Response - p_D=200 bar ,.n = 1500 r/min.

Figure 4.4: Main Pump Swash Plate Response - p_D=125 bar ,.n = 2000 r/min.

Figure 4.5: Main Pump Torque and Flow Rate during Torque Limiting.

Figure 4.6: LPCs Positions Experimental and Numerical Comparison.

Figure 4.7: Experimental and Numerical Downstream Pressures (p_{DS}) - Section 1.

Figure 4.8 Experimental and Numerical Downstream Pressures (p_{DS}) - Section 2.

Figure 4.9: Experimental and Simulation Boom Cycle.

Figure 4.10: Experimental and Simulation Arm Cycle.

Figure 4.11: Experimental and Simulation Bucket Cycle.

Figure 4.12: Experimental and Simulation Turret Cycle.

Figure 4.13: Experimental and Simulation Travel Cycle.

Figure 5.1: Sankey Diagram of the Trench Digging Cycle.

Figure 5.2: System Power Demand during the Trench Digging Cycle.

Figure 5.3: Sankey Diagram of the Boom User during the Rising Phase.

Figure 5.4: Sankey Diagram of the Boom User during the Lowering Phase.

Figure 5.5: Boom Power Demand during the Trench Digging Cycle.

Figure 5.6: Sankey Diagram of the Arm User during the Closing Phase.

Figure 5.7: Sankey Diagram of the Arm User during the Opening Phase.

Figure 5.8: Arm Power Demand during the Trench Digging Cycle.

Figure 5.9: Sankey Diagram of the Bucket User during the Closing Phase.

Figure 5.10: Sankey Diagram of the Bucket User during the Opening Phase.

Figure 5.11: Bucket Power Demand during the Trench Digging Cycle.

Figure 5.12: Sankey Diagram of the Turret User during the Accelerating Phase.

Figure 5.13: Sankey Diagram of the Turret User during the Braking Phase.

Figure 5.14: Turret Power Demand during the Trench Digging Cycle.

Figure 5.15: Sankey Diagram of the Grading Cycle.

Figure 5.16: System Power Demand during the Grading Cycle.

Figure 5.17: Dual Pump LS System Simplified ISO Scheme.

Figure 5.18: Pump 1 and Pump 2 Displacement During Simulated Trench Digging Cycle.

Figure 5.19: Dual Pump LS System with Junction Elements Simplified ISO Scheme.

Figure 5.20: Boom B →T Outlet Flow Area Optimization.

Figure 5.21: B → T Outlet Pressure Reduction.

Figure 5.22: Boom Rising Simulated Fuel Consumption Reduction.

Figure 5.23: Boom Rising Time Reduction.

Figure 5.24: $dp_{LS}{}'$ Increasing During Boom Rising Simulation.

Figure 5.25: Excavator Simplified ISO Scheme with Boom ERS.

Figure 5.26: Operating Modes of the ERS.

Figure 6.1: Causality of the HLA Inverse Model.

Figure 6.2: Causality of the Turret HRA Inverse Model.

Figure 6.3: Causality of the Hydraulic Lines Inverse Model.

Figure 6.4: Causality of the DFCV Section Inverse Model.

Figure 6.5: Causality of the Main Pump Inverse Model.

Figure 6.6: Causality of the Pilot Pump Inverse Model.

Figure 6.7: Causality of the Main Pump Torque Limiter Inverse Model.

Figure 6.8: Δp_{LS} Reduction with Main Pump Torque Map.

Figure 6.9: Causality of the Pilot Pump Inverse Model.

Figure 6.10: Causality of the Hydraulic Accumulator.

Figure 6.11: Boom Input – Trench Digging Cycle.

Figure 6.12: Arm Input – Trench Digging Cycle.

Figure 6.13: Bucket Input – Trench Digging Cycle.

Figure 6.14: Turret Input – Trench Digging Cycle.

Figure 6.15: Direct and Inverse Causality - Pump Flow Rate Comparison.

Figure 6.16: Direct and Inverse Causality - Pump Delivery Pressure Comparison.

Figure 6.17: Direct and Inverse Causality – ICE Torque Comparison.

Figure 6.18: Direct and Inverse Causality – Fuel Mass Flow Rate Comparison.

Figure 6.19: Direct and Inverse Causality – Fuel Consumption Comparison.

Figure 6.20: Inverse Causality Scheme of the Proposed ERS.

Figure 6.21: ERS Optimization Results.

Figure 6.22: Optimal Global ERS Control.

Figure 6.23: Optimal ERS Control for an Intermediate Cycle.

Figure 6.24: Control Strategy Logic Scheme.

Figure 7.1: HCV ISO Scheme.

Figure 7.2: HCV Prototype CAD Model.

Figure 7.3: Valve X Causality.

Figure 7.4: Valve Y Causality.

Figure 7.5: Valve Y Areas.

Figure 7.6: Valve 3 Causality.

Figure 8.1: Valve X – P→C Orifice Characterization ISO Scheme.

Figure 8.2: Valve X – Experimental and Simulation $(Q - \Delta p)_{PC}$ Characteristic Comparison.

Figure 8.3: Valve X – P→Y Orifice Characterization ISO Scheme.

Figure 8.4: Valve X – Experimental and Simulation $(Q - \Delta p)_{PY}$ Characteristic Comparison.

Figure 8.5: Valve 3 – A→R Orifice Characterization ISO Scheme.

Figure 8.6: Valve 3 – Experimental and Simulation $(Q - \Delta p)_{AR}$ Characteristic Comparison.

Figure 8.7: Valve Y Characterization ISO Scheme.

Figure 8.8: Valve Y – Experimental and Simulation $(Q - p_{V2-HCV})_Y$ Characteristic Comparison.

Figure 8.9: HCV Recovery – Reuse Simulation Test ISO Scheme.

Figure 8.10: Photograph of the HCV Recovery – Reuse Simulation Test Bench Configuration.

Figure 8.11: HCV Recovery – Reuse Simulation Test ISO Scheme – Initial Phase.

Figure 8.12: HCV Recovery – Reuse Simulation Test ISO Scheme – Recovery – Reuse Phase.

Figure 8.13: HCV Recovery – Reuse Simulation Test ISO Scheme –Reuse Phase.

Figure 8.14: Hydraulic accumulator and HCV Assembly Causality Scheme.

Figure 8.15: Inlet pressure (p_P) Experimental and Numerical Comparison.

Figure 8.16: Accumulator Net Flow Rate (Q_{ACC}) Experimental and Numerical Comparison.

Figure 8.17: Accumulator Pressure (p_{ACC}) Experimental and Numerical Comparison.

Figure 8.18: Hybrid Excavator System Experimental Setup ISO Scheme.

Figure 8.19: Photograph of the Hybrid Excavator Prototype – Accumulator Side.

Figure 8.20: Photograph of the Hybrid Excavator Prototype – HCV Side.

Figure 8.21: Boom Actuator Linear Displacement Experimental and Numerical Comparison – Boom Down-Up.

Figure 8.22: Accumulator Pressure (p_{ACC}) Experimental and Numerical Comparison – Boom Down-Up.

Figure 9.1: Sankey Diagram of the Trench Digging Cycle – 2LS Configuration.

Figure 9.2: Sankey Diagram of the Grading Cycle – 2LS Configuration.

Figure 9.3: Sankey Diagram of the Trench Digging Cycle – 2LSR.

Figure 9.4: Sankey Diagram of the Levelling Cycle – 2LSR.

Figure 9.5: 2LS and 2LSR Actuators Positions Comparison – Trench Digging Cycle.

Figure 9.6: 2LS and 2LSR dp_{LS} Comparison – Trench Digging Cycle.

Figure 9.7: Sankey Diagram of the Trench Digging Cycle – Reduced LS.

Figure 9.8: Sankey Diagram of the Levelling Cycle – Reduced LS.

Figure 9.9: Sankey Diagram of the Trench Digging Cycle – OFA.

Figure 9.10: Sankey Diagram of the Levelling Cycle – OFA.

Figure 9.11: Sankey Diagram of the Trench Digging Cycle – Boom ERS.

Figure 9.12: Sankey Diagram of the Levelling Cycle – Boom ERS.

Figure 9.13: Hydraulic Hybrid Excavator Concept (ES85ZT-H) Simplified ISO Scheme.

Figure 9.14: Sankey Diagram of the Trench Digging Cycle – ES85ZT-H.

Figure 9.15: Sankey Diagram of the Levelling Cycle – ES85ZT-H.

Contents of Tables

Table 2.1: Boundary Condition of the system.

Table 3.1: Transducer Main Features Efficiency Tests.

Table 3.2: Transducer Main Features Swash Plate Actuation Tests.

Table 3.3: Transducer Main Features Dynamic Tests.

Table 3.4: Transducer Main Features Regulator Calibration Test.

Table 3.5: Transducer Main Features DFCV Test.

Table 3.6: Transducer Main Features ICE Tests.

Table 3.7: Transducer Main Features Excavator Experimental Setup.

Table 3.8: Operating Conditions Weight Parameter on a Working Hour.

Table 3.9: Operating Conditions Mean Fuel Consumption.

Table 4.1: Experimental and Numerical Fuel Consumption Results.

Table 8.1: Transducer Main Features Valve X P→C Test.

Table 8.2: Transducer Main Features Valve X P→Y Test.

Table 8.3: Transducer Main Features Valve 3 A→R Test.

Table 8.4: Transducer Main Features Valve 3 A→R Test.

Table 8.5: Transducer Main Features Valve 3 A→R Test.

Table 8.6: Experimental and Numerical Fuel Consumption Results Hybrid Excavator.

Table 9.1: Numerical Fuel Consumption Reductions – 2LS System.

Table 9.2: Numerical Fuel Consumption Reductions – 2LSR System.

Table 9.3: Numerical Fuel Consumption Reductions – Reduced LS System.

Table 9.4: Numerical Fuel Consumption Reductions – Optimized Flow Area System.

Table 9.5: Numerical Fuel Consumption Reductions – ERS.

Table 9.6: Numerical Fuel Consumption Reductions – ES85ZT-H.

Abbreviations

The abbreviations are listed in order of appearance.

MHM = Mobile Hydraulic Machinery

ICE = Internal Combustion Engine

OC = Open Center

CC = Closed Center

CFS = Constant Flow Systems

NFC = Negative Flow Control

PFC = Positive Flow Control

LS = Load Sensing

FGU = Flow Generation Unit

DFCV = Directional Flow Control Valve

VBO = Virtual Bleed Off

EFM = Electronic Flow Matching

DC = Displacement Control

HT = Hydraulic Transformers

FS = Flow Summation

FSN = Flow Summation Node

SMISMO = Separate Meter-In Separate Meter-Out

DFP = Digital Fluid Power

E.G. = Electric Generator

E.M. = Electric Motor

PERS = Potential Energy Recovery System

OEM = Original Equipment Manufacturer

FC = Flow Compensator

PC = Pressure Compensator

TL = Torque Limiter

CFD = Computational Fluid Dynamic

FEM = Finite Element Method

PI = Proportional Integral

D = Delivery

PIL = Pilot

SUC = Suction

IN = Input

OUT = Output

LPC = Local Pressure Compensator

LPK = Local Piston Check

MS = Main Spool

DS = Downstream

BG = Bridge

SF = Selector Sphere

HLA = hydraulic Linear Actuator

P = Piston

R = Rod

HRA = Hydraulic Rotary Actuator

CH = Hydraulic Chamber

EB = Error Band

DOF = Degree of Freedom

PLM = Planar Mechanical Library

RL = Rotary Load

FS = Full Scale

LVDT = Linear Variable Differential Transformer

BSFC = Brake Specific Fuel Consumption

DAQ = Data Acquisition Device

LAN = Local Area Network

JCMAS = Japan Construction Machinery Association Standard

ERS = Energy Recovery System

ECU = Electronic Control Unit

OPT = Optimal

DP = Dynamic Programming

ESD = Energy Storage Device

HEV = Hybrid Electric Vehicle

EMS = Energy Management Strategy

ECMS = Equivalent Consumption Minimization Strategy

EFCOCS = Equivalent Fuel Consumption Control Strategy

RLS = Reduced Load Sensing

OFA = Optimized Flow Area

Chapter 1: **Energy Saving in Mobile Hydraulic Machinery**

Mobile hydraulic machinery (MHM) are widely used in many different applications, for example construction, forestry, agriculture, material handling and transportation, where no electric power nets are typically available, and thus the power generation unit is usually an internal combustion engine (ICE). These systems were typically designed focusing mainly on functionality and performances, with little or no focus on fuel consumption and emissions. The scenario of the next years is changing. The increasing fuel price and the more and more constrains imposed by the legislations, in terms of environment compatibility, are leading the mobile hydraulic machinery design toward energy saving solutions.

1.1 Mobile Hydraulic Machinery

For all the applications where an electrical power net source is not available, such as in construction, agricultural, forestry, material handling and transportation, the mobile machinery found an essential role [*1.1*].

In mobile machinery several actuators are usually operated simultaneously in order to perform the required duty. Hydraulic systems, due to their high power density, dynamic response, high forces and torques achieved by their actuators at slow velocity, heat dissipation characteristic, high versatility in the components positioning into the system layout, and easy power distribution to the actuators are the most adopted systems for mobile applications.

Figure 1 depicts the general power conversion and managing in MHM.

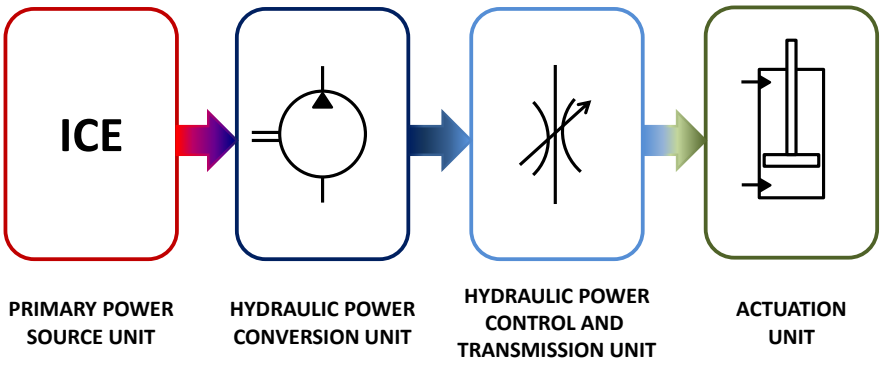

Figure 1.1: Power Conversion in Mobile Hydraulic Machinery.

The primary power source is typically an ICE (usually Diesel) which provides mechanical power to the system starting from the chemical energy of the fuel. The hydraulic power conversion unit converts the mechanical power into hydraulic power for the system, while the hydraulic power control and transmission unit distributes the hydraulic power to the actuation unit according to the operation to be accomplished.

In MHM the hydraulic power could be supplied either with an impressed flow or an impressed pressure, and controlled via resistance (valve controlled systems) or displacement units (displacement controlled systems) [*1.2*].

In mobile applications, where various actuators are often operated in parallel, valve controlled systems with a common flow generation unit found larger usage instead of displacement controlled systems, where just a displacement unit is required for each user, because of the minor required space and the lower investment.

1.1.1 Hydraulic Excavator

Hydraulic excavators are the most used MHM for earth-moving operations at a fixed operation site [*1.3*]. These mobile machines are standardized by the ISO 6746-1 [*1.4*].

The typical hydraulic excavator architecture is represented in Fig.1.2. The principal subsystems are: the under-carriage, composed of a frame for either the tracks or the wheels, depending on the excavator type (tracked or wheeled excavator), and the upper-carriage, also known as the turret, which is the rotating platform where the operator cabin, ICE, working hydraulics and the front excavation tool are placed.

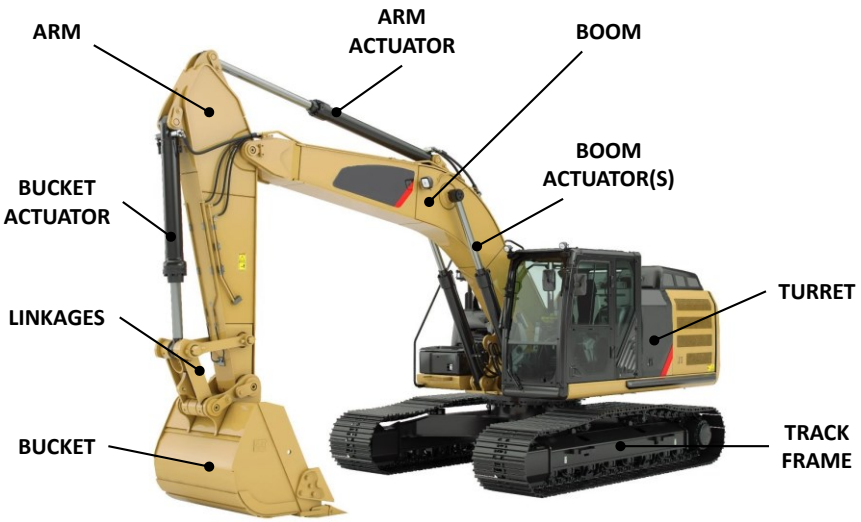

Figure 1.2: Hydraulic Excavator.

The front excavation tool, or the attachment, is composed of the boom, the arm, the bucket and the linkages. These components are connected together in order to accomplish the excavation, transportation and dumping operations.

The working hydraulics supplies the attachment with the required power to complete the desired duty through the usage of hydraulic actuators, either linear or rotary. The hydraulic power is generated via one or more pumps directly connected to the ICE, which provides mechanical power. The available hydraulic power is transferred to the hydraulic drives via pipes and valves according to the operator commands.

Concerning hydraulic excavators many different hydraulic system architectures can be exploited. Valve controlled systems are often used to control more than one hydraulic actuator in simultaneous operations with a single pumping unit [*1.2*]. These systems found large usage in excavators.

1.1.2 Valve Controlled Systems

In MHM the hydraulic power supplied by the flow generation unit (FGU) has to be distributed between the actuated hydraulic drives in the system, ensuring to the operator a fine control. This means controlling the actual flow rate to and from the users for all the possible working conditions[1] and loads[2]. In mobile machinery almost all the exploited hydraulic systems take advantage of the throttle control principle, i.e. use valves to control the flow rate, i.e. the users velocity, introducing as a consequence a not negligible throttle power loss in the system.

These systems can be classified in two different categories depending on the valve configuration in the neutral position: open-center (OC) or closed center (CC).

In the open-center systems, while all the main spools of the valve sections[3] are in their neutral position[4], the supply line (typically indicated with P) is connect to the reservoir line (indicated with T). On the contrary in closed-center systems, with the valve in the neutral position, there is no connection between P and T lines. In close-center systems it is recommended adopting a pressure relief valve to avoid pressure burst while passing from a valve working condition to the neutral one [*1.2*].

Nowadays the widely used hydraulic systems in mobile application are:

- OC Constant Flow Systems (CFS);
- OC Negative Flow Control (NFC);
- OC Positive Flow Control (PFC);
- CC Load Sensing (LS) Systems.

These systems differ for the type of circuit (OC and CC), for the type of flow generation unit adopted (fixed or variable displacement) and its control (open or closed loop).

In European market the state of the art are the LS systems [*1.5*], while in the Asian market NFC and PFC are the most adopted architectures [*1.6*].

[1] Standard functioning; Flow saturation; Torque limitation.
[2] The load can be resistive, when it is contrary to the actuator movement, or pulling, if it acts in the same direction of the actuator movement.
[3] A valve, or a distributor, is composed of a number of valve sections equal to the actuators in the system.
[4] The valve main spool is not actuated, thus there are no connections between the supply line and the valve workports.

Constant Flow Systems

Constant flow systems are OC hydraulic circuits often used in simple and/or small mobile machinery due to their low investment costs and robustness [*1.3*]. Figure 1.3 represents a simplified ISO scheme of a typical CFS.

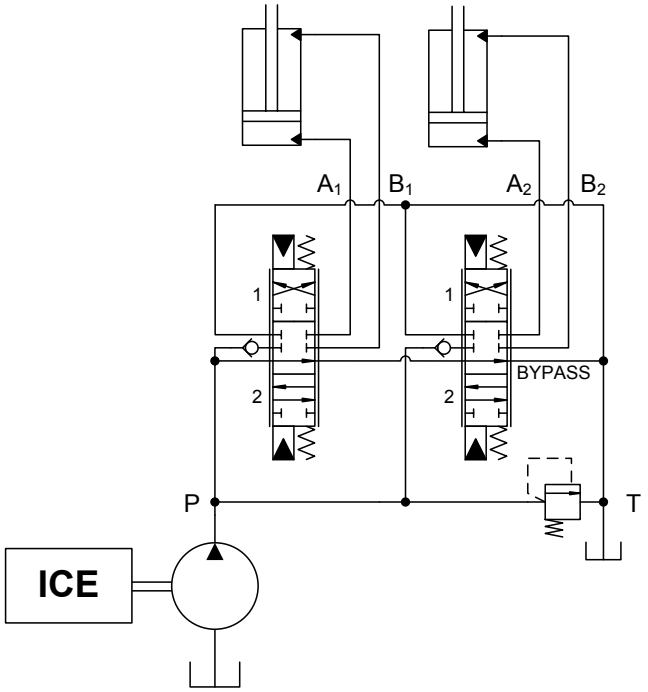

Figure 1.3: Open Center Constant Flow Rate Hydraulic System.

A fixed-displacement pump is adopted as a FGU in these system. The ICE operates at a constant speed so as to have a delivered flow rate by the FGU constant too.

During the standby functioning of the system, i.e. with all valve in the neutral position, the overall flow rate delivered by the pump passes through the bypass line (from P to T). Being the delivery pressure P, in this working mode, only function of the flow rate related losses, the bypass orifices of the valves are typically designed to have the flow areas larger as possible[5] in order to dissipate the less power amount as possible. Nevertheless the bypass energy dissipations are still not negligible. The power diagrams of single and parallel user operations, with the main spool partially displaced, are reported in Fig.1.4.

When just one user is activated, for example toward position 1 (Fig.1.3), i.e. the correspondent valve spool is displaced from the neutral position toward position 1, the bypass

[5] The limits are imposed by the valve overall dimensions.

orifice starts closing while the flow areas from P to workport[6] A_1 and from workport B_1 to T start opening. Reducing the bypass area the P line pressure starts rising. When the delivery pressure P reaches the user load pressure, imposed to workport A_1, a part of the pump delivery flow rate starts going to the user A line while the rest of it still go in the reservoir (T) through the bypass line, Fig.1.4 (A). Once reached the complete valve opening the entire pump flow rate will go to the user.

When more than one actuator is activated, during parallel operations, the same transient flow rate distribution occurs as previously, with the difference that the flow rate which does not go to the tank is divided between the activated users depending on their pressure according to the orifice equation [*1.7*]. Consequently the lower loaded user moves faster than the others ($Q_1 > Q_2$), Fig.1.4 (B). This kind of system allows the operator to feel the load variation on the activated users.

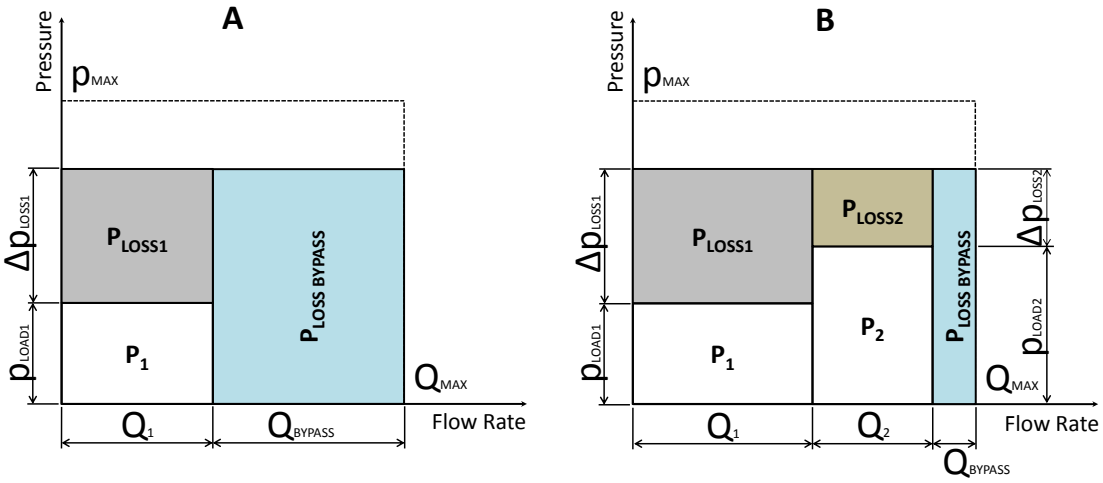

Figure 1.4: CFS Power Diagrams: A – Single User Operation, B – Parallel User Operation.

Negative Flow Control

The negative flow control [*1.8*] is an open center hydraulic system which uses valves similar to the ones of the CFS. The bypass orifice and line are still adopted, but a variable displacement pump is exploited instead of a fixed displacement one, thus reducing the bypass losses during the standby functioning.

Figure 1.5 shows the simplified ISO scheme of a generic NFC system layout.

[6] The valve workports are the ports that connects the valve ports to the actuator ports.

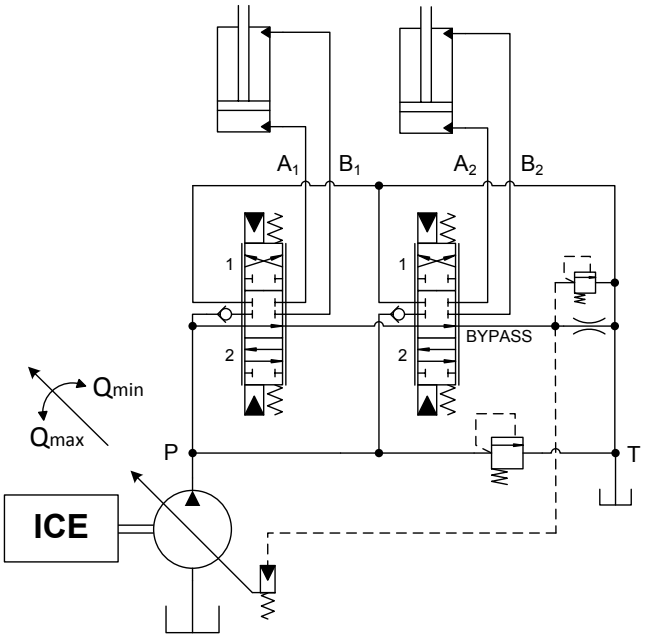

Figure 1.5: Open Center NFC Hydraulic System.

In NFC, the pump displacement is feedback controlled through a negative logic. If the pilot pressure of the pump controller raises the pump displacement reduces, conversely if the pilot pressure decreases the pump displacement increases [*1.9*].

This control logic takes advantages of the pilot pressure generator, composed of a measuring orifice (or a negative control orifice) and a pressure relief valve installed downstream of the bypass line (Fig.1.5). The measuring orifice causes a pressure drop proportional to the surplus flow rate in the bypass line.

During the standby functioning, i.e. when the users do not require any flow rate, a new equilibrium between the pump delivery flow rate and the pilot pressure is obtained, and the pump displacement is set to its minimum[7].

During parallel users operations the volume flow rate distribution still depends on the spools opening and users loads.

Figure 1.6 shows the power diagrams during both single and parallel users operations.

[7] The minimum displacement could not be equal to zero, because the pilot pressure is proportional to the flow rate in the bypass line, therefore even in standby functioning a minimum flow rate will be still delivered by the pump.

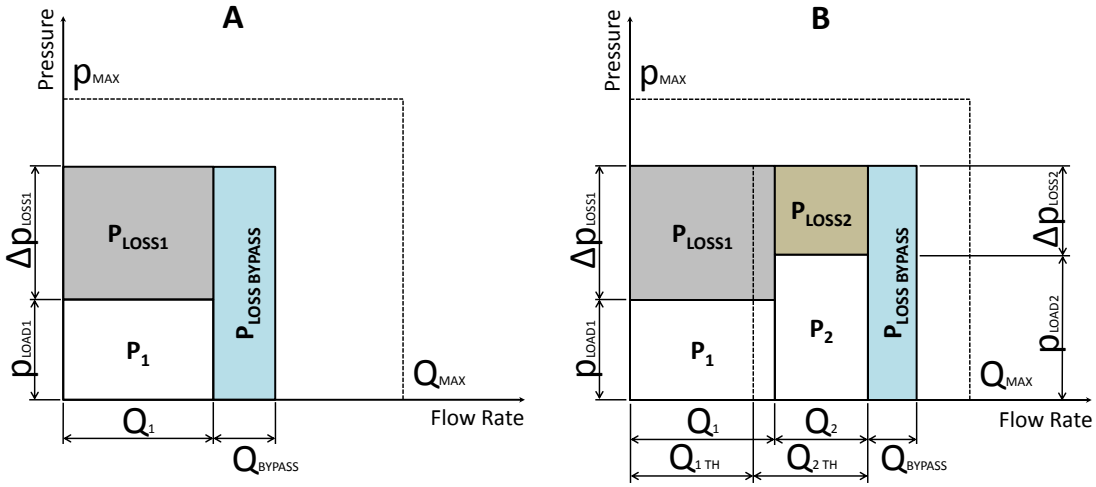

Figure 1.6: NFC Power Diagrams: A – Single User Operation, B – Parallel User Operation.

Positive Flow Control

The typical architecture of a positive flow control system [*1.10*] is represented in Fig.1.7. Open center directional flow control valves (DFCV) type are adopted, as in CFS and NFC, in combination with a variable displacement pump.

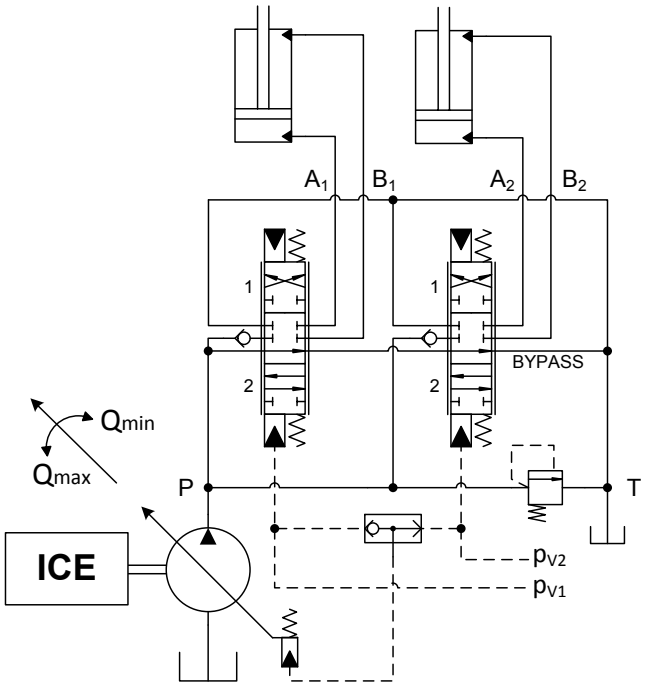

Figure 1.7: Open Center PFC Hydraulic System.

The pump displacement is feedforward controlled. The pilot pressure of the pump controller is equal to the maximum pilot pressure of the contemporary actuated valve section ($MAX\ (p_{V_i})$) detected via a combination of shuttle valves[8]. The pump displacement controller works in a positive logic. If the pilot pressure raises the pump displacement increases, conversely if the pilot pressure drops the pump displacement decreases.

This displacement control logic on one leads to fast pump response than feedback control systems (NFC and LS), but on the other hand during single operations the bypass losses are higher than NFC and LS. In fact, being the pump maximum displacement designed to provide the flow rate required during parallel users operations and being the pump displacement control not influenced by the number of activated users, during single user operations an excess flow rate will be provided by the pump.

Furthermore, during parallel operations the users still influence each other for flow rate distribution as well as the loads. On the contrary, during standby functioning the pump displacement could be set to zero[9] saving otherwise dissipated power.

Figure 1.8 reports the power diagrams associated to the single and parallel users operations in PFC.

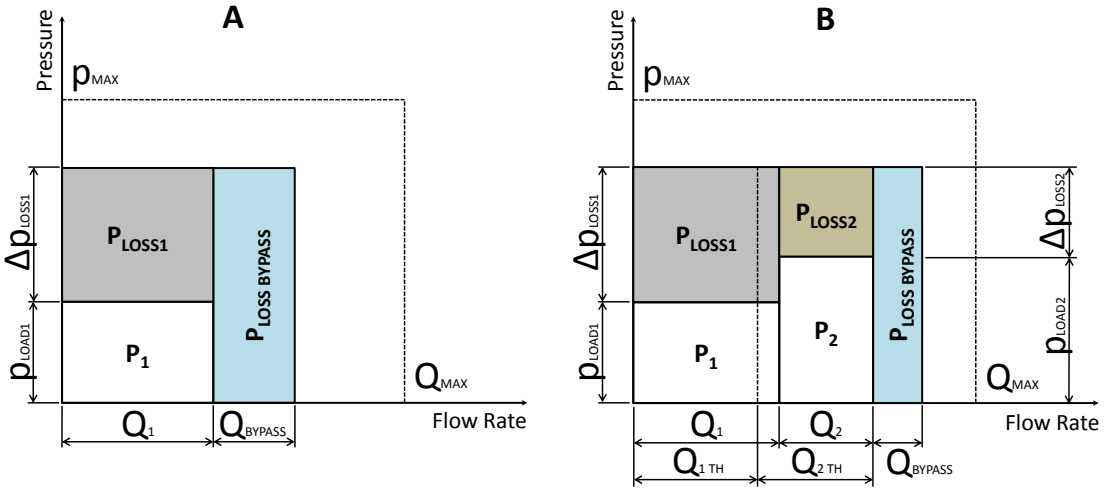

Figure 1.8: PFC Power Diagrams: A – Single User Operation, B – Parallel User Operation.

[8] For hydraulic-mechanical PFC systems. This system could be also electronically controlled.
[9] This statement is correct only if an auxiliary pilot pump is mounted in the hydraulic system, otherwise even in this system a minimum delivered flow rate for the pilot circuit has to be supplied by the main pump.

Load Sensing Systems

The load sensing (LS) systems equip the majority of MHM and for almost a decade have been considered the state-of-the-art regarding energy efficiency [*1.11*].

In LS systems the pump pressure P is controlled in a closed loop control mode, in a way that it is always higher than the highest load pressure in the system of a certain defined pressure amount [*1.12*], also known as pump margin, usually within 2 – 3 MPa. This, on one hand, enables to control each users flow rate independently on loads, but on the other hand power losses proportional to the flow rate are always present in such a system, across the meter-IN compensated orifice.

Many different architecture of LS systems can be exploited:

- the standard, without local compensator in the valves;
- the pre-compensated;
- the post-compensated.

The meter-IN orifice and the local pressure compensator guarantee a flow rate proportional to the operator command only. In fact, the local compensators maintain a constant and the same pressure drop across all the meter-IN orifices of the DFCV [*1.13*].

It has to be pointed out that the pressure drop across the metering orifices is not always constant, but depends on the operating mode[10].

According to the orifice equation [*1.7*], the flow rate division between the active users is proportional only to the correspondent meter-IN areas. This feature is provide both in pre-compensated and post-compensated valves, even if pre-compensated LS systems are still influenced by the loads, in fact the user with the highest actuator load could stop its movement. For this reason post-compensated LS system have a large usage in MHM. Moreover in case of pump flow saturation conditions, i.e. when the overall flow rate required by the activated users is higher than the pump maximum flow rate the pressure drop over all the control valves meter-IN orifices still remains constant but is proportionally reduced, always ensuring the actuator controllability.

Figure 1.9 reports the post-compensated LS system, also known as LS Flow Sharing system, typical architecture, while Fig.1.10 shows the related power diagrams during single and parallel user operations.

[10] Standard functioning; Flow saturation; Torque limitation.

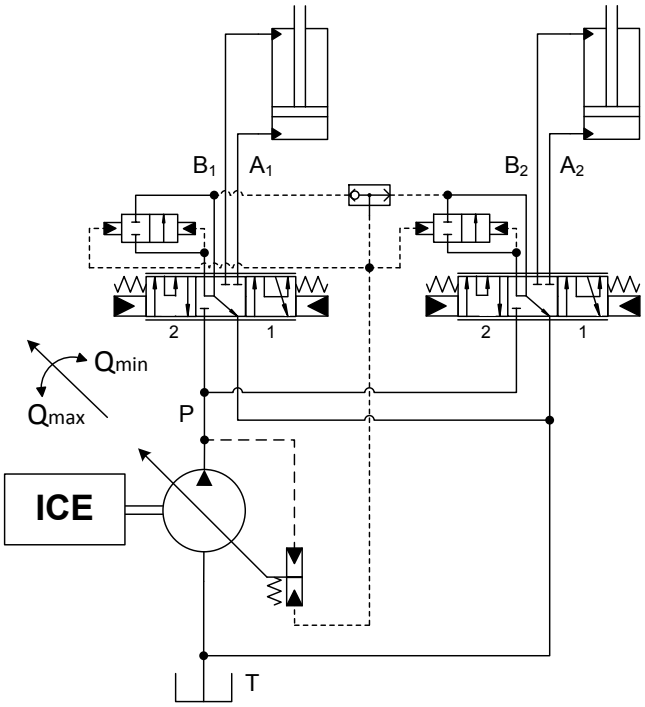

Figure 1.9: Closed Center LS Hydraulic System.

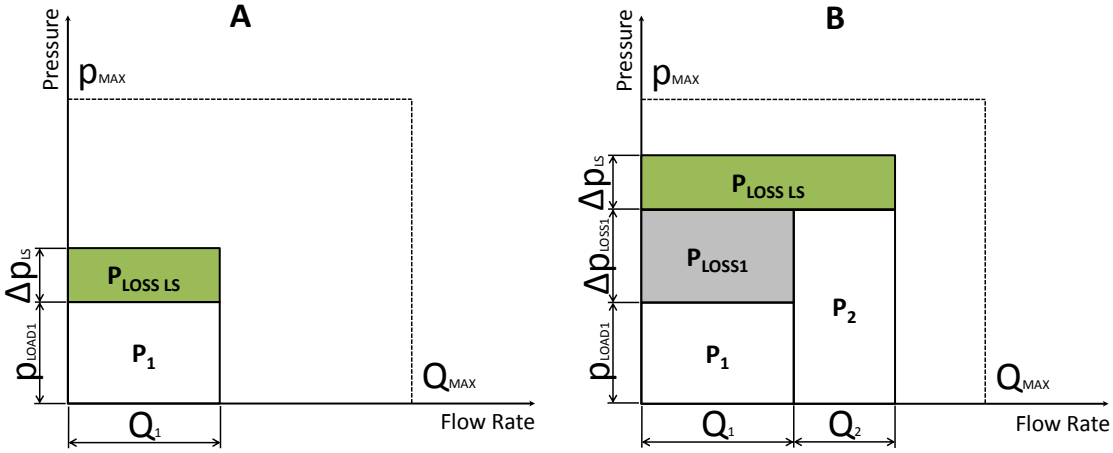

Figure 1.10: LS Power Diagrams: A – Single User Operation, B – Parallel User Operation.

1.2 Emission Regulation for Non-Road Vehicles

Starting from the ends of nineties, non-road engine emissions have increasingly become the principal focus of regulatory actions and air quality improvement strategies [*1.14*].

From 1997 in Europe and 1996 in U.S. the Directive 97/68/EC [*1.15*] and TIER Standard [*1.16*] were introduced in order to limit the CO_2 and NO_x[11] emissions.

The last emission standard applied are the STAGE IV and TIER 4, which further limit the CO, HC[12] and PM[13] emissions. Figure 1.11 reports the time history of the EU and US, or EPA (Environment Protection Agency), emission limits of the standards.

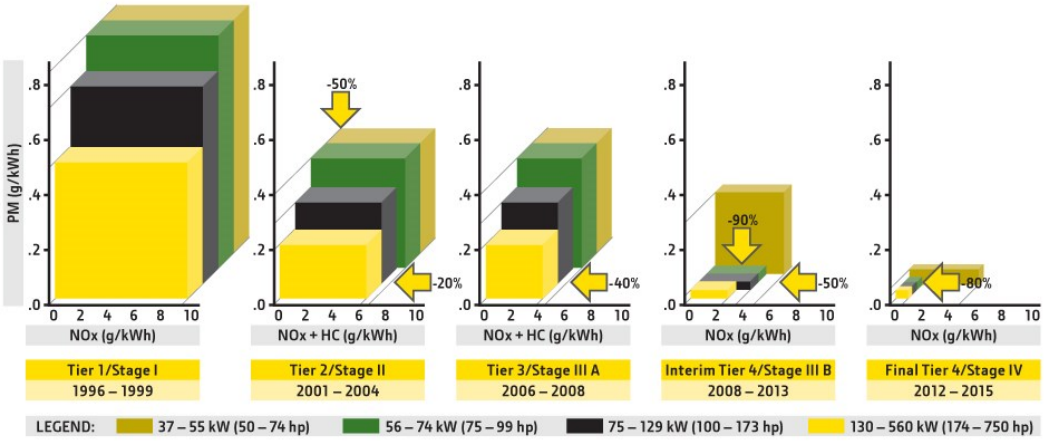

Figure 1.11: EU and EPA Emission Standards for Non-Road Engines [*1.17*].

In order to meet the TIER 4 and STAGE IV stringent emission regulations, the engine manufactures have increasingly introduced, through more and more advanced engine design, new components as EGRs[14] and exhaust gas after-treatment systems (oxidation catalyst, particulate filters, SCR[15] etc.).

If apparently these emission regulations do not directly affects fluid power systems, the interaction between the Diesel engine and the hydraulic system plays an important role as the overall efficiency and operation points affect the fuel consumption and the pollutant emissions [*1.18, 1.2*].

Manufacturers of MHM are now focusing on efficiency improvements of their systems, from the engines to the working hydraulic, including also energy recovery systems.

[11] Nitrogen Oxides (NO and NO_2).
[12] Hydrocarbons.
[13] Particulate Matter.
[14] Exhaust Gas Recirculation.
[15] Selective Catalytic Reduction.

1.3 Energy Saving Solutions in MHM

In order to meet the more tight regulations about pollutant emission for non-road MHM and to overcome the fuel prize increasing, the mobile machinery manufacturers and the scientific research programs are focusing on energy saving solutions, i.e. improving the overall system (ICE and working hydraulic) efficiency in order to maximize the fuel economy.

Nowadays, the state of the art for MHM hydraulic systems, and especially for excavators, are LS, NFC, PFC and CFS systems.

There are many different proposed approaches to increase the fuel efficiency [*1.3, 1.6*]:

- optimize the individual components;
- define new system control strategies;
- define new efficient hydraulic system architectures;
- optimize the matching between ICE and hydraulic system;
- hybridization and energy recuperation solutions.

An overall overview of the mentioned approaches will be presented in the next paragraphs and some examples will be reported.

1.3.1 Optimize Individual Components

Individual components optimization is the easiest and also the most common way to improve the systems efficiency [*1.6*].

Typically the friction losses reduction and the flow dynamic characteristic improvement are the most performed optimizations. These optimizations could take advantage of both numerical or experimental approaches, and some examples of different adopted methodology can be found in [*1.19, 1.20, 1.21, 1.22*] concerning hydraulic pumps and valves.

1.3.2 New System Control Strategy Definition

Another effective approach to increase the system fuel economy of MHM is the study of new control strategies for the system. The wide usage of electronic components and controls allowed new further improvements regarding energy efficiency and controllability on hydraulic systems.

In [*1.23*] the LS pressure level setting is variable with the engine speed adopting a proportional electro-hydraulic compensator on the pump.

A further solution is the VBO (Virtual Bleed Off) systems [*1.24*], from Bosch Rexroth AG, where a software and an electrically pressure-regulated pump are adopted to electronically reproduce the standard open center system without the typical related energy losses.

Moreover new system control strategies, taking advantages of LS system architecture, to reduce valve throttle losses, improving the fuel efficiency of the system, are presented in [*1.12, 1.25, 1.26*]. These systems are known as EFM (Electronic Flow Matching) or Flow-On-Demand systems.

1.3.3 New Efficient Hydraulic System Architectures

In addition to the standard MHM hydraulic architectures (LS, CFS, NFC, PFC) both industrial and academic researcher have been conducting activities to propose novel energy efficiency architectures for working hydraulics.

There are different approaches for new system architecture designs.

Considering hydraulic excavators, which are the most diffuse MHM in the construction field, during parallel users operations, the pump delivery pressure is imposed by the highest actuator load. A valid approach to optimize the system overall efficiency is that of separate in group the users with similar loads during the working cycle, thus limiting the throttle losses in the sections with the lower loads. In [*1.5*] is presented a LS system implementing this solution with an energy consumption reduced up to 30% in the performed working cycle. The hydraulic system architecture ISO scheme is reported in Fig.1.12.

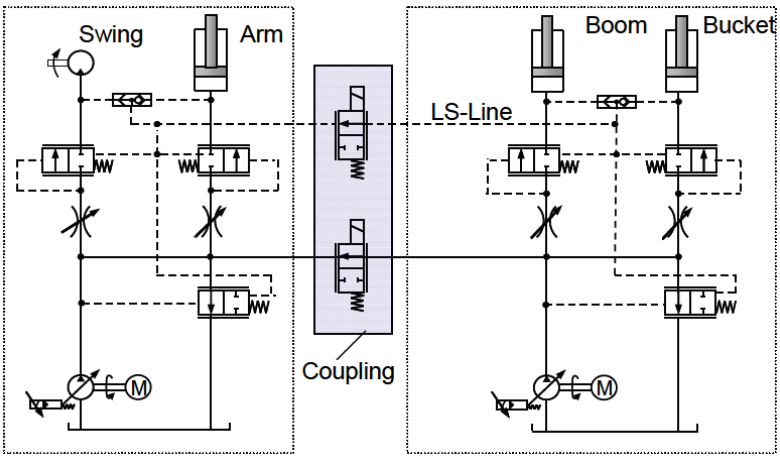

Figure 1.12: Electro-Hydraulic Dual-Circuit System [*1.5*].

In [1.27] is presented another novel hydraulic system architecture. In this system the turret is actuated exploiting a dedicated closed loop hydraulic circuit and the pump power has been reduced up to 12% compared to the standard system architecture, thus improving the fuel economy.

Throttle losses are related especially to valve controlled hydraulic systems, which exploits this principle in order to control the users velocities.

A novel system architecture, known as Displacement Control (DC) system [*1.28*], avoids throttle losses taking advantage of displacement units in closed loop circuit to control the related actuator, delivering the required power only leading to fuel saving up to 30% (measured by CAT during comparison tests). This system design typically requires a variable displacement unit for each user, thus raising the system investment cost.

Figure 1.13 shows an example of a DC system adopted for an excavator.

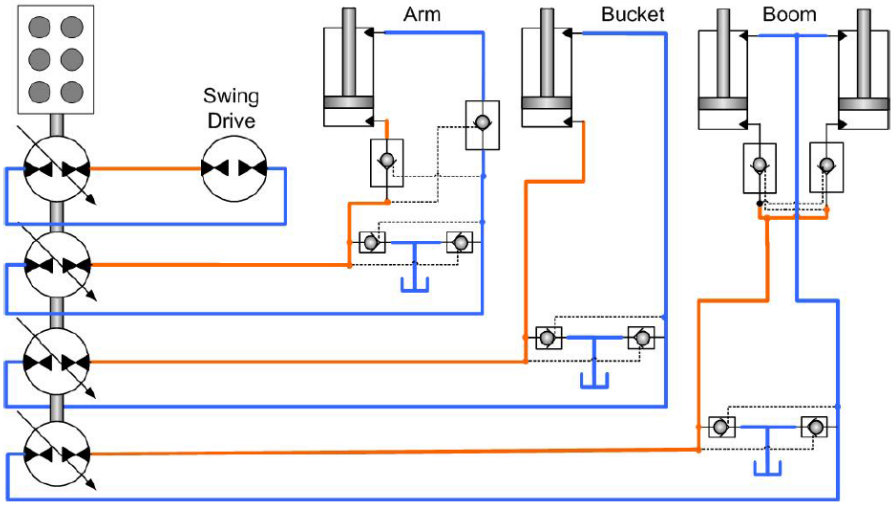

Figure 1.13: DC Hydraulic Circuit Architecture [*1.6*].

An alternative architecture exploits hydraulic machine to avoid throttle losses was presented in [*1.29*]. This system takes advantages of hydraulic transformers (HT). The hydraulic transformers use a constant pressure rail and optional accumulator to supply and control the linear actuators of the working hydraulic [*1.6*].

Figure 1.14 shows the HT controlling principle for a hydraulic linear actuator exploiting a directional control valve while Fig.1.15 depicts a simplified ISO scheme of an excavator involving HTs.

Another advantage in the use of DC or HT is the easy energy recovery in comparison to valve controlled architectures.

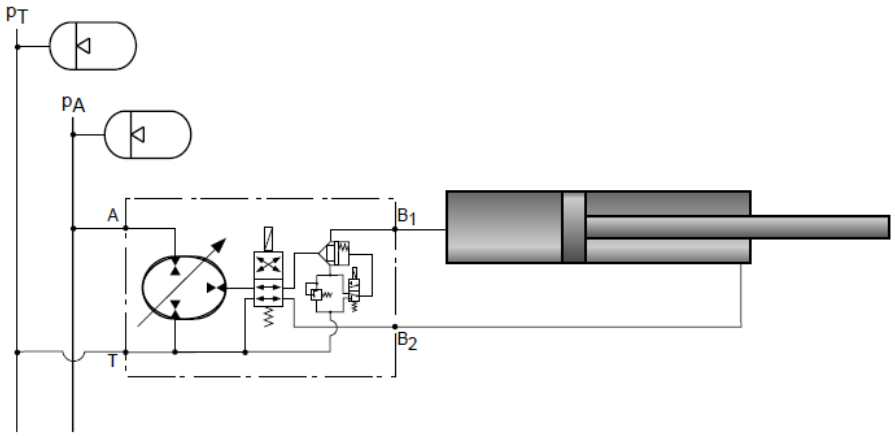

Figure 1.14: HT to Control a Linear Actuator using a Directional Valve [*1.6*].

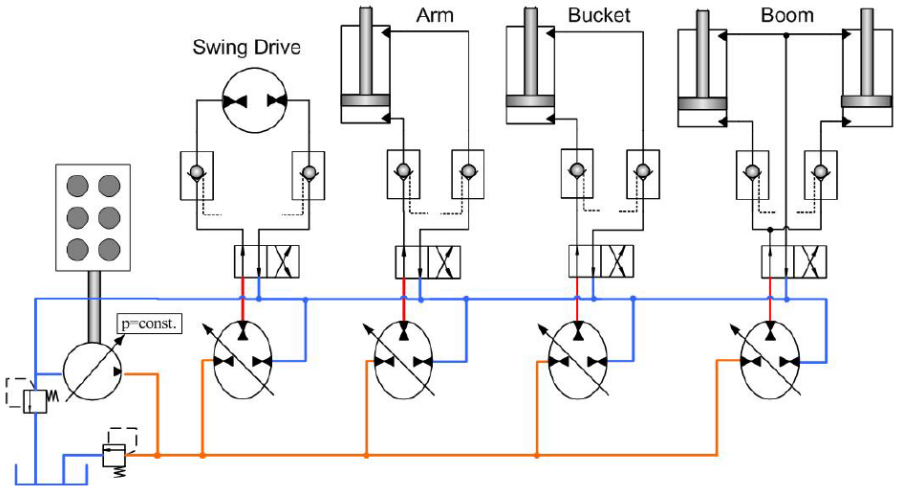

Figure 1.15: HT Circuit Architecture [*1.6*].

The flow summation (FS) system [*1.30*] is a novel hydraulic circuit architecture, Fig.1.16. This system was presented in the second half of 2011 by Husco® International.

The DFCV, as for the CFS, NFC and PFC, has the bypass line. In addition each section of the DFCV have a compensated meter-IN orifice. The meter-IN orifice (or source orifice) defines the pump delivery flow rate, taking advantage of the pump flow compensator, which tilts the pump swash plate until an equilibrium between the delivery pressure and the flow summation node (FSN) pressure plus the pump margin setting is reached.

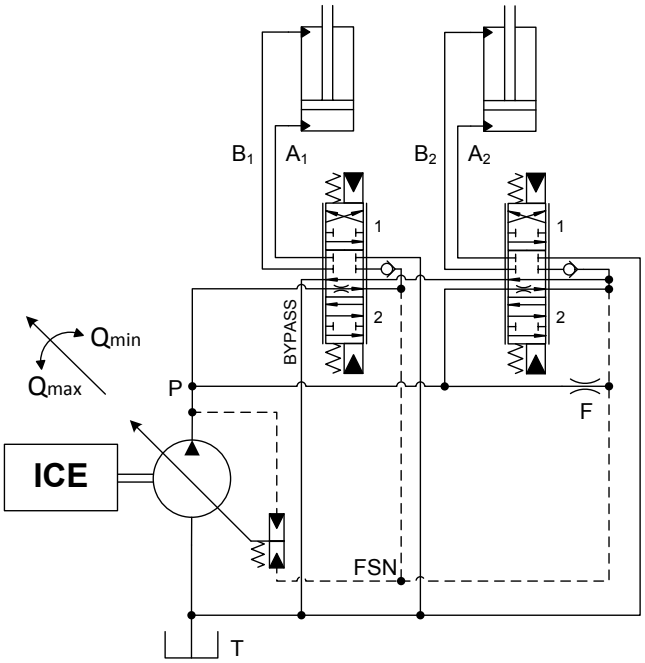

Figure 1.16: FS Hydraulic System.

During single user operations the pump delivery flow rate is exactly the one required by the activated user, avoiding excess flow rate like in other OC systems.

Differently, during parallel user operations the pump delivered flow rate is the summation of the flow rates required by each activated user, but its distribution between the users still depends on the users pressures.

The FS system joins the advantages of an open center system and of a LS variable displacement pump.

Many researchers have been studying for several years hydraulic valves with separate meter-IN separate meter-OUT control architecture.

This idea not only opens for a better dynamic performance of the hydraulic system, but also brings increased functionality of the system and further possibility of operating the hydraulic systems in an energy efficient way [*1.31*].

In standard valve controlled system the metering edges (inlet and outlet) of the valves are physically coupled (on the same spool) leading to meter-OUT losses proportional to the outlet flow area design.

Independent metering, also known as SMISMO (separate meter-IN separate meter-OUT), Fig.1.17, avoids this disadvantage leading to fuel saving up to 17% [*1.33*]. Moreover,

new control strategy could be introduced in order to enable regenerative mode or adapt the power demand to the ICE.

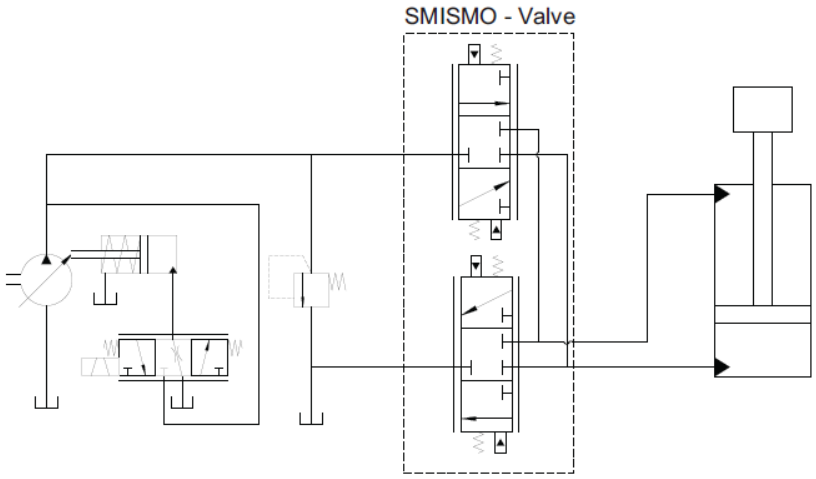

Figure 1.17: SMISMO Hydraulic System [*1.31*].

Digital fluid power (DFP) [*1.32*] is another hydraulic system architecture which enables new way of controlling the pump, the valves and the actuators of the MHMs.

In [*1.33*] a novel machinery architecture was presented and energy saving up to 22% (during simulations tests) has been pointed out in respect of a standard LS system.

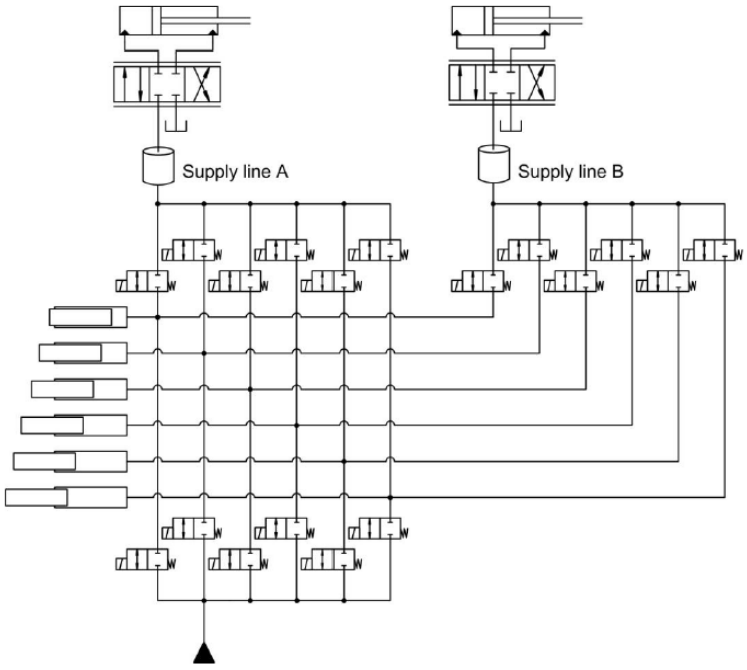

Figure 1.18: DFP Hydraulic System [*1.33*].

1.3.4 Optimize the Matching between ICE and Hydraulic System

Most of the research activities on energy saving in MHM are conducted with the aim of reducing the fuel consumption only focusing on subsystems optimization. This approach could have negative influence on the ICE efficiency [*1.3*].

The optimization of the matching between the hydraulic system and the ICE is one of the major challenge to improve the system overall efficiency and to reduce fuel consumption.

To this extent, hybrid architectures combined with energy-storage devices (electric, mechanical or hydraulic) seems very promising [*1.34*]. Virtual design based on simulation model [*1.35*] is an option to study and define control strategy to match hydraulic system and engine to make the best use of their operating characteristics.

1.3.5 Hybrid Systems and Energy Recovery Solutions

System hybridization and energy recovery solutions implementation have become important approaches for energy saving in MHM.

A hybrid system is a system with two or more different type of power sources. Up to now the ICE and an electrical power source are the most adopted hybrid systems type.

In automobile industry, hybridization of conventional power trains has been actively studied as fuel efficiency and low emissions short-term solution [*1.36*].

Nowadays also in the field of construction machinery, especially in hydraulic excavators, hybridization and energy recovery are playing an important role for energy saving and performance improvement [*1.37*].

Three different types of hybrid configuration are typically adopted [*1.38, 1.39*]:

- the series hybrid, Fig.1.19, in which the totality of the ICE power is converted in the secondary power source type (in most cases electrical power). This energy is used to feed the working system and when the available energy is more than the required, the surplus is stored in energy storage devices. In this systems the ICE typically works at a fixed speed near its optimal efficiency point;
- the parallel hybrid, in which the ICE and the secondary power sources are linked together with the working system, Fig.1.20. The working system could be feed only by the ICE, only by the secondary power source or by both of them according to the energy demand and the control strategy. In these systems the ICE speed has to be

controlled due to the requirements of the main power line. The secondary power source can only increase or decrease the ICE load in order to keep the engine working point near the maximum efficiency;

- the combined or compound hybrid is a combination between series and parallel hybrid solutions. These systems join the advantages of the other hybrid solutions, and is considered the best hybrid solution (of electrical type) for hydraulic excavators taking into consideration the development costs and fuel economy [*1.36, 1.37*], on the contrary initial investment is higher than for the other types.

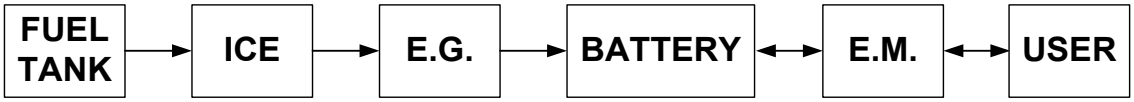

Figure 1.19: Series Hybrid System Architecture.

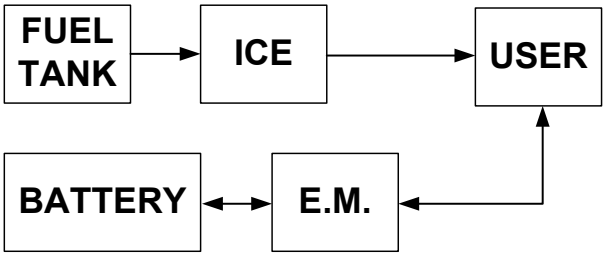

Figure 1.20: Parallel Hybrid System Architecture.

Hydraulic excavators and MHMs in general have typically multiple actuators, both linear and rotary. During the working cycles the ICE load is typically not constant, in fact large variations in workload occur.

In conventional excavators the ICE must be dimensioned in order to supply the required power during maximum peaks power demand by the hydraulic system [*1.39*], leading to oversize the ICE in comparison to the average requested power and let it works in low efficiency zone.

Hybrid technologies, combined with properly developed control strategies, enable a more effective power matching between the ICE and the working hydraulic [*1.38*], keeping the engine in its high efficiency region, Fig.1.21, and leading to the ICE downsizing [*1.40*].

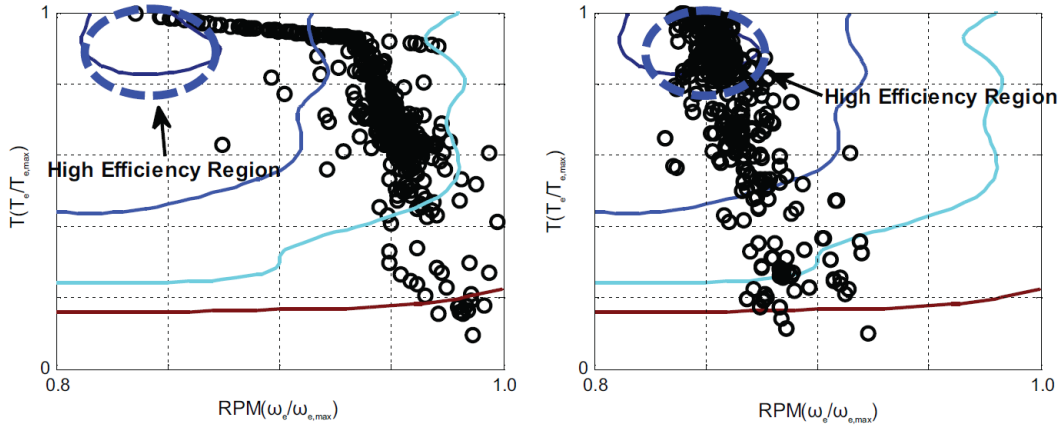

Figure 1.21: Example of ICE Operating Points in Conventional (a) and Hybrid (b) Excavator [*1.36*].

Electric hybrid solutions are widely diffused in many applications, from the on-road vehicles to off-road and earth-moving vehicles, but in the recent years even hydraulic hybrid solutions have been studied by both scientific and industrial researchers for the same applications.

Considering hydraulic excavators, which are the most diffuse MHM in construction, the most adopted hybrid systems are of the electrical type, but some new solutions adopting the hydraulic hybrid type are under study and development. The usage of a hydraulic hybrid solution in MHM on one hand has the advantage of having only one power conversion (from hydraulic into mechanical) instead of at least two in electric hybrid systems (from hydraulic into electric and then into mechanical), but on the other hand the adoption of electric hybrid systems enable, as example, the substitution of the rotary hydraulic actuators with electric motors (solution typically adopted for the turret swing motor) [*1.41*] leading to hydraulic power reduction and energy recovery.

In fact, energy recovery solutions, combined to hybrid systems, is another effective energy saving method [*1.37, 1.42*].

In general, two kinds of energy recovery systems are exploited in hydraulic excavators: the turret swing kinetic energy recovery during braking and the boom potential energy recovery during lowering. Both could take advantage of whether hydraulic or electric energy storage devices.

Many solutions have been presented by academic and industries. Figures 1.22 – 1.25 report some examples of hybrid systems integrated with energy recovery solutions of both electrical and hydraulic type.

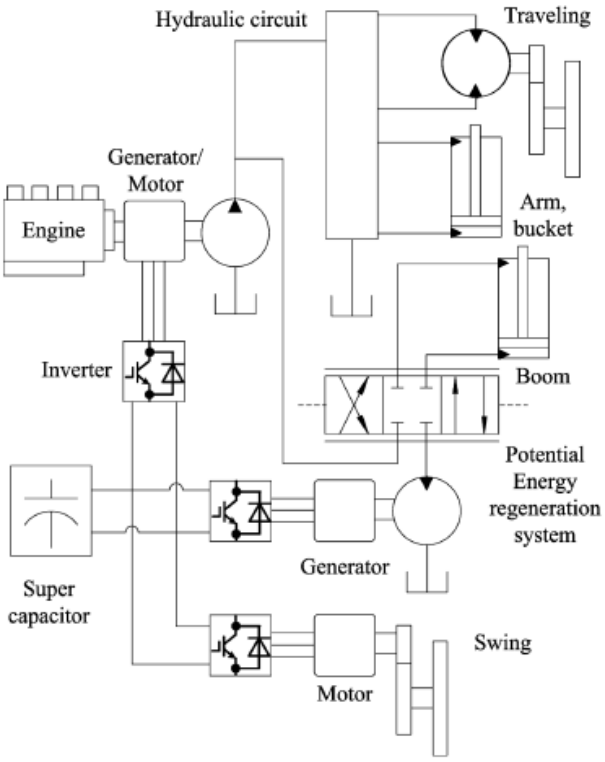

Figure 1.22: Configuration of Hybrid Hydraulic Excavator with PERS [*1.43*].

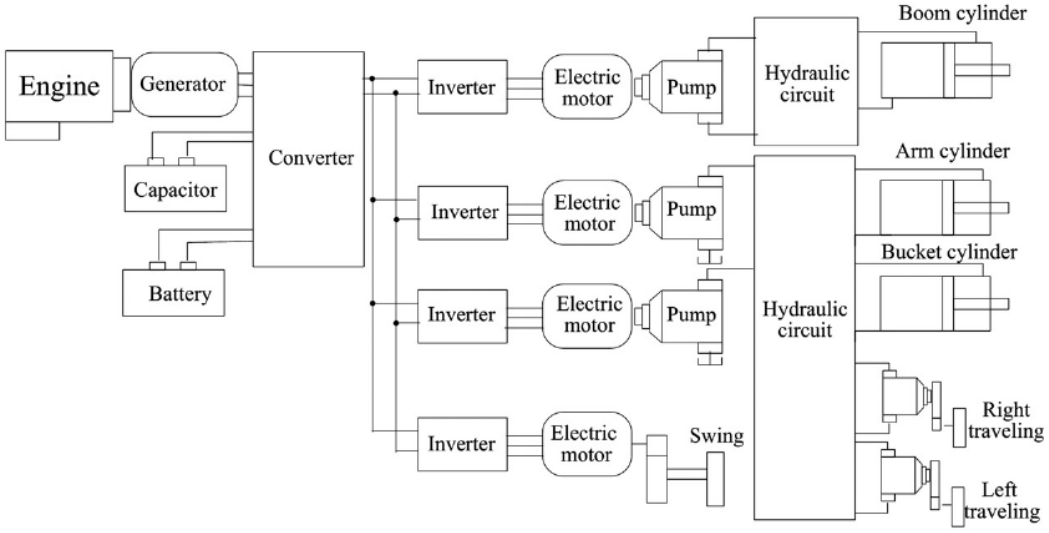

Figure 1.23: Electric Hybrid System Architecture of a Hydraulic Excavator [*1.44*].

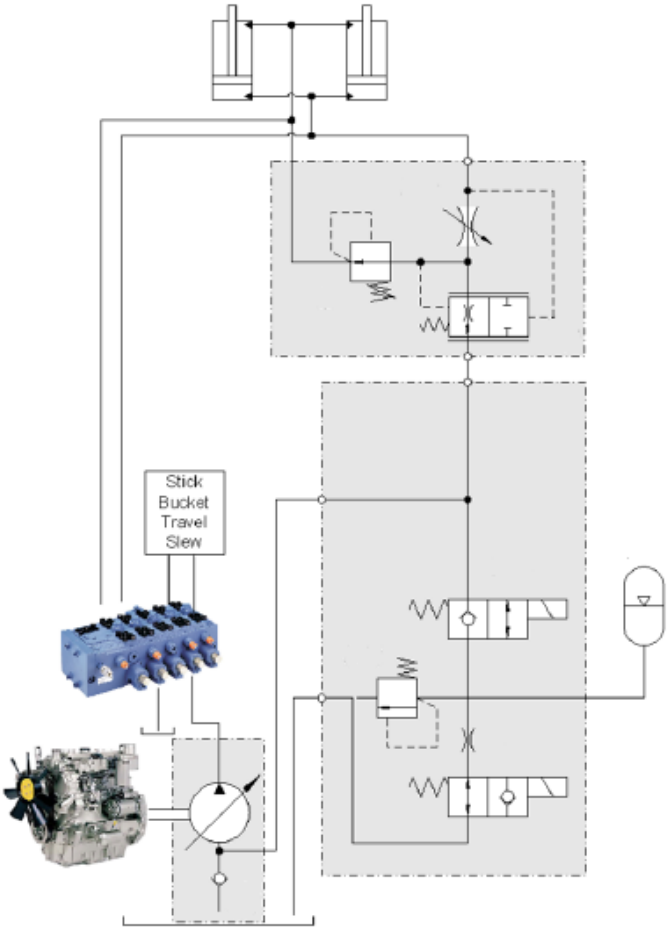

Figure 1.24: Hydraulic Hybrid System Architecture with Boom Energy Recovery [*1.45*].

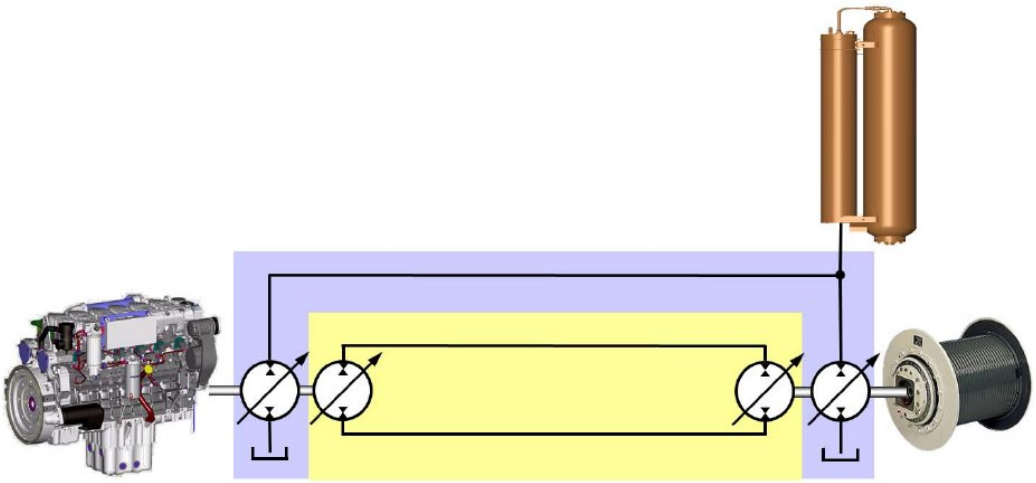

Figure 1.25: Liebherr Pactronic® System [*1.46*].

Some hybrid excavators are already available on the market from different OEMs. Caterpillar® produces the CAT336EH [*1.47*], Fig.1.26, which exploits a hydraulic energy recovery system for the turret decelerations. The recovered and stored energy in hydraulic accumulators is therefore reused during the turret accelerations. An energy saving percentage up to 30% is declared by the constructor.

Figure 1.26: Hydraulic Hybrid Excavator - Caterpillar 336EH.

Komatsu® realizes the PC200-8 Hybrid [*1.48*], Fig.1.27, which exploits an electric machinefor the turret action. During the turret decelerations the electric machine works as a generator recovering and storing energy in capacitors. Moreover, another electric machine, defined power generation motor, directly coupled with the ICE charges the capacitors during low loads operating mode of the working hydraulics, thus keeping the ICE in its optimal efficiency working region. The stored energy can be used for both the turret accelerations and to assist the main hydraulic pump of the excavator. A fuel saving percentage up to 25% is declared by the constructor compared to its standard version of this excavator.

Figure 1.27: Hydraulic Hybrid Excavator - Komatsu PC200-8 Hybrid.

Hitachi® manufactures the ZH200LC [*1.49*], Fig.1.28, adopts an electric hybrid solution. The turret rotation is provided with an electric machine instead of a hydraulic motor. During the turret deceleration phases the kinetic energy is converted and accumulated in electric capacitors.

Figure 1.28: Hydraulic Hybrid Excavator – Hitachi ZH200LC Hybrid.

Moreover a power generation assist motor, directly connected to the ICE, charges the capacitors when required. The stored energy can be used for both the turret accelerations and to assist the main hydraulic pump of the excavator. A fuel saving percentage up to 15% is declared by the constructor compared to the standard version of the same excavator model.

1.4 Discussion

In this chapter an overview of the state of the art related to hydraulic system exploited in MHM have been presented, focusing on architectures, features and power consumptions during single and multiple users operations.

Starting from these systems, several energy saving solutions have been studied and proposed, by both researchers and OEMs, in order to reduce the fuel consumption and the pollutant emission so as to meet the more and more tight regulations. Some solutions propose the adoption of new system architectures, others exploit new way to control the system and others adopt hybrid system architectures.

In the next chapters, starting from the literature review and the state of the art regarding hydraulic excavators, energy saving solutions for mobile machinery will be proposed and investigated.

References

1.1 *H. Murrenhoff. Trends and some recent developments in Mobile Hydraulics. Institute for Fluid Power and Controls. RWTH Aachen University. Germany.*

1.2 *M. Inderelst. Efficiency Improvements in Mobile Hydraulic Systems. Shaker Verlag. Aachen 2013. ISBN: 978-3-8440-1726-7.*

1.3 *S. Sgro. Concepts of Hydraulic Circuit Design Integrating the Combustion Engine. Shaker Verlag. Aachen 2014. ISBN: 978-3-8440-2660-3.*

1.4 *"Earth-moving machinery; definitions of dimension and symbols; base machine". ISO6746-1. 1988.*

1.5 *R. Finzel, S. Helduser, D.S. Jang. Electro-Hydraulic Dual-Circuit System to Improve the Energy Efficiency of Mobile Machines. 7th International Fluid Power Conference. Aachen 2010.*

1.6 *M. Inderelst, S. Losse, S. Sgro, H. Murrenhoff. Energy Efficient System Layout for Work Hydraulics of Excavators. The Twelfth International Conference on Fluid Power. May 18-20, 2011. Tampere. Finland.*

1.7 *J.F. Blackburn, G. Reethof, J. L. Sherarer. Fluid Power Control. The M.I.T. Press. Cambridge, Massachussetts, and London, England. ISBN 10-0262020068.*

1.8 *H.K. Choeng. (2011). Negative Control Type Hydraulic System. EP 2 341 193 A2. Application number: 10197176.0.*

1.9 *W. Liao, S. Chen, C. Chen, H. Du, F. Wang, N. Zhao. Research of Negative Flow Control Characteristics for Axial Piston Pump Based on Hydraulic and Mechanical Co-simulation. 3rd International Conference on System Science, Engineering Design and Manufacturing Informatization. 2012. IEEE* 978-1-4673-0915-8/12.

1.10 *M.A. Cobo, R.G. Ingram, E.A. Reiners, M.F. Vande Wiele. (1999). Positive flow Control System. Application number: US 976,152.*

1.11 *K. Heybroek, J. Larsson, J-O Palmberg. The Potential of Energy Recuperation in Valve Controlled Mobile Hydraulic Systems. The 11th Scandinavian Conference on Fluid Power. SICFP'09. June 2-4. 2009. Linkoping. Sweden.*

1.12 *R. Finzel, S. Helduser. Energy-Efficient Electro-Hydraulic Control Systems for Mobile Machinery/Flow Matching. 6th International Fluid Power Conference. 2008. Dresden. Germany.*

1.13 *R. Finzel, S. Helduser. New Electro-Hydraulic Control Systems for Mobile Machinery. Fluid Power and Motion Control. 2008.*

1.14 National Emission Inventory (NEI) Air Pollutant Emission Trends Data. U.S. Environmental Protection Agency (EPA). 2005. Available on: http://www.epa.gov/ttn/chief/trends/index.html#tables.

1.15 Emission Standard Directive 97/68/EC. Available on: http://ec.europa.eu/enterprise/sectors/mechanical/documents/legislation/emissions-non-road/index_en.htm.

1.16 Non Road Diesel Engine EPA TIER Standards. Available on: http://www.epa.gov/otaq/nonroad-diesel.htm.

1.17 https://www.deere.com/en_US/services_and_support/engine-information/understanding-emission-regulations/understanding-emission-regulations.page

1.18 R- Paoluzzi. Trends and Constrains for Fluid Power in Mobile Machinery. Proceedings of the 7th JFPS. Symposium on Fluid Power. 2008. Toyama.

1.19 M. Borghi, E.Specchia, B. Zardin (2009). Numerical Analysis of the Dynamic Behaviour of Axial Piston Pumps and Motors Slipper Bearings. SAE International Journal of passenger cars - Mechanical System, vol. 2, p. 1285-1302, ISSN: 1946-3995.

1.20 M. Zecchi, M. Ivantysynova (2012). Cylinder Block / Valve Plate Interface – a Novel Approach to Predict Thermal Surface. In 8th International Fluid Power Conference Dresden, March 26-28, 2012.

1.21 Wu, D., Burton, R., Schoenau, G., Bitner, D. (2007). Analysis of a Pressure – Compensated Flow Control Valve. In ASME Journal of Dynamic Systems, Measurement and Control, March 2007, Vol.129, pp. 203-211.

1.22 C. Dolcin, F. Ferretti, C. Striegan, M. Scolari. Development of Semi-Empirical Model of Electro-Hydraulic Spool Positioning Systems for Load Sensing Flow Sharing Mains Valve. Proceedings of the 7th FPNI PhD Symposium on Fluid Power. 2012. Reggio Emilia. Italy.

1.23 A. Lettini, M. Havermann, M. Guidetti, A. Fornaciari. Improved Functionalities and Energy Saving Potential on Mobile Machines Combining Electronics with Flow Sharing Valve and Variable Displacement Pump. 7th International Fluid Power Conference. 2010. Aachen. Germany.

1.24 http://www.boschrexroth.com/en/xc/products/product-groups/mobile-hydraulics/systems-and-functional-modules/virtual-bleed-off-vbo/index.

1.25 M. Scherer, M. Geimer, B. Weiss. Contribution on Control Strategies of Flow-On-Demand Hydraulic Circuits. The 13th Scandinavian International Conference on Fluid Power. SICFP2013. Linkoping. Sweden.

1.26 M. Axin, B. Eriksson, J.O. Palmberg. Energy Efficient Load Adopting System without Load Sensing – Design and Evaluation. The 11th Scandinavian Conference on Fluid Power. SICFP2009. Linkoping. Sweden.

1.27 K. Kim, H. Ahn, D.S. Jang. Development of the Independent Swing System for a Fuel Efficient Hydraulic Excavator. Proceedings of the 8th International Fluid Power Conference. IFK2012. Dresden. Germany.

1.28 J. Zimmermann, M. Ivantysynova.. Reduction of Engine and Cooling Power by displacement Control. Proc. of 6th FPNI-PhD Symp. 2010. West Lafayette, USA.

1.29 G. Vael, P. Acthen, J. Potma. Cylinder Control with Floating Cup Hydraulic Transformer. The 8th Scandinavian Conference on Fluid Power. SICFP2003. Tampere. Finland.

1.30 J.L. Pfaff, E.P. Hamkins. (2012). Flow Summation System for Controlling a Variable Displacement Hydraulic Pump. Application number: US 8,215,107B2.

1.31 A.H. Hansen, H.C. Pedersen, T.O. Andersen, L. Wachmann. Investigation of Energy Saving Separate Meter-In Separate Meter-Out Control Strategies. The 12th Scandinavian Conference on Fluid Power- SICFP2011. Tampere. Finland.

1.32 M. Linjama. Digital Fluid Power – State of the Art. The 12th Scandinavian Conference on Fluid Power. SICFP2011. Tampere. Finland.

1.33 M. Karvonen, M. Heikkila, M. Huova, M. Linjama, K. Huhtala. Simulation Study – Improving Efficiency in Mobile Boom by Using Digital Hydraulic Power Management System. The 12th Scandinavian International Conference on Fluid Power. SICFP2011. Tampere. Finland.

1.34 A. Gambarotta, P. Casoli, N. Pompini, L. Riccò (2014) .Co-simulation and control-orientated modelling in the development of a hydraulic hybrid system" , 14th Stuttgart International Symposium "Automotive and Engine Technology" Stoccarda (D) 18-19 Marzo 2014.

1.35 P. Casoli, A. Gambarotta N. Pompini, L. Riccò. "Coupling excavator hydraulic system and internal combustion engine models for the Real-Time simulation" Control Engineering Practice (2015), pp. 26-37 DOI information: 10.1016/j.conengprac.2015.04.003.

1.36 *H. Kim, J. Choi, K. Yi. Development of Supervisory Control Strategy for Optimized Fuel Consumption of the Compound Hybrid Excavator. Proceedings of the Institution of Mechanical Engineering, Part D: Journal of Automobile Engineering. 2012. DOI: 10.1177/0954407012447019.*

1.37 *T. Wang, Q. Wang, T. Lin. Improvement of Boom Control Performance for Hybrid Hydraulic Excavator with Potential Energy Recovery. Automation in Construction 30(2013) 161-169. http://dx.doi.org/10.1016/j.autcon.2012.11.034.*

1.38 *D. Wang, C. Guan, S. Pan, M. Zhang, X. Lin. Performance Analysis of Hybrid Excavator Powertrain Hybridization. Automation in Construction 10(2009) 249-257. doi: 10.1016/j.autcon.2008.10.001.*

1.39 *M. Erkkila, F. Bauer, D. Feld. Universal Energy Storage and Recovery System – A Novel Approach for Hydraulic Hybrid. The 13th Scandinavian Conference on Fluid Power. SICFP2013. Linkoping. Sweden.*

1.40 *Bosch Rexroth. Hydraulic Fly-Wheel (HFW). http://www.boschrexroth.com/en/xc/products/product-groups/mobile-hydraulics/systems-and-functional-modules/hydraulic-flywheel-hfw/index*

1.41 *M. Ochiai, S. Ryu. Hybrid in Construction Machinery. Proceeding of the 7th JFPS International Symposium on Fluid Power. 2008. Toyama. ISBN: 4-931070-07-X.*

1.42 *T. Lin, Q. Wang, B. Hu, W. Gong. Research on the Energy Regeneration Systems for Hybrid Hydraulic Excavators. Automation in Construction 19 (2010) 1013-1026. doi:10.1016/j.autcon.2010.08.002.*

1.43 *T. Wang. Q. Wang. Design and Analysis of Compound Potential Energy Regeneration System for Hybrid Hydraulic Excavator. Proceedings of the Institution of Mechanical Engineering, Part I: Journal of Systems and Control Engineering. 2012. DOI: 10.1177/0959651812456642.*

1.44 *T. Lin, Q. Wang, B. Hu, W. Gong. Development of Hybrid Powered Hydraulic Construction Machinery. Automation in Construction 19 (2010) 11-19. doi:10.1016/j.autcon.2009.09.005.*

1.45 *J. Amrhein. PRB – Regeneration of Potential Energy while Boom-Down. Proceedings of the 8th International Fluid Power Conference. IFK2012. Dresden. Germany.*

1.46 *K. Schneider. Liebherr Pactronic – Hybrid Power Booster. Proceedings of the 8th International Fluid Power Conference. IFK2012. Dresden. Germany.*

1.47 *http://www.cat.com/en_AU/articles/customer-stories/hybrid-excavatorkeepsrailprojectontrack.html.*

1.48 http://www.komatsu.com/CompanyInfo/press/20080513151136045 88.html.

1.49 http://www.hitachi.com/environment/showcase/solution/industrial/hybrid_excavator.html.

Chapter 2: **Excavator Mathematical Modelling**

This chapter deals with the excavator under investigation mathematical modelling.

A brief description of the machinery is initially reported, then the mathematical modelling approach will be presented and discussed as well as the sub-systems mathematical models.

2.1 Eurocomach® ES85ZT Excavator

The MHM selected for the study of energy saving solutions, presented and discussed in this thesis, is a middle size excavator manufactured by the Eurocomach® [*2.1*], reported in Fig.2.1.

Figure 2.1: Eurocomach® ES85ZT Excavator.

The ES85ZT is a middle size excavator, with an operative weight of 9000 kg, equipped with a Yanmar® naturally aspired Diesel engine (ICE) of 3319 cm^3 with a maximum rated power of 46.3 kW at 2200 r/min.

The hydraulic system is of the Load Sensing Flow Sharing type.

The FGU is composed of a variable displacement axial piston pump, which is the main pump of the system, with a maximum displacement of 84 cm^3/r, belonging to the MVP series by Casappa®, controlled via a flow compensator (FC), a pressure compensator (PC) and a torque limiter (TL), and of a fixed displacement external gear pump, which is the system pilot pump, with a displacement of 9.17 cm^3/r, belonging to the PL series manufactured by Casappa®. The pilot circuit pressure is kept constant at a value of 3 MPa via a pressure relief valve.

The DFCV is composed of LS Flow Sharing valve sections, one for each user, and belongs to the DPX series manufactured by Walvoil®.

The standard users of the excavator are the boom, arm, bucket, blade and boom-swing cylinders, and the turret and travels motors.

The excavator OEM declares a mean fuel consumption of 8.7 l/h during the typical working cycle.

Figure 2.2 reports the simplified ISO scheme of the excavator hydraulic circuit, where only the main users are reported, while its complete ISO scheme is reported in Appendix 1.

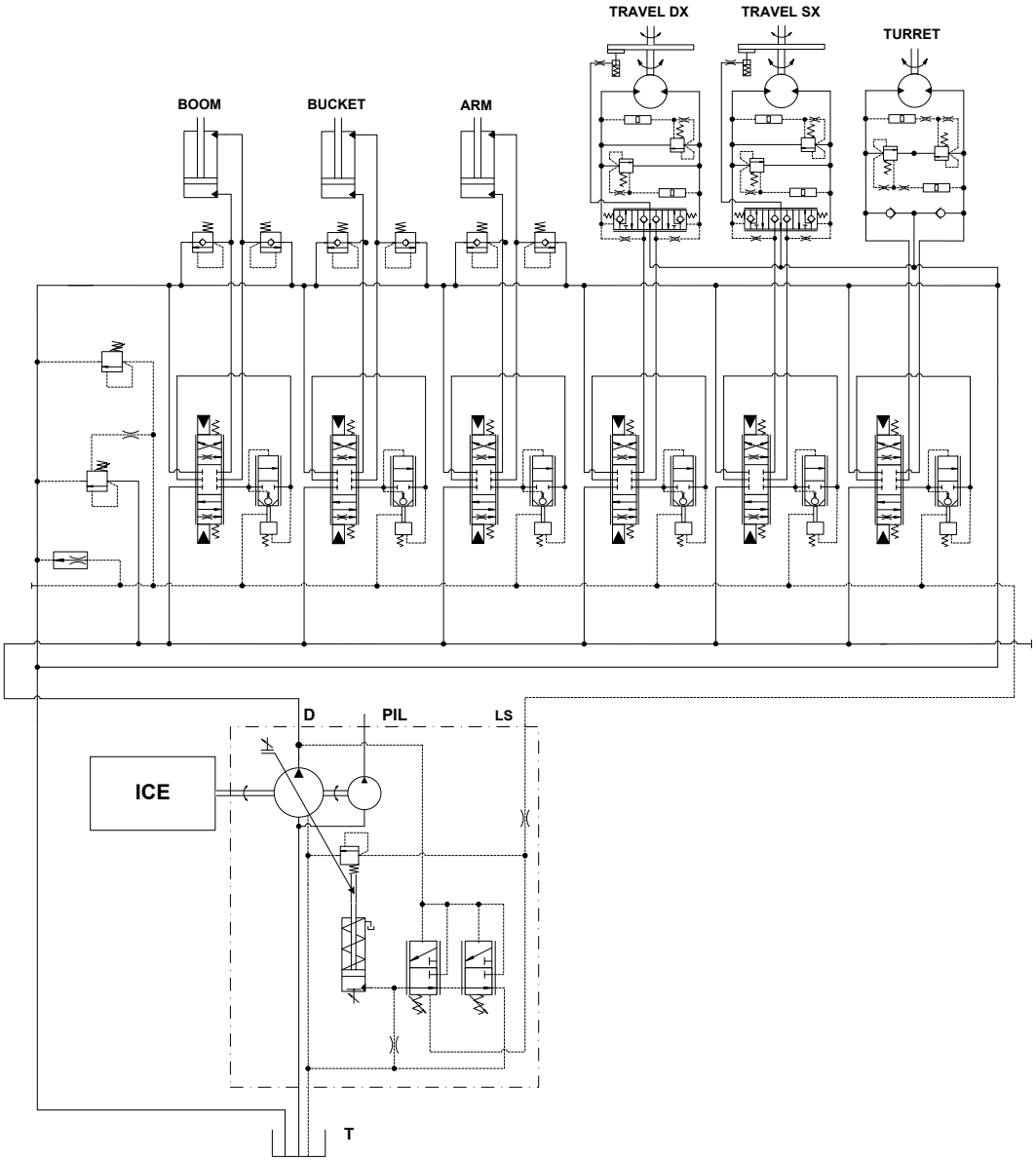

Figure 2.2: ES85ZT Simplified ISO Scheme.

2.2 Mathematical Modelling

The mathematical modelling of physical systems has become one of the most adopted tool for engineering research, from the design of new components to the system optimization and control.

The available mathematical approaches differ for the types of simplifications adopted considering the modelled system. The larger the number of physical phenomenon and the higher their spatial distribution[16] are, the system complexity and computational time required to solve the equations will increase. Thus the more suitable modelling approach has to be firstly selected according to the objective of the study.

For example, many researchers take advantage of the 3-D modelling approach combining the CFD and/or the FEM in order to model complex physical phenomenon in components [*2.2, 2.3, 2.4, 2.5*]. Others, which study the system control, adopt more simplified modelling approaches, where the physical phenomenon considered are lumped in elements of the system, based on transfer functions [*2.6, 2.7*] or neural networks [*2.8*]. Recent studies on complex system, like excavators, have been conducted exploiting different modelling approaches, from a very simplified methodology, adopting several map based models [*2.9*], only focused on energy consumption of the machine, to others which model the hydraulic system exploiting a lumped parameter approach, considering many different physical phenomenon [*2.10*], but requiring long computational time.

The aim of this thesis is that of propose and optimize energy saving solutions for mobile hydraulic systems and quantify their impact on both the machinery fuel consumption and performance[17], even during transient functioning. Consequently a modelling approach which considers the dynamic response[18] of the components is necessary.

A lumped parameter modelling approach, with the usage of some map based correlations, has been adopted for the dynamic modelling of the excavator.

The assumptions made and the boundary conditions of the system are listed below:

- constant atmospheric conditions: air density and temperature;
- constant reservoir pressure;

[16] When modelling a physical system it is possible consider a distributed system, in which all dependent variables are functions of time and one or more spatial variables (solvable with partial differential equations), or a lumped system, in which the dependent variables of interest are a function of only the time (solvable with ordinary differential equations).
[17] Compared with the standard version of the machinery, which is the baseline.
[18] In a variable displacement axial piston pump the main dynamic is that related to the swash plate tilting, while if a directional flow control valve is the main spool positioning.

- constant hydraulic fluid temperature, viscosity and bulk modulus;
- fluid inertial effects were neglected;
- mechanical bodies were considered as rigid;
- one degree of freedom for mechanical joints;
- no friction in revolute pairs.

Table 2.1 reports the numerical value of the constant parameters.

Table 2.1: Boundary Conditions of the System.	
Air Density	1.16 kg/m^3
Air Temperature	25°C
Reservoir Pressure	0.05 MPa
Hydraulic Fluid Temperature	40°C
Hydraulic Fluid Absolute Viscosity	51 cP
Hydraulic Fluid Bulk Modulus	1700 MPa

Other assumptions made will be stated in the detailed description of the sub-systems models.

The mathematical models were developed using the LMS AMESim® software.

2.2.1 Diesel ICE

The mathematical modelling of the ICE for fuel consumption prediction in MHM model has always been a non-trivial challenge. Typically those who studies the hydraulic system evaluate the power consumption at the FGU shaft [*2.9*], others [*2.10*] consider the ICE as just a static fuel consumption map.

Although the pump speed is typically kept constant during the simulated working cycle.

A recent study [2.11] has pointed out the not negligible impact of transient on fuel consumption. Moreover the ICE speed variates during the working cycle because of the influence of the torque required by the working hydraulics.

For these reasons the ICE mathematical model developed and presented is able to both calculate the engine fuel consumption and simulate the engine regulator behaviour during the performed cycles.

Figure 2.3 represents the ICE input/output causality, while Fig.2.4 reports the ICE block diagram adopted for the modelling.

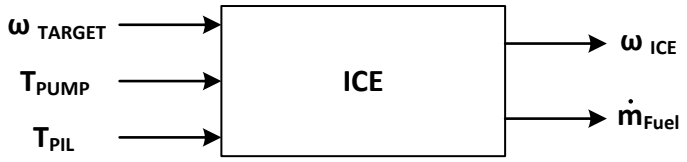

Figure 2.3: Diesel ICE Causality.

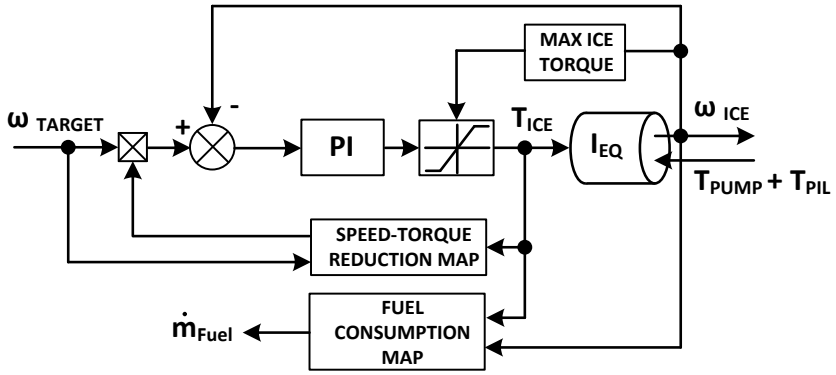

Figure 2.4: Diesel ICE Block Diagram.

The ICE model consists of a feedback circuit where a PI regulator calculates the engine torque (T_{ICE}), (*Eq.2.1*), required for reducing the error between the speed set point (ω_{Target}) and the actual speed (ω_{ICE}).

$$T_{ICE^*} = \left[\left(\omega_{Target} - \omega_{ICE}\right) \cdot k_p\right] + \left[k_i \int \left(\omega_{Target} - \omega_{ICE}\right) dt\right] \qquad (2.1)$$

The engine torque at different angular velocities is limited to the higher value declared by the manufacturer. (*Eq.2.2*)

$$\begin{cases} if\ T_{ICE^*} < T_{MAX}(\omega_{ICE}) \rightarrow\ T_{ICE} = T_{ICE^*} \\ if\ T_{ICE^*} \geq T_{MAX}(\omega_{ICE}) \rightarrow\ T_{ICE} = T_{MAX}(\omega_{ICE}) \end{cases} \qquad (2.2)$$

The PI regulator parameters have been defined in order to match the engine speed variations observed in transient operations during the experimental activity. Since the rotational speed at which the engine levels out decreases when the torque increases, an experimental map (see Chapter 3) has been introduced in the model for calculating a reduction coefficient for the set point speed as a function of the engine torque.

The actual engine speed (ω_{ICE}), (*Eq.2.3*), results from the dynamic equilibrium of a rotary load, whose moment of inertia (I_{EQ-IP}) equals the summation of FGU one and the ICE one, and the viscous and Coulomb friction torques, defined just considering the FGU one.

$$T_{ICE} - (T_{PUMP} + T_{PIL}) = \dot{\omega}_{ICE} \cdot I_{EQ-IP} + \omega_{ICE} \cdot b_{FGU} + T_{C_{FGU}} \qquad (2.3)$$

The instantaneous engine fuel consumption ($\dot{m}_{Fuel}$) is obtained from a steady state fuel consumption map as a function of torque and rotational speed defined experimentally (see Chapter 3).

2.2.2 Flow Generation Unit

The FGU, as previously mentioned, is composed of a main pump, a variable displacement axial piston pump, and of a pilot pump, an external gear pump. The detailed ISO scheme of the FGU is reported in Fig.2.5.

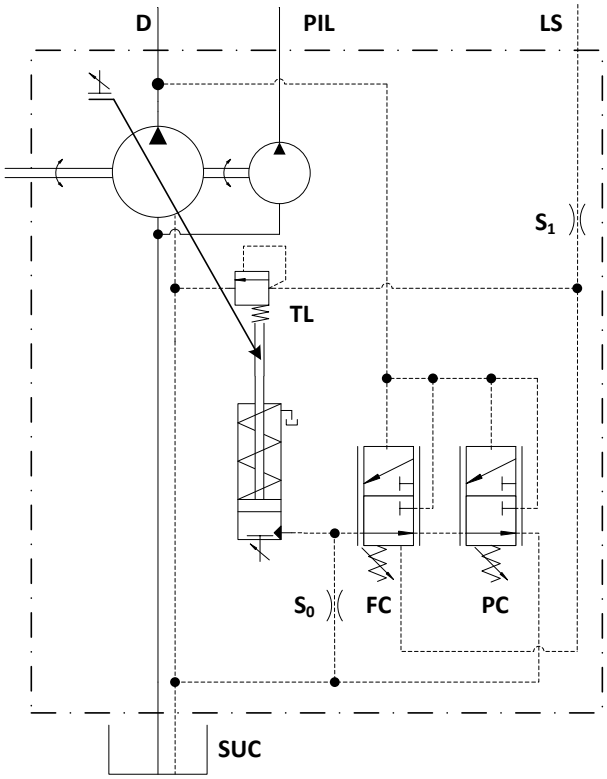

Figure 2.5: ISO Scheme of the FGU.

Being these two units linked together on the same shaft of the ICE, even in standby functioning of the excavator, i.e. when no movements of the implement hydraulics are required by the operator and thus the main pump displacement is almost zero, the ICE imposed load is due to the main pump dragging and to the pilot pump working condition. Therefore, a dragging load has been experimentally defined (see Chapter 3), and consequently not considered into the hydraulic-mechanical efficiency defined map.

Main Pump

The main pump is controlled via three regulators: the FC, which maintains the pressure drop between the LS pressure and the pump delivery (D) pressure almost constant by tilting the swash plate of the pump; the PC, which limits the maximum pump delivery pressure; and the TL, which limits the maximum pump torque modulating[19] the LS pressure sensed in the FC dedicated port. Figure 2.6 reports the theoretical operative power diagram of the main pump functioning.

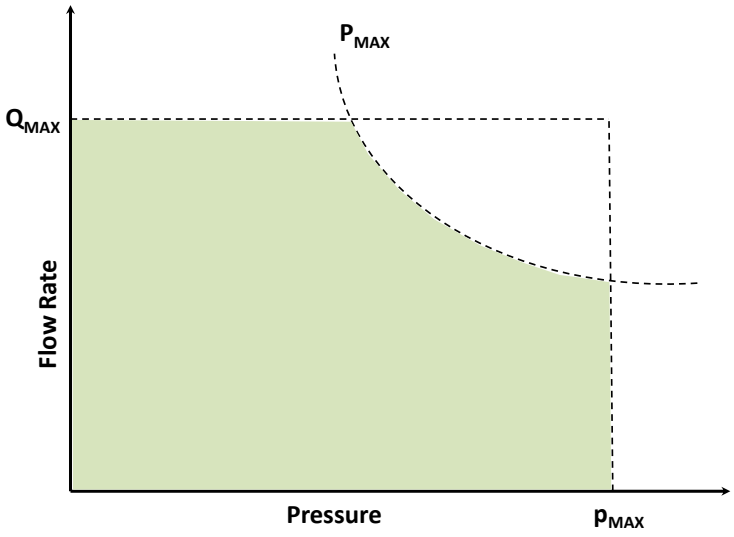

Figure 2.6: Main Pump Power Diagram.

The main pump model reproduces its principal dynamics, i.e. the swash plate tilting, which is the slowest dynamic in this sub-system. A simplified modelling approach based on both physical equations and experimental correlations has been adopted. Figure 2.7 reports the input/output causality of the main pump and its regulators.

[19] The modulation of the TL is possible to the presence of the calibrated orifice S_1, which allow to uncouple the LS pressure defined in the system and the LS pressure sensed by the FC. When the TL acts, due to a higher torque required in comparison of the TL calibration, the LS pressure sensed by the FC regulator is lower than the real LS pressure of the system.

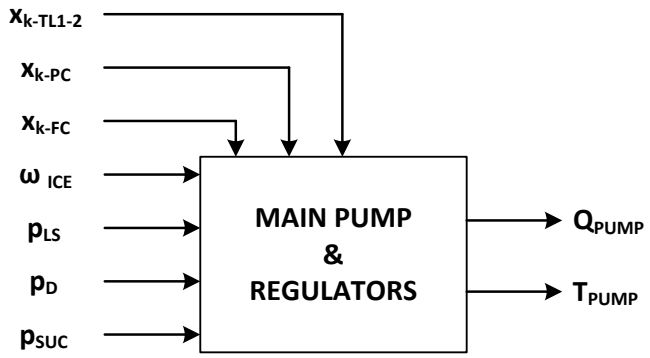

Figure 2.7: Main Pump and Regulators Causality.

The pump outlet flow rate (Q_{PUMP}), (*Eq.2.4*), and the pump torque (T_{PUMP}), (*Eq.2.5*), are both function of the instantaneous swash plate angular position (α) and the pump efficiencies.

$$Q_{PUMP} = \omega_{ICE} \cdot V_d(\alpha) \cdot \eta_V(p_D, \omega_{ICE}, \alpha) \tag{2.4}$$

$$T_{PUMP} = \frac{V_d(\alpha) \cdot (p_D - p_{SUC})}{2\pi} \cdot \frac{1}{\eta_{hm}(p_D, \omega_{ICE}, \alpha)} \tag{2.5}$$

The volumetric and hydro-mechanical efficiency were experimentally identified [*2.12*], according to the ISO4409-1986 standard, varying the pump differential pressure between pump delivery and suction ports, the pump speed and the pump swash plate position. Figure 2.8 represents the pump normalized overall efficiency at maximum displacement.

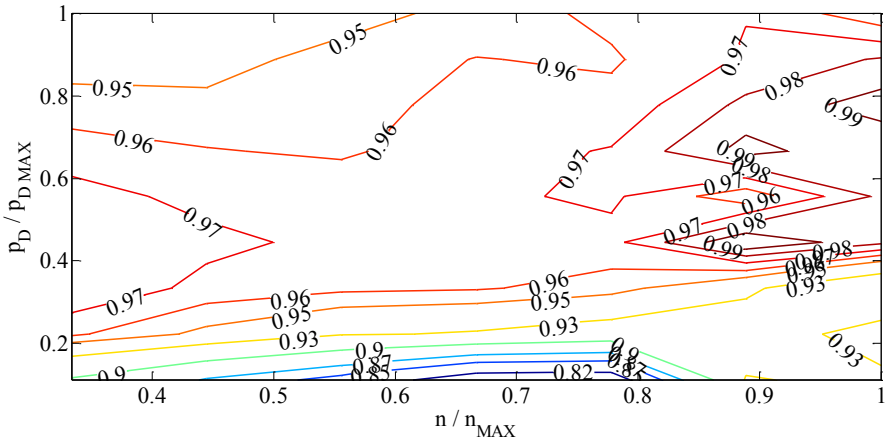

Figure 2.8: Pump Normalized Overall Efficiency η_g/η_{gMAX} at $\alpha/\alpha_{MAX}=1$.

The swash plate instantaneous angular position (α) is evaluated by (*Eq.2.6*), which defines the swash plate equilibrium due to the acting forces as represented in the scheme of Fig.2.9.

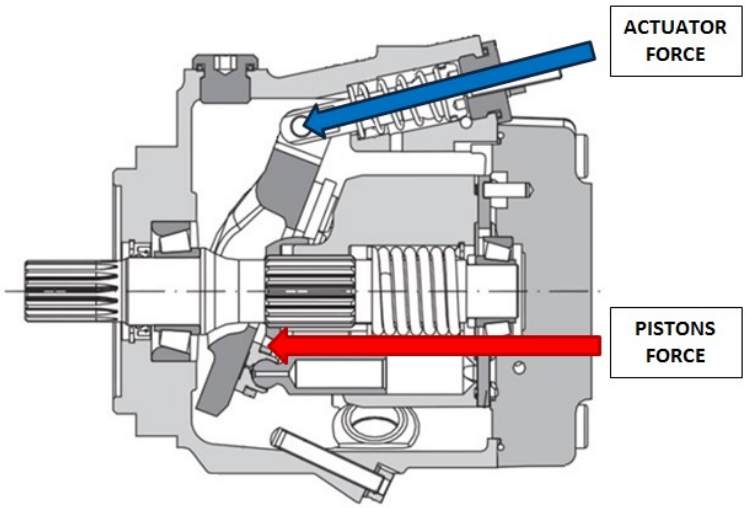

Figure 2.9: Pump Swash Plate Free Body Diagram.

$$I_{EQ-SP} \cdot \ddot{\alpha} + b_{SP} \cdot \dot{\alpha} = \sum_{n=1}^{N} T_n - T_{ACT} \qquad (2.6)$$

The I_{EQ-SP} is the term that summarizes the swash plate inertia considering also the pistons and slippers[20]. It was defined with the aid of the pump CAD assembly. The swash plate assembly viscous friction coefficient (b_{SP}) was set on the basis of a dedicated experimental activity [*2.13*] (see Chapter 3).

$\sum_{n=1}^{N} T_n$ is the resulting torque due to the contribution of the n-th piston force acting on the swash plate. The determination of this torque is typically obtained through a detailed modelling of the pumping system, where all the pistons are modelled, requiring the identification of a large numbers of parameter (e.g., pressure of each pumping piston, damping effects, pistons masses, lengths and diameters, valve plate geometry, etc.) [*2.14*]. Being the intent that of replicating the swash plate dynamics and neither that of optimizing nor designing the pumping unit, an experimental correlation has been defined [*2.13*] (see Chapter 3) for the pistons resulting torque. This was achieved by measuring the pressure in the swash plate actuator chamber at given values of pump delivery pressure (p_D), pump speed (ω_{ICE}), and

[20] The n-th piston-slipper moment of inertia has been reported on the swash plate rotary axis with the aid of the Huygens theorem.

swash plate angular position (α). During steady-state functioning conditions since $\dot{\alpha} \cong 0$, and $\ddot{\alpha} \cong 0$, (*Eq.2.6*) becomes (*Eq.2.7*).

$$\sum_{n=1}^{N} T_n = T_{ACT} \tag{2.7}$$

Knowing the area of the control actuator piston (A_{ACT}) and the arm of the actuating force (r_{ACT}), (*Eq.2.7*) can be rewritten as (*Eq.2.8*).

$$\sum_{n=1}^{N} T_n = p_{ACT}(p_D, \omega_{ICE}, \alpha) \cdot A_{ACT} \cdot r_{ACT} \tag{2.8}$$

Figure 2.10 reports the experimental correlation defined through a surface fitting tool, between the pressure in the pump actuator chamber and the swash plate angular position and the pump outlet pressure, for a variation of the pump shaft rotational speed between 850 r/min – 2300 r/min.

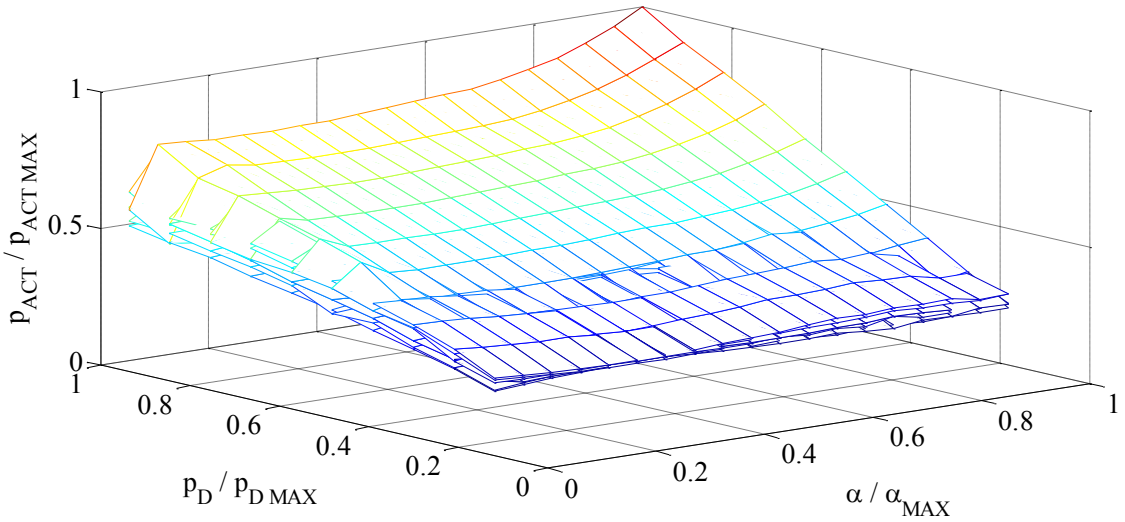

Figure 2.10: $p_{ACT}(p_D, \omega_{ICE}, \alpha)$ Experimental Correlation.

The swash plate actuator torque is evaluated by (*Eq.2.9*), in both dynamic and steady-state conditions.

$$T_{ACT} = p_{ACT} \cdot A_{ACT} \cdot r_{ACT} \tag{2.9}$$

The swash plate actuator chamber pressure is instantaneously defined by the pump regulators (FC, PC and TL) depending on the actual working conditions and the regulator calibrations.

Figure 2.11 represents the schematic drawing of the FC and PC regulators assembly while Fig.2.12 reports its fluid dynamic model.

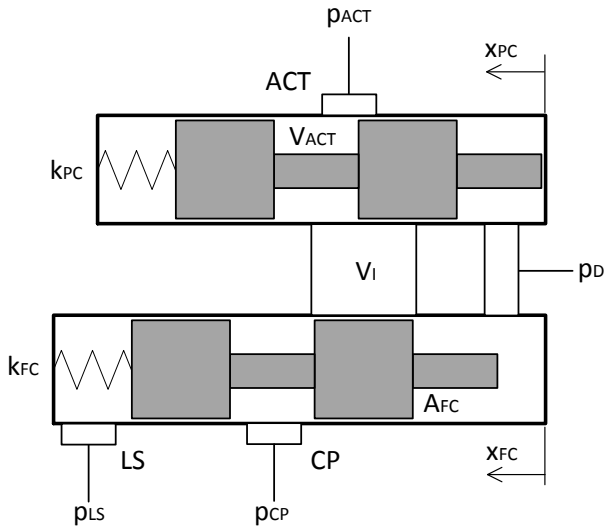

Figure 2.11: Schematic Drawing of the FC and PC Regulator Assembly.

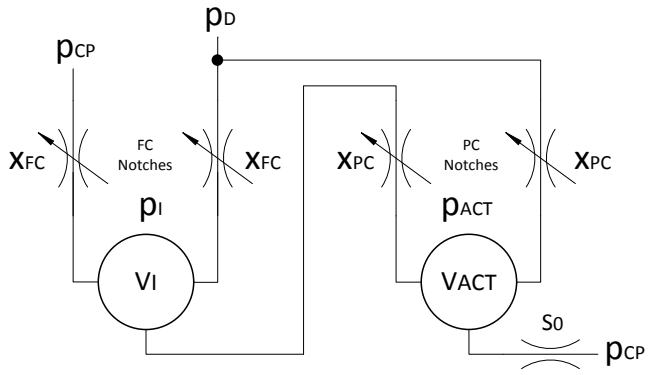

Figure 2.12: Fluid Dynamic Model of the FC and PC Regulator Assembly.

According to the schematic drawing and to the fluid dynamic model scheme reported, (*Eq.2.10*) defines the instantaneous variation of pressure of the swash plate actuator chamber.

$$\frac{dp_{ACT}}{dt} = \frac{B}{\rho} \cdot \frac{1}{V_{ACT}} \cdot \sum \dot{m}_{ACT} \qquad (2.10)$$

The summation term represents the net mass flow rate entering or leaving the actuator chamber volume. This is obtained by considering the contribution of all orifices connected to the considered volume, (*Eq.2.11*).

$$\sum \dot{m}_{ACT} = \dot{m}_{PC1} + \dot{m}_{PC2} - \dot{m}_{S0} \tag{2.11}$$

According to the conventions made in the modelling scheme previously reported, the mass flow rates of (*Eq.2.11*) are defined in (*Eq.2.12*), (*Eq.2.13*) and (*Eq.2.14*) respectively.

$$\begin{cases} if\ (p_I - p_{ACT}) \geq 0 \rightarrow \dot{m}_{PC1} = \rho \cdot cd_{PC1} \cdot A_{PC1}(x_{PC}) \cdot \sqrt{\dfrac{2|p_I - p_{ACT}|}{\rho}} \\ if\ (p_I - p_{ACT}) < 0 \rightarrow \dot{m}_{PC1} = -\rho \cdot cd_{PC1} \cdot A_{PC1}(x_{PC}) \cdot \sqrt{\dfrac{2|(p_I - p_{ACT})|}{\rho}} \end{cases} \tag{2.12}$$

$$\dot{m}_{PC2} = \rho \cdot cd_{PC2} \cdot A_{PC2}(x_{PC}) \cdot \sqrt{\frac{2|p_D - p_{ACT}|}{\rho}} \tag{2.13}$$

$$\dot{m}_{S0} = \rho \cdot cd_{S0} \cdot A_{S0} \cdot \sqrt{\frac{2|p_{ACT} - p_{CP}|}{\rho}} \tag{2.14}$$

The pressure in the intermediate chamber (p_I), between the FC and the PC, is evaluated through (*Eq.2.15*).

$$\frac{dp_I}{dt} = \frac{B}{\rho} \cdot \frac{1}{V_I} \cdot \sum \dot{m}_I \tag{2.15}$$

The net mass flow rate (*Eq.2.16*) to the intermediate chamber is defined by the mass flow rates entering (*Eq.2.17*) and leaving (*Eq.2.18*) the considered volume.

$$\sum \dot{m}_I = \dot{m}_{FC1} - \dot{m}_{FC2} \tag{2.16}$$

$$\dot{m}_{FC1} = \rho \cdot cd_{FC1} \cdot A_{FC1}(x_{FC}) \cdot \sqrt{\frac{2|p_D - p_I|}{\rho}} \tag{2.17}$$

$$\dot{m}_{FC2} = \rho \cdot cd_{FC2} \cdot A_{FC2}(x_{FC}) \cdot \sqrt{\frac{2|p_I - p_{CP}|}{\rho}} \qquad (2.18)$$

The PC and the FC instantaneous spool positions, (*Eq.2.19*) and (*Eq.2.20*) respectively, are evaluated through the Newton's second law. Static and dynamic friction forces are evaluated by use of the Karnopp friction model and considering the Stribeck effect, static and dynamic friction coefficients are assumed to be constant, while hydrodynamic forces have been neglected.

$$\ddot{x}_{PC} \cdot m_{PC} + \dot{x}_{PC} \cdot c_{PC} + (x_{PC} + x_{k-PC}) \cdot k_{PC} = p_D \cdot A_{PC} \qquad (2.19)$$

$$\ddot{x}_{FC} \cdot m_{FC} + \dot{x}_{FC} \cdot c_{FC} + (x_{FC} + x_{k-FC}) \cdot k_{FC} = (p_D - p_{LS'}) \cdot A_{FC} \qquad (2.20)$$

Where x_k are the regulators springs pre-compressions.

Figures 2.13 and Fig.2.14 depict the TL schematic drawing and its fluid dynamic model scheme respectively.

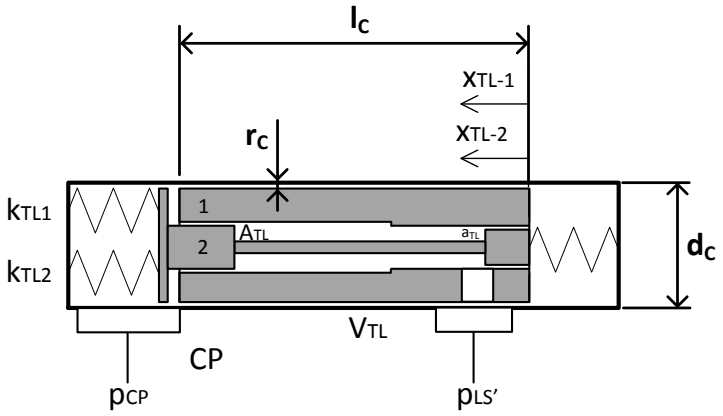

Figure 2.13: Schematic Drawing of the TL Regulator.

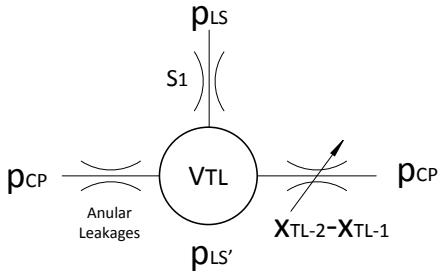

Figure 2.14: Fluid Dynamic Model of the TL Regulator.

The LS modulated pressure ($p_{LS'}$) is defined by the TL action. Since the pump torque is lower than the maximum permitted one $p_{LS'} = p_{LS}$ otherwise $p_{LS'} < p_{LS}$ and it is evaluated through (*Eq.2.21*).

$$\frac{dp_{LS'}}{dt} = \frac{B}{\rho} \cdot \frac{1}{V_{LS'}} \cdot \sum \dot{m}_{LS'} \tag{2.21}$$

The net mass flow rate (*Eq.2.22*) to the torque limiter chamber is defined by the mass flow rates entering (*Eq.2.23*) and leaving (*Eq.2.24*), (*Eq.2.25*), (*Eq.2.26*) the chamber volume.

$$\sum \dot{m}_{LS'} = \dot{m}_{S1} - \dot{m}_{TL} - \dot{m}_{L1} - \dot{m}_{L2} \tag{2.22}$$

$$\dot{m}_{S1} = \rho \cdot cd_{S1} \cdot A_{S1} \cdot \sqrt{\frac{2|p_{LS} - p_{LS'}|}{\rho}} \tag{2.23}$$

$$\dot{m}_{TL} = \rho \cdot cd_{TL} \cdot A_{TL}(x_{TL2} - x_{TL1}) \cdot \sqrt{\frac{2|p_{LS} - p_{CP}|}{\rho}} \tag{2.24}$$

$$\dot{m}_{L1} = \rho \cdot \frac{\pi \cdot d_{C-TL} \cdot (r_{C-TL})^3}{12 \cdot \mu \cdot l_{C-TL}} \cdot |p_{LS'} - p_{CP}| \tag{2.25}$$

$$\dot{m}_{L2} = \rho \cdot k_{L_{L2}} \cdot |p_{LS'} - p_{CP}| \tag{2.26}$$

The TL external spool instantaneous position, (*Eq.2.27*), is defined through a geometrical correlation function of the swash plate angular position, at which is mechanically linked. While the TL internal spool instantaneous position is defined by (*Eq.2.28*).

$$x_{TL1} = f(\alpha) \tag{2.27}$$

$$\ddot{x}_{TL2} \cdot m_{TL2} + \dot{x}_{TL2} \cdot c_{TL} + (x_{k-TL1} \cdot k_{TL1} + x_{k-TL2} \cdot k_{TL2}) + (x_{TL2} - x_{TL1}) \cdot (k_{TL2} + k_{TL1}) = (A_{TL} - a_{TL}) \cdot p_{LS'} \tag{2.28}$$

The maximum values of the discharge coefficients of each orifice of the regulators have been set on the basis of literature [*2.15*], thereafter the instantaneous discharge coefficient value is evaluated as a function of Reynolds number, to account for partially developed or fully turbulent conditions.

Pilot Pump

The pressure of the excavator pilot circuit is maintained at a constant value of 3 MPa in order to allows the users control. The pilot pump, whose input/output causality scheme is reported in Fig.2.15, is pressure controlled via a pressure relief valve which limits the pilot pressure.

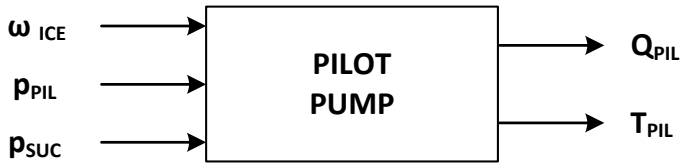

Figure 2.15: Pilot Pump Causality.

The pilot pump flow rate and torque are defined through (*Eq.2.29*) and (*Eq.2.30*) respectively.

$$Q_{PIL} = \omega_{ICE} \cdot V_d \cdot \eta_V \tag{2.29}$$

$$T_{PIL} = \frac{V_d \cdot (p_{PIL} - p_{SUC})}{2\pi \cdot \eta_{hm}} \tag{2.30}$$

Volumetric and hydraulic-mechanical efficiencies were considered as constant.

2.2.3 Directional Flow Control Valve

The directional flow control valve (DFCV) or distributor of the excavator is composed of a number of valve sections equal to the excavator users. In this section the mathematical model of a single section will be presented. Figure 2.16 reports its ISO scheme.

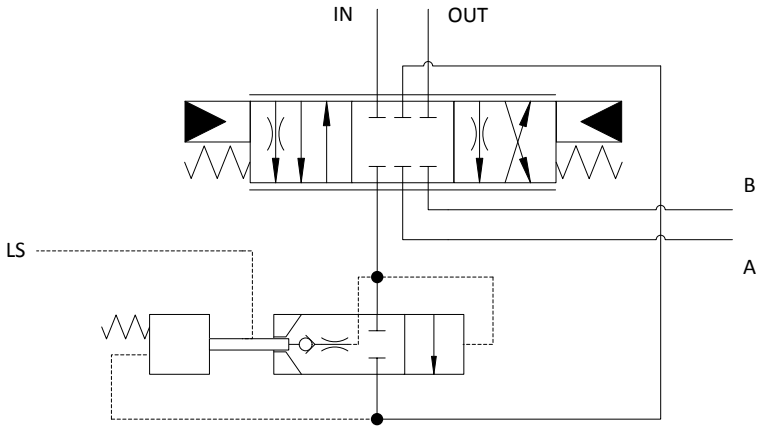

Figure 2.16: ISO Scheme of a Valve Section.

The valve section controls the related user inlet flow rate, i.e. the user velocity. A downstream local pressure compensator (LPC) is incorporated into the valve, which enables the LS flow sharing functionalities.

The valve has principally three operating modes: as a single user, or main loaded user, which defines the distributor LS[21] pressure; as a lower charged user, during multiple user operations, where the LPC throttle the flow rate in order to maintain the meter-IN orifice pressure drop[22] equal to the main loaded section; and as a check valve, if the load pressure is higher than the maximum system pressure, the LPC is mechanically closed by the local piston check (LPK) avoiding backflows.

Flow sharing is a useful feature when flow saturation condition[23] occurs. In this situation the meter-IN orifices pressure drop could not be kept at the desired value and thus a proportional reduction across all sections occurs. Consequently the activated users receive reduced flow rates without stop moving. This aspect is particularly useful in application where several simultaneously users are activated in the typical operating cycles, as for excavators.

[21] In this distributor, composed by nine valve sections, the LS pressure signal is common and is equal to the activated user with the highest load. This enables the LS compensation in the other less charged users.
[22] The meter-IN pressure drop is theoretically equal to the LS pressure drop defined by the pump FC. This metering pressure drop is maintained constant in each sections of the distributor by the LPCs.
[23] When the required flow rate by the users is higher than the maxim delivered flow rate by the main pump.

For the mathematical modelling, the following assumptions have been made:

- the valve main spool (MS) dynamics was neglected;
- the adjacent chambers were lumped together, when possible;
- internal leakages were neglected;
- hydro-dynamic forces were not considered.

Figure 2.17 reports the input/output causality assumed for the modelling of a valve section.

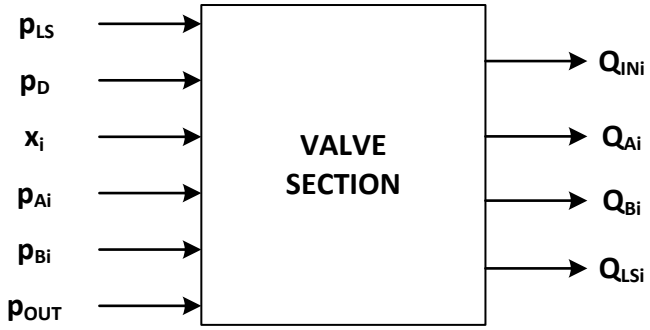

Figure 2.17: Valve Section Causality.

Figures 2.18 and 2.19 represent the valve section schematic drawing and fluid dynamic model respectively.

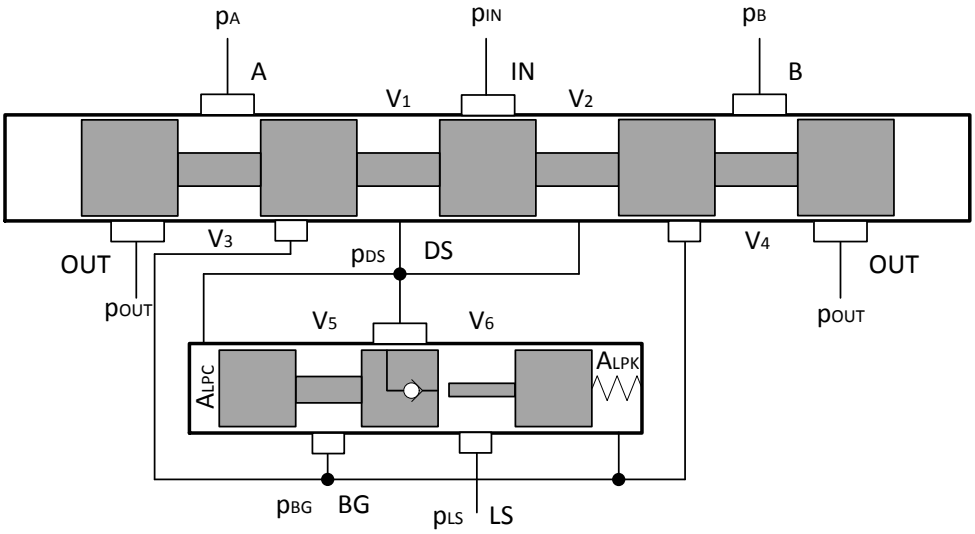

Figure 2.18: Schematic Drawing of a Valve Section.

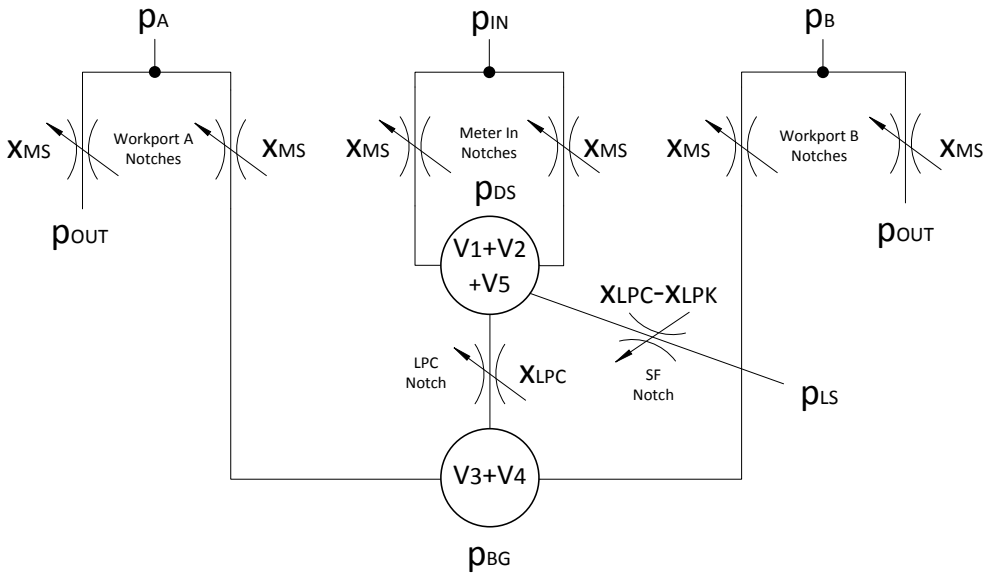

Figure 2.19: Fluid Dynamic Model of a Valve Section.

According to the schematic drawing and the fluid dynamic model scheme reported, the output variables of the model can be evaluated.

(*Eq.2.31*) defines the instantaneous variation of the downstream pressure (DS) in the internal chamber between the metering notches and the LPC.

$$\frac{dp_{DS}}{dt} = \frac{B}{\rho} \cdot \frac{1}{V_{DS}} \cdot \sum \dot{m}_{DS} \qquad (2.31)$$

The DS internal chamber volume is defined by (*Eq.2.32*), where V_1, V_2 and V_5 were defined with the aid of the valve section CAD model.

$$V_{DS} = V_1 + V_2 + V_5 \qquad (2.32)$$

The summation term, (*Eq.2.33*), represents the net mass flow rate entering or leaving the DS chamber volume. This is obtained by considering the contribution of all the orifices connected to the considered volume.

$$\sum \dot{m}_{DS} = \dot{m}_{IN1} + \dot{m}_{IN2} - \dot{m}_{LPC} - \dot{m}_{LS} \qquad (2.33)$$

According to the adopted conventions, the mass flow rates of (*Eq.2.33*) are defined by (*Eq.2.34*), (*Eq.2.35*), (*Eq.2.36*) and (*Eq.2.37*) respectively.

$$\dot{m}_{IN1} = \rho \cdot cd_{IN1} \cdot A_{IN1}(x_{MS}) \cdot \sqrt{\frac{2|p_D - p_{DS}|}{\rho}} \tag{2.34}$$

$$\dot{m}_{IN2} = \rho \cdot cd_{IN2} \cdot A_{IN2}(x_{MS}) \cdot \sqrt{\frac{2|p_D - p_{DS}|}{\rho}} \tag{2.35}$$

$$\dot{m}_{LPC} = \rho \cdot cd_{LPC} \cdot A_{LPC}(x_{LPC}) \cdot \sqrt{\frac{2|p_{DS} - p_{BG}|}{\rho}} \tag{2.36}$$

$$\dot{m}_{LS} = \rho \cdot cd_{SF} \cdot A_{SF}(x_{LPC} - x_{LPK}) \cdot \sqrt{\frac{2|p_{DS} - p_{LS}|}{\rho}} \tag{2.37}$$

x_{MS} is the valve section main spool position, which is an input of this sub-system defined by the operator model (presented in the section 2.2.8).

The total inlet flow rate (Q_{IN_i}) and the LS flow rate (Q_{LS_i}) can be defined through (*Eq.2.38*) and (*Eq.2.39*).

$$Q_{IN_i} = \frac{\dot{m}_{IN1} + \dot{m}_{IN2}}{\rho} \tag{2.38}$$

$$Q_{LS_i} = \frac{\dot{m}_{LS}}{\rho} \tag{2.39}$$

The LPC and LPK instantaneous spool positions are defined by (*Eq.2.40*) and (*Eq.2.41*) respectively.

$$\begin{cases} if\ p_{BG} \leq p_{D_{MAX}} \rightarrow \ddot{x}_{LPC} \cdot m_{LPC} + \dot{x}_{PC} \cdot c_{LPC} = (p_{DS} - p_{LS}) \cdot A_{LPC} \\ if\ p_{BG} > p_{D_{MAX}} \rightarrow x_{LPC} = x_{LPK} \end{cases} \tag{2.40}$$

$$\ddot{x}_{LPK} \cdot m_{LPK} + \dot{x}_{LPK} \cdot c_{LPK} + x_{LPK} \cdot k_{LPK} = (p_{BG} - p_{LS}) \cdot A_{LPK} \tag{2.41}$$

The bridge (BG) pressure (p_{BG}) is evaluated through (*Eq.2.42*).

$$\frac{dp_{BG}}{dt} = \frac{B}{\rho} \cdot \frac{1}{V_{BG}} \cdot \sum \dot{m}_{BG} \tag{2.42}$$

The BG chamber volume is defined by (*Eq.2.43*), where V_3 and V_4 were calculated with the aid of the valve section CAD model.

$$V_{BG} = V_3 + V_4 \tag{2.43}$$

The summation term, (*Eq.2.44*), represents the net mass flow rate entering or leaving the BG chamber volume. This is obtained by considering the contribution of all the orifices connected to the considered volume,.

$$\sum \dot{m}_{BG} = \dot{m}_{LPC} - \dot{m}_{A_{i-1}} - \dot{m}_{B_{i-2}} \tag{2.44}$$

According to the conventions made in the modelling scheme previously reported the mass flow rates of (*Eq.2.44*) are defined in (*Eq.2.45*) and (*Eq.2.46*) respectively.

$$\dot{m}_{A_i} = \rho \cdot cd_{A_i} \cdot A_{A_i}(x_{MS}) \cdot \sqrt{\frac{2|p_{BG} - p_{A_i}|}{\rho}} \tag{2.45}$$

$$\dot{m}_{B_i} = \rho \cdot cd_{B_i} \cdot A_{B_i}(x_{MS}) \cdot \sqrt{\frac{2|p_{BG} - p_{B_i}|}{\rho}} \tag{2.46}$$

The outlet mass flow rates from the valve section workports are defined by (*Eq.2.47*) and (*Eq.2.48*).

$$\dot{m}_{A_{i-OUT}} = \rho \cdot cd_{A_{i-OUT}} \cdot A_{A_{i-OUT}}(x_{MS}) \cdot \sqrt{\frac{2|p_{A_i} - p_{OUT}|}{\rho}} \tag{2.47}$$

$$\dot{m}_{B_{i-OUT}} = \rho \cdot cd_{B_{i-OUT}} \cdot A_{B_{i-OUT}}(x_{MS}) \cdot \sqrt{\frac{2|p_{B_i} - p_{OUT}|}{\rho}} \tag{2.48}$$

The discharge coefficients maximum value of each valve section orifice was characterized through a dedicated experimental activity on the excavator.

Finally the workports flow rates can be defined by (*Eq.2.49*) and (*Eq.2.50*).

$$Q_{A_i} = \frac{\dot{m}_{A_i} + \dot{m}_{A_{i-OUT}}}{\rho} \tag{2.49}$$

$$Q_{B_i} = \frac{\dot{m}_{B_i} + \dot{m}_{B_{i-OUT}}}{\rho} \tag{2.50}$$

Generic examples for the valve section orifices area are reported in Fig.2.20.

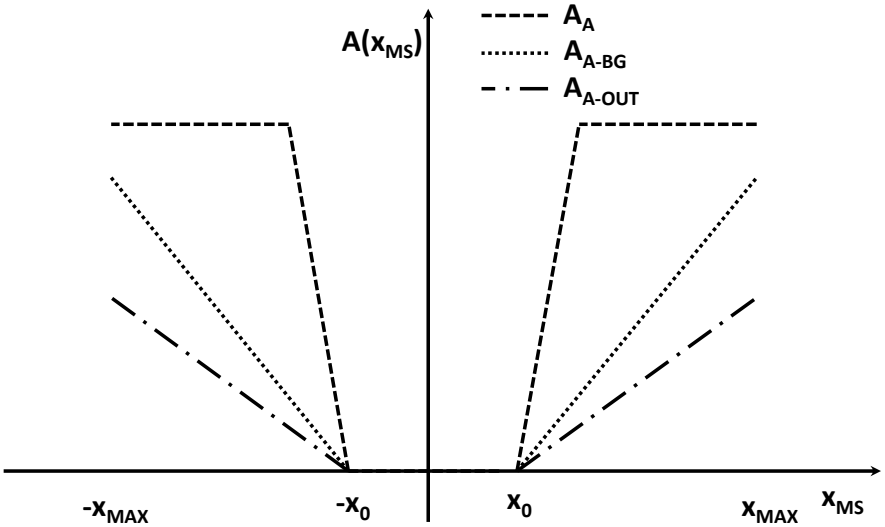

Figure 2.20: Generic Example of Valve Section Orifices Areas.

2.2.4 Hydraulic Linear Actuator

The hydraulic linear actuators (HLA), or cylinders, mounted on the excavator are of double acting single-rod type. The following assumptions have been made for the modelling:

- the cylinder was considered as rigid (i.e. not deformable);
- the external leakages were neglected;
- the friction effect in revolute pairs were lumped in the linear actuator friction model.

Figure 2.21 reports the input/output causality of the HLA, while Fig.2.22 represents its modelling scheme.

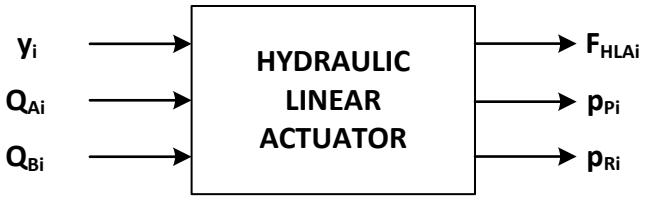

Figure 2.21: Hydraulic Cylinder Causality.

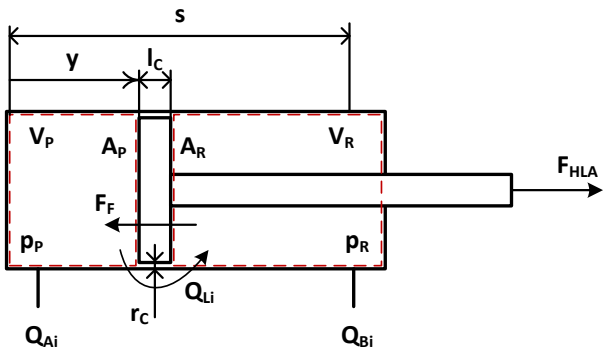

Figure 2.22: Hydraulic Cylinder Modelling Scheme.

According to the continuity equation [*2.16*], the pressure variations in the piston (P) and in the rod (R) chambers volumes are evaluated by (*Eq.2.51*) and (*Eq.2.52*) respectively.

$$\frac{dp_{P_i}}{dt} = \frac{B}{V_{P_i}} \cdot \left(Q_{A_i} - Q_{Li} - A_{P_i} \cdot \frac{dy_i}{dt} \right) \qquad (2.51)$$

$$\frac{dp_{R_i}}{dt} = \frac{B}{V_{R_i}} \cdot \left(Q_{B_i} + Q_{Li} + A_{R_i} \cdot \frac{dy_i}{dt} \right) \qquad (2.52)$$

The control volumes of the piston and rod chambers are calculated with (*Eq. 2.53*) and (*Eq.2.54*), while the internal leakages flow rate are defined by (*Eq.2.55*).

$$V_{P_i} = A_{P_i} \cdot y_i \tag{2.53}$$

$$V_{P_i} = A_{R_i} \cdot (s_i - y_i) \tag{2.54}$$

$$Q_{Li_i} = \frac{\pi \cdot d_{C-HLA_i} \cdot \left(r_{C-HLA_i}\right)^3}{12 \cdot \mu \cdot l_{C-HLA_i}} \cdot \left|p_{P_i} - p_{R_i}\right| \tag{2.55}$$

The force exerted by the hydraulic cylinder is obtained summing the pressure and frictional forces, (*Eq.2.56*), while the frictional forces are defined by (*Eq.2.57*), where F_{C-HLA_i} and c_{HLA_i} were defined according to experimental results (see Chapter 3).

$$F_{HLA_i} = \left(A_{P_i} \cdot p_{P_i} - A_{R_i} \cdot p_{R_i}\right) - F_{F-HLA_i} \tag{2.56}$$

$$F_{F-HLA_i} = sign(\dot{y}_i) \cdot \left(F_{C-HLA_i} + c_{HLA_i} \cdot \dot{y}_i\right) \tag{2.57}$$

2.2.5 Hydraulic Rotary Actuator

The hydraulic rotary actuators (HRA), or hydraulic motors, mounted on the excavator are related to the turret and the tracks. The turret one is a fixed displacement hydraulic motor, while the tracks ones are variable displacement hydraulic motors.

Figure 2.23 reports the input/output causality of a HRA, while Fig.2.24 represents its modelling scheme.

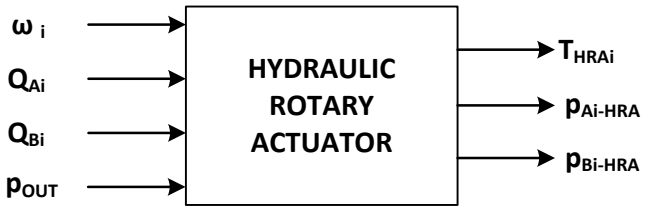

Figure 2.23: Hydraulic Motor Causality.

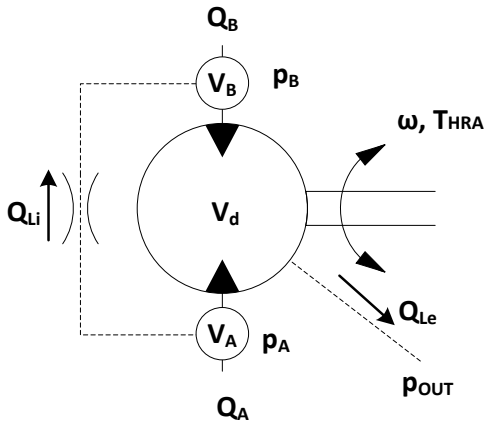

Figure 2.24: Hydraulic Motor Modelling Scheme.

The pressure variation in the volumes of the ports A and B are evaluated through (*Eq.2.58*) and (*Eq.2.59*).

$$\frac{dp_{A_{i-HRA}}}{dt} = \frac{B}{V_{A_{i-HRA}}} \cdot \left(Q_{A_i} - Q_{Li} - Q_{Le_A} - V_d \cdot \frac{\omega_i}{2\pi}\right) \tag{2.58}$$

$$\frac{dp_{B_{i-HRA}}}{dt} = \frac{B}{V_{B_{i-HRA}}} \cdot \left(Q_{B_i} + Q_{Li} - Q_{Le_B} + V_d \cdot \frac{\omega_i}{2\pi}\right) \tag{2.59}$$

The volumes V_A and V_B, of the HRA, were assumed to be constant. The internal and external leakages flow rates are defined by (*Eq.2.60*), (*Eq.2.61*) and (*Eq.2.62*).

$$Q_{Li} = k_{Li_{i-HRA}} \cdot \left|p_{A_i} - p_{B_i}\right| \tag{2.60}$$

$$Q_{Le_A} = k_{Le_{i-HRA}} \cdot \left|p_{A_i} - p_{OUT}\right| \tag{2.61}$$

$$Q_{Le_B} = k_{Le_{i-HRA}} \cdot \left|p_{B_i} - p_{OUT}\right| \tag{2.62}$$

The ideal hydraulic motor torque is defined by (*Eq.2.63*). When the hydraulic machine works as a motor, i.e. during the turret accelerations, the real exerted torque is decreased by hydro-mechanical efficiency, conversely when the hydraulic machine works as a pump, i.e. during the turret decelerations, the hydro-mechanical efficiency has an opposite effect [*2.14*].

$$T_{HRA_i} = \frac{V_d \cdot \left(p_{A_{i-HRA}} - p_{B_{i-HRA}}\right)}{2\pi} \tag{2.63}$$

2.2.6 Hydraulic Line Resistance

The hydraulic lines pressure losses due to friction, between the FGU and the DFCV, the distributor and the actuators, and the distributor and the reservoir, whose modelling causality is reported in Fig.2.25, have been modelled lumping all the resistance section and elements and assuming a laminar flow, according to the experimental results (see Chapter 3).

Figure 2.25: Hydraulic Line Causality.

The pressure drop in the hydraulic lines are evaluated through (*Eq.2.63*), while (*Eq.2.64*) and (*Eq.2.65*) define the outlet flow rates and pressures.

$$\Delta p_{LINE-i} = k_{L_{i-LINE}} \cdot Q_{IN-i} \tag{2.63}$$

$$Q_{OUT-i} = Q_{IN-i} \tag{2.64}$$

$$p_{OUT-i} = p_{IN-i} + \Delta p_{LINE-i} \tag{2.65}$$

2.2.7 Hydraulic Chamber

The hydraulic chambers are capacitance elements characterized by a control volume (V_{CH_i}), where the instantaneous hydraulic fluid pressure is defined, which connect resistance elements. Figure 2.26 reports their modelling causality scheme.

According to the continuity equation [*2.16*], the chamber pressure is evaluated through (*Eq.2.66*), where the volume variations where neglected.

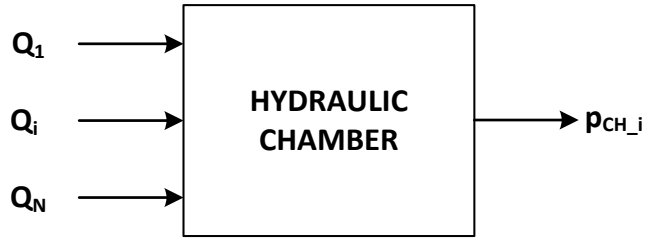

Figure 2.26: Hydraulic Chamber Causality.

$$\frac{dp_{CH_i}}{dt} = \frac{B}{V_{CH_i}} \cdot \sum_{i=1}^{N} Q_i \tag{2.66}$$

2.2.8 Operator

In order to conduct comprehensive comparison analyses of different machine configurations, presented in Chapter 5 and analysed in Chapter 9, the repeatability of the performed working cycles has to be ensured. Therefore an operator mathematical model has been developed. This model does not try to replicate the way of thinking or the problem solving of a real human operator [*2.17*], but just defines main spools positions (x_i) of the DFCVs in order to minimize the error between the front excavation tool simulated actual positioning and the reference one (see Chapter 3). Figure 2.27 represents the operator causality scheme, while Fig.2.28 depicts its modelling scheme.

Figure 2.27: Operator Causality.

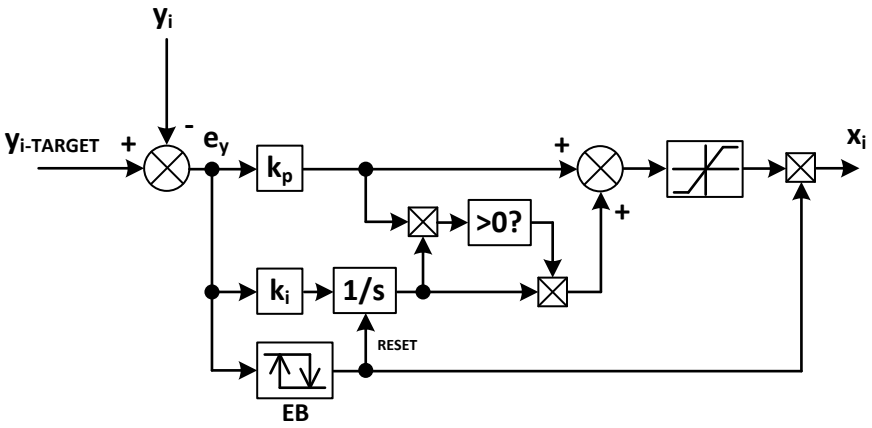

Figure 2.28: Operator Modelling Scheme.

The operator model is based on a PI regulator. The target actuator position (y_{TARGET_i}) is compared with its actual position (y_i), thus defining the error (e_{y_i}) (*Eq.2.67*).

$$e_{y_i} = y_{TARGET_i} - y_i \qquad (2.67)$$

The spool position (x_i) is calculated summing a proportional (k_{P_i}) and an integral (k_{I_i}) actions referred to the error. In order to avoid actuation delay, when the user direction change is required, the proportional and the integral actions are compared. If their product is over zero the integral part is still summed to the proportional one, otherwise it is not.

Minimum and maximum limit positions have been imposed to the spool position. Moreover, in order to avoid continuous corrections by the operator model, which would introduces main spool oscillations, an error band (EB) of tolerance has been introduced to define when no actuator position correction is required. If the error value is within the EB limits the operator does not make any correction, and the integral part is reset at the same time.

The system equation (*Eq.2.68*) represents mathematically the operator.

$$\begin{cases} if\ e_{y_i} \in E.B. \rightarrow x_i = 0; \\ \begin{cases} if\ e_{y_i} \notin E.B. \\ if\ sign\left(k_{P_i} \cdot e_{y_i}\right) = sign\left(k_{I_i} \cdot \int e_{y_i} dt\right) \end{cases} \rightarrow x_i = k_{P_i} \cdot e_{y_i} + k_{I_i} \cdot \int e_{y_i} dt\,; \\ \begin{cases} if\ e_{y_i} \notin E.B. \\ if\ sign\left(k_{P_i} \cdot e_{y_i}\right) \neq sign\left(k_{I_i} \cdot \int e_{y_i} dt\right) \end{cases} \rightarrow x_i = k_{P_i} \cdot e_{y_i} \end{cases} \tag{2.68}$$

2.2.9 Excavator Kinematics

Dynamic models of the excavator users, concerning the front equipment, the turret and travels, have been developed in order to consider the actual forces and torques on the respective hydraulic actuators during the working cycles.

Figure 2.29 reports the excavator kinematics input/output causality scheme.

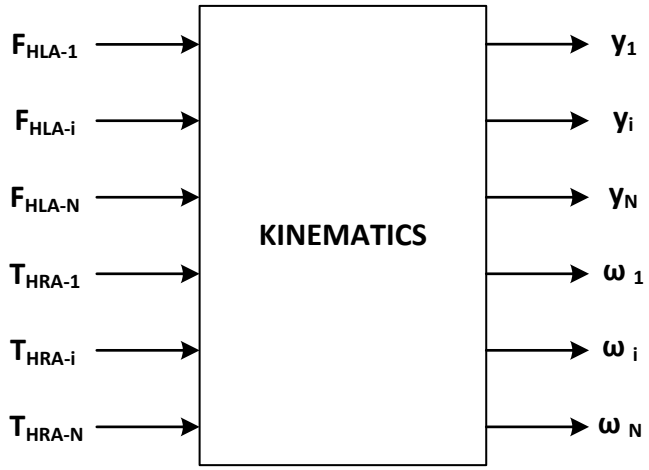

Figure 2.29: Excavator Kinematics Causality.

Front Equipment

The mathematical model of the 3-DOF front equipment, Fig.2.30, was realized through the AMESim® Planar Mechanical Library (PLM) based on the Lagrange equations [*2.18*].

The model is composed of five rigid bodies (BOOM, ARM, BUCKET, LINK-1, LINK-2) connected together through revolute pairs and linear actuators.

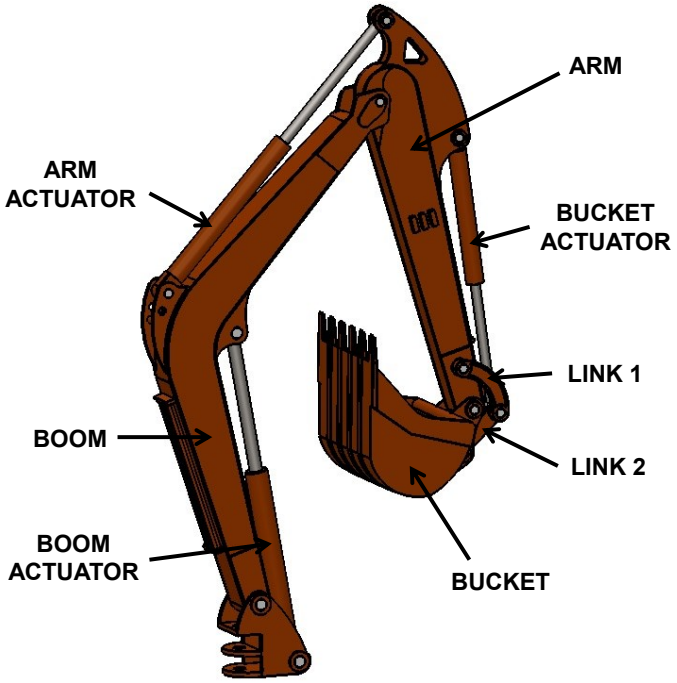

Figure 2.30: Front Equipment of the Excavator.

The planar dynamic behaviour of each body has been completely defined introducing the following parameters:

- mass of the body;
- position of the center of gravity;
- moment of inertia of the body relative to an axis perpendicular to the plane of movement and passing through the center of gravity;
- position of the joints.

These parameters have been evaluated with the aid of the 3D CAD model of the linkage. The bodies initial positions are evaluated starting from the imposed position through the Baumgarte stabilization method applied to the constraint equations [*2.19*].

The forces which two connected bodies exchange in revolute joints are calculated using linear spring stiffness ($k_{x_{ij}}, k_{y_{ij}}$) and damping coefficient ($b_{x_{ij}}, b_{y_{ij}}$) by (*Eq.2.69*) and (*Eq.2.70*).

$$F_{x_{ij}} = k_{x_{ij}} \cdot (x_i - x_j) + b_{x_{ij}} \cdot (\dot{x}_i - \dot{x}_j) \quad (2.69)$$

$$F_{y_{ij}} = k_{y_{ij}} \cdot (y_i - y_j) + b_{y_{ij}} \cdot (\dot{y}_i - \dot{y}_j) \quad (2.70)$$

Where ($x_i,\ y_i$) and ($x_j,\ y_j$) are the pivot joint coordinates relative to the *i-th* and *j-th* bodies. The forces and torques exerted by the linear and rotary actuators, connected to the kinematics model, on the bodies in the defined points and with the direction of the line passing through these points. Since the mass of the actuators is not negligible, its effect has been incorporated in the boom, arm and bucket rigid bodies.

The planar dynamic model described does not take into account neither the centrifugal forces nor the Coriolis forces acting on the implement bodies during the turret rotations. Moreover, the bucket-soil interaction force during the excavation cycle has not been considered, even if few mathematical models [*2.20*] were available in literature, in order to limit the stochastic influence of this interaction on the performed working cycles executed.

Turret and Travels

The turret and travels mathematical model consists of a rotational load (RL) with constant inertia and both Coulomb friction (T_{C-RL_i}) and viscous friction (b_{RL_i}) terms. The dynamic equilibrium of these rotational loads is described through (*Eq.2.71*).

$$I_{RL_i} \cdot \dot{\omega}_i + b_{RL_i} \cdot \omega_i + T_{C-RL_i} = T_{HRA_i} - T_{RL_i} \quad (2.71)$$

The RLs viscous friction coefficients have been defined on the basis of the experimental activity (see Chapter 3).

Concerning the turret, the term (T_{RL}) is equal to zero, moreover the moment of inertia of the turret changes with the position of the front equipment, thus an equivalent constant value has been calculated as the arithmetic mean between the maximum and the minimum values corresponding to the extreme positions that the front equipment reaches during the considered duty cycles. This assumption was done according to a simplified mathematical modelling approach adopted.

2.3 Discussion

In this chapter the mathematical model of the hydraulic excavator under study has been presented, focusing on the sub-systems causality and models description.

Appendix 2 reports the standard machinery mathematical model global causality.

The developed model has been calibrated and validated (see Chapter 4) on the basis of dedicated experimental activities (see Chapter 3).

This model has been utilized to propose and analyse novel energy saving solutions (see Chapter 5 and Chapter 9) compared to the standard excavator layout.

Symbols

Symbol	Definition	Unit
a, A	Area	$[m^2]$
b	Rotary Viscous Friction Coefficient	[N·m/(rad/s)]
B	Bulk Modulus	[Pa]
c	Linear Viscous Friction Coefficient	[N/(m/s)]
cd	Orifice Discharge Coefficient	[-]
d	Diameter	[m]
e	Linear Error	[m]
F	Force	[N]
F_C	Coulomb Friction Force	[N]
I	Moment of Inertia	$[kg·m^2]$
k	Spring Stiffness	[N/m]
k_I	Integral Correction Coefficient	$[s^{-1}]$
k_L	Laminar Leakage Coefficient	$[m^3/(Pa·s)]$
k_{Le}	External Leakage Coefficient	[m3/(Pa·s)]
k_P	Proportional Correction Coefficient	[-]
l_C	Contact Length	[m]
m	Mass	[kg]
$\dot{m}$	Mass Flow Rate	[kg/s]
n	Rotary Velocity	[r/min]
p	Pressure	[Pa]
Q	Volumetric Flow Rate	$[m^3/s]$
r	Force Lever Arm	[m]
r_C	Radial Clearance	[m]
s	Linear Actuator Maximum Stroke	[m]
T	Torque	[N·m]
T_C	Coulomb Friction Torque	[N·m]
V	Volume	$[m^3]$

Vd	Volumetric Displacement	[m^3/r]
x	Spool Linear Position	[m]
Symbol	**Definition**	**Unit**
xk	Spring Initial Compression Position	[m]
y	Linear Actuator Stroke	[m]
α	Angular Position	[rad]
η_{hm}	Hydraulic-mechanical Efficiency	[-]
η_V	Volumetric Efficiency	[-]
μ	Fluid Dynamic Viscosity	[Pa·s]
ρ	Fluid Density	[kg/m^3]
ω	Angular Velocity	[rad/s]
Subscripts	**Definition**	
A	Workport A	
ACT	Actuator	
B	Workport B	
BG	Bridge	
CH	Chamber	
CP	Pump Case	
D	Delivery	
DS	Downstream	
EQ	Equivalent	
F	Friction	
FC	Flow Compensator	
FGU	Flow Generation Unit	
HLA	Hydraulic Linear Actuator	
HRA	Hydraulic Rotary Actuator	
i	i-th	
I	Intermediate	
ICE	Internal Combustion Engine	
IN	Inlet	
IP	ICE - Pump	
j	j-th	
Le	External Leakage	
Li	Internal Leakage	
LPC	Local Pressure Compensator	
LPK	Local Piston Check	
LS	Load Sensing	
MAX	Maximum	
MS	Main Spool	
n	n-th	
OUT	Outlet	
P	Piston	
PC	Pressure Compensator	

PIL	Pilot
R	Rod
RL	Rotary Load
SF	Selector Sphere
SUC	Suction
TL	Torque Limiter

References

2.1 *http://www.eurocomach.com/es-85-zt.html.*

2.2 *D. Mizell, M. Ivantysynova. Material Combinations for the Piston-Cylinder Interface of Axial Piston Machines: A Simulation Study. FPNI2014-7841. Proceeding of the 8th FPNI Ph.D Symposium on Fluid Power. FPNI2014. Lappeenranta. Finland.*

2.3 *B. Zhang, B. Xu, C. Xia, H. Yang. Modelling and Simulation on Axial Piston Pump Based on Virtual Prototype Technology. Chinese Journal of Mechanical Engineering. Vol.22, No. 1, 2009. doi: 10.3901/CJME.2009.01.000.*

2.4 *M. Zecchi, M. Ivantysynova. An Investigation of Micro Surface Shaping on the Cylinder block/Valve Plate Inter-Face Performances through a Novel Thermo-Elasto-Hydrodynamic Model. Proceeding of the 7th FPNI Ph.D Symposium on Fluid Power. FPNI2012. Reggio Emilia. Italy.*

2.5 *S. Dhar, A. Vacca, A. Lettini. A Novel ElastoHydrodynamic Model for the Lubricating Gaps in External Gear Machines: Evaluation of Axial bBalance. Proceeding of the 7th FPNI Ph.D Symposium on Fluid Power. FPNI2012. Reggio Emilia. Italy.*

2.6 *Williamson C., Shinok L., Ivantysynova M. (2005). Active Vibration Damping for an Off-Road Vehicle with Displacement Controlled Actuators. International Journal of Fluid Power, vol. 10 n. 3. pp 5-16.*

2.7 *H. Schulte. Control-Oriented Modelling of Hydrostatic Transmissions using Takagi-Sugeno Fuzzy Systems. IEEE 2007, doi: 1-4244-1210-2/07.*

2.8 *K.H. Chu, Y. Kang, Y.F. Chang, Y.L. Liu, C.W. Chang. Model-Following Controller Based on Neural Network for Variable Displacement Pump. JSME International Journal. Series C, Vol.46, No. 1,2003. Pags.176-187.*

2.9 *D. Zimmerman, M. Pelosi, C. A. Williamson, M. Ivantysynova. Energy Consumption of an LS Excavator Hydraulic System. Proceedings of IMECE2007.2007 ASME, November 11-15, 2007, Seattle, Washinghton, USA. IMECE2007-42267.*

2.10 *G. Altare, D. Padovani, N. Nervegna. A commercial Excavator: Analysis, Modelling and Simulation of the Hydraulic Circuit. SAE 2012 Commercial Vehicle Engineering Congress, Rosemont, Illinois, USA, 13-14 September 2012. doi: 10.4271/2012-01-2040.*

2.11 *M. Lindgren. A Transient Fuel Consumption Model for Non-Road Mobile Machinery. Journal of Biosystems Engineering (2005). Vol.91, pp 139-147. doi:10.1016/j.biosystemseng.2005.03.011.*

2.12 *P. Casoli, A. Gambarotta, N. Pompini, L. Riccò. Development and application of co-simulation and control-oriented modelling in the improvement of performance and energy saving of mobile machinery. Energy Procedia, Volume 45, 2014, Pages 849–858. Elsevier. doi:10.1016/j.egypro.2014.01.090.*

2.13 *P. Casoli, N. Pompini, L. Riccò. Simulation of an Excavator Hydraulic System using Nonlinear Mathematical Models. Strojinski vestnik Journal of Mechanical Engineering.Journal of Mecanical Engineering.*

2.14 *J. Ivantysyn , M Ivantysynova. In: Hydrostatic Pumps and Motors. Tech Books International, New Delhi,2003, India. ISBN: 81-88305-08.*

2.15 *D. McCloy, H.M. Martin. "Control of Fluid Power: Analysis and Design", Ellis Horwood Limited. 1980. ISBN: 0-85312-135-4.*

2.16 *J.F. Blackburn, G. Reethof, J. L. Sherarer. Fluid Power Control. The M.I.T. Press. Cambridge, Massachussetts, and London, England. ISBN 10-0262020068.*

2.17 *A. McGordon, J.E.W. Paxon, C. Cheng, R.P. Jones, P.A. Jennings. Development of a driver model to study the effects of real-world driver behavior on the fuel consumption. Proceedings of the IMechE Vol.225 Part D: J. Automobile Engineering. doi: 10.1177/0954407011409116.*

2.18 *LMS Imagine.Lab AMESim. Planar Mechanical Library Rev 13. User's Guide.*

2.19 *Shih-Tin Lin. "Stabilization of Baumgarte's" Method Using the Runge-Kutta Approach, ASME Journal of Mechanical Design, vol. 124, no. 4, p. 633-641, DOI:10.1115/1.1519277.*

2.20 *W. Grzesikiewicz. Dynamics of a ground digging tool. XI scientific Conference Problems of Work Machines,konferencja Naukova Problem Maszyn Roboczych) Polska: Zakopane, 1998.*

Chapter 3: **Experimental Activity on the Standard Excavator**

This chapter deals with the experimental activity carried out on the standard version of the hydraulic excavator under study.

The experimental activity is divided in test bench and on the field activities. The firsts have the aim of characterize the excavator components and validate their mathematical models. The seconds have both the purpose of characterizing the machinery sub-systems and defining the standard excavator fuel consumption.

3.1 Test Bench Experimental Activities

The experimental activities described in the following paragraphs were carried out with the aid of the test rig, for hydraulic components, available at the Industrial Engineering Department of the University of Parma.

The activities involved the excavator FGU, in particularly the main pump, and the excavator DFCV, performed in order to characterize both the static and the dynamic behaviour of these sub-systems as well as validate their mathematical models.

3.1.1 Flow Generation Unit

The experimental activities performed on the FGU were focused on the determination of the volumetric and hydraulic-mechanical efficiency maps, the correlation between the swash plate actuator pressure and the selected parameters of interest during different working conditions characterizing the swash plate tilting dynamic response as well as the regulators action during the functioning.

Efficiency Tests

The FGU is a multiple pump composed of a LS variable displacement axial piston pump and an external gear pump linked together on the same shaft.

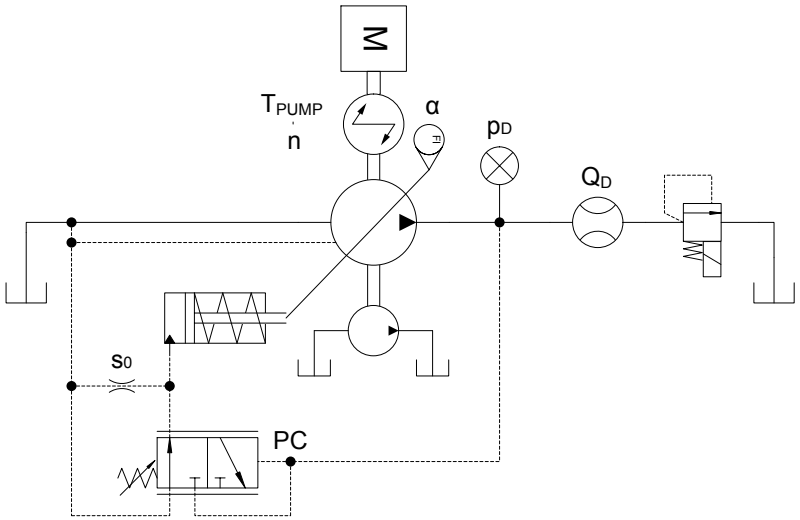

Figure 3.1: FGU Efficiency Tests ISO Scheme.

The efficiency tests have been performed according to [*3.1*], where the testing procedure is described.

Figure 3.1 represents the test bench ISO scheme configuration during the efficiency tests, while Fig.3.2 reports a test bench photograph in the same configuration. Table 3.1 reports the main features of the utilized transducers.

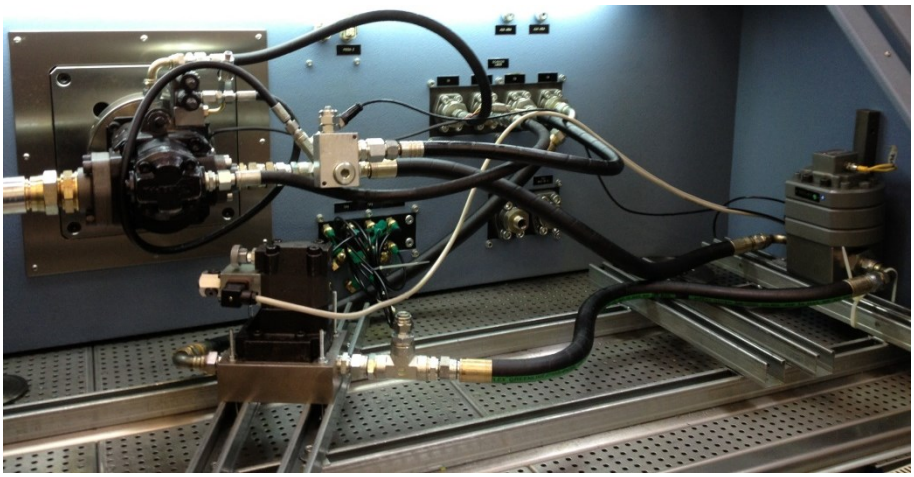

Figure 3.2: Photograph of the Test Bench during the FGU Efficiency Tests.

Table 3.1: Transducer Main Features Efficiency Tests.		
Symbol	Transducer Type	Main Features
n	HBM® Encoder	12000 r/min
T_{PUMP}	HBM® Torque Meter	500Nm ±0.03% FS
α	Angular Position Transducer	-
p_D	TRAFAG® Pressure Transducer	0 – 400 bar ±0.1% FS
Q_D	VSE® Flow Meter	300 l/min ±0.2% FS

The volumetric efficiency (η_V) and the hydraulic-mechanical efficiency (η_{hm}) have been defined as function of the pump delivery pressure (p_D), velocity (n) and displacement (V_d) (which is directly related to the swash plate position (α)), at a constant temperature of the hydraulic fluid, maintained equal to 50°C.

Figure 3.3 represents the main pump overall efficiency maps adopted in the mathematical model of the pump.

The instantaneous values of the volumetric and hydro-mechanical efficiencies are evaluated through a linear interpolation of the experimental points.

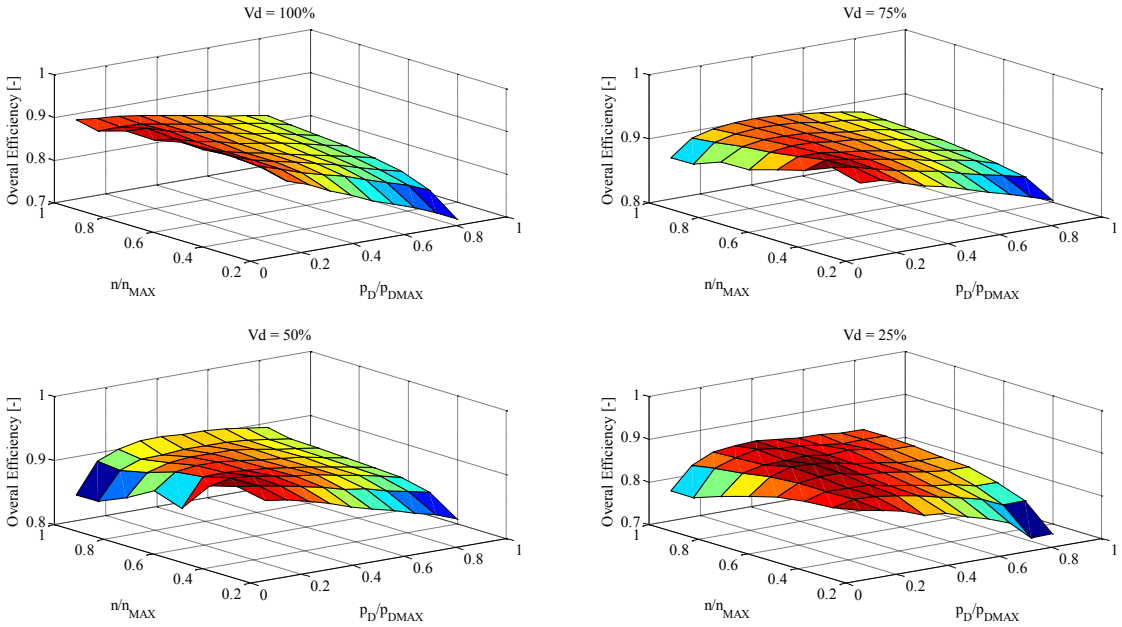

Figure 3.3: Main Pump Overall Efficiency at different Pump Displacement.

Being the FGU a multiple pump, the hydraulic-mechanical efficiency maps related to the main pump do not take into account the drag torque contribution which has been defined through a dedicated experimental test in which the main pump displacement was set to zero, with the aid of the physical end-stops.

The drag torque was measured, Fig.3.4, since the pump velocity was increased through defined steps.

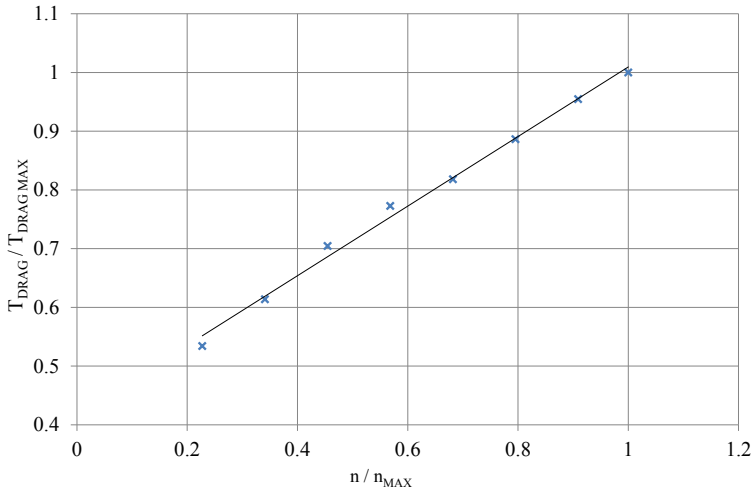

Figure 3.4: FGU Drag Torque.

Swash Plate Actuation Pressure

The main pump of the hydraulic system is a variable displacement unit. The instantaneous pump displacement is directly correlated to the swash plate angular position. (*Eq.2.6*) defines the dynamic equilibrium of the swash plate.

The resulting torque from the contribution of each n-th piston force, acting on the swash plate, is defined as $\sum_{n=1}^{N} T_n$. Since $\dot{\alpha} \cong 0$ during steady state working condition, an experimental characterization has been obtained between the swash plate actuator pressure and the delivery pressure (p_D), speed (ω_{ICE}) and swash plate angular position (α) of the pump.

Figure 3.5 reports the test bench configuration ISO scheme adopted during the characterization of the actuator pressure of the swash plate.

Tab.3.2 lists the main features of the transducers utilized

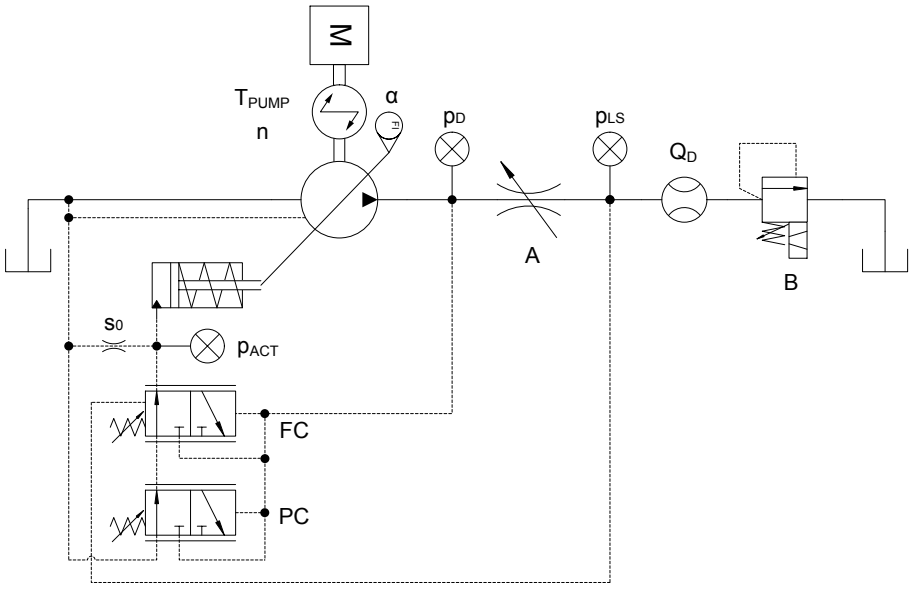

Figure 3.5: Swash Plate Actuation Pressure Characterization ISO Scheme.

Table 3.2: Transducer Main Features Swash Plate Actuation Tests.		
Symbol	Transducer Type	Main Features
n	HBM® Encoder	12000 r/min
T_{PUMP}	HBM® Torque Meter	500Nm ±0.03% FS
α	Angular Position Transducer	-
p_D, p_{LS}, p_{ACT}	TRAFAG® Pressure Transducer	0 – 400 bar ±0.1% FS
Q_D	VSE® Flow Meter	300 l/min ±0.2% FS

Through the usage of the proportional flow control valve (A) and the proportional pressure regulator valve (B) the swash plate position (α) and the load pressure (p_{LS}) were respectively imposed at different values during the tests.

Maintaining the test bench electric motor (M) velocity (n) and the load pressure set at constant values and proportionally varying valve A opening (through a step variation cycle), from the minimum to the maximum opening, the experimental correlation between the actuator pressure and the swash plate position was defined.

The variation range for the electric motor velocity was defined from 850 r/min to 2200 r/min, while the load pressure variation range was defined according to the pump operating limits.

Figure 3.6 represents the experimental points acquired during both the swash plate angular position increasing and reducing phases, pointing out the hysteresis trend.

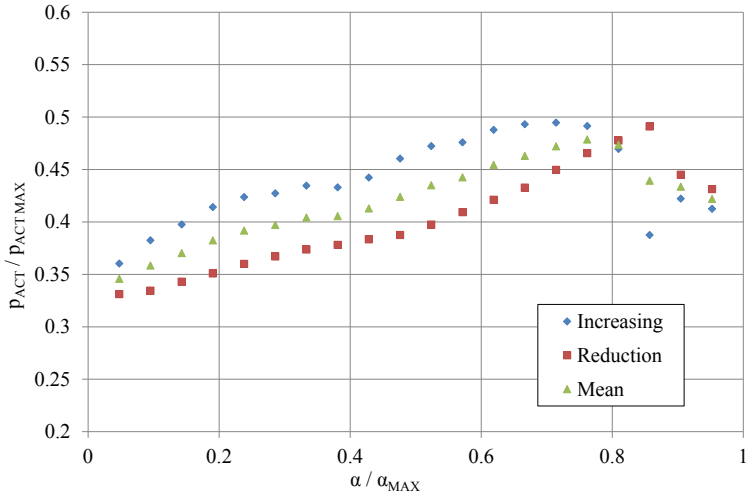

Figure 3.6: Swash Plate Actuation Pressure Acquired Points.

For each working point a mean value has been assumed for the swash plate actuator pressure. Figure 2.10 (see Chapter 2) represents the correlation obtained fitting the experimental mean values for the swash plate actuator pressure.

Main Pump Dynamic Tests

The dynamic tests conducted on the FGU main pump of the excavator were focused on the evaluation of the viscous friction coefficient b_{SP}, (*Eq.2.6*) (see Chapter 2), which characterizes the swash plate dynamic behaviour together with the swash plate equivalent inertia.

Since the swash plate equivalent inertia, evaluated with the aid of the pump CAD model, can be considered as constant, the pump dynamic behaviour typically depends on the working conditions. Therefore the pump step response was characterized at different operating points, i.e. with different boundary conditions, in order to define an equivalent value for the viscous friction coefficient b_{SP}.

Figure 3.7 reports the test rig configuration ISO scheme during the dynamic tests, while the transducer features are reported in Tab.3.3.

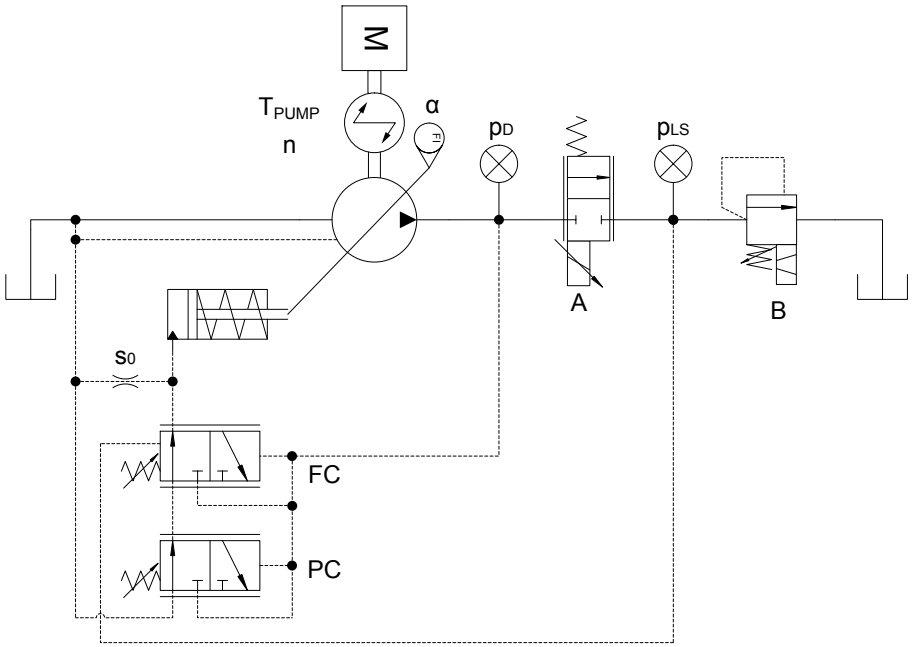

Figure 3.7 Main Pump Dynamic Tests Setup ISO Scheme.

Table 3.3: Transducer Main Features Dynamic Tests.		
Symbol	Transducer Type	Main Features
n	HBM® Encoder	12000 r/min
T_{PUMP}	HBM® Torque Meter	500Nm ±0.03% FS
α	Angular Position Transducer	-
p_D, p_{LS}	TRAFAG® Pressure Transducer	0 – 400 bar ±0.1% FS Response Time ~ 1 ms

The load pressure (p_{LS}) was controlled, and kept at a constant value, through the usage of the proportional pressure regulator valve B, while a step variation input was imposed with the aid of the proportional valve A. Three different testing conditions were performed at different pump velocities and imposed load pressures.

The swash plate angular position (α) variation was acquired with an appropriate sampling rate according to the Nyquist-Shannon theorem in order to avoid aliasing.

Examples of the acquired data during a step variation of the input are reported in Fig.3.8 and Fig.3.9.

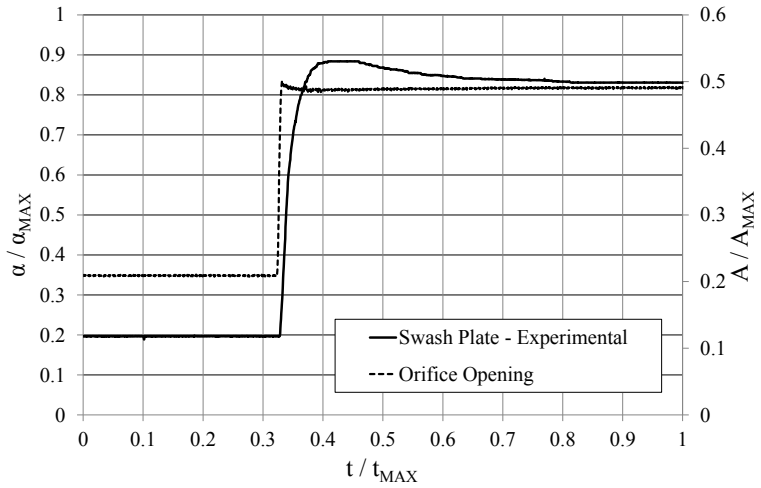

Figure 3.8: Dynamic Test Input/Output.

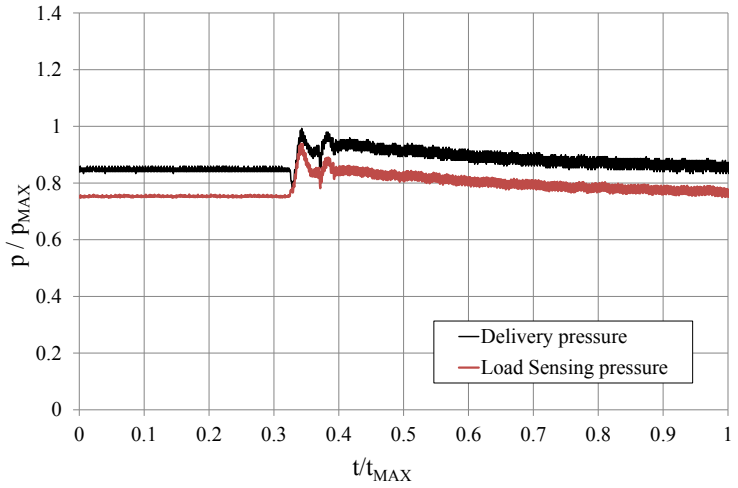

Figure 3.9: Dynamic Test Pressures Variations.

Main Pump Regulators Calibration

The main pump of the excavator is controlled by means of three regulators. During the working cycles of the excavator the flow compensator (FC) controls the pump displacement, the torque limiter (TL) modulates the LS pressure, while the pressure compensator (PC) acts only when the maximum system pressure is reached.

The mathematical models of the regulators have been calibrated on the basis of the reported experimental activity.

The excavator main pump was characterized with the aid of the test bench configured according to the ISO scheme reported in Fig.3.10.

Table 3.4 reports the adopted transducer main features.

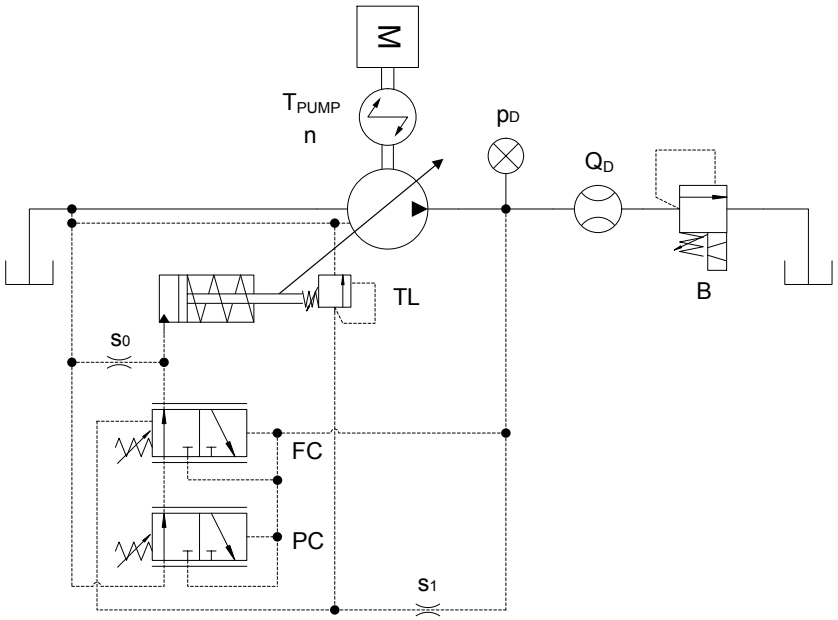

Figure 3.10: Main Pump Regulator Calibration Test ISO Scheme.

Table 3.4: Transducer Main Features Regulator Calibration Test.		
Symbol	Transducer Type	Main Features
n	HBM® Encoder	12000 r/min
T_{PUMP}	HBM® Torque Meter	500Nm ±0.03% FS
p_D	TRAFAG® Pressure Transducer	0 – 400 bar ±0.1% FS
Q_D	VSE® Flow Meter	300 l/min ±0.2% FS

Maintaining the pump velocity (n) at a constant value, equal to 2200 r/min which is the same velocity adopted during the test field activities, and controlling the pump delivery pressure (p_D) through valve B, the pump torque and delivery flow rate profiles were defined, Fig.3.11.

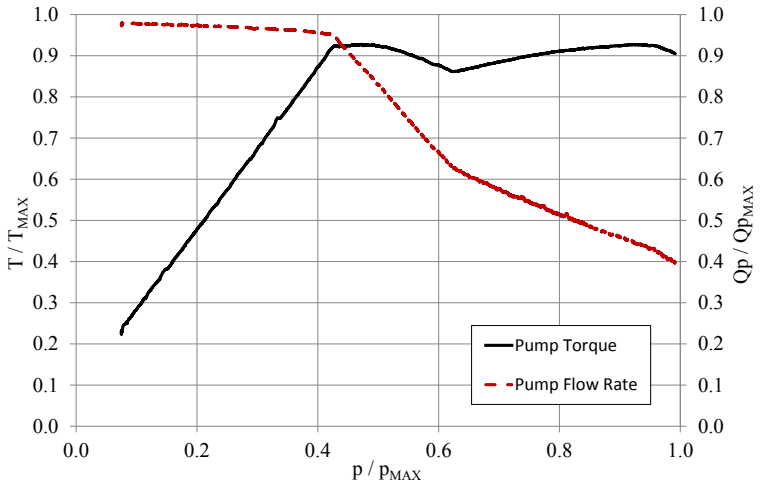

Figure 3.11: Main Pump Torque and Flow Rate During Regulator Calibration Test.

3.1.2 Directional Flow Control Valve

The experimental activity performed on the test bench regarding the excavator DFCV was focused on the local pressure compensator (LPC) model calibration and validation.

During multiple sections working condition, as described in Chapter 2, the LPC of the main loaded user does not throttle the flow rate between the workport and the metering orifice, while the LPCs of the other section do throttle the flow rates in order to maintain the meter-IN orifice pressure drop the same in each section.

The LPCs flow areas ($A_{LPC_i}(x_{LPC_i})$) are known, thus the performed test had the aim of characterize the LPCs discharge coefficients (c_{d_i}) and verify the mathematical models during multiple users working conditions.

The test bench ISO scheme configuration is reported in Fig.3.12 and Fig.3.13 reports a photograph of the assembly.

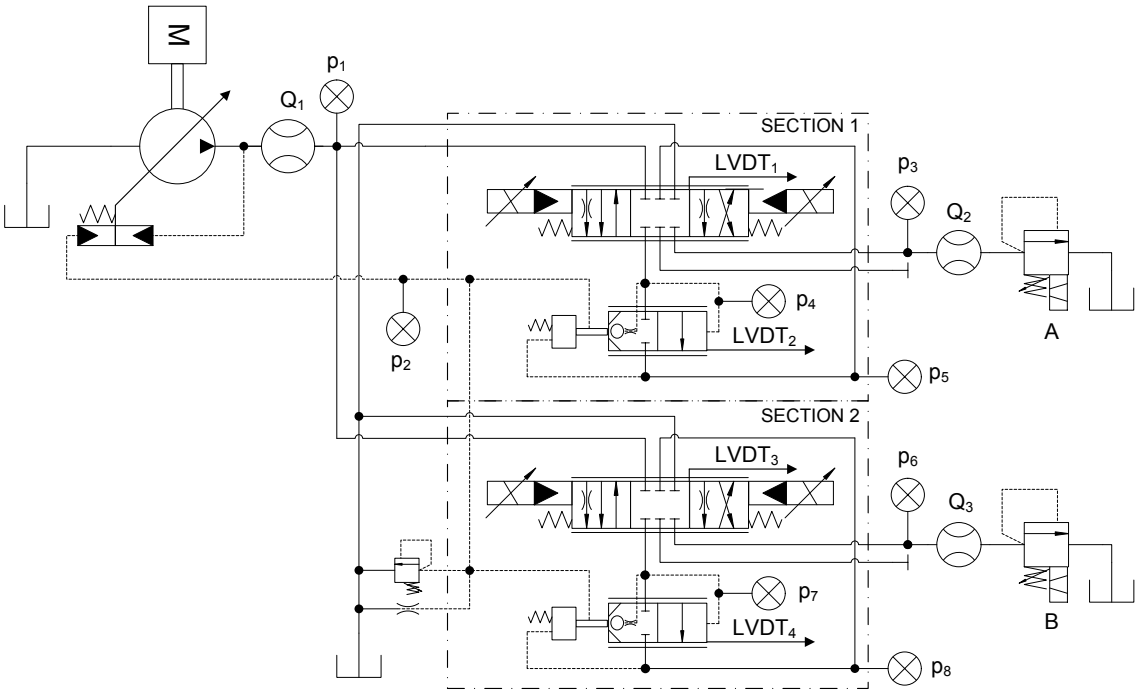

Figure 3.12: DFCV Test Bench ISO Scheme.

The DFCV was composed of two valve sections. The valves main spools and LPCs were instrumented with LVDTs in order to measure their instantaneous positions.

The sections outlet flow rates and the total inlet flow rate were measured with the aid of three volumetric flow meters.

The loads of the sections were imposed exploiting two proportional pressure regulator valves (A and B). The pressures in the system were measured with pressure transducers.

The adopted transducers main features are reported in Tab.3.5.

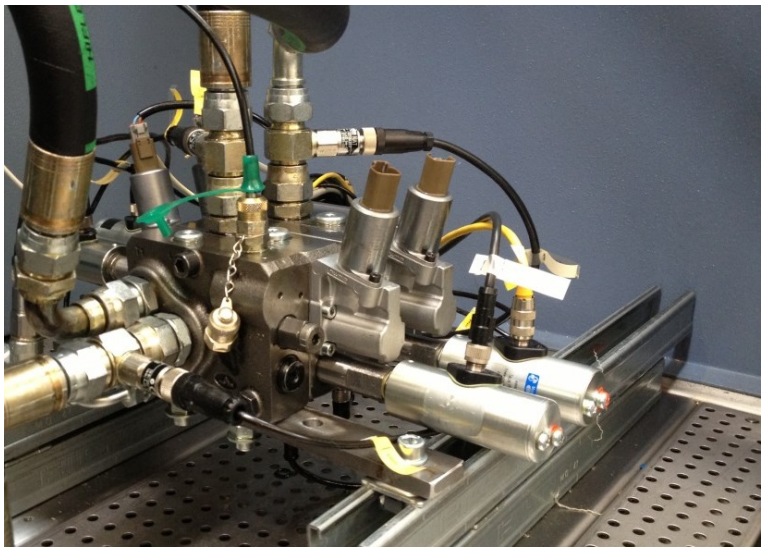

Figure 3.13: Photograph of the Test Bench Configuration during DFCV Test.

Table 3.5: Transducer Main Features DFCV Test.

Symbol	Transducer Type	Main Features
$p_1 - p_8$	TRAFAG® Pressure Transducer	0 – 400 bar ±0.1% FS
Q_1	VSE® Flow Meter	300 l/min ±0.2% FS
Q_2	VSE® Flow Meter	150 l/min ±0.2% FS
Q_3	VSE® Flow Meter	80 l/min ±0.2% FS
$LVDT_i$	Magnet-Schultz® Position Transducer	±15 mm Linearity Error ±0.1% FS

Figure 3.14 and Fig.3.15 report the sections main spool positions and load pressures respectively.

These experimental data have been imposed as input to the mathematical model as well as the pump LS setup, set equal to 1.5 MPa, velocity, set equal to 1500 r/min and the oil temperature set at 50°C.

The comparison between the experimental data and the numerical ones are reported in Chapter 4.

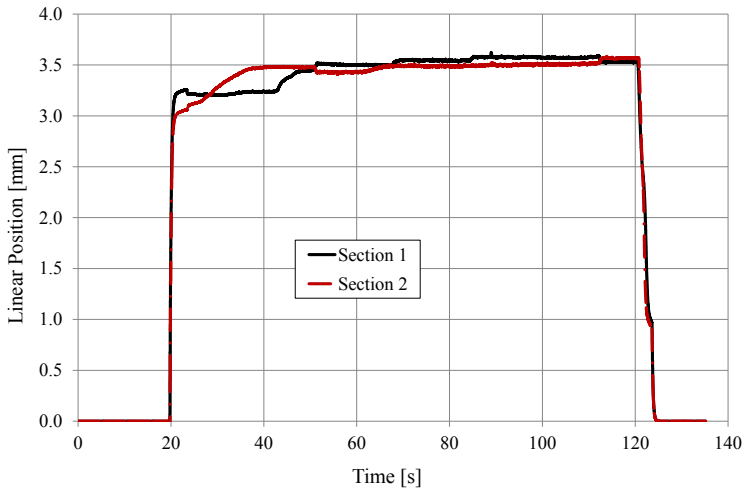

Figure 3.14: DFCV Sections Experimental Main Spool Positions.

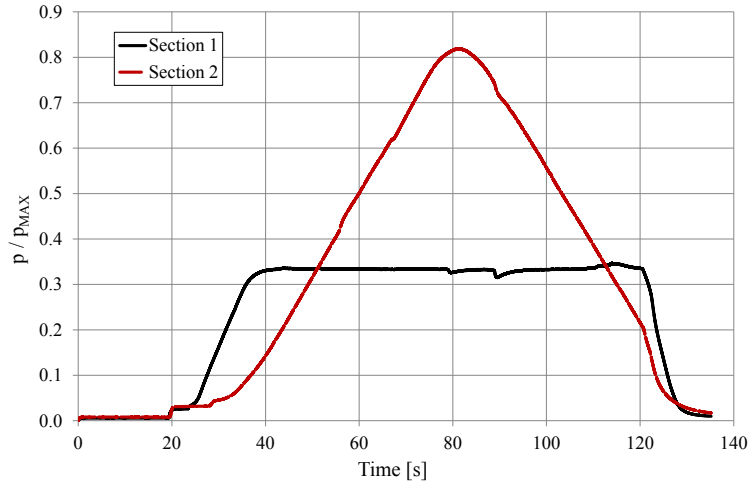

Figure 3.15: DFCV Sections Experimental Load Pressures.

3.2 Machinery Experimental Activities

The experimental activities carried out on the standard excavator aimed to the characterization of ICE, the DFCV sections discharge coefficients, the hydraulic lines pressure losses coefficients, the turret inertia and frictions coefficients, the HLAs friction forces, the standard machinery fuel consumption evaluation and the definition of the reference working position of the actuators during the working cycles.

3.2.1 Internal Combustion Engine

The experimental activity performed on the ICE was mainly focused on the definition of the BSFC map and the speed reduction with torque map.

The standard hydraulic circuit of the excavator, Fig.2.2 (Chapter 2), has been modified according the ISO scheme reported in Fig.3.16 in order to carry out the tests on the ICE.

The main pump displacement was set to its maximum and the TL was removed.

The load pressure (p_1) at the pump outlet was imposed through the usage of the proportional valve B, thus controlling the pump torque, so as the ICE torque.

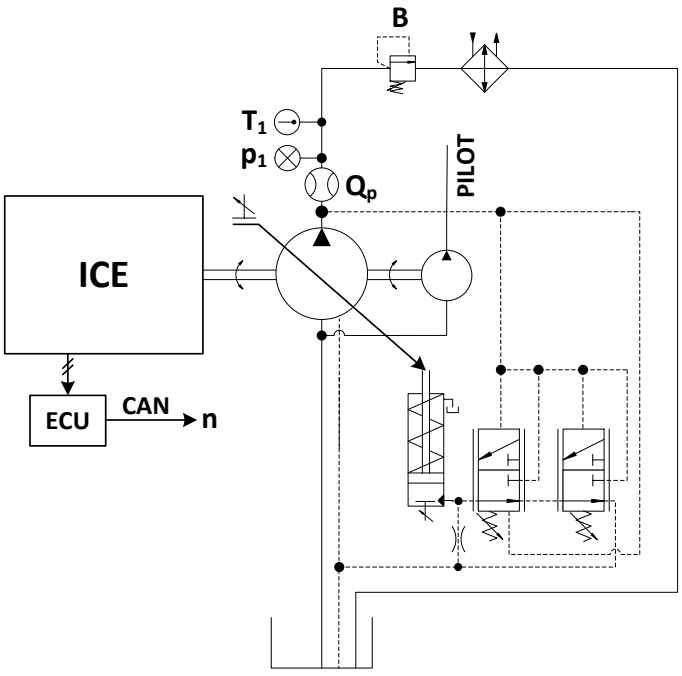

Figure 3.16: ISO Scheme of the ICE Experimental Tests.

The utilized transducers main features are listed in Tab.3.6. The ICE speed was acquired via CAN bus, through the ECU of the ICE.

Table 3.6: Transducer Main Features ICE Tests.		
Symbol	Transducer Type	Main Features
p_1	TRAFAG® Pressure Transducer	0 – 600 bar ±0.3% FS
Q_P	Parker® Turbine Flow Meter	10 – 300 l/min < ±1% FS
T_1	Parker® Temperature Transducer	-25°C to +125°C ±2% FS

The fuel feeding system has been properly modified according to the scheme reported in Fig.3.17 in order to bypass the machinery fuel tank during the testing phases.

Since valve 1 and 2 are disabled the fuel feeding system functions as usual. The fuel feeding pump suction is connected to the machinery fuel tank as well as the fuel return line from the rail. On the contrary, when valve 1 and 2 are enabled the feeding pump is connected to the suction tank (S) while the fuel return line is deviated to the return tank (R).

This system allowed to measure the effective injected fuel over time during the testing phases only, thus defining the injected fuel mass flow rate.

The photographs of the modified fuel feeding system and the ICE testing configuration are reported in Fig.3.18 and Fig.3.19 respectively.

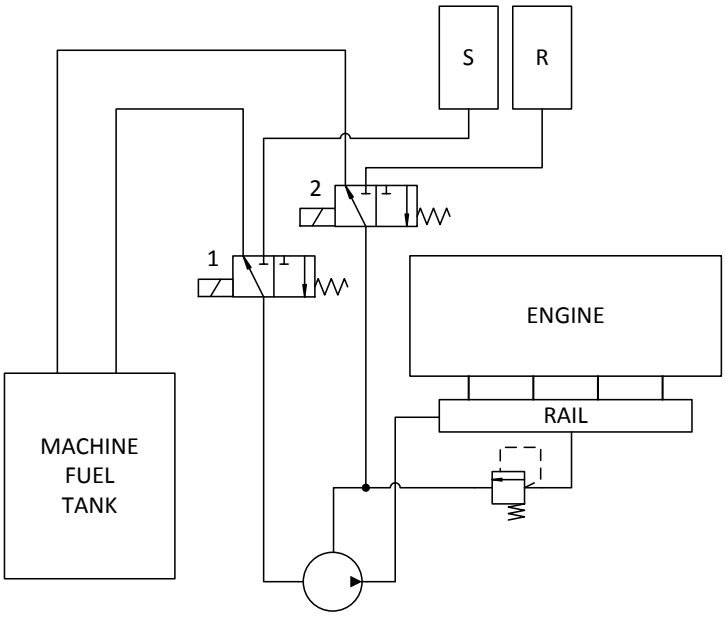

Figure 3.17: Excavator Diesel Tank Deviation System Scheme.

Figure 3.18: Excavator Diesel Tank Deviation System Photograph.

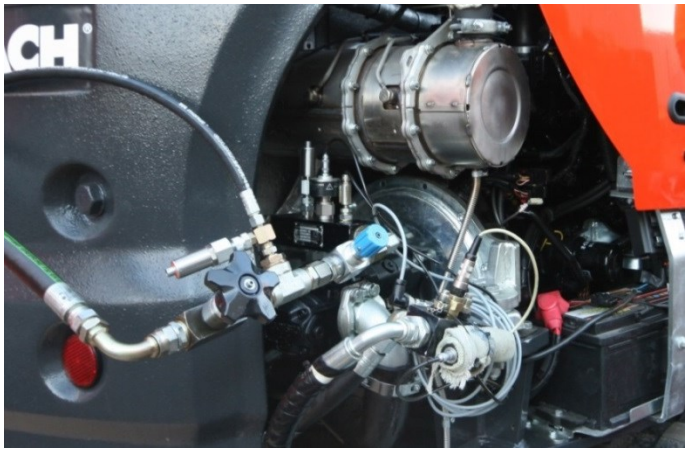

Figure 3.19: ICE Tests Configuration Photograph.

During the BSFC map characterization the ICE was maintained at a constant speed value while the imposed torque was varied through defined values. The actual torque acting on the engine was defined knowing the pump efficiency maps. The BSFC map of the ICE was defined for different speeds, from 900 r/min to 2200 r/min, Fig.3.20.

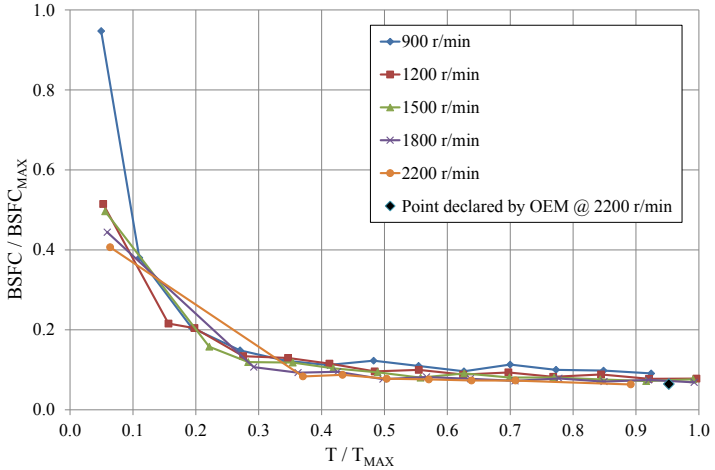

Figure 3.20: ICE BSFC Map at Different Speeds.

Figure 3.21 shows the experimental ICE speed variation with torque. These curves were determined for different ICE speeds and have been introduced in the ICE mathematical model in order to recreate these behaviours.

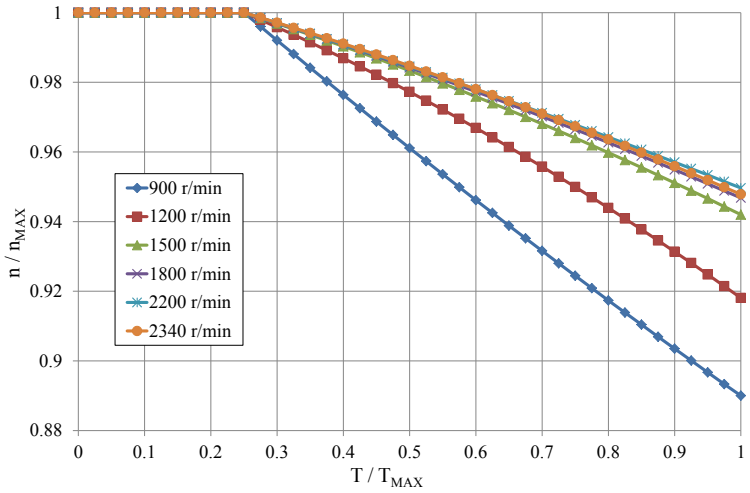

Figure 3.21: ICE Speed Variation with Torque.

3.2.2 Excavator Experimental Setup

The excavator hydraulic system was instrumented as reported in Fig.3.22 in order to measure the required variables for the evaluation of the DFCV sections discharge coefficients, the hydraulic lines pressure drop coefficients and the hydraulic actuators friction forces. The parameters, defined through the experimental data, have been used to calibrate the mathematical model of the standard version of the excavator.

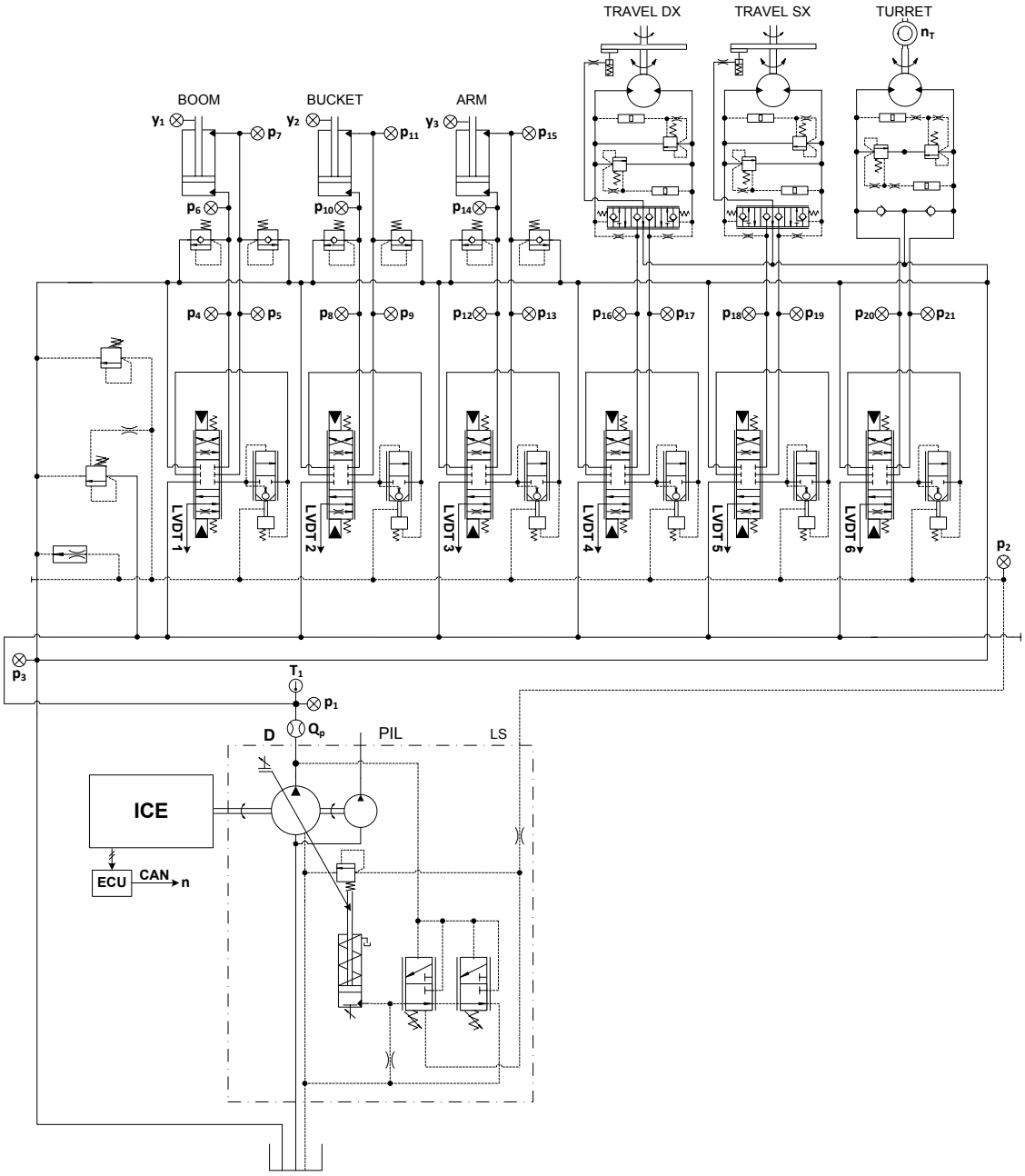

Figure 3.22: Standard Hydraulic Excavator System Experimental Setup ISO Scheme.

The variables of interest were the ICE speed (n), the main pump outlet flow rate (Q_p) and pressure (p_1), the LS and return lines pressures (p_2, p_3), the users main spool positions ($LVDT_{1-6}$), the users and hydraulic actuators workports pressures (p_{4-21}), and instantaneous positions (y_{1-3}).

Table 3.7 reports the main feature of the adopted transducers, while Fig.3.23 (A) and Fig.3.23 (B) report the photographs of the excavator FGU and DFCV instrumented respectively.

Table 3.7: Transducer Main Features Excavator Experimental Setup.

Symbol	Transducer Type	Main Features
Q_P	Parker® Turbine Flow Meter	10 – 300 l/min < ±1% FS
T_1	Parker® Temperature Transducer	-25°C to +125°C ±2% FS
p_1, p_2	TRAFAG® Pressure Transducer	0 – 600 bar ±0.3% FS
p_3	TRAFAG® Pressure Transducer	0 – 60 bar ±0.3% FS
$p_4 - p_{21}$	TRAFAG® Pressure Transducer	0 – 400 bar ±0.1% FS
$LVDT_i$	Magnet-Schultz® Position Transducer	±15 mm Linearity Error ±0.1% FS
y_1, y_2, y_3	Celesco® Linear Position Transducer	1000 mm Accuracy ±0.02% FS
ns	Ifm Electronic GmbH®	NPN Photocell
n	CAN Signal from ICE	0 – 2350 r/min

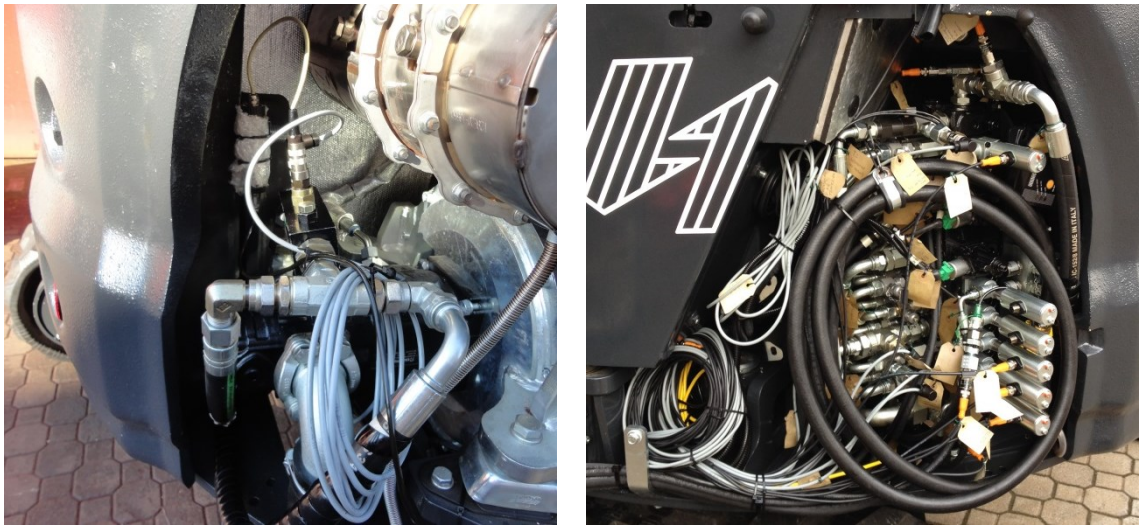

(A) **(B)**

Figure 3.23: FGU and DFCV Instrumented.

Fig.3.24 shows the data acquisition system configuration. Three data acquisition devices (DAQ), from CS series by imc Meßsysteme GmbH®, were connected and synchronized together through a master-slave configuration. The utilized transducers were directly connected to the DAQs, which both supply the transducers and condition the signals.

A local area network (LAN) was created to interface the DAQs with a computer through the usage of a router, thus allowing to save the acquired experimental data.

The data acquisition system was supplied using an inverted directly connected to the battery of the excavator, thus converting a 12 V DC electric source into a 220 V AC electric source. A photograph of the realized data acquisition system installed on the excavator is reported in Fig.3.25.

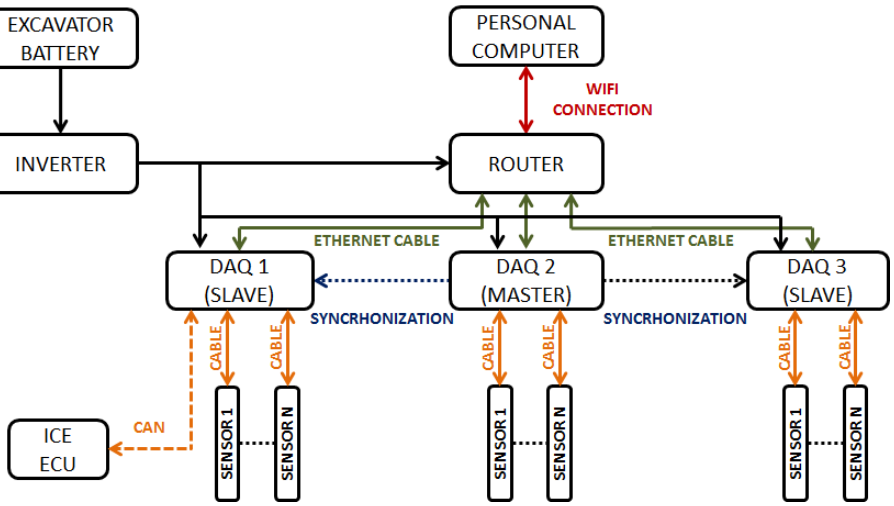

Figure 3.24: Data Acquisition System Configuration.

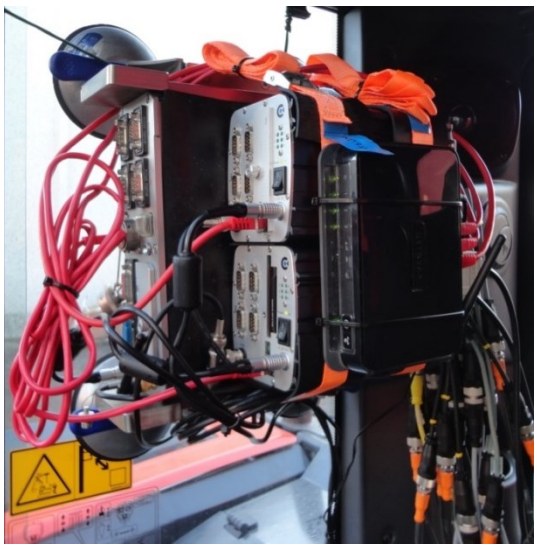

Figure 3.25: Data Acquisition System Photograph.

3.2.3 Excavator Characterization Tests

This part of the experimental activity had the purpose of characterize the hydraulic system of the excavator in order to calibrate the mathematical model.

Concerning the definition of the hydraulic lines pressure drop characteristics, single user cycles were performed. For each user a slow and a fast actuator movements cycles were accomplished. The linear hydraulic actuators were actuated between the two stroke limits while for the rotary hydraulic actuator, i.e. the turret one, a 90 degree return[24] cycle was realised.

Figure 3.26 shows the photographs of the performed movements for the bucket single movement tests.

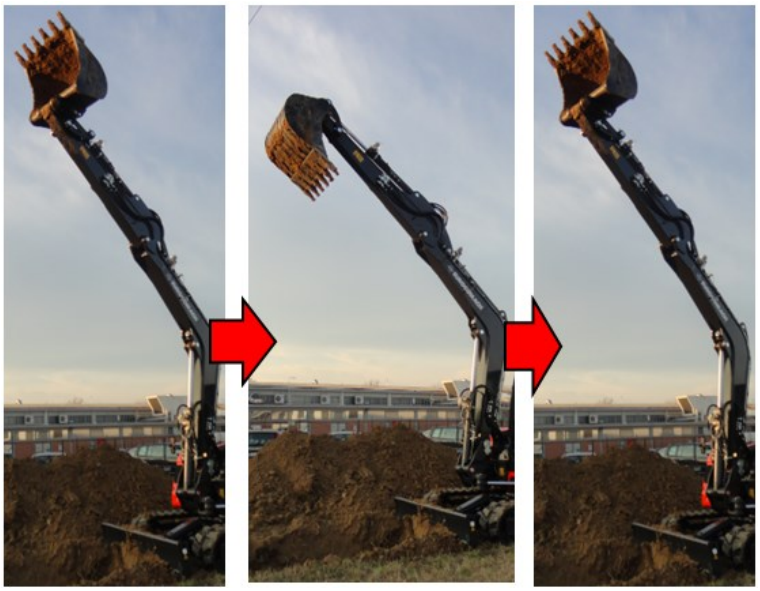

Figure 3.26: Single Movement Test Limit Positions: Bucket.

The acquired data during the bucket slow and fast single movement cycles are reported as example in Fig.3.27 and Fig.3.28 respectively being the procedure the same for all the other users.

The reported curves represent the pressure variation at the workports A and B of the DFCV section and at the piston and the rod ports of the hydraulic actuator. Therefore the lines pressure drop can be defined for both the slow and fast actuator movements.

Combining the results the bucket hydraulic line pressure drop coefficient depending on the flow rate were defined, Fig.3.29. As can be seen the pressure drop characteristic can be approximated with a linear correlation.

[24] Go and back movements.

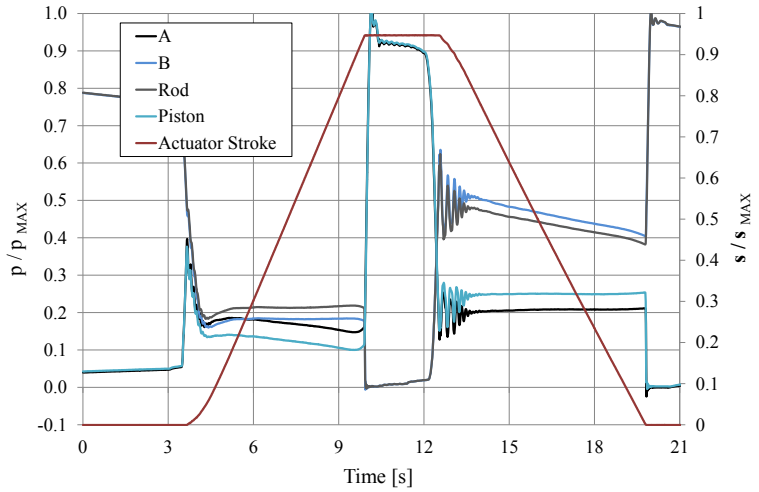

Figure 3.27: Bucket Slow Single Movement Cycle.

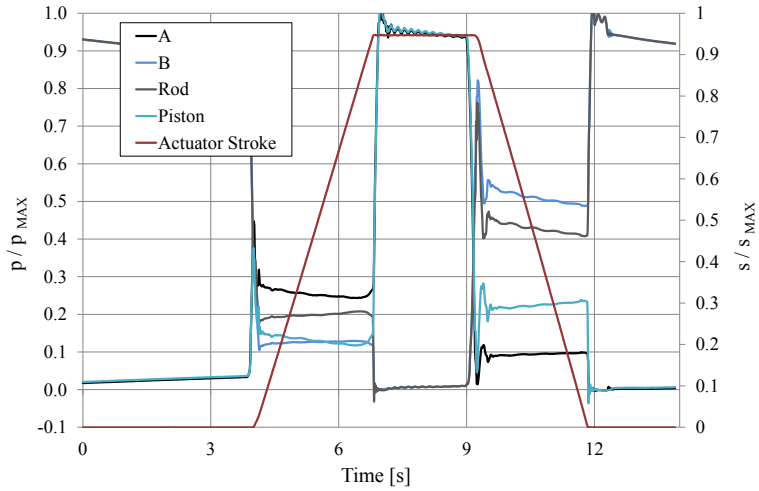

Figure 3.28: Bucket Fast Single Movement Cycle.

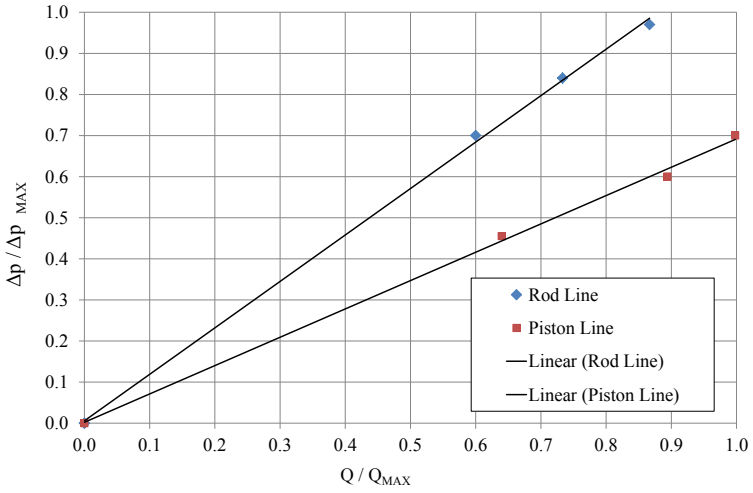

Figure 3.29: Pressure Drop Characteristic of the Bucket Hydraulic Lines.

A similar procedure was adopted to evaluate the turret friction torque over the turret rotational speed, Fig.3.30.

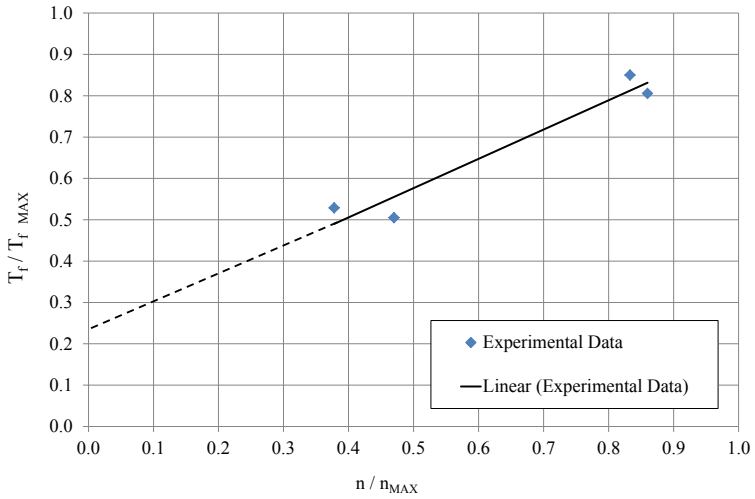

Figure 3.30: Turret Fiction Torque.

The slow and fast single user cycles were also exploited for the DFCV discharge coefficients and for the linear hydraulic actuators friction forces evaluation.

The same operating conditions were imposed to the mathematical model and through static parameters optimization procedure the model was calibrated.

3.2.4 Excavator Fuel Consumption Tests

The fuel consumption of the standard excavator was experimentally evaluated according to the JCMAS standard [*3.2*].

The standard considers four different operating conditions:

- trench digging;
- grading;
- travelling;
- idling.

Moreover, in the standard are also defined, depending on the bucket volumetric capacity, the limit positions for the front excavation tool and the turret, as well as the average cycles time duration and the number of consecutive movements repetitions to be respected in the operating conditions. No interaction between the bucket and the soil is considered.

Figure 3.31 and Fig.3.32 represent the position limits to respect during the trench digging and grading cycles respectively, while Fig.3.33 shows the sequential position of the implement hydraulic during the trench digging cycle.

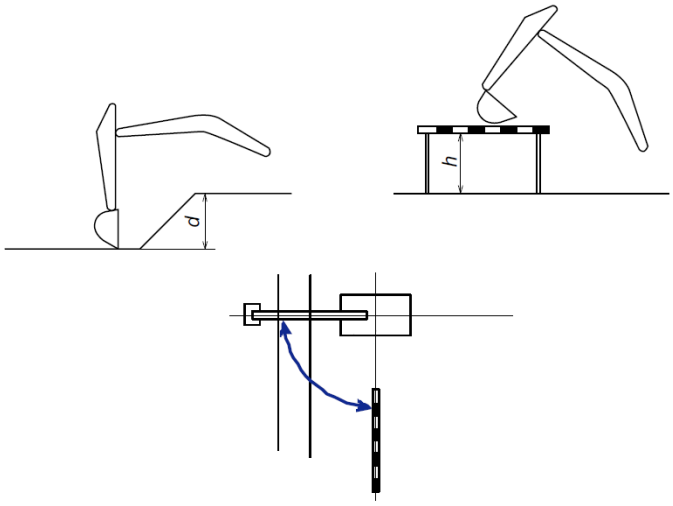

Figure 3.31: Trench Digging Limit Positions.

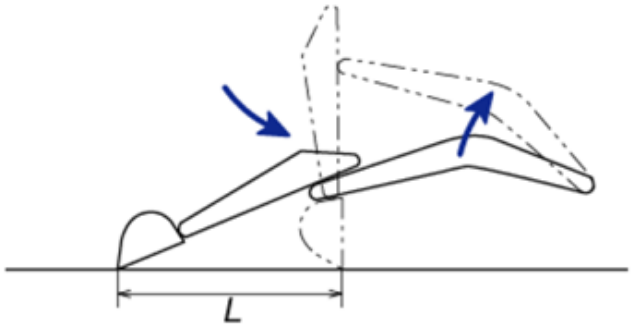

Figure 3.32: Grading Limit Positions.

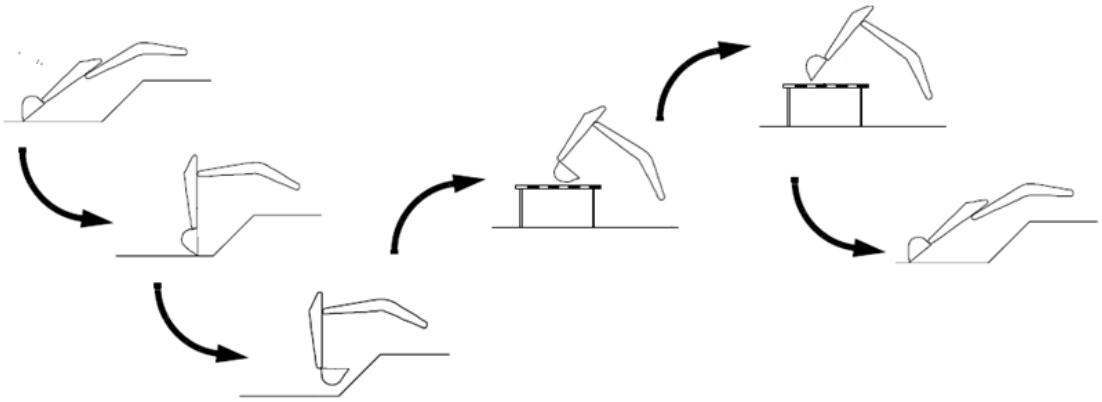

Figure 3.33: Trench Digging Sequential Positions.

Figure 3.34 reports the photograph of the excavator on the testing field set to recreate the position limit defined in the JCMAS.

Figure 3.34: Excavator Photograph on Testing Field.

The number of repetitions of the operating conditions were incremented an appropriate number of times, compared to the times defined by the standard, in order to minimize the stochastic influences on the mean fuel consumption calculated.

The mean value of the fuel consumption is defined by (*Eq.3.1*) for each operating condition.

$$\overline{mf} = \frac{1}{N}\sum_{i=1}^{N} mf_i \qquad (3.1)$$

The combined standard uncertainties [*3.3*] with a 95% confidence level were defined by (*Eq.3.2*).

$$U_{95} = 2 \cdot \left[s_{\overline{mf}}{}^2 + u_M{}^2\right]^{\frac{1}{2}} \qquad (3.2)$$

u_M is the measuring uncertainty of the instrumentation adopted (an electronic balance for the measure of the burned fuel).

The sample standard deviation of the mean is defined through (*Eq.3.3*).

$$s_{\overline{mf}} = \frac{s_{mf}}{\sqrt{N}} \qquad (3.3)$$

Finally the standard deviation (s_{mf}) is evaluated through (*Eq.3.4*).

$$s_{mf} = \left[\frac{1}{N-1} \cdot \sum_{i=1}^{N} \left(mf_i - \overline{mf}\right)^2\right]^{\frac{1}{2}} \qquad (3.4)$$

The hourly equivalent fuel consumption ($\overline{mf}_{JCMAS}$) is defined according to (*Eq.3.5*), defined by the standard.

$$\overline{mf}_{JCMAS} = \overline{mf}_{DIGGING} \cdot C_1 + \overline{mf}_{GRADING} \cdot C_2 + \overline{mf}_{TRAVEL} \cdot C_3 + \overline{mf}_{IDLING} \cdot C_4 \qquad (3.5)$$

Table 3.8 reports the value of the parameter defining the operating conditions weight on a typical excavator working hour.

Table 3.8: Operating Conditions Weight Parameter on a Working Hour.		
Symbol	Value	Unit
C_1	129	[cycles/h]
C_2	162	[cycles/h]
C_3	340	[m/h]
C_4	0.15	[-]

The experimentally defined fuel consumptions are finally listed in Tab.3.9.

Table 3.9: Operating Conditions Mean Fuel Consumption.		
Symbol	Value	U_{95} [%]
$\overline{mf}_{DIGGING}$	33.25 [g/cycle]	± 3.57
$\overline{mf}_{GRADING}$	10.34 [g/cycle]	± 7.9
$\overline{mf}_{TRAVEL}$	3.29 [g/m]	± 8.2
$\overline{mf}_{IDLING}$	1331 [g/h]	± 6.2
$\overline{mf}_{JCMAS}$	8.62 [l/h]	± 2.87

3.2.5 Reference Working Cycles

The mathematical model validation, concerning the fuel consumption prediction, has to be referred to the working cycles defined by the JCMAS standard and performed during the experimental activity, in order to numerically evaluate the excavator fuel consumption during the cycles (see Chapter 4).

Referring to the different operating conditions (trench digging, grading, travelling and standby), while for both the travelling and the standby the input for the model are easily definable (during the standby none of the user is activated and for the travelling the track main spool are displaced to their maximum stroke), for the trench digging and the grading cycles it becomes essential the definition of the reference actuator position ($y_{i-TARGET}$) (see Chapter 2) required by the operator model, for each of the activated user.

Figure 3.35, Fig.3.36 and Fig.3.37 report the reference actuator piston target positions for the boom, the arm and the bucket concerning the trench digging cycle.

The reference curves (the black ones) were defined, for the linear actuators, on the basis of the experimental actuator piston position, obtained through the position transducer (y_1, y_2, y_3), of five different performed movements.

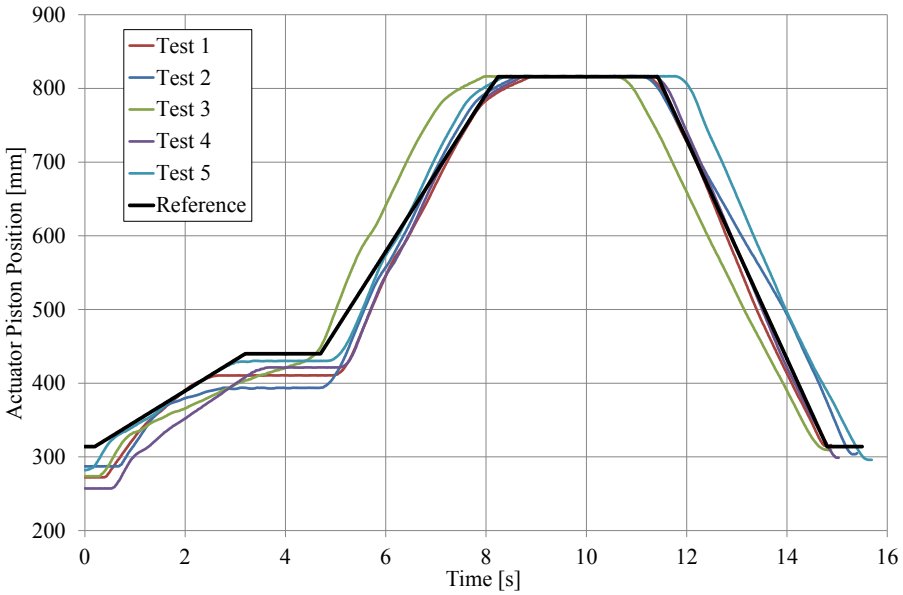

Figure 3.35: Boom Reference Actuator Position – Trench Digging Cycle.

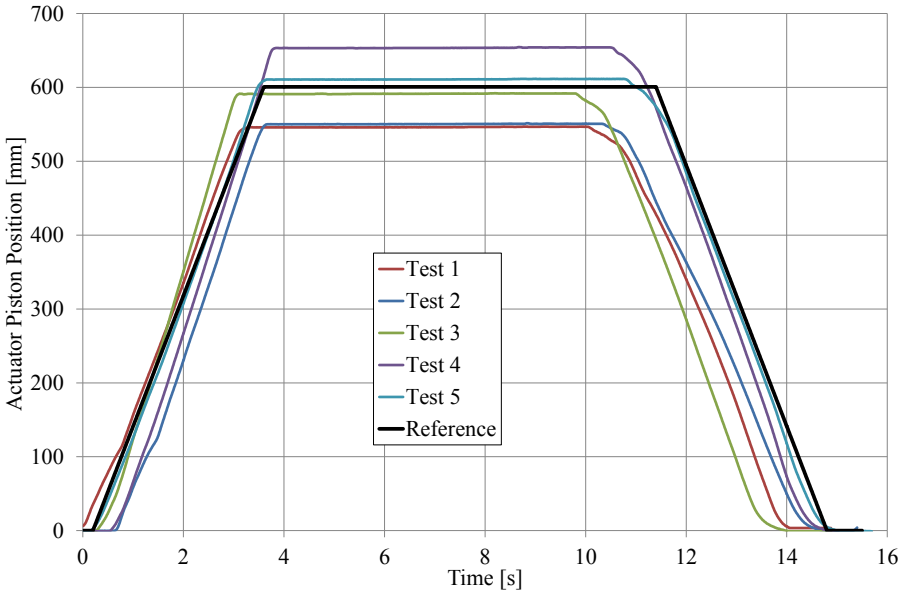

Figure 3.36: Arm Reference Actuator Position – Trench Digging Cycle.

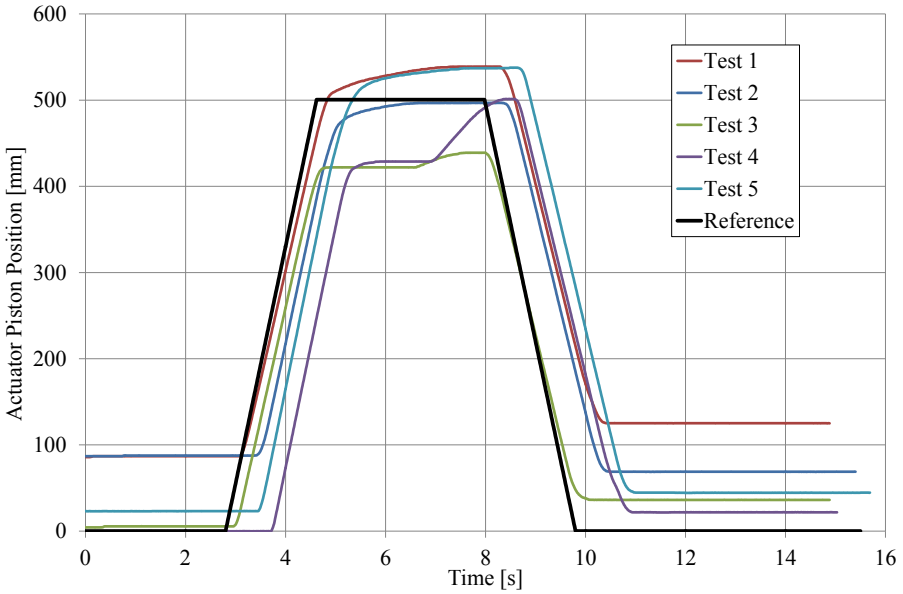

Figure 3.37: Bucket Reference Actuator Position – Trench Digging Cycle.

The same definition procedure was exploited for the reference actuator piston target positions for the boom and the arm regarding the grading cycle.

Figure 3.38 and Fig.3.39 report the comparison between the reference curves defined (the black ones) and the experimental positions during five performed movements.

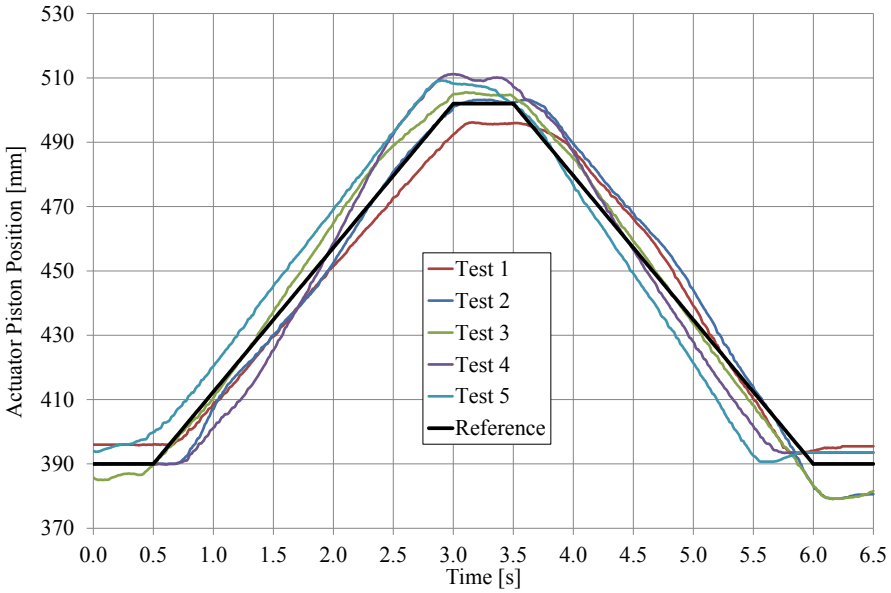

Figure 3.38: Boom Reference Actuator Position – Grading Cycle.

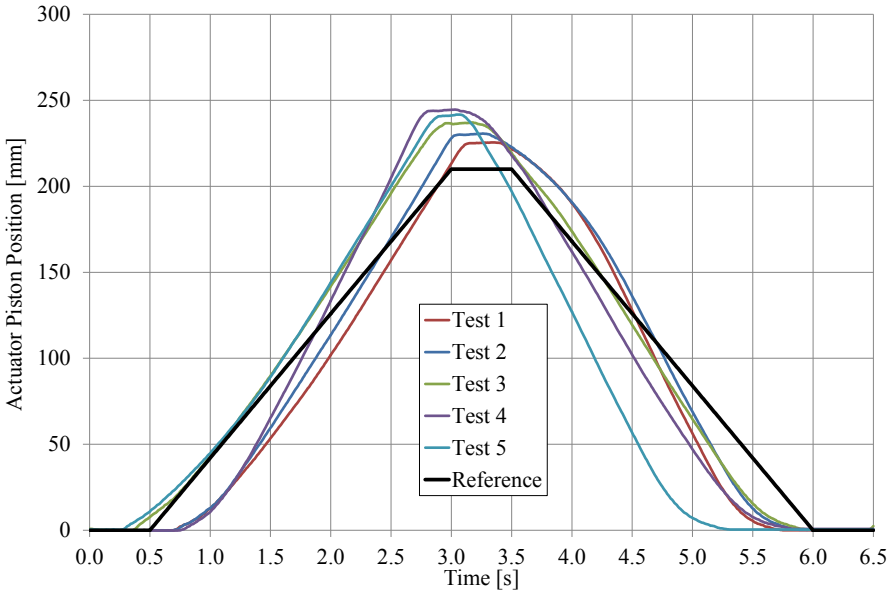

Figure 3.39: Arm Reference Actuator Position – Grading Cycle.

Symbols

Symbol	Definition	Unit
A	Orifice Area	[m^2]
n	Rotary Velocity	[r/min]
p	Pressure	[Pa]
Q	Volumetric Flow Rate	[m^3/s]
T	Torque	[N·m]
α	Angular Position	[rad]
ω	Angular Velocity	[rad/s]

References

3.1 *ISO 4409-1986. Hydraulic fluid power – Positive displacement pumps, motors and integral transmissions – Determination of steady-state performance.*

3.2 *JCMAS H020:2007. Earth-moving machinery – Fuel consumption on hydraulic excavator – Test Procedure.*

3.3 *H.W. Coleman, W.G. Steele. Experimentation, Validation and Uncertainty Analysis for Engineers. John Wiley & Sons, Inc. ISBN 978-0-470-16888-2.*

Chapter 4: **Standard Excavator Model Validation**

In this chapter the mathematical model of the standard excavator under study, presented in Chapter 2, will be validated on the basis of the experimental results obtained during the dedicated experimental activities, both on test bench and on the field, described in detail in Chapter 3.

4.1 Flow Generation Unit

The FGU model was calibrated on the basis of the experimental results obtained during the efficiency, swash plate actuator pressure, dynamic response and regulator tests.

The experimental defined maps concerning the main pump efficiencies, volumetric and hydraulic-mechanical, and the static correlation between the swash plate actuator pressure and the operating parameters (Fig.2.10) have been inserted in the model as well as the swash plate equivalent inertia (I_{EQ-SP}) and the related viscous friction coefficient (b_{SP}).

During the simulation the same operating and boundary conditions of the performed experimental tests were imposed to the FGU model. Then the numerical and experimental results were compared.

Figure 4.1 reports the experimental and numerical results comparison between the swash plate actuator pressure during a quasi-steady step variation of the pump speed with constant load pressure and flow rate.

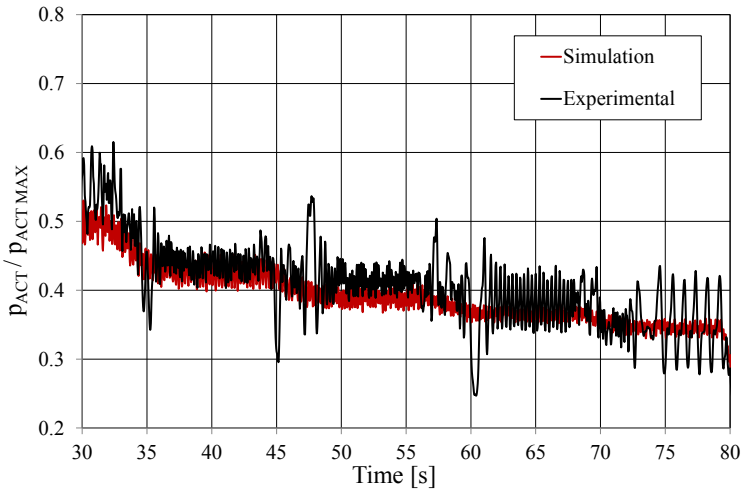

Figure 4.1: FGU Main Pump Swash Plate Actuation Pressure.

The good match of the results points out the capability of the main pump model to reproduce a realistic swash plate actuator pressure to equilibrate the swash plate under the operating conditions variation.

Figure 4.2, Fig.4.3 and Fig.4.4 represent the comparison between the numerical and experimental swash plate position during the dynamic step response tests at different operating conditions.

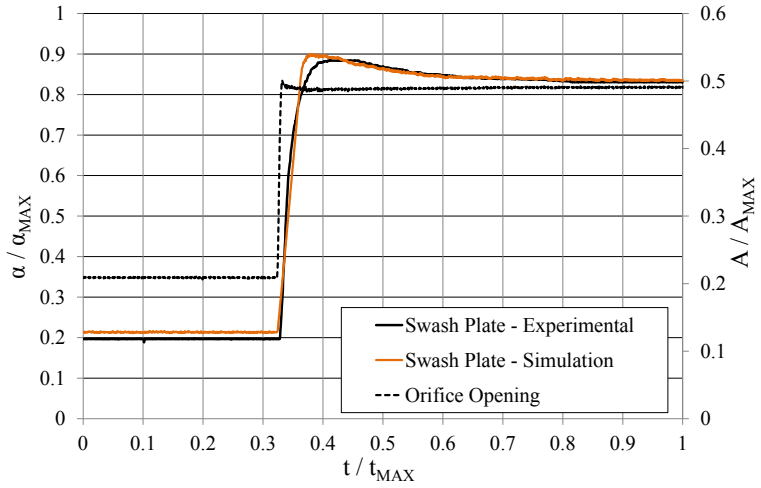

Figure 4.2: Main Pump Swash Plate Response - p_D=125 bar ,.n = 1500 r/min.

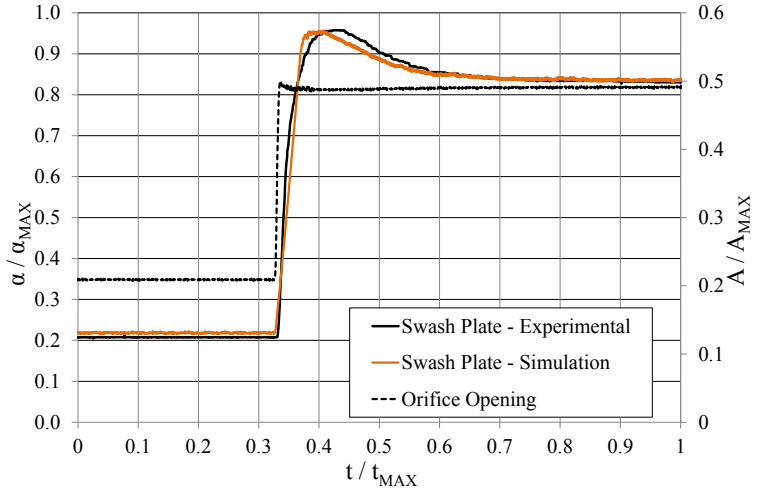

Figure 4.3: Main Pump Swash Plate Response - p_D=200 bar ,.n = 1500 r/min.

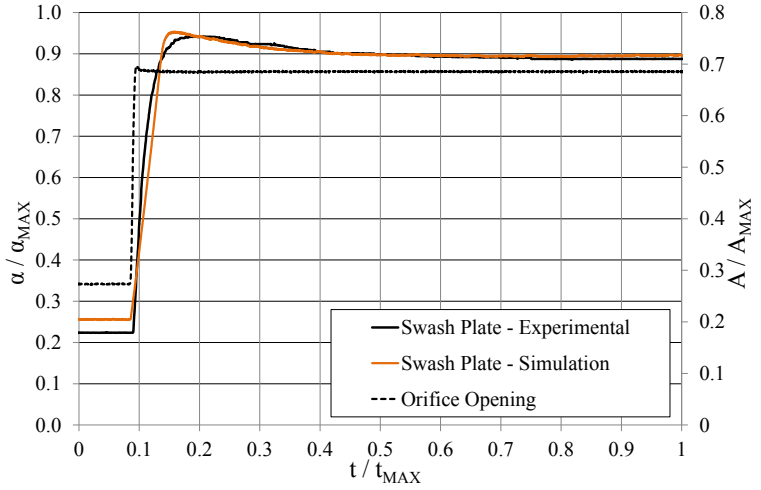

Figure 4.4: Main Pump Swash Plate Response - p_D=125 bar ,.n = 2000 r/min.

The results comparison validates the main pump mathematical model under dynamic working conditions.

Finally, Fig.4.5 reports the experimental and numerical results comparison obtained during the main pump regulators validation test.

The mathematical models of the regulators are able to replicate the actual functioning, limiting the absorbed torque by reducing the pump outlet flow rate since the load pressure exceeds the maximum allowed value (function of the instantaneous pump displacement).

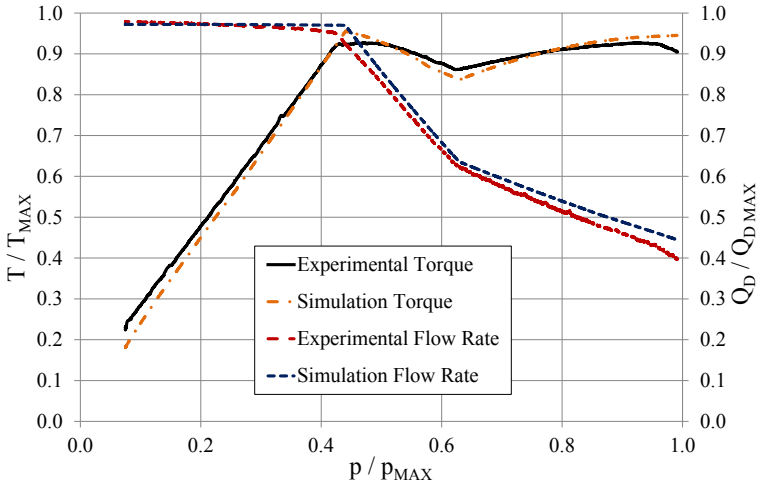

Figure 4.5: Main Pump Torque and Flow Rate during Torque Limiting.

4.2 Directional Flow Control Valve

The experimental activity carried out on the DFCV was focused on the LPC mathematical model validation, which is crucial in order to reproduce the actual operating modes of the valve sections.

A dedicated experimental activity, according to the test bench configuration reported in the ISO scheme of Fig.3.12, was performed. Once defined the LPCs discharge coefficients, the same operating conditions were simulated with the mathematical model.

Figure 4.6 depicts the experimental and numerical LPCs positions of the two valve sections, while Fig.4.7 and Fig.4.8 report the numerical and experimental valve sections downstream pressures (p_{DS}) comparison respectively.

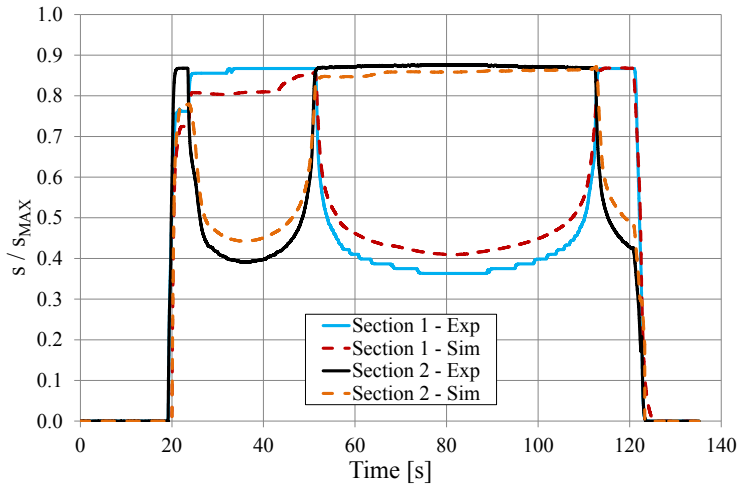

Figure 4.6: LPCs Positions Experimental and Numerical Comparison.

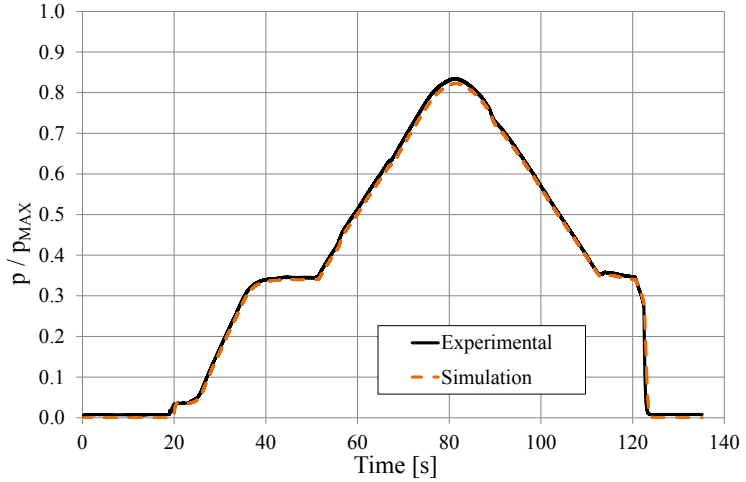

Figure 4.7: Experimental and Numerical Downstream Pressures (p_{DS}) - Section 1.

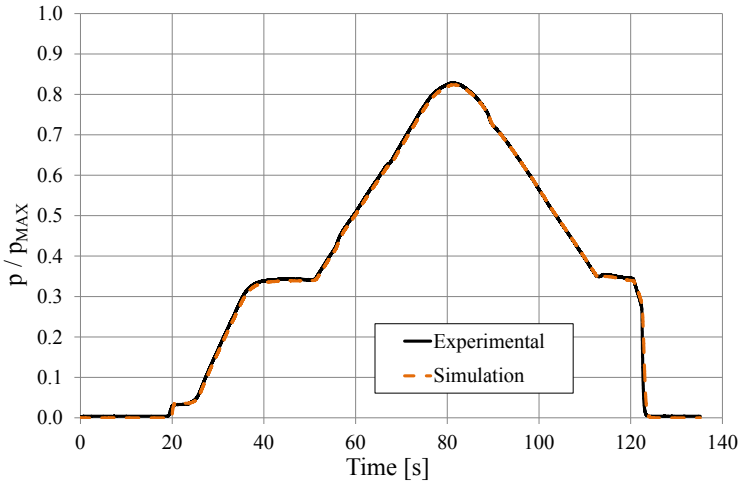

Figure 4.8 Experimental and Numerical Downstream Pressures (p_{DS}) - Section 2.

As can be noticed, there is a good match between the reported curves.

The downstream pressures (p_{DS}) assume almost the same instantaneous value in the two valve sections, for both the experimental test and the simulation.

The comparison points out the capability of the LPC model to keep a constant pressure drop between the valves inlet and the downstream chambers under operating condition variations, as in the real system. Therefore the LPC mathematical model is validated.

4.3 Complete Standard Excavator

The experimental activities carried out on the excavator, described in detail in Chapter 3, were designed for the system characterization as well as the mathematical model calibration.

The single user cycles have been exploited in order to define the actuator friction forces and torques contribution, the turret inertia, the hydraulic lines resistance coefficients and the DFCV sections discharge coefficients (for both the metering and the outlet notches).

Once calibrated the mathematical model the experimental tests were simulated with the aid of the excavator mathematical model for each single user. Fig.4.9 – Fig.4.13 report the experimental and numerical results comparison. The reported variables are the ICE speed, the main pump delivered flow rate and the system pressure.

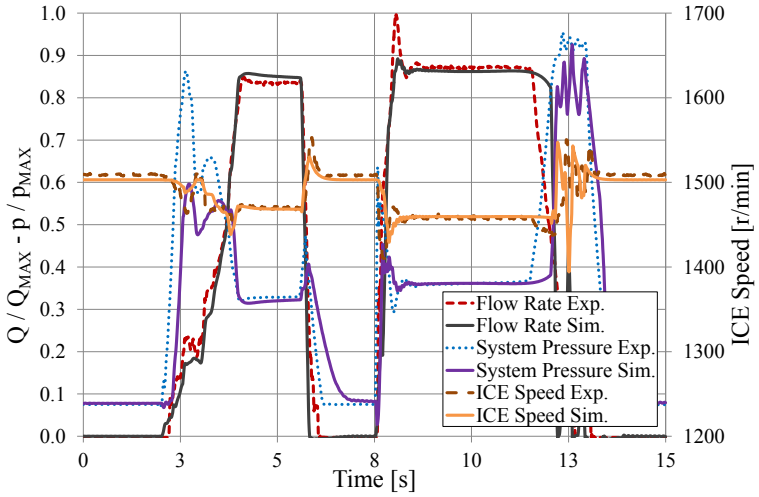

Figure 4.9: Experimental and Simulation Boom Cycle.

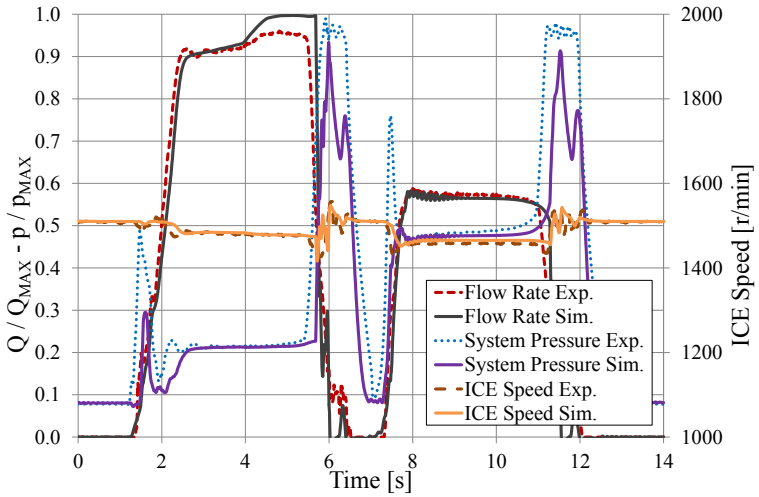

Figure 4.10: Experimental and Simulation Arm Cycle.

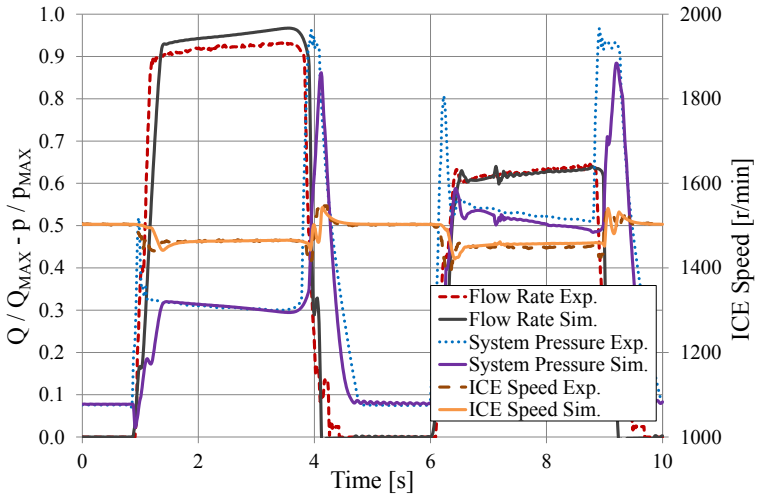

Figure 4.11: Experimental and Simulation Bucket Cycle.

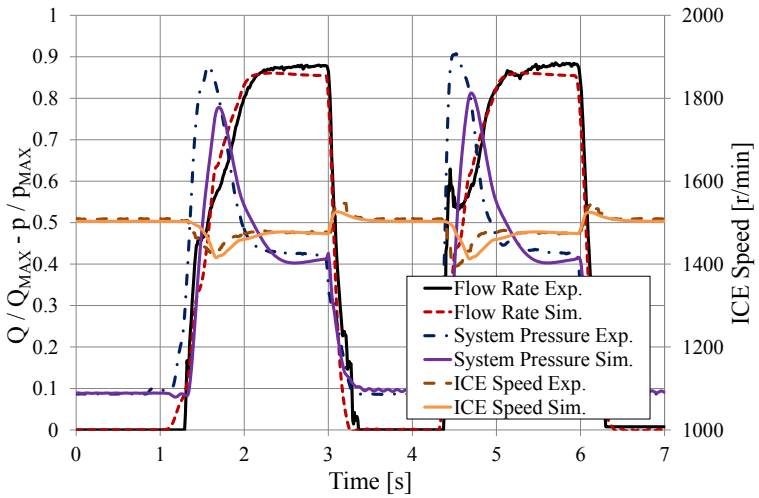

Figure 4.12: Experimental and Simulation Turret Cycle.

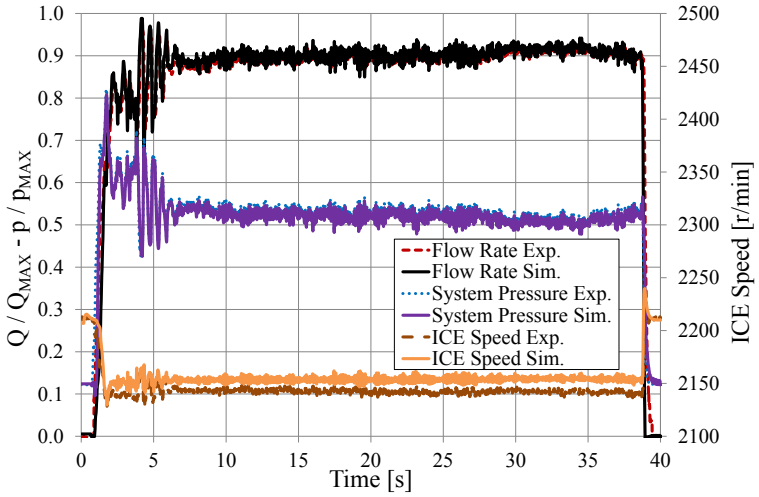

Figure 4.13: Experimental and Simulation Travel Cycle.

As can be observed from the reported comparisons, the excavator mathematical model results match in a very satisfying manner the experimental data during both transient and steady-state operating conditions, therefore validating the complete standard excavator mathematical model developed for the estimation of the hydraulic and mechanical variables.

The noticeable differences during the transients could found justification in the modelling simplifications done in order to keep short the computation time.

Concerning the model capability of predicting the fuel consumption, the comparison between the experimental and the numerical fuel consumption results are reported in Tab.4.1.

Table 4.1: Experimental and Numerical Fuel Consumption Results.

Symbol	Experimental	U_{95} [%]	Numerical	$\frac{mf_{SIM}-mf_{EXP}}{mf_{EXP}}$ [%]
$\overline{mf}_{DIGGING}$	33.25 [g/cycle]	± 3.57	34.12 [g/cycle]	+2.61
$\overline{mf}_{GRADING}$	10.34 [g/cycle]	± 7.9	10.53[g/cycle]	+1.83
$\overline{mf}_{TRAVEL}$	3.29 [g/m]	± 8.2	3.26 [g/m]	-1.06
$\overline{mf}_{IDLING}$	1331 [g/h]	± 6.2	1330 [g/h]	-0.08
$\overline{mf}_{JCMAS}$	8.62 [l/h]	± 2.87	8.78 [l/h]	+1.86

Being the percentage differences between numerical and experimental fuel consumption ($\frac{mf_{SIM}-mf_{EXP}}{mf_{EXP}}$) always within the combined uncertainty limits, experimentally defined for each operating modes, the model fuel consumption prediction capability are validated.

Chapter 5: **Energy Saving Solutions for LS Hydraulic Systems**

In this chapter some energy saving solutions to reduce the fuel consumption of the machinery under study will be proposed and described in detail.

The proposed solutions have been defined on the basis of an energy analysis conducted on the standard excavator hydraulic system with the aid of the mathematical model, presented and validated in the previous chapters.

5.1 Energy Analysis of the Standard Excavator Hydraulic System

In Chapter 4 the excavator mathematical model has been validated on the basis of the experimental results both for the definition of the hydraulic system variables and for the fuel consumption predictions capability during the simulated working cycles.

In this chapter a comprehensive and detailed energy analysis will be conducted for the standard hydraulic system of the excavator, with the aid of its mathematical model, in order to evaluate the energy dissipations and to propose different solutions to improve the machinery overall efficiency.

The reported results in these energy analyses refer to the simulations of the trench digging and the grading working cycles, defined by the JCMAS standard [3.2], which are the most performed operating conditions for the working hydraulic of an excavator.

As previously stated, during both the experimental and the simulated working cycles the interaction between the bucket and the terrain was neither performed nor modelled. Therefore the energy dissipations in the system refer to the working hydraulic usage for just moving the kinematics in air, which represents the most performed movements during the performed working cycles.

This will not affect the energy recuperation analysis presented in the next paragraphs, because the useful operating phases[25] for energy recuperations during the reference working cycles [*3.2*] are typically performed when the excavated material is already dumped.

5.1.1 Trench Digging Cycle

In this section are reported the energy analysis concerning the trench digging working cycle.

Figure 5.1 represents the energy flow along the hydraulic system during the simulated cycle.

The ICE overall efficiency on the cycle is of about the 27%. Starting from the ICE mechanical energy, which represents the total amount of energy entering the system, all the energy dissipations in the system have been quantified.

[25] The useful operating phases for energy recuperations are the ones where the loads acting on the hydraulic actuators are typically pulling.

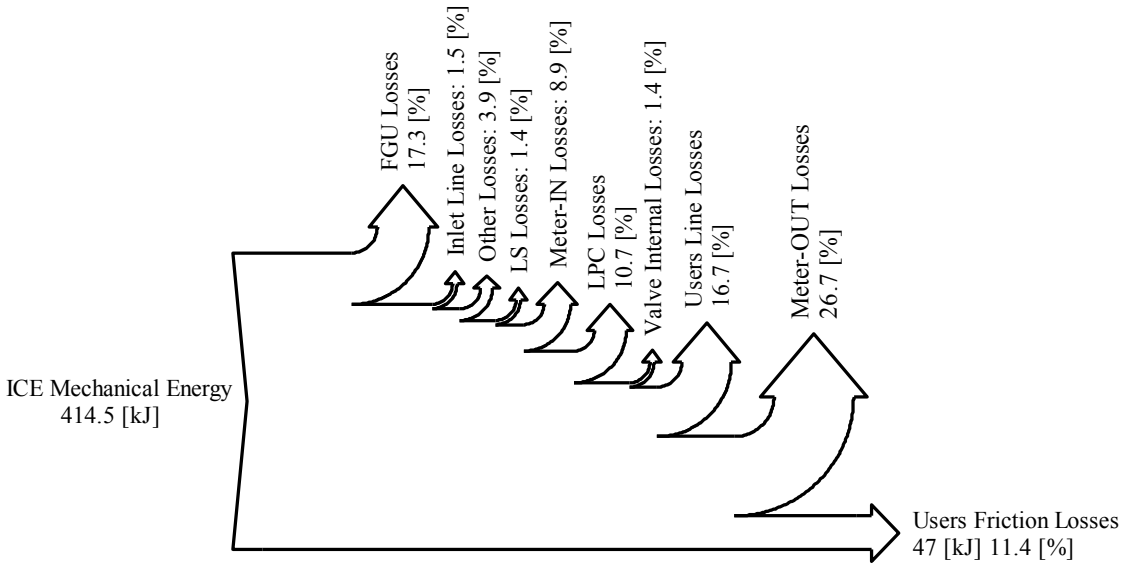

Figure 5.1: Sankey Diagram of the Trench Digging Cycle.

As can be observed from the energy flow diagram, about 17% of the inlet energy is dissipated by the FGU, which has an overall efficiency of about 82% on the cycle. These energy dissipations are related both to the volumetric and hydraulic-mechanical losses.

Other energy losses due to lamination in the inlet hydraulic lines, between the FGU and the DFCV as well as in the pressure relief valves, represent approximately the 5.4 % of the total energy amount.

The 77.3% of the total inlet energy enters into the DFCV and then is divided through the different activated valve sections. The energy dissipations related to the DFCV, reported in Fig.5.1, represent the summation of each users related dissipations. A more detailed analysis concerning each user will be further presented.

The main amount of energy dissipations in the distributor are related to the meter-IN orifices, the LPCs and the meter-OUT orifices and quantified as the 8.9%, 10.7% and 16.7% respectively. Other minor energy losses in the distributor are related to the internal losses and to the LS losses both of about 1.4%.

Considerable energy dissipations occur between the DFCV and the hydraulic actuators workports due to laminations along the hydraulic lines, and quantified in about 16.7% of the total.

Referring to the defined reference working cycles (Chapter 3) the required energy to perform the kinematics movements is due only to the hydraulic actuators related friction forces and torques, which represent the effective work in the considered cycle. In fact, being the implements initial and final position coincident in the working cycles, the total energy amount

to move the kinematics is related to frictions and is quantified in about the 11.4% of the total inlet energy, since the energy used to increase the potential and the mechanical energy of each implement during some phases is then fed back to the system during the next phases. These considerations will be more clear analysing the user energy consumption in detail.

Figure 5.2 reports the power demand in the system during the trench digging cycle, coherently with the energy flow reported in Fig.5.1.

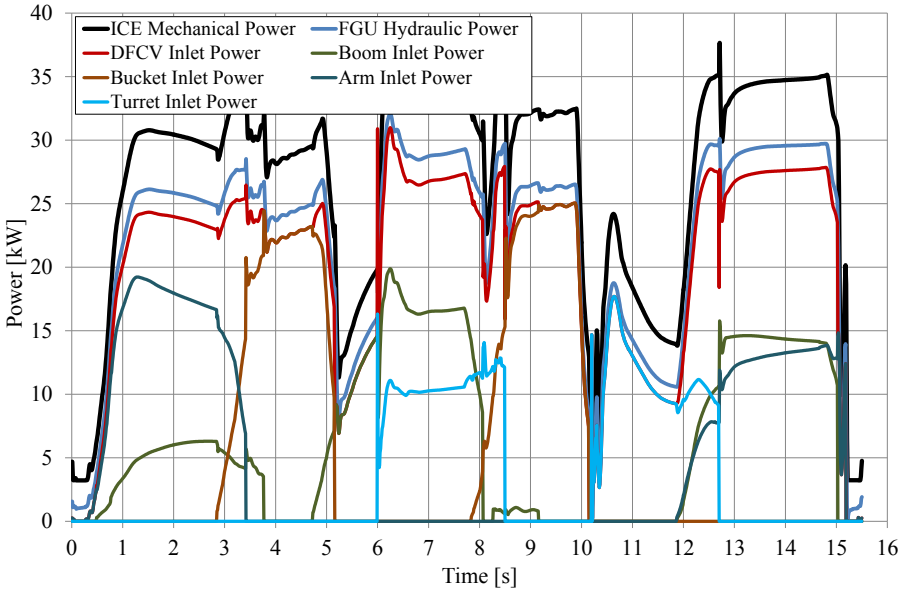

Figure 5.2: System Power Demand during the Trench Digging Cycle.

The black line is the ICE mechanical power while the light-blue is the overall hydraulic power delivered by the FGU. The total hydraulic power entering the DFCV is represented by the red line, which is equal to the summation of the users power demand defined by the others reported curves.

Observing the power demand of the users during the cycle, it is possible to point out that some users are contemporary actuated, the boom and the arm, and the boom and the turret, while others are never actuated at the same time, the boom and the bucket, and the arm and the turret. During the parallel users operations, as previously described for LS systems, the users requiring lower pressure amounts than the loadest section have the major energy dissipations, due to lamination, in the LPCs in order to meet the LS control logic, being very inefficient.

A very effective method to reduce the energy dissipations in the LPCs is that of dividing the users in two separate groups thus adopting two LS pump instead of one.

This solution will be further presented and described in the next sections in order to quantify the related energy saving amount.

Another method for the improvement of the hydraulic system energy efficiency is reduce the hydraulic actuators size. Therefore on one hand the flow rates in the hydraulic lines are reduced and as a consequence the energy dissipations due to lamination in the hydraulic lines are reduced too, but on the other hand the system working pressures have to be increased in order to accomplish the same operating tasks. This imposes the usage of hydraulic pumps, components and actuator designed to endure under more critic working conditions. Otherwise instead of reducing the hydraulic actuators size, the same result could be achieved increasing the hydraulic lines internal diameters. These solutions will not be investigated in this analysis.

A further effective solution to reduce the meter-IN energy losses is that of reducing the pump margin setup. This solution will be further investigated in the next sections.

Concerning the meter-OUT energy losses of the DFCV a further analysis considering the users actuation phases is required in order to evaluate other possible energy saving solutions.

Users Energy Analysis on Trench Digging Cycle

Considering the boom, Fig.5.3 and Fig.5.4 represent the energy flow related to the rising and the lowering phases respectively, while Fig.5.5 reports its power demand during the trench digging cycle.

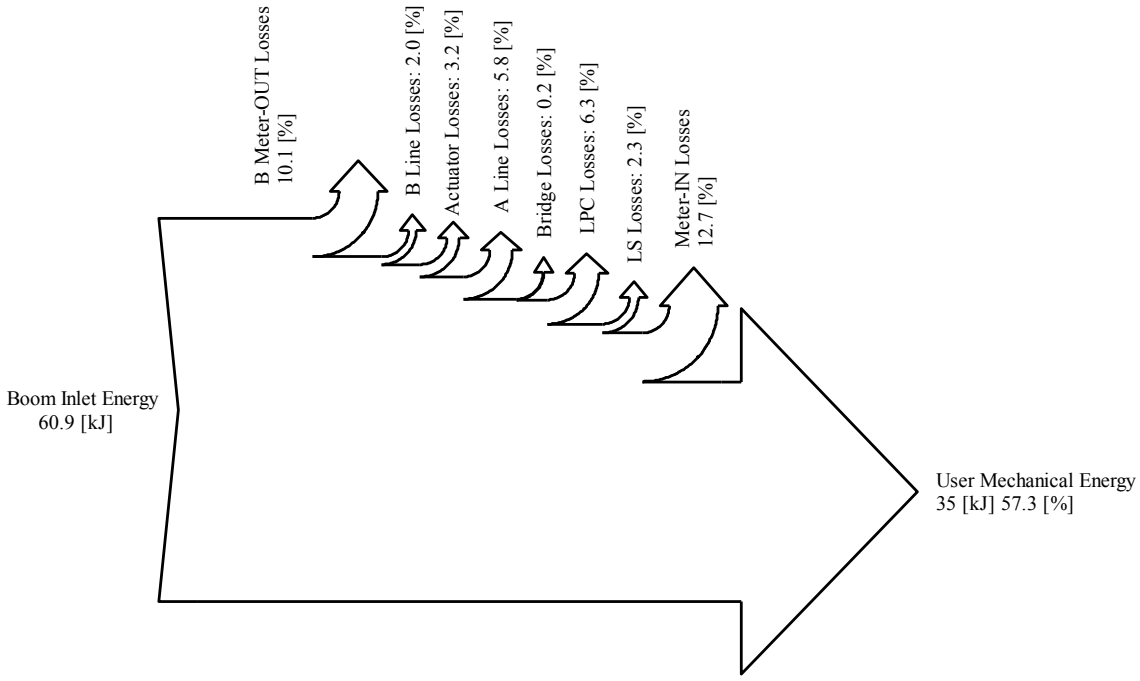

Figure 5.3: Sankey Diagram of the Boom User during the Rising Phase.

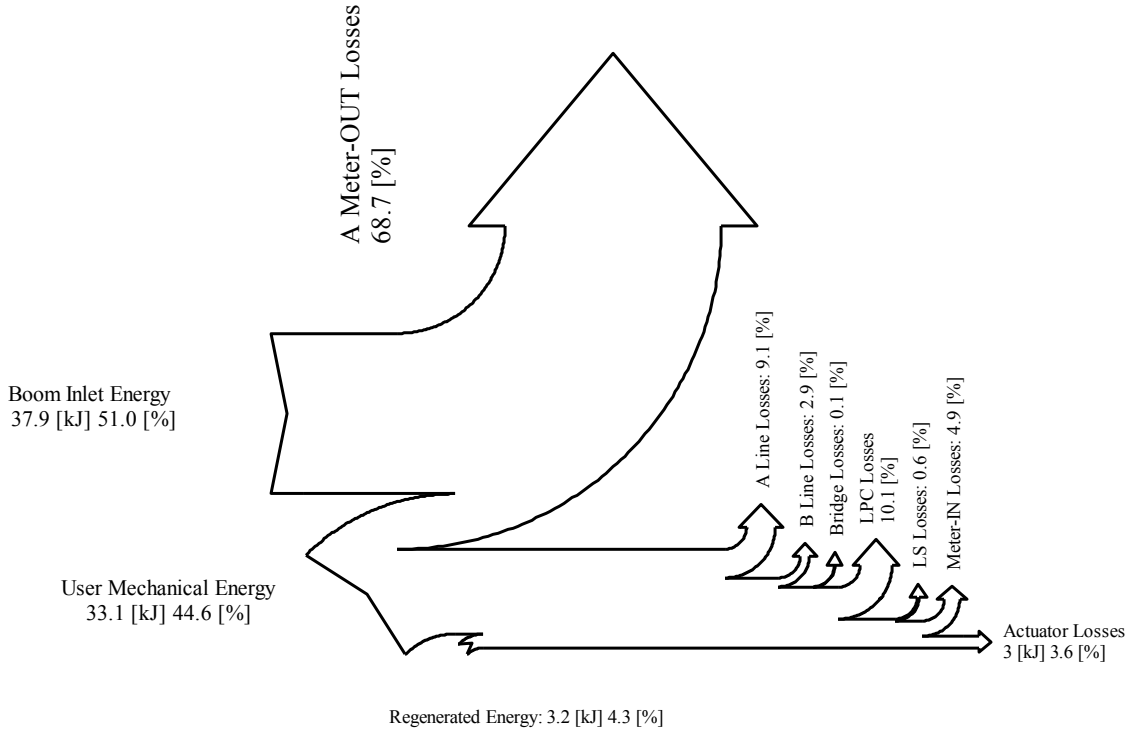

Figure 5.4: Sankey Diagram of the Boom User during the Lowering Phase.

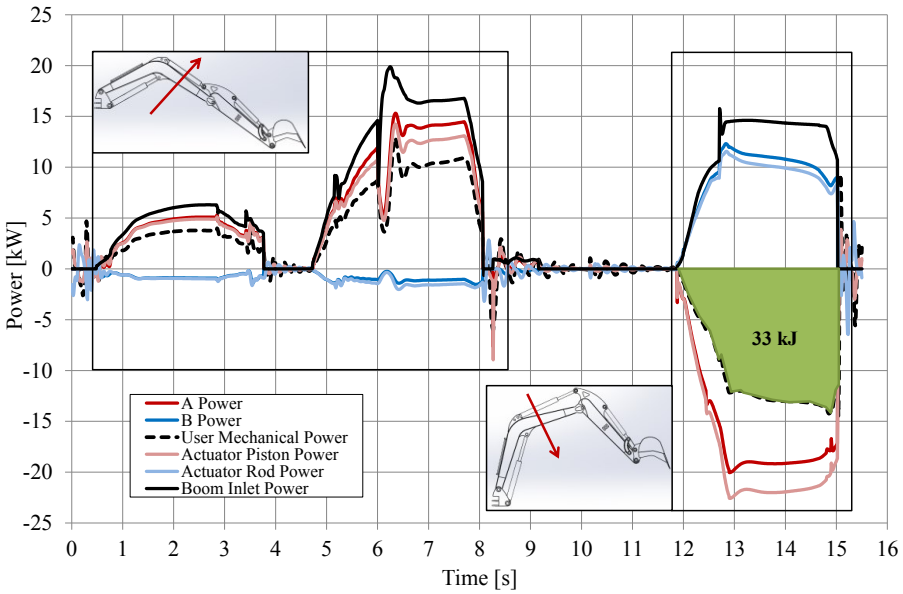

Figure 5.5: Boom Power Demand during the Trench Digging Cycle.

During the boom rising phase, which is composed of two sequential movements, Fig.5.5, most of the entering energy, in the valve section, is exploited to increase the boom potential energy due to the implement rising referring to the initial position.

In this working phase the force acting on the boom actuator is resistant, due to the boom mass, thus neither possibility of cavitation in the rod side of the actuator nor implement fugue could occur. Therefore the meter-OUT energy losses could be reduced through the optimization of the outlet orifice flow area.

During the lowering phase, the boom could be moved just exploiting its potential energy, but in order to maintain the control of the velocity the cavitation in the rod side of the actuator has to be avoided. Consequently the flow area of the meter-OUT (A→T) orifice was designed to be very narrow. Thus the meter-OUT related energy losses are considerably higher than the available potential energy, quantified in about the 68.7% of the total available energy during this phase, due to further entering energy to accomplish the boom lowering at the desired velocity. This means that during the boom lowering phase the boom is literally pushed down.

As can be noticed, about the 4.3% of the available energy is directly recovered through a regeneration system within the valve main spool.

Adopting an energy recovery system (ERS) in order to control the boom lowering and recover otherwise wasted energy is another effective energy saving solution.

Similar considerations could be done considering the arm. Figure 5.6 and Fig.5.7 represent the energy flow during the closing and the opening movements respectively, while Fig.5.8 reports the arm cycle related power demand.

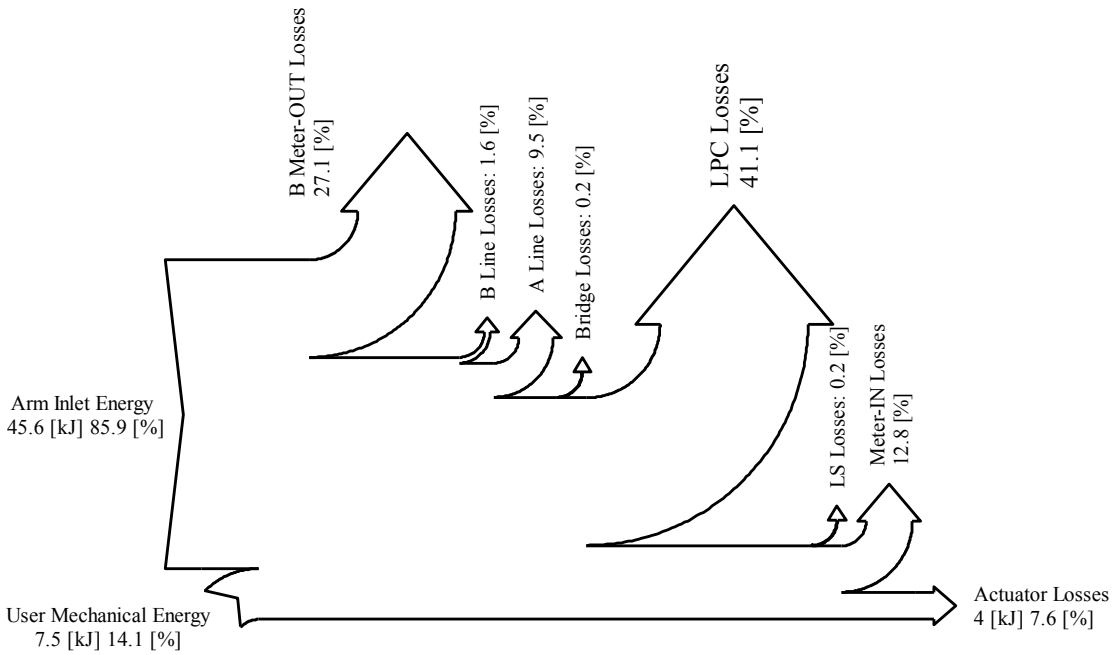

Figure 5.6: Sankey Diagram of the Arm User during the Closing Phase.

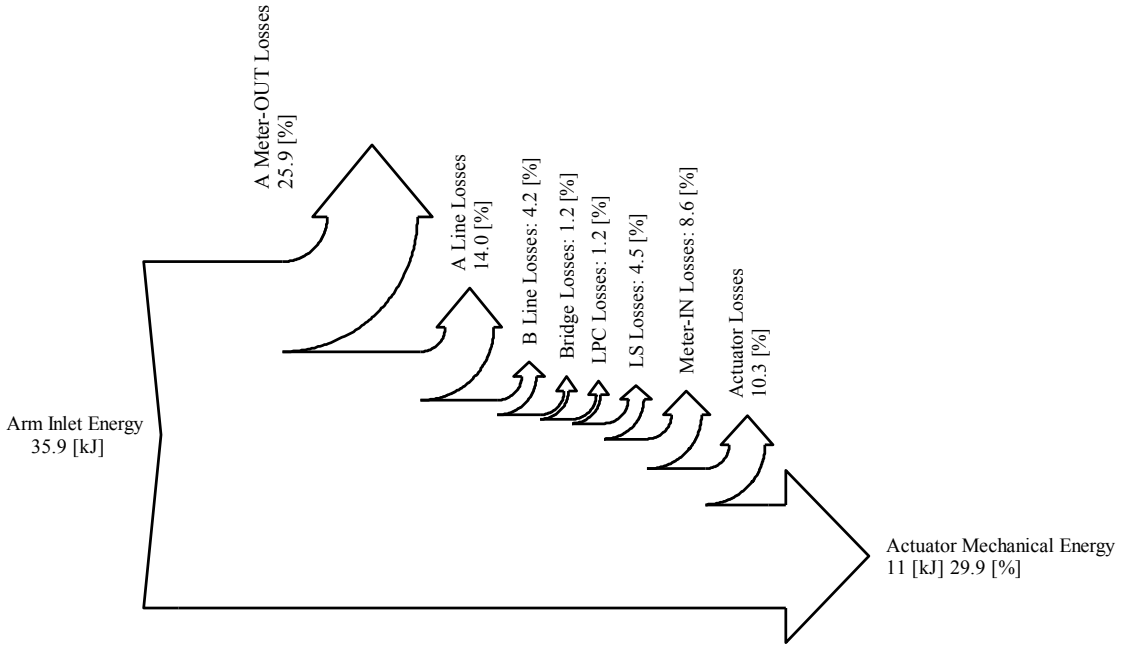

Figure 5.7: Sankey Diagram of the Arm User during the Opening Phase.

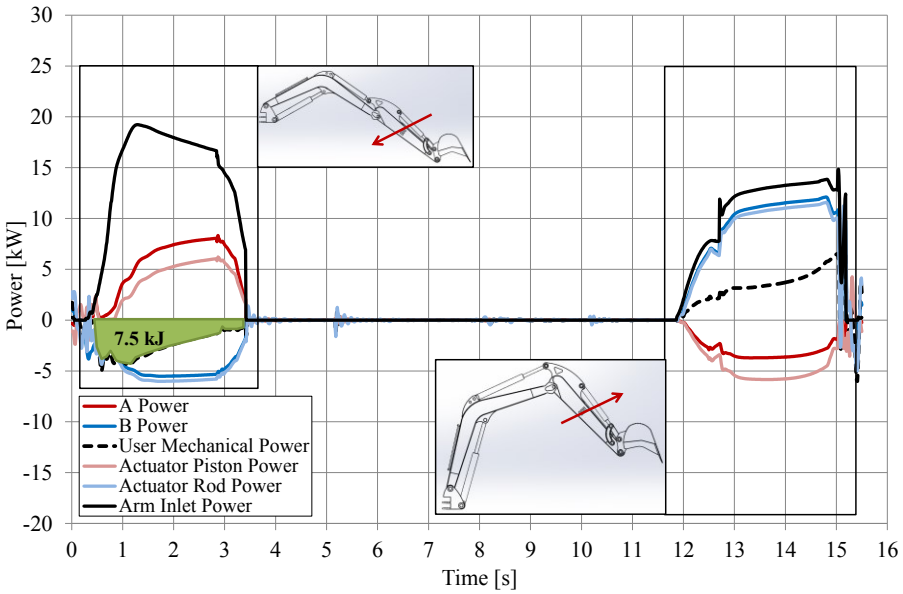

Figure 5.8: Arm Power Demand during the Trench Digging Cycle.

During the arm closing movement the force acting on the hydraulic actuator is pulling due to the kinematics mass and position. As previously for the boom, in order to maintain the control the cavitation in the piston side of the hydraulic actuator has to be avoided, thus the flow area of the outlet orifice is designed to be narrow too. Therefore the meter-OUT energy losses, quantified in 27.1%, are due to the arm potential energy and further entering energy dissipations.

Even for this user an amount of the wasted energy in the meter-OUT could be recovered exploiting an ERS.

During this phase the LPC energy dissipations, Fig.5.6, are quantified in 41.1% of the total available energy due to the contemporary activation of the arm and the boom, confirming the possibility of reducing the energy dissipation dividing the system users in different groups, as previously indicated.

Considering now the arm opening phase, as similarly for the boom rising phase, the load acting on the hydraulic actuator is typically resistant and thus optimizing the outlet orifice flow area the meter-OUT energy losses could be further reduced.

Referring to the bucket, Fig.5.9 and Fig.5.10 represent the energy flow related to the closing and opening phases respectively, while Fig.5.11 reports its power demand during the trench digging cycle.

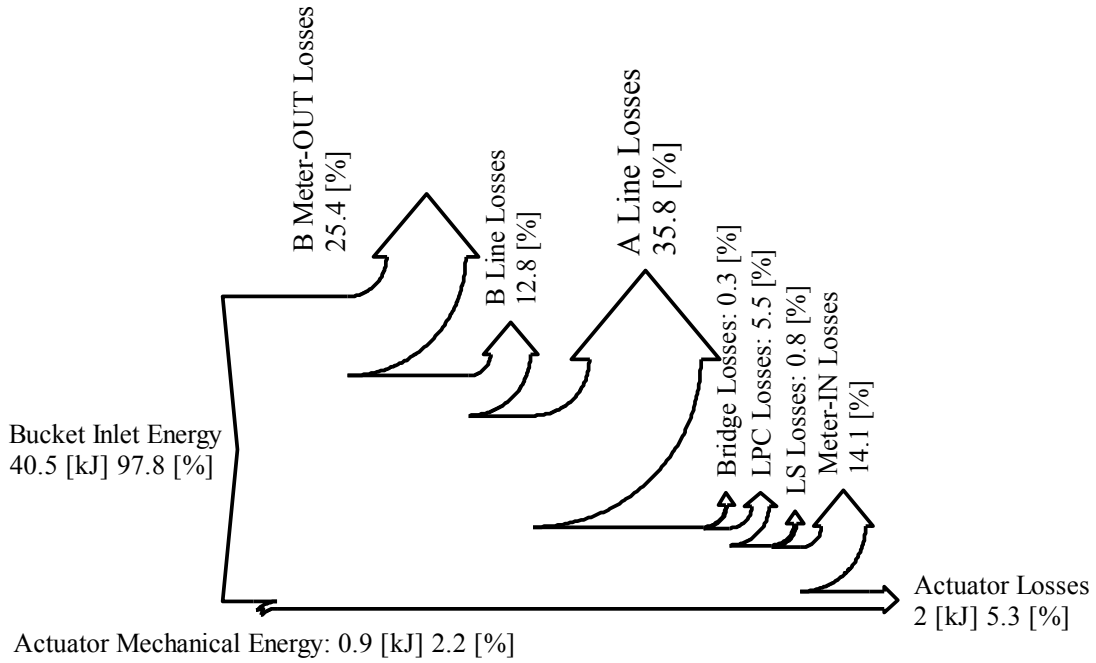

Figure 5.9: Sankey Diagram of the Bucket User during the Closing Phase.

Concerning both the bucket closing and opening phases, the main energy dissipations are related to the lamination in the hydraulic lines between the DFCV and the actuator, quantified in about 50%. In fact between the bucket valve section workports and the hydraulic actuator ones the A and B hydraulic lines length is about 9.5 m.

The meter-OUT energy losses could be reduced optimizing the outlet orifices flow area as in the other users.

During these phases the load acting on the bucket hydraulic actuator is pulling for just a brief part of the closing movement while is resistant during the opening phase and thus energy recovery is not considerable.

Being this user actuated singularly, the LPC energy dissipations are less than 1%.

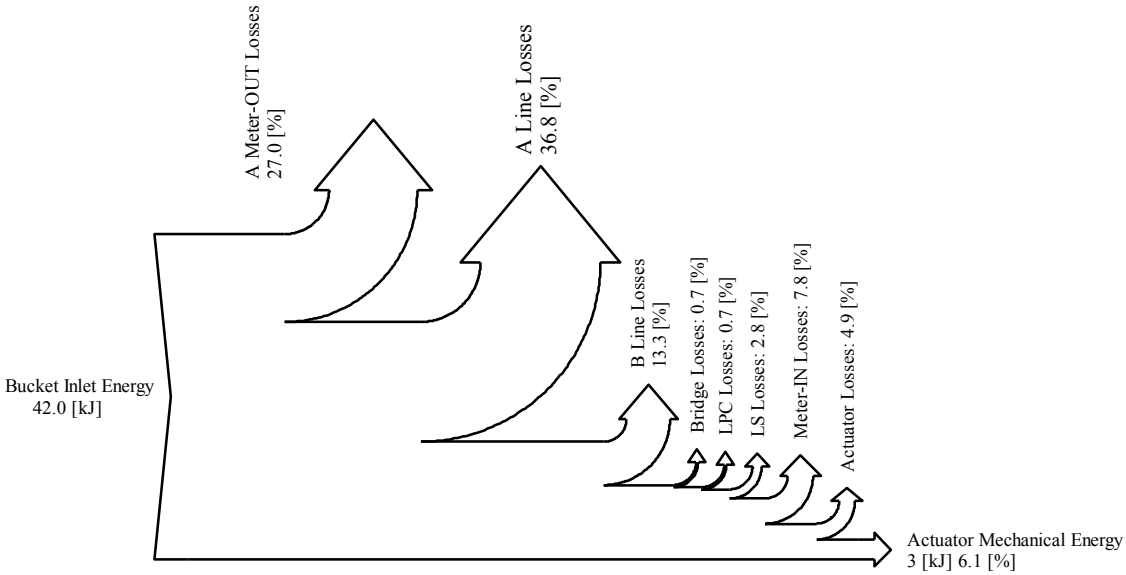

Figure 5.10: Sankey Diagram of the Bucket User during the Opening Phase.

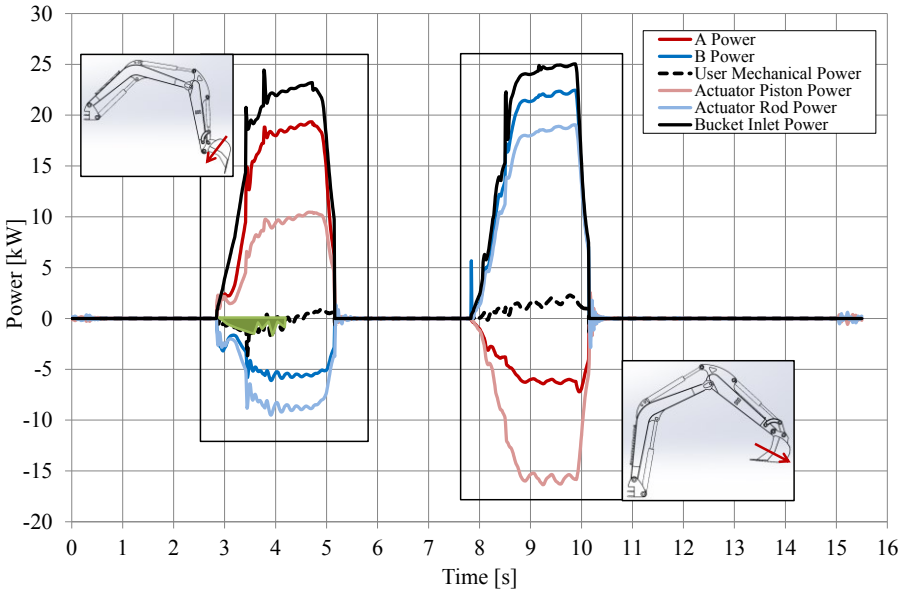

Figure 5.11: Bucket Power Demand during the Trench Digging Cycle.

Considering the turret, Fig.5.12 and Fig.5.13 represent the energy flow related to the accelerating and decelerating phases during a 90 degree swing movement, while Fig.5.14 reports the turret overall power demand during the trench digging cycle.

Analysing the energy flow along the hydraulic actuation system of the turret, the LPCs energy dissipations, quantified in about 16% of the entering energy, could be reduced if the turret will be neither actuated contemporary with the boom neither the arm.

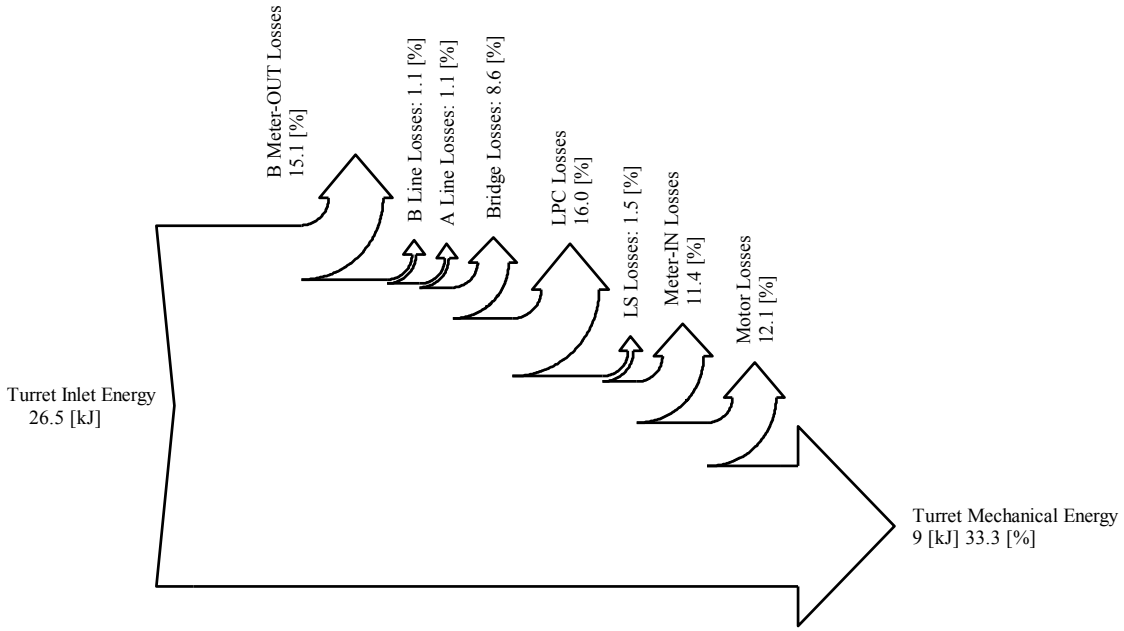

Figure 5.12: Sankey Diagram of the Turret User during the Accelerating Phase.

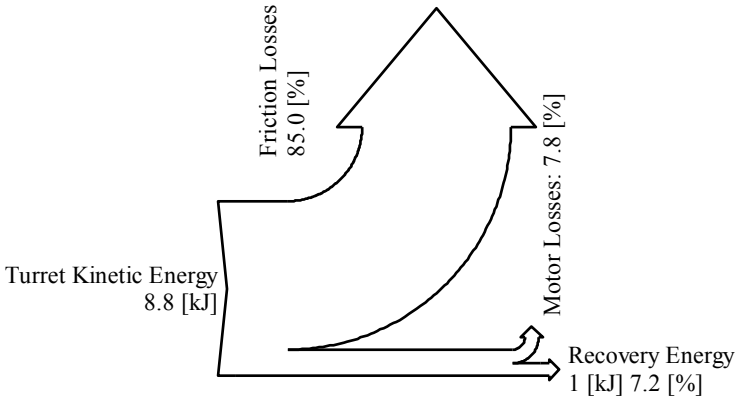

Figure 5.13: Sankey Diagram of the Turret User during the Braking Phase.

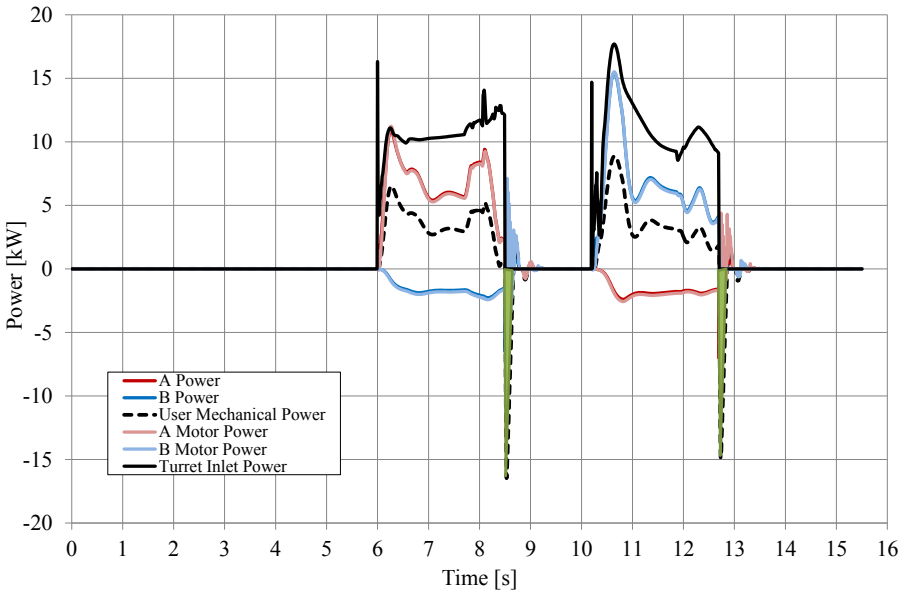

Figure 5.14: Turret Power Demand during the Trench Digging Cycle.

The meter-IN losses could be reduced decreasing pump margin setting, while the meter-OUT losses reduction, differently than the previous users, require the outlet section architecture modification (solution does not investigated in this thesis).

Another important consideration regards the amount of recoverable energy during the turret deceleration phases, which are represented by the green areas in Fig.5.14.

The total laminated energy on the pressure relief valves during and for the braking of the turret is quantified in about 7.2% of the total kinetic energy for each braking phases (two in a single trench digging cycle), which is about the 3.7% of the total required energy to actuate the turret during one rotation.

The energy recovery percentage related to the turret, for this excavator size, is not very promising for the implementation of a dedicated ERS.

5.1.2 Grading Cycle

In this section are reported the energy analyses concerning the grading working cycle. Figure 5.15 represents the energy flow along the hydraulic system during the simulated cycle while Fig.5.16 reports the power demand in the system.

The ICE overall efficiency on the cycle is 27.39%. The total amount of energy entering the system is considered equal to ICE mechanical energy. The energy dissipations along the system are then quantified.

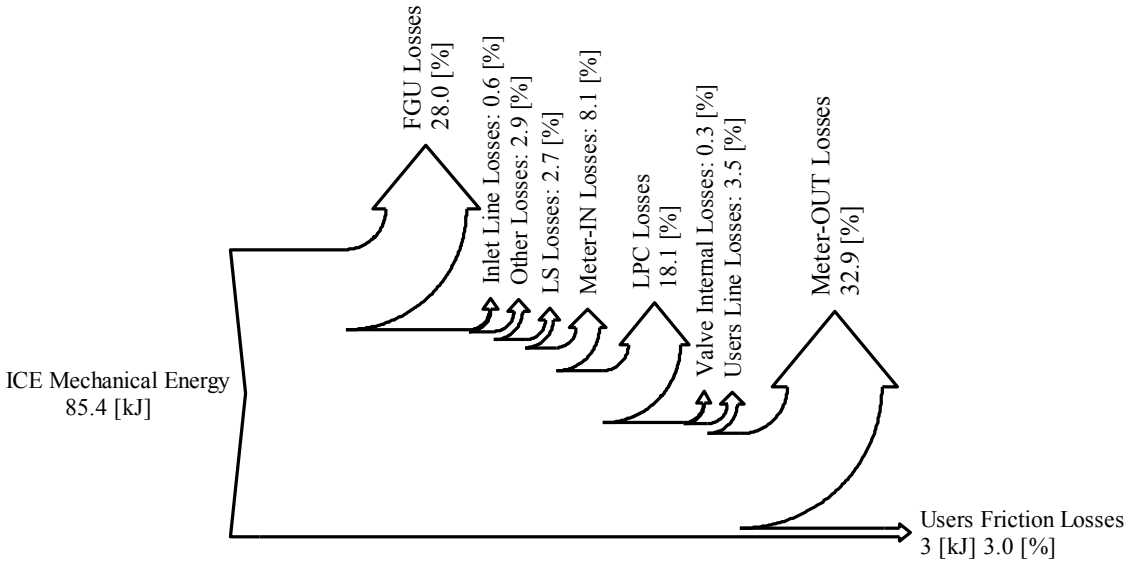

Figure 5.15: Sankey Diagram of the Grading Cycle.

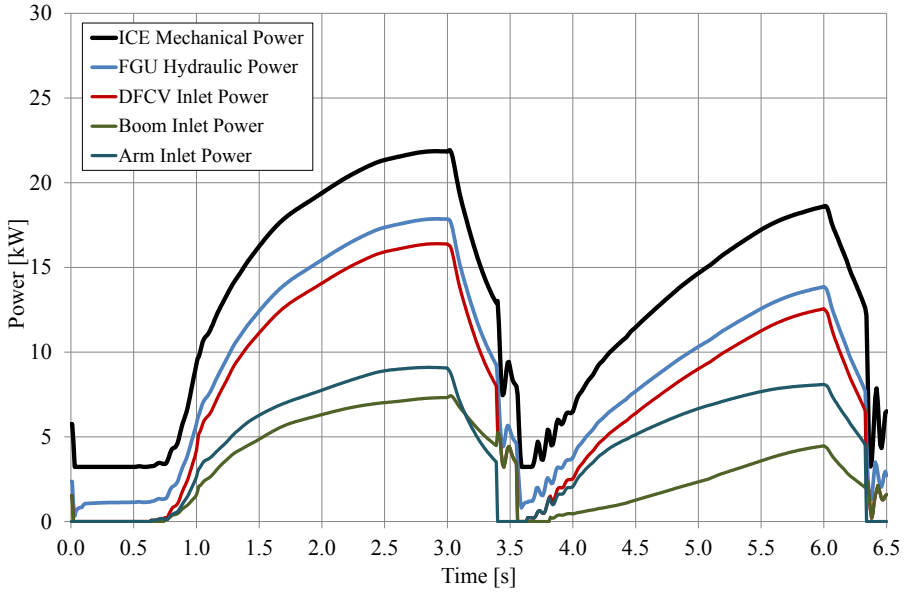

Figure 5.16: System Power Demand during the Grading Cycle.

About 28% of the inlet energy is dissipated by the FGU, which has an overall efficiency on the cycle of about 72%. The FGU energy dissipations in the grading cycle are higher than those in the trench digging cycle, because the FGU overall efficiency is lower during the grading cycle due to the lower flow rates and thus minor pump displacement.

On the contrary, being the flow rate reduced, the energy losses, due to lamination, in the hydraulic lines, both the inlet ones (between the FGU and the DFCV) and the users ones (between the DFCV and the hydraulic actuators workports), quantified in the 0.6% and 3.5% respectively, are reduced.

The LS line and other energy dissipations represent the 2.7% and the 2.9% of the total energy amount respectively.

The energy dissipations related to the DFCV represent the summation of all the actuated users dissipations during the grading cycle, i.e. the boom and the arm.

In the grading cycle, if compared with the trench digging cycle, the meter-IN energy dissipations are almost the same, evaluated in about 8% of the total energy, while the LPCs and the meter-OUT energy losses are increased, quantified in about the 18% and the 33% respectively.

Even for the grading cycle, the energy saving solutions, pointed out for the trench digging cycle and further presented in the next sections, could be exploited in order to improve the machinery overall efficiency.

5.2 Proposed Energy Saving Solutions

In this section will be presented different energy saving solutions for the excavator under investigation and LS hydraulic system in general. The correspondent energy analyses and the fuel consumption reduction will be discussed and presented in Chapter 9.

The presented solutions have been defined starting from the considerations carried out on the energy dissipations concerning both the trench digging and the grading cycle, which are the most performed operating conditions of an excavator.

5.2.1 Dual Pump LS System

During parallel users operations have been pointed out that the users requiring the lower pressure demands to accomplish their tasks have the high energy dissipations, due to lamination, in the related LPCs.

An effective solution to reduce these energy dissipations is to divide the users in two separate groups and thus adopting two LS pump instead of one.

According to the power demand charts for both the trench digging cycle, Fig.5.2, and the grading cycle, Fig.5.16, the users[26] have been divided in two groups:

- group 1: Boom, Bucket, Travel DX;
- group 2: Arm, Turret, Travel SX.

The simplified ISO scheme of the proposed dual pump LS system is reported in Fig.5.17 according to the user defined grouping.

[26] In the defined groups and ISO scheme have been listed and reported only the activated users during the considered working cycles. The others (the blade, the boom swing and the auxiliary) were not reported.

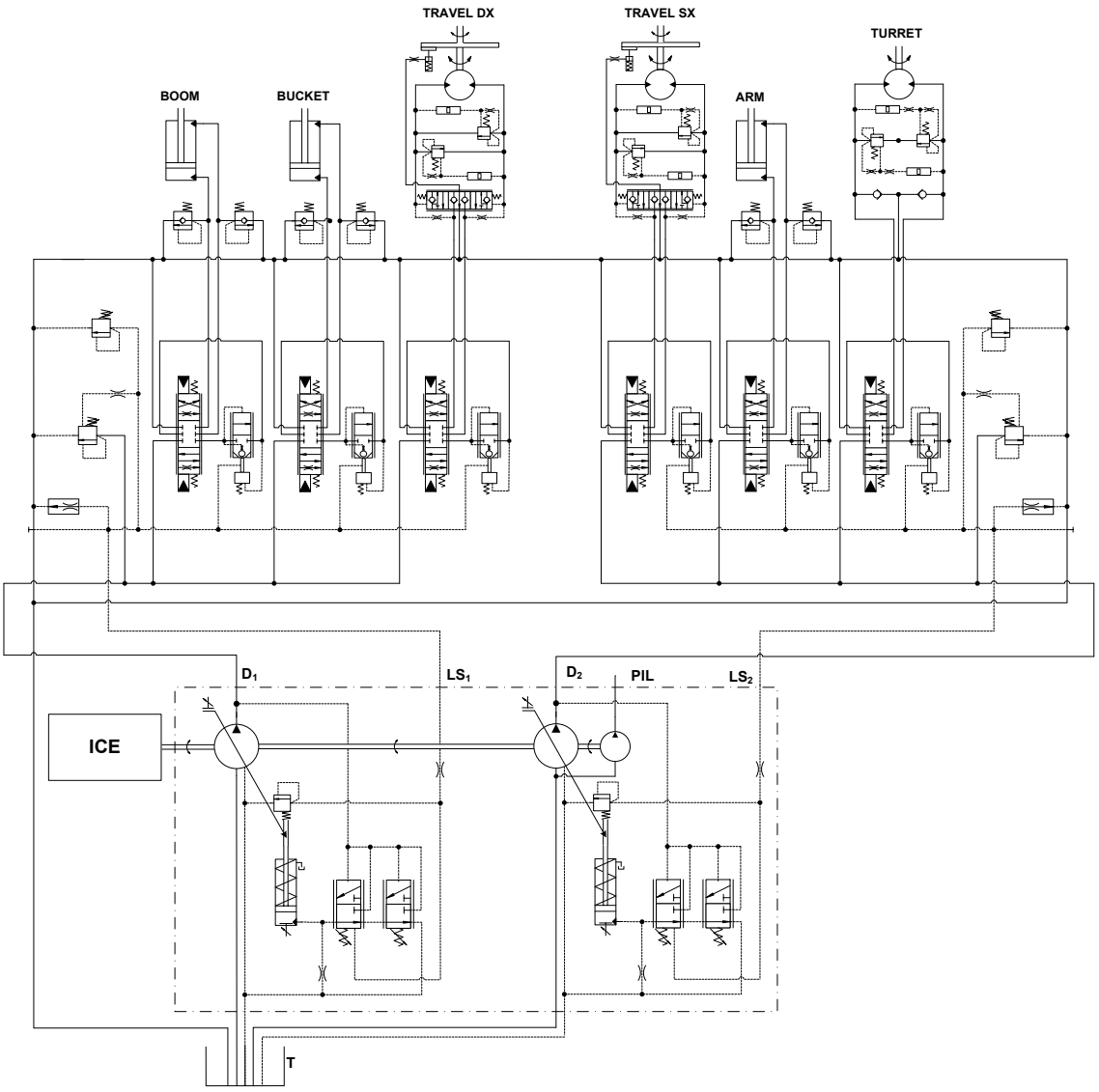

Figure 5.17: Dual Pump LS System Simplified ISO Scheme.

The proposed dual pump LS system configuration takes advantage of two LS variable displacement pumps having the same size of the original one, i.e. with the same maximum displacement of 84 cm^3/r.

The two pumps maximum permitted torques have been imposed equal to the half of the maximum torque of the standard system.

The obtained results related to this system configuration will point out the advantages, in terms of energy saving, of having a system exploiting two LS pumps instead of one (see Chapter 9).

Figure 5.18 reports the instantaneous displacement of pump 1 and pump 2 during the simulated trench digging cycle.

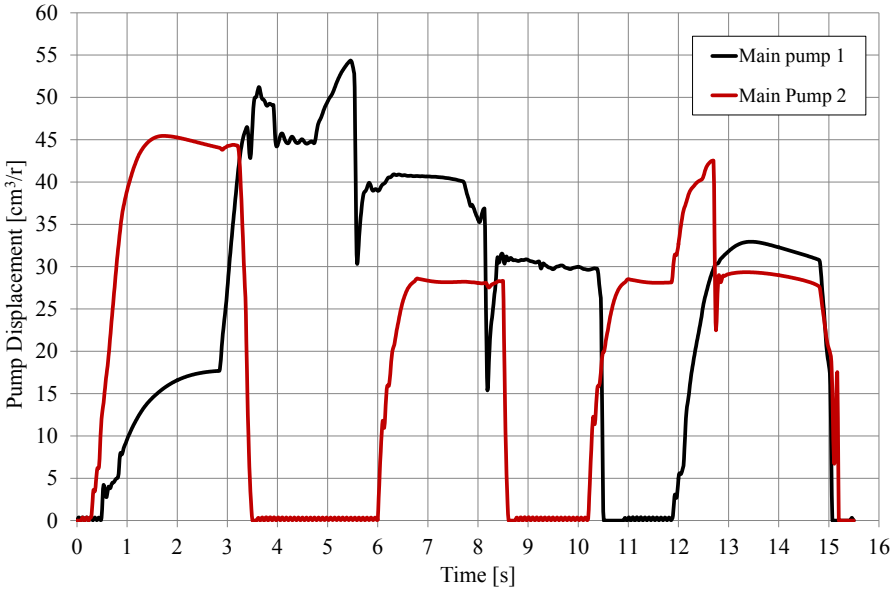

Figure 5.18: Pump 1 and Pump 2 Displacement During Simulated Trench Digging Cycle.

As can be observed, the maximum displacement reached by each of the pump during the cycle is always lower than 60 cm^3/r. Moreover, being axial piston pumps overall efficiency higher with the pump displacement, Fig.3.3 (see Chapter 3), the usage of two pumps with lower size, in terms of maximum displacement, would further improve the hydraulic system efficiency.

Therefore a second version of the dual pump LS system exploiting two variable displacement units with a maximum displacement of 60 cm^3/r [27] has been proposed.

The results related to this further configuration will point out the advantages, in terms of energy saving, of having a system exploiting two LS pumps with an optimized sizing (see Chapter 9).

Finally Fig.5.19 represents a third configuration for this system architecture, where a junction element, composed of two ON/OFF valves, within the DFCV, which allows the union of the two pumps according to the defined control strategies.

This particular system configuration will not be further investigated in this thesis.

[27] This pump size have been defined according to the consideration reported in this section and to the available model from Casappa's catalogue.

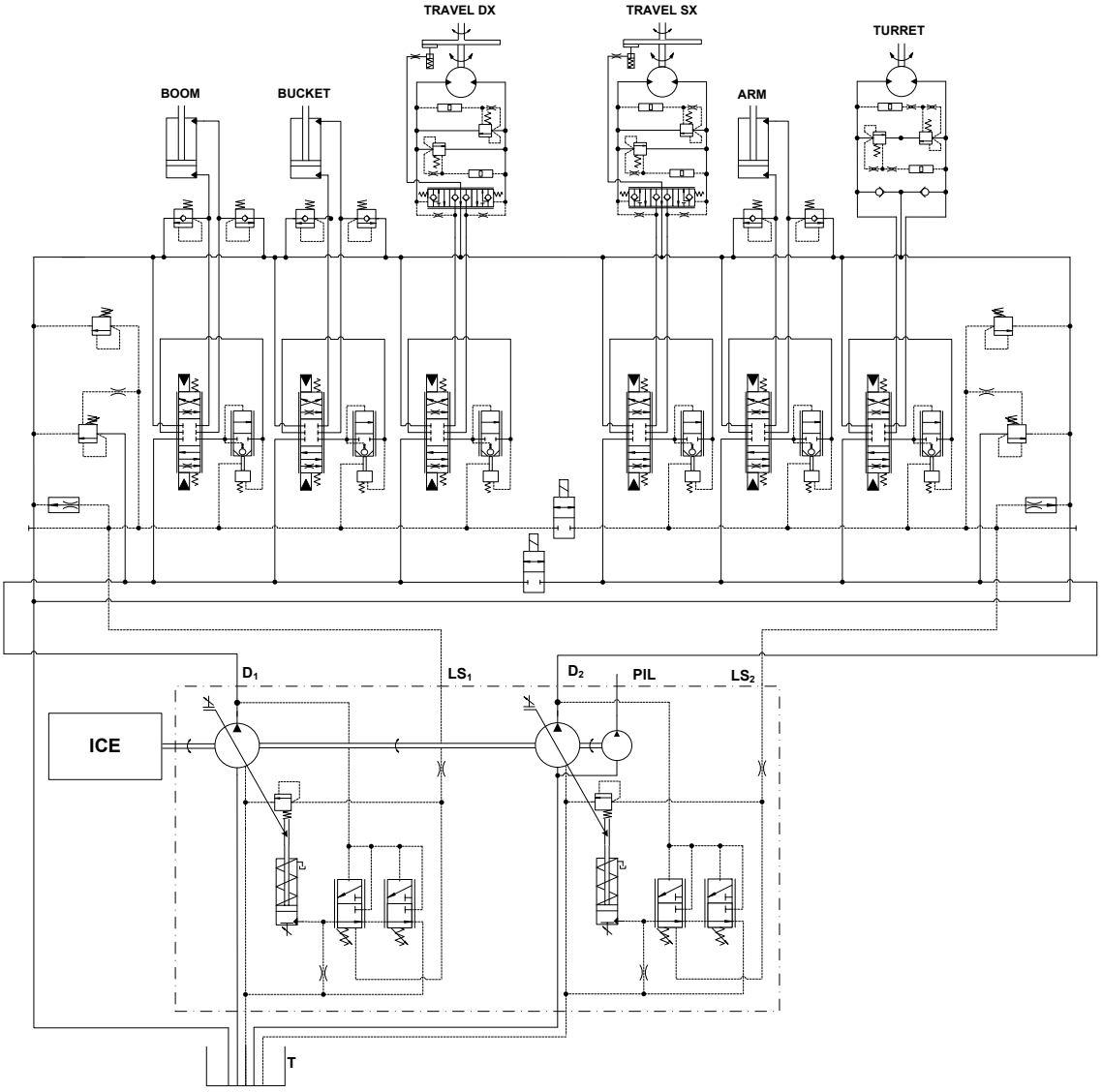

Figure 5.19: Dual Pump LS System with Junction Elements Simplified ISO Scheme.

5.2.2 Reduced Pump Margin LS System

LS systems on one hand ensure a proportional flow rates to the valve opening only, i.e. the actual flow rate is not affected by the loads variations. But on the other hand, are characterized, in addition to the other typical energy dissipations, by further meter-IN energy losses due to lamination across the compensated meter-IN orifice.

(*Eq.5.1*) defines the flow rate along the pressure compensated orifice of a generic LS system.

$$Q = k \cdot A(x) \cdot \sqrt{\Delta p_{LS}} \tag{5.1}$$

The differential pressure (Δp_{LS}) across the meter-IN orifice, in presence of the TL regulator is defined by (*Eq.5.2*).

$$\begin{cases} \Delta p_{LS} = \Delta p_{LS}^{*} \rightarrow if\ the\ TL\ does\ not\ act \\ \Delta p_{LS} < \Delta p_{LS}^{*} \rightarrow if\ the\ TL\ acts \end{cases} \tag{5.2}$$

Where (Δp_{LS}^{*}) is the pump margin setting of the FC.

The instantaneous dissipated power, due to lamination, is evaluated through (*Eq.5.3*) while the related energy dissipation, in the considered operating cycle (of a duration of T seconds) is defined by (*Eq.5.4*).

$$P_{LOSS} = Q \cdot \Delta p_{LS} \tag{5.3}$$

$$E_{LOSS} = \int_0^T P_{LOSS} \cdot dt \tag{5.4}$$

The energy losses can be reduced decreasing the pump margin (Δp_{LS}^{*}) setting. This operation is not trivial. If the pump margin is reduced too much, compared to the original setting, and no further change is introduced in the system (i.e. the modification of the meter-IN orifices flow areas, etc.), the users movements will result slower, and thus the machine performances could results unsatisfactory for the operators. Therefore, in the performed analysis, a 5% reduction of the original pump margin setting has been introduced in order to not penalize the machine performance, but still allowing energy saving improvement. The results analysis, will be reported and discussed in Chapter 9.

5.2.3 Optimization of the outlet flow areas

From the energy analyses carried out on the standard hydraulic system of the machinery under study have been pointed out that the energy dissipations related to the meter-OUT orifices represents a significant part of the total inlet energy, for both the trench digging and the grading cycles.

The meter-OUT energy losses consist of the energy dissipation while the loads acting on the hydraulic actuators are both resistant and pulling.

The energy dissipations related to the pulling loads are caused by the very narrow orifice sections adopted in order to maintain the control of the users even under harsh operating conditions. On the contrary, the energy dissipations related to the resistant loads could be further reduced optimizing the flow areas of the outlet orifices, having the confidence to not introduce adverse working conditions, e.g. load fugue or cavitation.

If this last considerations are almost valid for the arm and the bucket, regarding the boom some other aspects have to be considered.

In fact, a typical performed functional operation is that of using the front excavation tool as a pivot during the machinery undercarriage rotations. During this operating condition the undercarriage is partially lifted by the implement. Once rotated, the undercarriage is then lowered.

Considering the lowering phase, the opened meter-OUT orifice is the one typically exploited while the boom is lifted (concerning the trench digging and the grading cycles) when the loads are resistant. On the contrary, during this operating condition the load acting on the hydraulic actuator of the boom is pulling due to the machinery weight. Therefore, the optimization concerning the boom meter-OUT orifice is a trade-off between functionality and efficiency.

Figure 5.20 reports the B → T areas. The black curve represents the original normalized flow area, the red one is the maximum opening area trend according to the geometrical dimension of the valve and the spool, while the blue curve is the optimized flow area.

As can be seen, the original trend of the area has been maintained for the new optimized outlet flow area in order to meet the functionality requirements previously described.

Boom rising simulations have been performed to compare both the efficiency and the performance improvement exploiting the optimized outlet flow area instead of the standard one. The optimized (OPT) outlet flow area has been compared with both the original (STD) and the maximum (MAX) available outlet flow areas in order to justify its dimensioning.

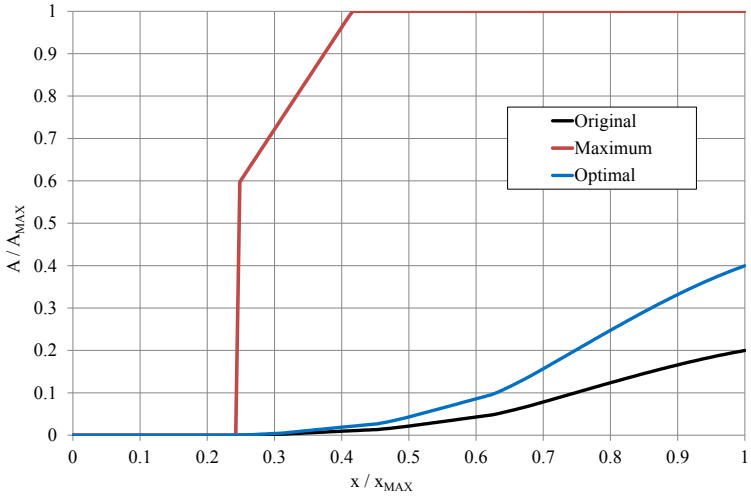

Figure 5.20: Boom B → T Outlet Flow Area Optimization.

The boom rising cycles simulations have been performed imposing different main spool opening, 25%, 50%, 75% and 100% of the useful stroke[28], in order to verify the optimization advantages in different operating conditions.

Figure 5.21 reports the outlet B → T pressure reduction adopting the MAX and the OPT outlet flow areas compared to the STD one.

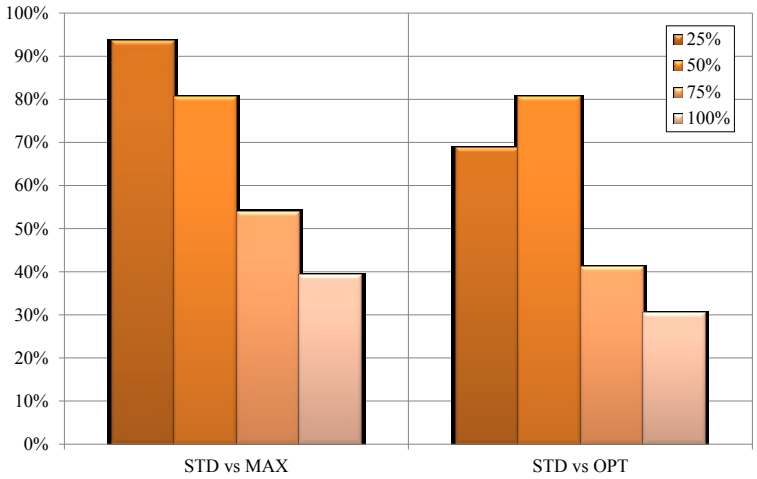

Figure 5.21: B → T Outlet Pressure Reduction.

The usage of the optimized outlet flow area reduces the outlet pressure, and consequently the inlet pressure too, of a very considerable percentage compared to the original area. Moreover only for little opening of the valve (25%) substantial differences between the

[28] The useful stroke considers only the part of the total spool stroke in which the flow area is not zero, i.e. if an underlap is present it will be not considered.

MAX and the OPT areas are significant, while for the other main spool positions the outlet pressure reduction are very similar. Furthermore, observing the fuel consumption reduction estimations, reported in Fig.5.22, the usage of the of the OPT outlet flow area just slightly reduce the fuel consumption reduction.

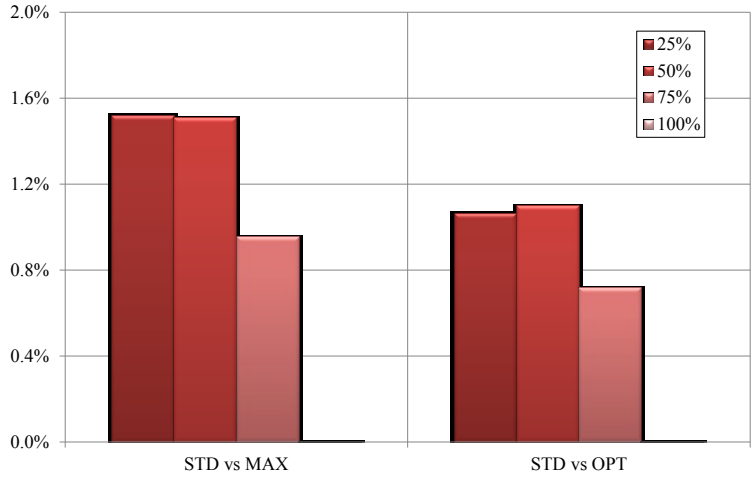

Figure 5.22: Boom Rising Simulated Fuel Consumption Reduction.

Other advantages related to adoption of the OPT outlet area concern the movements velocities improvements, Fig.5.23, due to the differential pressure across the meter-IN orifice ($dp_{LS}{}'$) increasing, Fig.5.24, being the TL action reduced in comparison to the system exploiting the original outlet area.

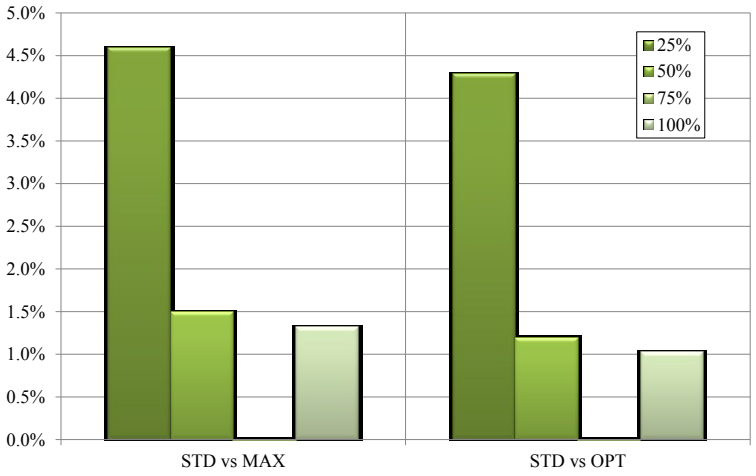

Figure 5.23: Boom Rising Time Reduction.

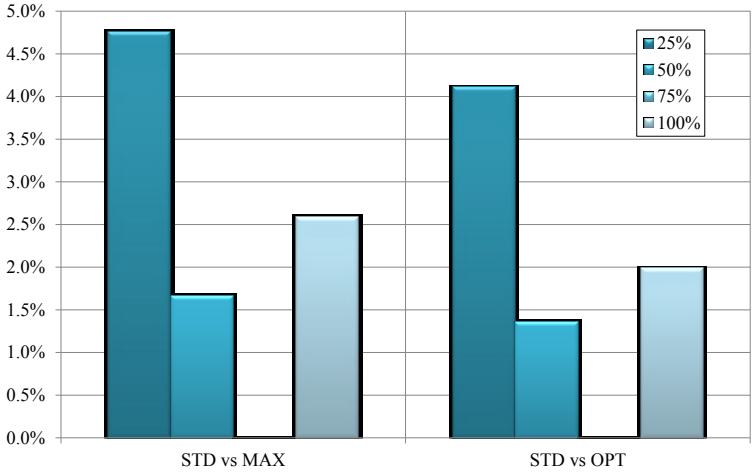

Figure 5.24: $dp_{LS}{}'$ Increasing During Boom Rising Simulation.

The reported results comparison pointed out that the usage of the optimized outlet flow area instead of the maximum available outlet area introduces only slight reductions in term of energy saving in favor of limited functionality problems, e.g. controllability or cavitation, during other performed operating condition do not considered in the JCMAS standard.

Concerning the arm and the bucket, the outlet flow areas related to the A → T orifices have been increasing of about 50% starting from the original flow areas trend.

The turret outlet sections were not modified.

The energetic analysis related to this configuration will be presented and further discussed in Chapter 9.

5.2.4 Boom Energy Recovery System

The energy analyses conducted on the standard hydraulic system of the excavator pointed out that the energy dissipation related to the meter-OUT orifice during the boom lowering phase are quantified in about 69% of the boom total available energy during this phase.

As previously analysed, the dissipation percentage amount concerns the boom potential energy, regenerated energy and part of the entering energy from the pump, meaning that, during the lowering, the boom is literally pushed down.

Many studies available in the literature, as reported in Chapter 1, have been conducted as well as many patents have been deposited concerning solutions for the recovery and reuse of otherwise wasted energy, due to lamination. ERSs seems to be the best solution to the problem.

Considering in particular the boom, a ERS has the function of both avoid the implement fugue and recover the larger amount of available energy.

The ERS for the excavator under investigation has been designed to recover only the potential energy from the front equipment, since the predicted energy saving potential from turret was considered insufficient for justifying the additional costs [*5.1*].

Figure 5.25 reports the simplified ISO scheme of the excavator hydraulic system with the proposed novel ERS architecture.

The ERS is composed of four components:

- a Hybrid Control Valve (HCV);
- a hydraulic accumulator;
- a pilot pump/motor;
- an Electronic Control Unit (ECU).

The HCV is a valve block composed of three ON/OFF directional flow control valves (X, 3, 4), a pressure relief valve (5) and a proportional flow control valve (Y).

The valve X allows directing the flow from the piston side of the boom cylinder to the hydraulic accumulator (recovery mode) or to the boom DFCV section (standard mode).

Since in some operating conditions the accumulator pressure could be not enough to balance the front equipment weight, the proportional valve Y throttles the flow rate thus maintaining the control on the boom descent avoiding both the implement fugue and cavitation.

Pressure relief valve 5 preserves the accumulator from overpressures.

Valve 4 serves to empty the accumulator when the ERS is turn off or the machinery is not working.

The recovered energy is then used to feed a hydraulic motor so as to reduce the engine load and consequently reduce the fuel consumption. The reuse phase is enabled by means of valve 3, which connects the hydraulic accumulator with the hydraulic motor.

In the proposed ERS the pilot pump, of the standard hydraulic system of the excavator, has been modified in order to be exploited even as recovery motor. This choice has been made with the purpose of limiting both the recovery system cost and the space required on the excavator.

The ECU controls valves X, Y, 3 and 4 according to the control strategies defined (see Chapter 6) on the basis of the accumulator pressure (p_{ACC}) and the pilot pressure of the boom flow control valve ($p_{V2\text{-}BOOM}$), which are the input.

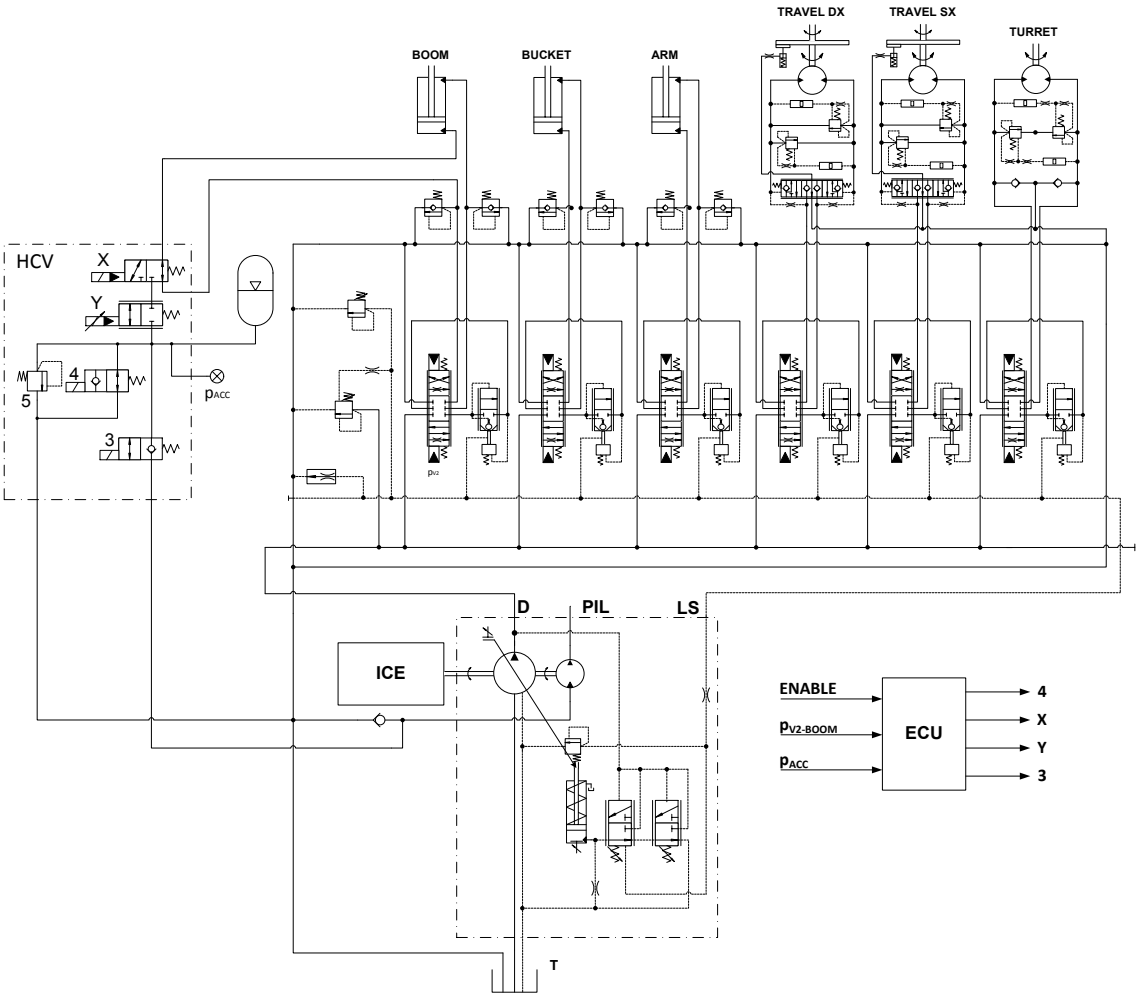

Figure 5.25: Excavator Simplified ISO Scheme with Boom ERS.

Figure 5.26 shows the ERS during the different operating modes: recovery mode (A), recovery and reuse mode (B) and reuse mode (C). The activated valves and hydraulic lines are highlighted in red.

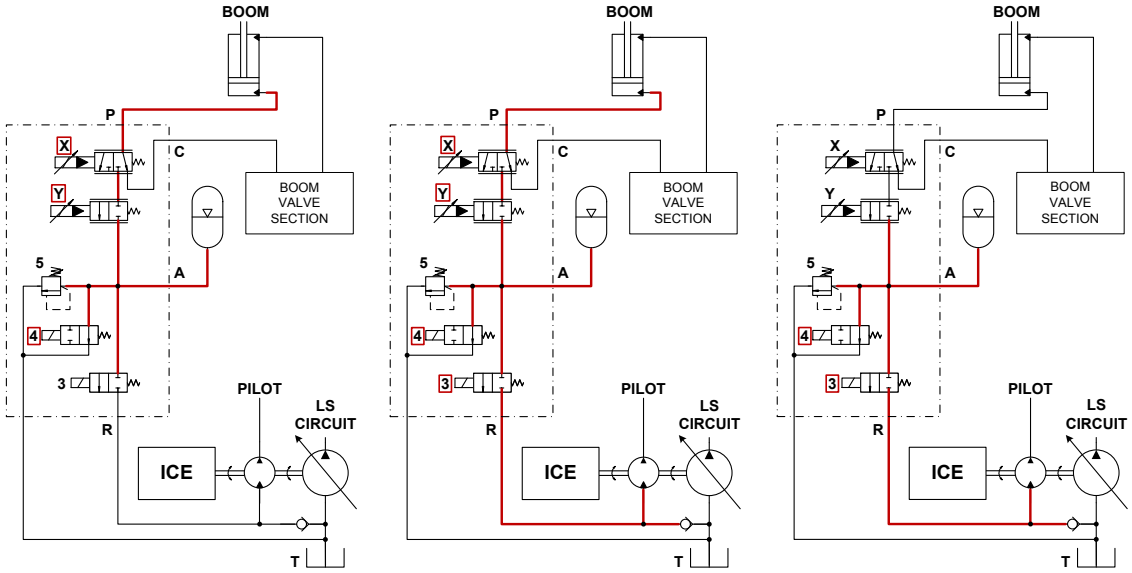

Figure 5.26: Operating Modes of the ERS.

The effectiveness, i.e. the energy saving capability, of the proposed ERS strongly depends on both its control strategy and components dimensions (valves, accumulator, motor, etc.). For this reason, a parameters optimization on the proposed ERS layout and the definition of an optimal control strategy are crucial in order to evaluate the performance, in term of energy saving, related to this ERS (see Chapter 6).

The energetic analysis related to this configuration will be presented and discussed in Chapter 9.

5.3 Discussion

A detailed energy analysis of the standard excavator hydraulic system has been presented in this chapter, discussing the energy dissipations in the system during both the trench digging and the grading cycles of the JCMAS standard.

These analysis have led to the definition of different solutions for the energy saving in LS hydraulic systems, among which hydraulic system layout modification, valves optimization, pump setting modification and energy recovery system introduction.

These proposed solutions have been presented and described in detail in this chapter, while the related energy saving capability will be presented in Chapter 9.

References

5.1 *P. Casoli, A. Gambarotta, N. Pompini, L. Riccò. Hybridization Methodology based on DP Algorithm for Hydraulic Mobile Machinery – Application to a Middle Size Excavator. Automation in Construction. Volume 61, January 2016, Pages 42–57. doi:10.1016/j.autcon.2015.09.012.*

Chapter 6: **Energy Recovery System Optimal Dimensioning**

In this chapter the optimal dimensioning of the proposed ERS will be presented and described in detail.

The optimization procedure concerned both the components sizing and the definition of the control strategy to be implemented on the machinery.

The presented methodology takes advantage of the dynamic programming (DP) algorithm.

In the initial section of this chapter an overview of the typically adopted optimization techniques will be reported, while in the next sections will be presented the exploited optimization procedure and the results.

6.1 Optimal Energy Management Strategies

In Chapter 5 different energy saving solutions were proposed on the basis of the energy analyses carried out on the standard hydraulic system of the excavator under investigation, among them even a novel ERS architecture.

The proposed ERS recovers energy from the boom actuator during the implement lowering. Then, the recovered energy, storage in an energy storaged device (ESD) (a hydraulic accumulator), is reused taking advantage of the hydraulic pump/motor of the excavator pilot circuit.

The combination between the standard hydraulic system of the excavator and the proposed ERS defines a novel hydraulic hybrid architecture for such a machinery.

The optimal energy management in hybrid electric vehicles (HEV) has been one of the most studied problems in the last two decades, according to the related number of paper present in the literature, while the interest on hydraulic hybrid mobile machinery is current.

The energy management strategies (EMS) have typically the primal purpose of minimizing the fuel consumption, i.e. optimizing the fuel economy, over a certain task, or a set of defined tasks.

At each instant of time, the strategy, implemented in the controller, must decide the optimal components activation to achieve the fuel consumption minimization target. Therefore numerical dynamic optimization methods, instead of static ones, are usually exploited for the evaluation of optimal control laws.

The energy management strategies can be classified into two categories, rule-based and optimization-based strategies.

Rule-based algorithms on one hand are simple to implement, easy to use, and suitable to implement for real-time control, but on the other hand the tuning of the rules is based on both trial-and-error and heuristic approaches, which often requires time to achieve satisfactory performance and fuel consumption reduction targets.

Optimization-based algorithms, among which Pontryagin's minimum principle [*6.1*], equivalent consumption minimization strategy (ECMS) [*6.2, 6.3*], equivalent fuel consumption control strategy (EFCOCS) [*6.4*] and dynamic programming (DP) [*1.36, 6.5*] have the objective to compute the best fuel economy of the machinery under investigation on the target tasks.

In this thesis, the optimization procedure for both the ERS components size and the EMS takes advantage of the DP algorithm, which will be further presented in the next section.

6.1.1 Dynamic Programming Optimization Method

The DP algorithm, introduced in [*6.6*] and further described in [*6.7*], is based on the principle of optimality, i.e. an optimal control policy has the propriety that whatever the initial state and the initial decision are, the remaining decision must constitute an optimal policy with regard to the results from the initial decision.

Concerning engineering optimization problems DP algorithm found large usage, as an example, when developing energy management control strategies [*1.36, 6.5, 6.8, 6.9, 6.10*].

The EMSs optimization through the DP optimization-based methodology guarantees to obtain a global optimal control strategy for the investigated hybrid machinery over a defined time horizon if the associated working cycle is known in advance.

This means that, taking advantage of the optimality principle, the DP algorithm can find the optimal solution backward in time by searching for all the defined states, which results as the upper bound, i.e. the optimal benchmark, for developing EMSs of the considered system architecture.

Unfortunately the DP optimal results are non-causal and not implementable in real-time controller. Therefore, starting from the optimal non-causal EMS, a control strategy based on rules can be derived after an accurate DP results post-processing analysis for the rules extraction.

Considering the proposed hydraulic hybrid excavator layout, Fig.5.25, the DP algorithm has been adopted for the definition of the optimal set of EMSs for each ERS components size combination, thus obtaining the optimal combination distribution, further exploited for the best components size combination to be adopted.

The optimization methodology, presented in the next sections, has been carried out by means of a Matlab® function developed and described in [*6.11*], which require the definition of the objective function and the mathematical model of the considered system.

The mathematical model of the hydraulic hybrid excavator for the DP optimization purpose is presented in detail in the next section.

6.2 Excavator Inverse Causality Model

The adopted optimization procedure is based on the DP algorithm which has the characteristic of solving non-linear, time variant, constrained, discrete-time approximation of continuous time dynamic model optimization problems.

Therefore, in order to solve the backward-in-time optimization problem the mathematical model, presented in Chapter 2, has to be further simplified and its causality reverted.

The computational time to solve a DP optimization problem is exponential in the number of states and input [*6.10*]. Therefore, being the number of the defined input fixed, the number of the system states (i.e. the number of differential equations) have to be limited as much as possible, thus all the non-essential dynamics of the model have been neglected. Consequently, when reversing the model causality, all the sub-models have been reduced to pure algebraic models based on a Quasi-Steady formulation.

This last assumption is justified because the typical time constants associated with hydraulic components, like hydraulic chambers pressure variations, flow rates variation and the swash plate tilting of the variable displacement unit are very low, i.e. high frequency phenomenon, compared to the characteristics time of the performed working tasks.

These assumption will be confirmed by the comparison between excavator direct and inverse causality models results presented in section 6.2.9.

If these assumption can be acceptable for the standard hydraulic system of the excavator, considering the introduction of the proposed ERS, with the introduction of an energy storage device (a hydraulic accumulator), it becomes clear that its dynamics cannot be further neglected as greatly affect the behaviour of the novel system and being considerably slower than the previous mentioned ones.

In the following sections the sub-systems inverse causality models will be presented in detail.

6.2.1 Hydraulic Linear Actuator

Figure 6.1 shows the HLA inverse model causality. The piston velocity (v_{HLA_i}) is assumed to be positive during the extension movement of the piston while the piston force (F_{HLA_i}) is positive when the piston pulls the connected kinematics element.

The following assumptions were done for the modelling: no internal and external leakages were considered, the static friction has been neglected and the cavitation of the fluid was not considered.

Figure 6.1: Causality of the HLA Inverse Model.

The flow rates at the piston (Q_{A_i}) and the rod (Q_{B_i}) workports are evaluated through (*Eq.6.1*) and (*Eq.6.2*) respectively.

$$Q_{A_i} = v_{HLA_i} \cdot A_P \tag{6.1}$$

$$Q_{B_i} = -v_{HLA_i} \cdot A_R \tag{6.2}$$

The piston and the rod pressure are defined, according to the sign of the input velocity (v_{HLA_i}), by (*Eq.6.3*) and (*Eq.6.4*).

$$\begin{cases} v_{HLA_i} \geq 0 \\ p_{P_i} = \dfrac{p_{C_i-OUT} \cdot \left(A_R + k_{\Delta p_i}\right) + F_{C_i} + k_{v_i} \cdot \left|v_{HLA_i}\right| + F_{HLA_i}}{A_P + k_{\Delta p_i}} \end{cases} \tag{6.3}$$

$$\begin{cases} v_{HLA_i} < 0 \\ p_{R_i} = \dfrac{p_{C_i-OUT} \cdot \left(A_P + k_{\Delta p_i}\right) + F_{C_i} + k_{v_i} \cdot \left|v_{HLA_i}\right| - F_{HLA_i}}{A_R + k_{\Delta p_i}} \end{cases} \tag{6.4}$$

The counter pressure (p_{C_i-OUT}) is due to the resistance introduced by both the outlet orifice of the valve section controlling the user and the related hydraulic line losses.

6.2.2 Turret Hydraulic Rotary Actuator

The inverse model causality of the turret HRA is represented in Fig.6.2.

The following assumptions were done for the modelling: neither internal nor external leakages were considered and the cavitation of the fluid was not considered.

Figure 6.2: Causality of the Turret HRA Inverse Model.

The HRA speed (n_{HRA}) and torque (T_{HRA}) are evaluated knowing the transmission ratio related to the planetary rotation gear box (τ), according with (*Eq.6.5*) and (*Eq.6.6*).

$$n_{HRA} = n_{TURRET} \cdot \tau \tag{6.5}$$

$$T_{HRA} = \frac{T_{TURRET}}{\tau} \tag{6.6}$$

Both the flow rates and the pressures at the workport A and B are defined, depending on the functioning of the HRA of the turret as a motor or a pump as well as the turret rotation direction, by (*Eq.6.7*), (*Eq.6.8*), (*Eq.6.9*) and (*Eq.6.10*) respectively.

$$\begin{cases} n_{TURRET} \cdot T_{TURRET} \geq 0 \\ n_{TURRET} \geq 0 \\ Q_{A-HRA} = \dfrac{n_{HRA} \cdot V_{d_{HRA}}}{\eta_V} \\ Q_{B-HRA} = -Q_{A-HRA} \\ p_{A-HRA} = p_{C-OUT-TURRET} + \dfrac{T_{HRA} \cdot 2\pi}{V_{d_{HRA}} \cdot \eta_{hm}} \\ p_{B-HRA} = p_{C-OUT-TURRET} \end{cases} \tag{6.7}$$

$$\begin{cases} n_{TURRET} \cdot T_{TURRET} \geq 0 \\ n_{TURRET} < 0 \\ Q_{A-HRA} = -Q_{B-HRA} \\ Q_{B-HRA} = \dfrac{n_{HRA} \cdot V_{d_{HRA}}}{\eta_V} \\ p_{A-HRA} = p_{C-OUT-TURRET} \\ p_{B-HRA} = p_{C-OUT-TURRET} + \dfrac{T_{HRA} \cdot 2\pi}{V_{d_{HRA}} \cdot \eta_{hm}} \end{cases} \tag{6.8}$$

$$\begin{cases} n_{TURRET} \cdot T_{TURRET} < 0 \\ n_{TURRET} \geq 0 \\ Q_{A-HRA} = n_{HRA} \cdot V_{d_{HRA}} \cdot \eta_V \\ Q_{B-HRA} = -Q_{A-HRA} \\ p_{A-HRA} = p_{C-OUT-TURRET} + \dfrac{T_{HRA} \cdot 2\pi}{V_{d_{HRA}}} \cdot \eta_{hm} \\ p_{B-HRA} = p_{C-OUT-TURRET} \end{cases} \tag{6.9}$$

$$\begin{cases} n_{TURRET} \cdot T_{TURRET} < 0 \\ n_{TURRET} < 0 \\ Q_{A-HRA} = -Q_{B-HRA} \\ Q_{B-HRA} = n_{HRA} \cdot V_{d_{HRA}} \cdot \eta_V \\ p_{A-HRA} = p_{C-OUT-TURRET} \\ p_{B-HRA} = p_{C-OUT-TURRET} + \dfrac{T_{HRA} \cdot 2\pi}{V_{d_{HRA}}} \cdot \eta_{hm} \end{cases} \tag{6.10}$$

6.2.3 Hydraulic User Lines Losses

Figure 6.3 depicts the inverse model causality of the i-th user hydraulic line losses. This sub-system evaluates the pressure losses due to the hydraulic line resistance between the i-th user and the correspondent DFCV section.

Figure 6.3: Causality of the Hydraulic Lines Inverse Model.

The outlet flow rates are the same of the inlet ones, while the outlet pressures are calculated through (*Eq.6.11*) and (*Eq.6.12*).

$$p_{A_i} = p_{P_i} + k_{L-A_i} \cdot |Q_{A_i}| \tag{6.11}$$

$$p_{B_i} = p_{R_i} + k_{L-B_i} \cdot |Q_{B_i}| \tag{6.12}$$

The outlet counter pressure is evaluated according to the related user velocity input by (*Eq.6.13*) and (*Eq.6.14*) respectively.

$$\begin{cases} v_{HLA_i} \geq 0 \\ p_{C-OUT-i} = p_{C-IN-i} + k_{L-B_i} \cdot |Q_{B_i}| \end{cases} \quad (6.13)$$

$$\begin{cases} v_{HLA_i} < 0 \\ p_{C-OUT-i} = p_{C-IN-i} + k_{L-A_i} \cdot |Q_{A_i}| \end{cases} \quad (6.14)$$

6.2.4 Directional Flow Control Valve

The DFCV inverse causality model is composed of a number of valve section equal to the number of the considered users. The single user section inverse model causality is represented in Fig.6.4.

This sub-system defines the i-th user flow rate required by the pump, the related LS, the counter pressures and the outlet flow rate to the tank.

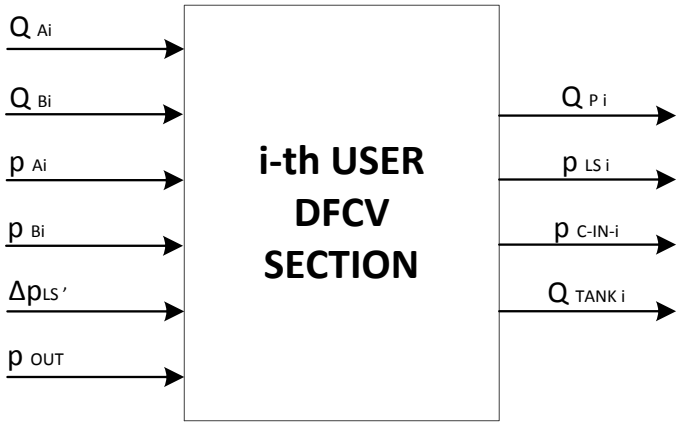

Figure 6.4: Causality of the DFCV Section Inverse Model.

The output variables are evaluated by (*Eq.6.15*) and (*Eq6.16*) according to the velocity sign of the user hydraulic actuator.

$$\begin{cases} v_i \geq 0 \\ Q_{P_i} = Q_{A_i} \\ p_{LS_i} = p_{A_i} \\ Q_{TANK_i} = Q_{B_i} \\ p_{C-IN-i} = \dfrac{{Q_{B_i}}^2 \cdot \rho}{2 \cdot {cd_{B-OUT_i}}^2 \cdot A_{B-OUT_i}(x_{MS_i})^2} + p_{OUT} \\ A_{A_i}(x_{MS_i}) = \dfrac{Q_{A_i}}{cd_{A_i}} \cdot \sqrt{\dfrac{\rho}{2 \cdot \Delta {p_{LS}}'}} \end{cases} \tag{6.15}$$

$$\begin{cases} v_i < 0 \\ Q_{P_i} = Q_{B_i} \\ p_{LS_i} = p_{B_i} \\ Q_{TANK_i} = Q_{A_i} \\ p_{C-IN-i} = \dfrac{{Q_{A_i}}^2 \cdot \rho}{2 \cdot {cd_{A-OUT_i}}^2 \cdot A_{A-OUT_i}(x_{MS_i})^2} + p_{OUT} \\ A_{B_i}(x_{MS_i}) = \dfrac{Q_{B_i}}{cd_{B_i}} \cdot \sqrt{\dfrac{\rho}{2 \cdot \Delta {p_{LS}}'}} \end{cases} \tag{6.16}$$

For both the cases the main spool position (x_{MS_i}) is evaluated taking advantage of the map based correlation between the flow areas of the inlet orifices ($A_{A_i}(x_{MS_i})$, $A_{B_i}(x_{MS_i})$) and the spool position itself.

The outlet pressure (p_{OUT}), which is the same for each user section is defined according to (*Eq.6.17*).

$$p_{OUT} = p_{TANK} + k_{L-HE} \cdot \left(\sum_{i=1}^{N} Q_{TANK_i} + Q_{PIL} \right) \tag{6.17}$$

The hydraulic tank pressure (p_{TANK}) has been considered as constant and equal to 0.05MPa, while the heat-exchanger (HE) pressure drop coefficient (k_{L-HE}) was defined according to the experimental results.

Finally, once defined each user output, the DFCV outputs, i.e. the pump flow rate (Q_P) and the LS pressure of the system (p_{LS}) are evaluated through (*Eq.6.18*) and (*Eq.6.19*) respectively.

$$Q_{P_{MAIN}} = \sum_{i=1}^{N} Q_{P_i} + Q_{BLEED_{LS}} \tag{6.18}$$

$$p_{LS} = MAX(p_{LS_i}) \quad (6.19)$$

($Q_{BLEED_{LS}}$) is the flow rate loss via the LS line bleed valve (*Eq.6.20*), which is a fixed orifice typically mounted on the LS line in order to limit the pressure memory effect thus making the system more reactive to the operator requests.

$$Q_{BLEED_{LS}} = f(\sqrt{p_{LS}}) \quad (6.20)$$

6.2.5 Flow Generation Unit

The FGU inverse causality model is composed of the main pump, the pilot pump and the main pump torque limiter.

Main Pump

The main pump inverse model causality is represented in Fig.6.5. This sub-model defines the torque required by the main pump of the excavator.

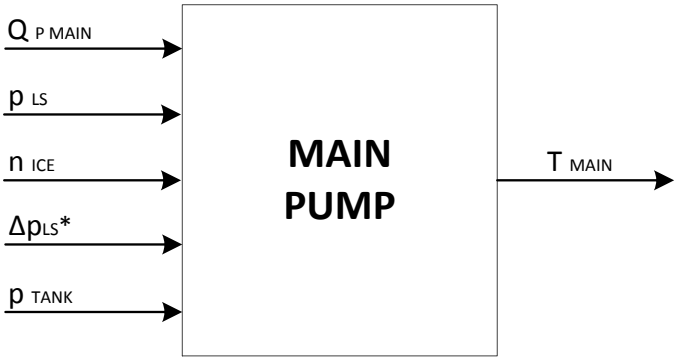

Figure 6.5: Causality of the Main Pump Inverse Model.

To evaluate the main pump torque, starting from the available input, a first iterative procedure for the definition of the actual pump displacement is performed. Only a single iteration is performed due to the simplified nature of this inverse model.

The theoretical pump displacement is calculated by (*Eq.6.21*), while the pump delivery and differential pressure are evaluated through (*Eq.6.22*) and (*Eq.6.23*).

$$V_{d_{MAIN}}{}' = \frac{Q_{P_{MAIN}}}{n_{ICE}} \tag{6.21}$$

$$p_D = p_{LS} + \Delta p_{LS}{}^{*} \tag{6.22}$$

$$\Delta p_{MAIN} = p_D - p_{TANK} \tag{6.23}$$

The volumetric efficiency can be now obtained exploiting the volumetric efficiency map experimentally defined, being $\eta_{V_{MAIN}}{}' = f\left(V_{d_{MAIN}}{}', \Delta p_{MAIN}, n_{ICE}\right)$.

After this first iteration, a second pump displacement can be evaluated, (*Eq.6.24*), including the pump volumetric losses.

$$V_{d_{MAIN}}{}'' = \frac{Q_{P_{MAIN}}}{n_{ICE} \cdot \eta_{V_{MAIN}}{}'}, \tag{6.24}$$

Knowing the pump displacement and the operating conditions, the pump hydraulic-mechanical efficiency can be defined through the correspondent experimental map, being $\eta_{hm_{MAIN}} = f\left(V_{d_{MAIN}}{}'', \Delta p_{MAIN}, n_{ICE}\right)$.

Finally the main pump torque is evaluated through (*Eq.6.25*).

$$T_{MAIN} = \frac{\Delta p_{MAIN} \cdot V_{d_{MAIN}}{}''}{2\pi \cdot \eta_{hm_{MAIN}}} + k_{T-DRAG_{FGU}} \cdot n_{ICE} + T_{C_{FGU}} \tag{6.25}$$

Pilot Pump

The pilot pump model causality is represented in Fig.6.5. In this case, the model does not present an inverse causality, but as in the direct model this sub-model defines both the pilot torque and flow rate according with (*Eq.6.26*) and (*Eq.6.27*).

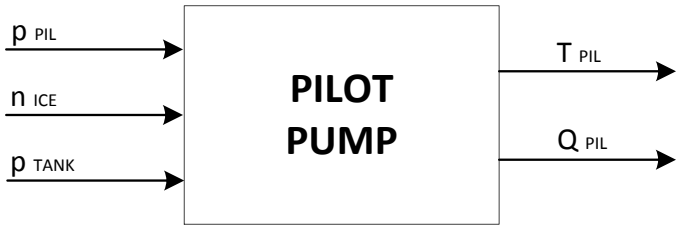

Figure 6.6: Causality of the Pilot Pump Inverse Model.

$$Q_{PIL} = V_{d_{PIL}} \cdot n_{ICE} \cdot \eta_{V_{PIL}} \tag{6.26}$$

$$T_{PIL} = \frac{V_{d_{PILOT}} \cdot (p_{PIL} - p_{TANK})}{2\pi \cdot \eta_{hm_{PIL}}} \tag{6.27}$$

Both the volumetric and the hydraulic-mechanical efficiencies have been considered as constant.

6.2.6 Main Pump Torque Limiter

This model is essential in order to evaluate the actual differential pressure on the meter-IN of the DFCV sections. Since in the direct causality model the TL directly acts on the LS pressure, reducing it when necessary, in the inverse causality model the LS pressure is evaluated through the knowledge a priori of the actual differential pressure ($\Delta p_{LS}{}'$). Therefore a dedicated main pump TL model has been developed and Fig.6.7 reports its modelling causality scheme.

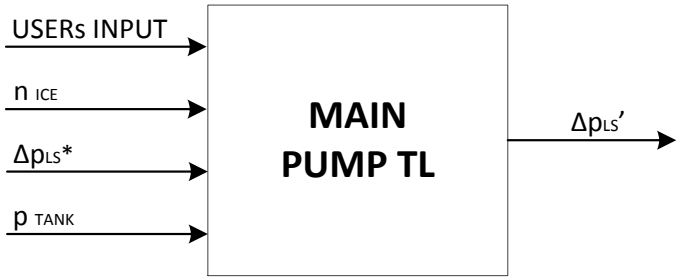

Figure 6.7: Causality of the Main Pump Torque Limiter Inverse Model.

The input of the TL model are the ICE speed (n_{ICE}), the hydraulic tank pressure (p_{TANK}), the pump margin setting ($\Delta p_{LS}{}^{*}$) and the users input, i.e. the actuators velocities and forces or torques.

Internally all the so far presented sub-models are properly connected to recreate the excavator inverse causality model, see Appendix 3, in order to calculate the required torque by the hydraulic system with no torque limiter actions ($T_{MAIN}{}^{*}$), i.e. with a constant differential pressure on the meter-IN of the DFCV sections, set equal to the pump margin setting.

Once evaluated $T_{MAIN}{}^{*}$ through the usage of the Δp_{LS} reduction map, Fig.6.8 (defined with the aid of the direct causality model), the correspondent value of the actual differential pressure ($\Delta p_{LS}{}'$) can be defined for the inverse model.

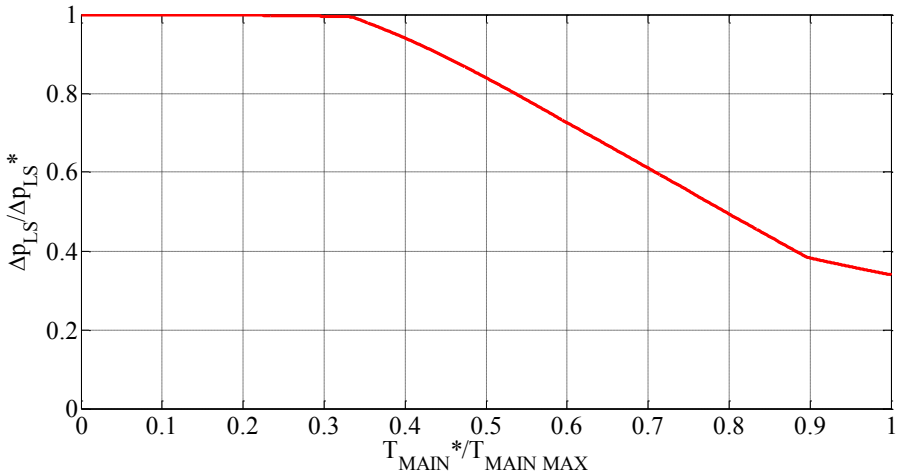

Figure 6.8: Δp_{LS} Reduction with Main Pump Torque Map.

6.2.7 Internal Combustion Engine

Figure 6.9 shows the ICE inverse model causality. This model defines the fuel mass flow rate burned during each simulation step of the working cycle performed taking advantage of the experimentally defined BSFC map (see Chapter 3).

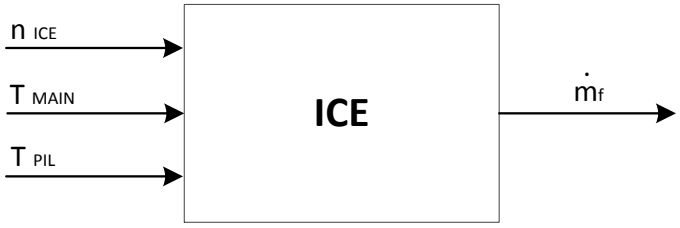

Figure 6.9: Causality of the Pilot Pump Inverse Model.

6.2.8 Hydraulic Accumulator

The inverse causality model of the excavator, as previously stated, will be exploited in order to define the optimal control strategy and optimize the ERS components size, among which the hydraulic accumulator pre-charge pressure and volume.

A bladder type hydraulic accumulator has been selected for the ERS.

Figure 6.10 shows the accumulator model causality.

Figure 6.10: Causality of the Hydraulic Accumulator.

The accumulator, pre-charged with gaseous Nitrogen, is modelled assuming an adiabatic transformation through a polytropic gas law (*Eq.6.28*).

$$p \cdot V^{\gamma} = const \tag{6.28}$$

The pressure time derivative in the internal volume of the hydraulic accumulator is defined by (*Eq.6.29*), obtained differentiating (*Eq.6.28*).

$$\frac{dp_{ACC}}{dt} = -\gamma \cdot \frac{p_{ACC}}{V_{ACC}} \cdot \frac{dV_{ACC}}{dt} \tag{6.29}$$

The accumulator volume variation depends on the inlet and outlet flow rates according to (*Eq.6.30*).

$$\frac{dV_{ACC}}{dt} = -Q_{IN} + Q_{OUT} \tag{6.30}$$

6.2.9 Inverse Causality Model Validation

In this paragraph the inverse causality model of the excavator, Appendix 4, composed of the sub-models presented in the previous section and implemented in the Simulink® environment has been validated in order to perform the ERS optimization.

The excavator fuel consumption strongly depends on the operating conditions as well as on the machinery layout and the energy management strategy.

The validation of the inverse causality model of the excavator becomes essential to be confident on the predicted results, thus the validation procedure will be focused on the model

capability in the evaluation of the variables of interest for the fuel consumption definition. These variables will be compared with the same calculated by the validated direct causality excavator model. Once validated, the inverse model will be exploited in the proposed ERS optimization procedure.

Since the trench digging cycle, of the standardized earth-moving machinery test procedure JCMAS H20:2007 [*3.2*] selected as the reference working procedure, is the most performed one and with the highest energy recovery possibility, due to the large boom piston excursion, the ERS optimization has been conducted on this operating cycle.

The direct causality model of the standard excavator was exploited to perform the simulations of the previously mentioned standardized working cycles, defining the reference (i.e. standard machine fuel consumption).

Being the excavator kinematics not included in the inverse causality model, starting from the trajectories prescribed by the JCMAS standard and knowing masses and geometries of the excavator components, the velocities of the hydraulic actuators and, from dynamic equilibrium, the exerted forces and torques to the actuators can be obtained from the direct excavator model. This forces (or torques) and velocities have been adopted as the input for the HLAs and HRA in the inverse model.

Figure 6.11, Fig.6.12, Fig.6.13 and Fig.6.14 report the boom, arm, bucket and turret input relative to the trench digging cycle of the actuated users.

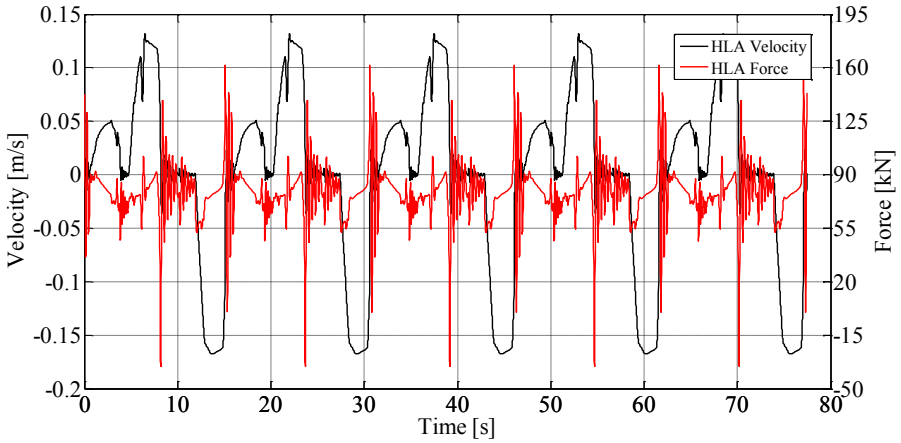

Figure 6.11: Boom Input – Trench Digging Cycle.

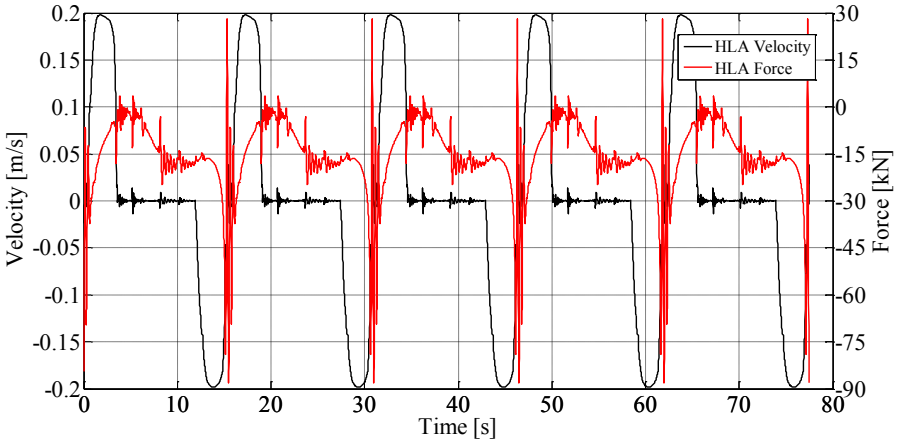

Figure 6.12: Arm Input – Trench Digging Cycle.

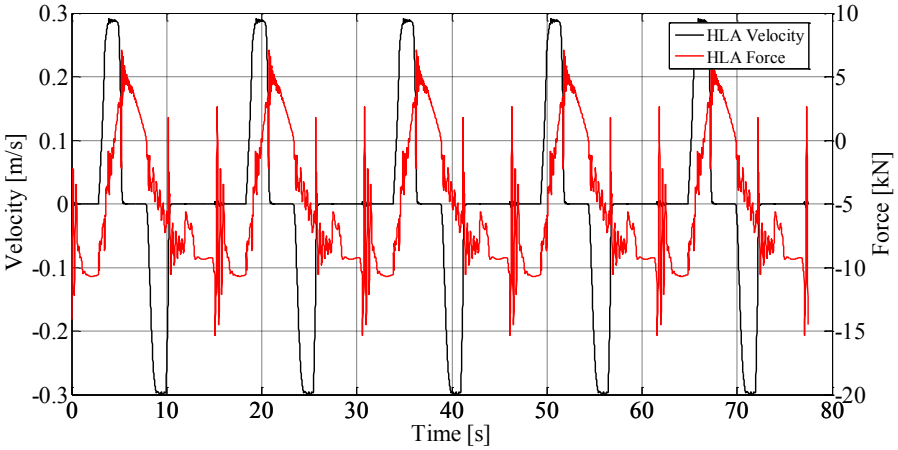

Figure 6.13: Bucket Input – Trench Digging Cycle.

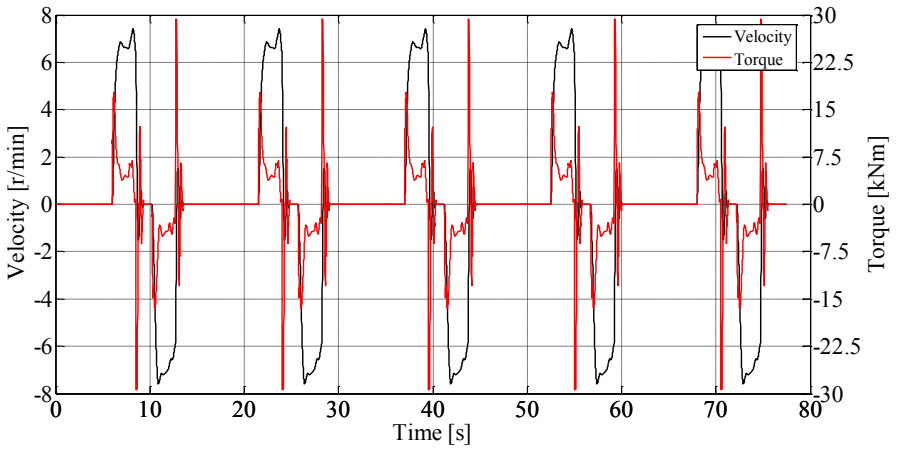

Figure 6.14: Turret Input – Trench Digging Cycle.

Figure 6.15, Fig.6.16, Fig.6.17, Fig.6.18 and Fig.6.19 report the comparison between the direct and the inverse causality models calculated variables.

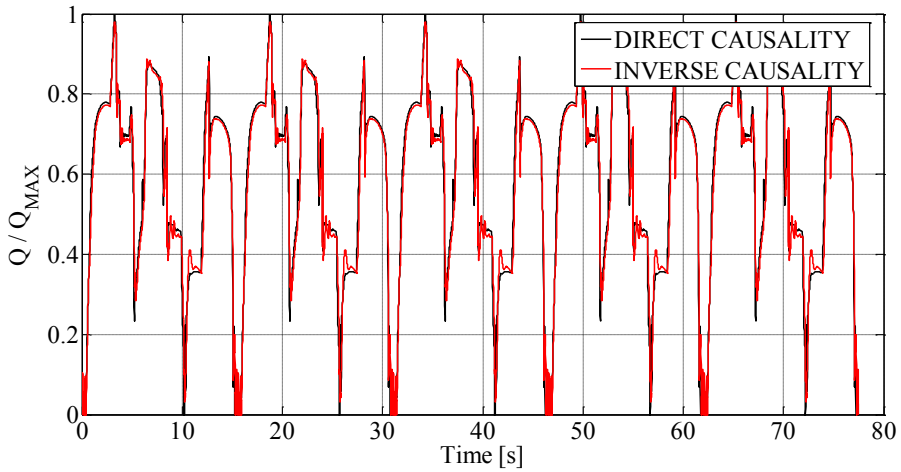

Figure 6.15: Direct and Inverse Causality - Pump Flow Rate Comparison.

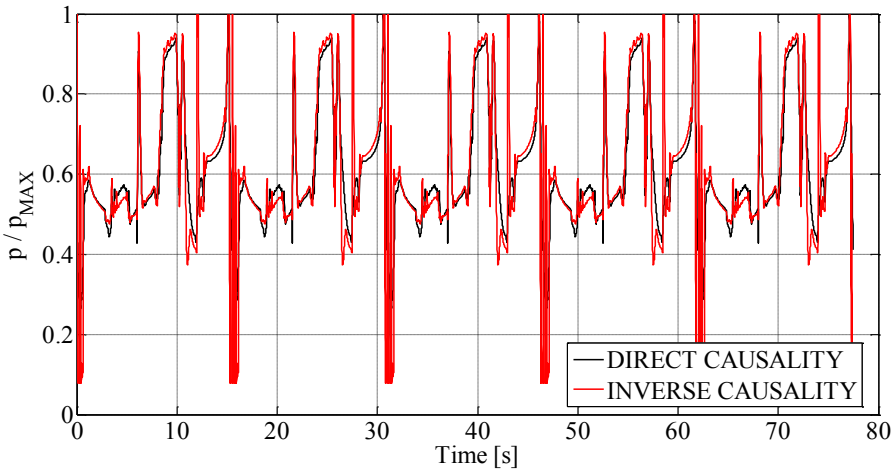

Figure 6.16: Direct and Inverse Causality - Pump Delivery Pressure Comparison.

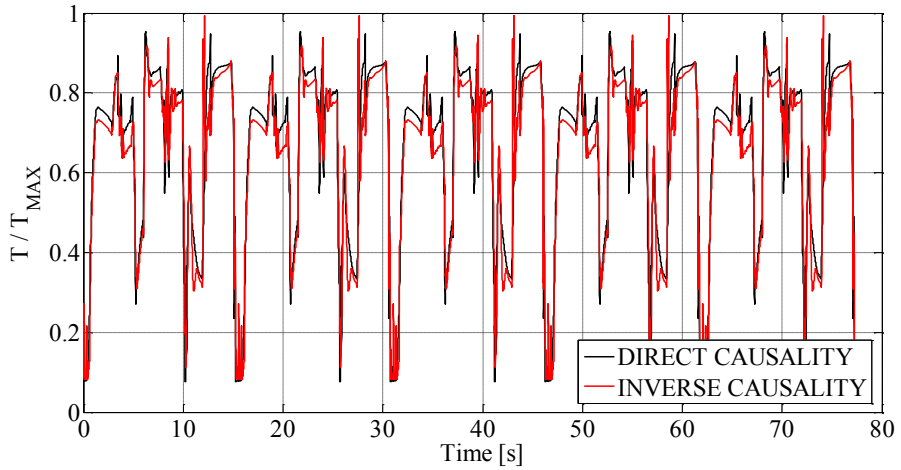

Figure 6.17: Direct and Inverse Causality – ICE Torque Comparison.

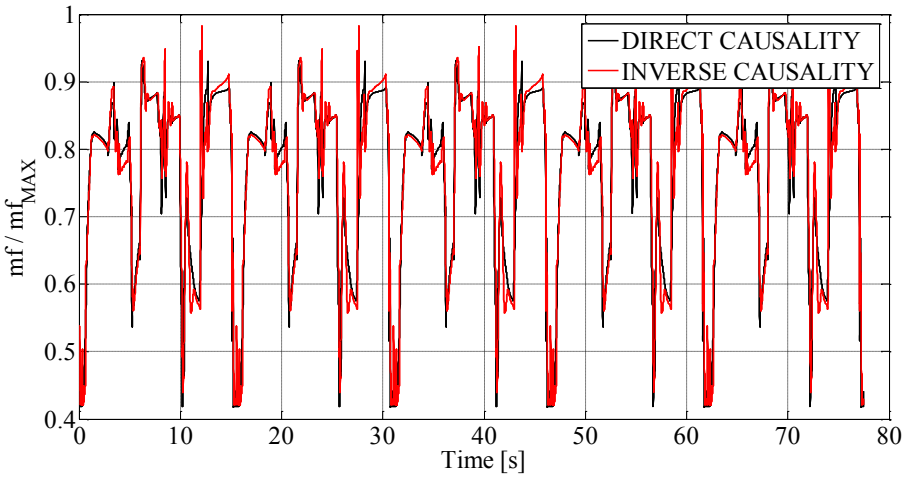

Figure 6.18: Direct and Inverse Causality – Fuel Mass Flow Rate Comparison.

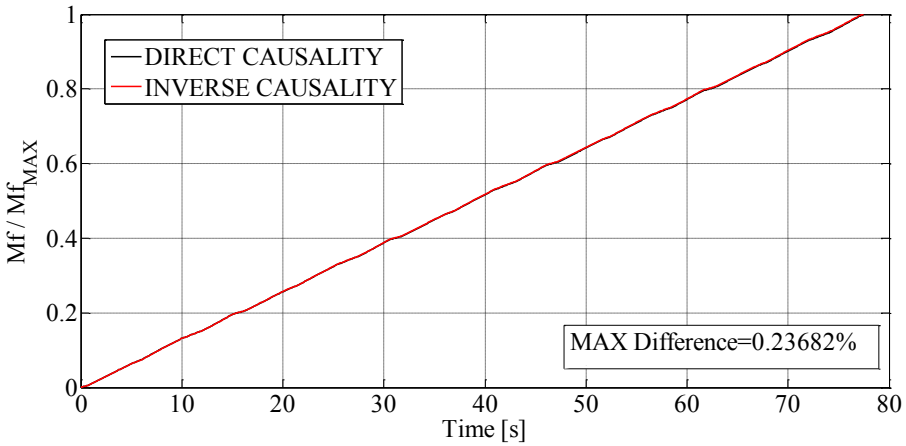

Figure 6.19: Direct and Inverse Causality – Fuel Consumption Comparison.

Despite of the Quasi-Steady assumption, there is a great agreement between the compared inverse and direct causality models variables, i.e. the pump flow rate and delivery pressure, the ICE torque, the fuel mass flow rate and the fuel consumption.

Concerning the fuel consumption the evaluated maximum difference is lower than 0.25%.

In conclusion the developed inverse causality model of the excavator can be considered validated.

6.3 Optimization of the Excavator Boom ERS

In this section the boom ERS components and the optimal control strategy will be respectively sized and defined.

The first step is to insert the ERS in the inverse causality model of the excavator. Then the optimization problem will be defined and finally the results presented.

6.3.1 Inverse Causality Model with the ERS

The ERS inverse causality model is reported in Fig.6.20. This system consists of the HCV, and the hydraulic accumulator, as described in detail in Chapter 5, while the pilot pump has been modified according to the functioning as a pump/motor. The overall inverse causality hybrid excavator model is reported in Appendix 5.

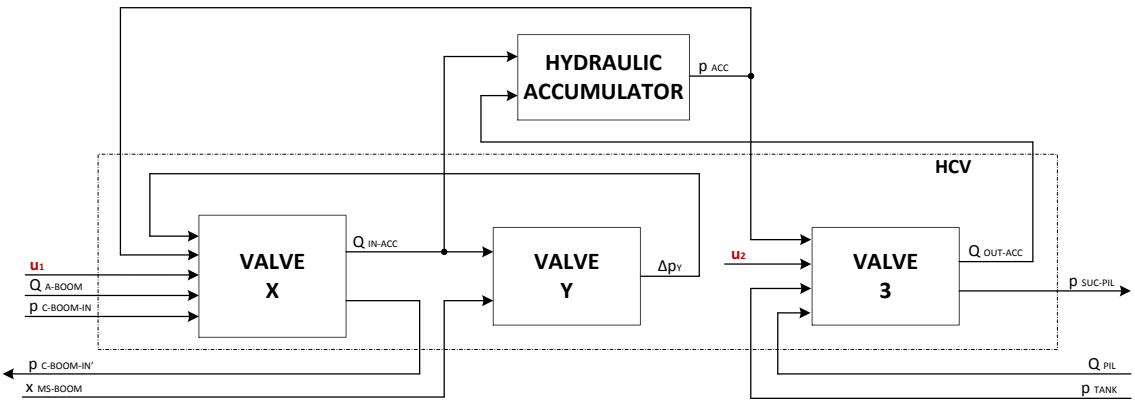

Figure 6.20: Inverse Causality Scheme of the Proposed ERS.

The adoption of the proposed ERS introduces additional pressure losses even when no energy recovery is performed (*Eq.6.31*).

$$\begin{cases} u_1 = 0 \\ u_2 = 0 \\ Q_{IN-ACC} = 0 \\ p_{C-BOOM-IN'} = p_{C-BOOM-IN} + \Delta p_X \\ \Delta p_X = k_X \cdot f\left(Q_{A-BOOM}{}^2\right) \\ Q_{OUT-ACC} = 0 \\ p_{SUC-PIL} = p_{TANK} \end{cases} \tag{6.31}$$

Concerning the recovery mode, Fig.5.26 (A), the mathematical description of the ERS is summarized by (*Eq.6.32*).

$$\begin{cases} u_1 = 1 \\ u_2 = 0 \\ Q_{IN-ACC} = Q_{A-BOOM} \\ p_{C-BOOM-IN'} = \Delta p_X + \Delta p_Y + p_{ACC} \\ \Delta p_X = k_X \cdot f\left({Q_{A-BOOM}}^2\right) \\ \Delta p_Y = k_Y \cdot f\left({Q_{IN-ACC}}^2\right) \cdot f(x_{MS-BOOM}) \\ Q_{OUT-ACC} = 0 \\ p_{SUC-PIL} = p_{TANK} \end{cases} \quad (6.32)$$

The recovery and reuse mode, Fig.5.26 (B) is mathematically described by (*Eq.6.33*).

$$\begin{cases} u_1 = 1 \\ u_2 = 1 \\ Q_{IN-ACC} = Q_{A-BOOM} \\ p_{C-BOOM-IN'} = \Delta p_X + \Delta p_Y + p_{ACC} \\ \Delta p_X = k_X \cdot f\left({Q_{A-BOOM}}^2\right) \\ \Delta p_Y = k_Y \cdot f\left({Q_{IN-ACC}}^2\right) \cdot f(x_{MS-BOOM}) \\ Q_{OUT-ACC} = Q_{PIL} \\ p_{SUC-PIL} = p_{ACC} + \Delta p_3 \\ \Delta p_3 = k_3 \cdot f\left({Q_{OUT-ACC}}^2\right) \end{cases} \quad (6.33)$$

Finally the reuse mode only, Fig.5.26 (C), is modelled by (*Eq.6.34*).

$$\begin{cases} u_1 = 0 \\ u_2 = 1 \\ Q_{IN-ACC} = 0 \\ p_{C-BOOM-IN'} = p_{C-BOOM-IN} + \Delta p_X \\ \Delta p_X = k_X \cdot f\left({Q_{A-BOOM}}^2\right) \\ Q_{OUT-ACC} = Q_{PIL} \\ p_{SUC-PIL} = p_{ACC} + \Delta p_3 \\ \Delta p_3 = k_3 \cdot f\left({Q_{OUT-ACC}}^2\right) \end{cases} \quad (6.34)$$

6.3.2 Optimization Problem Definition

The effectiveness, i.e. the fuel consumption reduction, of a hybrid layout strongly depends on both the control strategy and the components dimensions.

For this reason, the parameters optimization of the proposed ERS has been carried out allowing the comparison of different parameters combinations, leading to the minimum fuel consumption reduction achievable by the proposed hybrid layout.

The optimization target are the accumulator volume (V_{ACC}), the initial accumulator pressure (p_0), i.e. the gas pressure when the accumulator is completely discharged, and the equivalent diameter of the valve Y flow area at fully open position (d_{EQ}).

The optimal solution was searched exploring all the combinations resulting from the following parameters variation ranges:

- $V_{ACC} \in [\,4, 5, 6, 10]$, according to the available accumulator sizes;
- p_{MIN} from 5 bar to 50 bar with an increasing step of 5 bar;
- d_{EQ} from 4 mm to 10 mm with an increasing step of 0.5 mm.

In order to perform the optimization procedure, applying the DP algorithm, thus minimizing the fuel consumption, the system equations have been rearranged in a discrete state space representation form, (*Eq.6.35*). The actuators input are treated as known external disturbances (or solicitations), thus obtaining time invariant correlations f and g.

$$\begin{cases} x(k+1) = f\big(x(k), u(k), w(k)\big) \\ y(k) = g(x(k), u(k), w(k)) \end{cases} \tag{6.35}$$

The state variable ($x(k)$) corresponds to the accumulator pressure (p_{ACC}), for the considered problem, and the state update equation [$f\big(x(k), u(k), w(k)\big)$] is derived from (*Eq.6.29*), function of external disturbances and control valves actuation.

The term ($u(k)$) is a vector representing the behaviour of the set of controls valves, controlling both the flow rate entering and leaving the hydraulic accumulator. Concerning the proposed ERS it is composed of ($u_1(k)$) and ($u_2(k)$).

The term ($w(k)$) represents the external solicitations acting on the actuators.

The output ($y(k)$) is the fuel mass flow rate burned by the ICE at every time step in order to guarantee the required power output.

The time step (Δt) has been set equal to 0.01 *s*, which has been found to guarantee low computational time for problem resolution and good accuracy in the integration of the state space equation.

The control variables managed by the DP algorithm are the valve X position ($u_1(k)$), which enables the recovery phase, and the valve 3 position ($u_2(k)$), which enables the reuse phase. Both these valves are controlled according to an ON/OFF strategy.

Valve Y is differently controlled proportionally to the main spool position ($x_{MS-BOOM}$) of the boom DFCV section.

Some boundary constraints have been imposed to the problem (Eq.6.35) on the:

- accumulator pressure, i.e. the state of the system (to maintain safe operating conditions), $x(k) \in \lfloor x_{min}, x_{max} \rfloor$, where $x_{max} = 4 \cdot x_{min}$;
- rod chamber pressure of the boom HLA (to avoid cavitation during the recovery phases) $p_{R-BOOM} > 0$;
- ICE engine maximum torque, $T_{ICE}(k) \in \lfloor T_{ICE,min}(n_{ICE}), T_{ICE,max}(n_{ICE}) \rfloor$.

The objective of the optimization is the minimization of the cost (*Eq.6.36*), corresponding to the fuel consumption during the working cycle.

$$J_\pi(x_0) = \sum_{k=1}^{N-1} y(k) \cdot \Delta t \qquad (6.36)$$

$x_0 = x(p_{MINi})$ is the initial accumulator pressure, chosen equal to x_{MIN}, and $\pi = \{\overrightarrow{u_0}, \overrightarrow{u_1}, \dots, \overrightarrow{u_N}\}$ is the generic control policy adopted for controlling the energy storage, while the hydraulic accumulator final state $x_f = x(N)$ has been constrained to be equal to the initial state of the accumulator (p_{MIN}).

For every combination of the hydraulic accumulator parameters (V_{ACC}, p_{MIN}) and equivalent diameter of valve Y (d_{EQ}) the objective of the optimization is the determination of the optimal control policy (*Eq.6.37*) minimizing fuel consumption.

$$\pi^* = \arg\ min_\pi\ J_\pi(x_0) \qquad (6.37)$$

The corresponding cost $J^* = J_{\pi^*}(x_0)$ would be used in the comparison of the different parameters combinations thus obtaining the optimal ERS components sizing.

6.3.3 Optimization Results

In this section the ERS optimization results concerning both the components and the EMS are reported and analysed. Therefore the optimal components size and control strategy are defined.

The contour graphs reported in Fig.6.21 show the maximum fuel saving percentage obtainable for the considered optimization problem and parameters combinations with the adoption of the optimal control strategy defined by the DP algorithm.

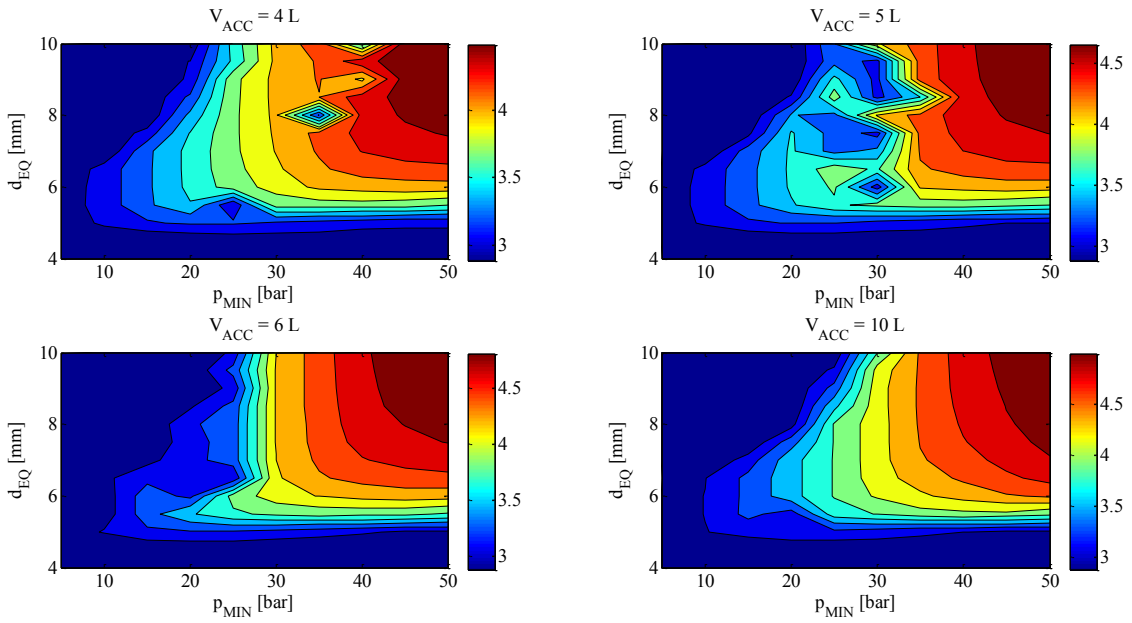

Figure 6.21: ERS Optimization Results.

The maximum fuel saving percentage is about 5%[29], obtained with both a 6 L and 10 L hydraulic accumulator. Since the difference is very small, a 6 L accumulator was preferred for its compactness being the available space limited on the excavator under investigation.

The optimal parameters combination which achieves the overall maximum fuel saving percentage is: $p_{MIN} = 40\ bar$, $V_{ACC} = 6\ L$ and $d_{EQ} = 9.5\ mm$.

This parameter combination defines the ERS best configuration while the DP optimal control laws (u_1, u_2) are applied to govern the opening of the corresponding valves (X, 3), Fig.6.20, therefore defining the instantaneous accumulator pressure.

[29] Considering the trench digging cycle of the JCMAS H020:07

Figure 6.22 reports the optimal control laws and the correspondent accumulator pressure during a complete digging cycle (five sequential repetitions), while Fig.6.23 shows an intermediate digging cycle for a better understanding of the optimal control laws.

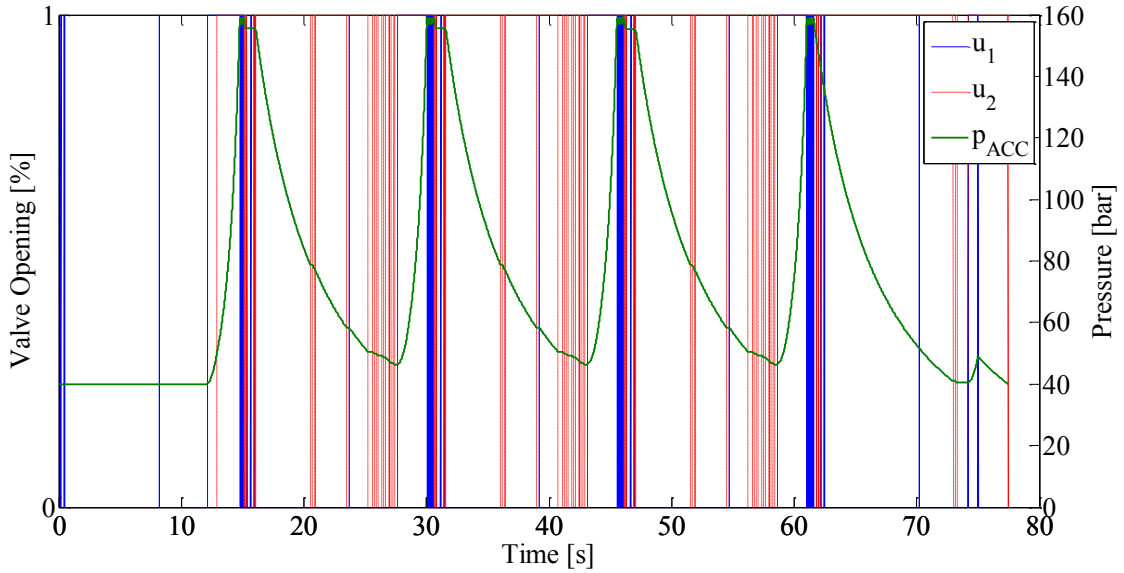

Figure 6.22: Optimal Global ERS Control.

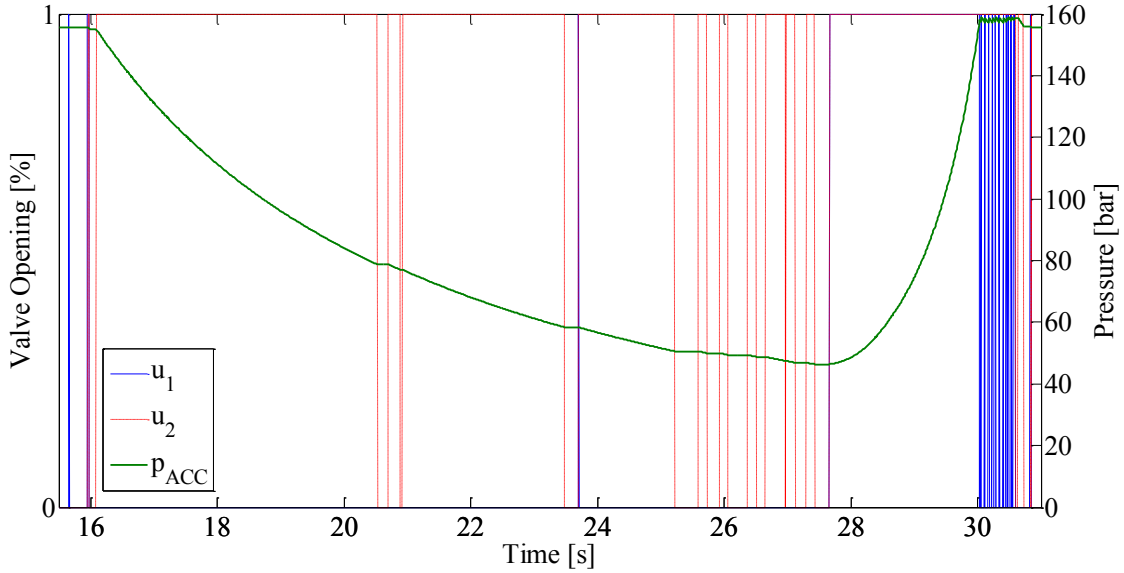

Figure 6.23: Optimal ERS Control for an Intermediate Cycle.

The optimal control strategy defined by the DP algorithm is not causal, i.e. not directly implementable on an ECU. Therefore a suboptimal rule-based control strategy has been defined starting from this optimal control strategy.

The accumulator pressure (p_{ACC}) and the boom flow control valve pilot pressure ($p_{V2-BOOM}$) have been selected as the input variables of the control strategy since they showed a strong relationship with the control variables u_1 and u_2, furthermore an Enable input has been inserted in order to disable the ERS.

The logic scheme of the defined control strategy implemented on the ECU is reported in Fig.6.24.

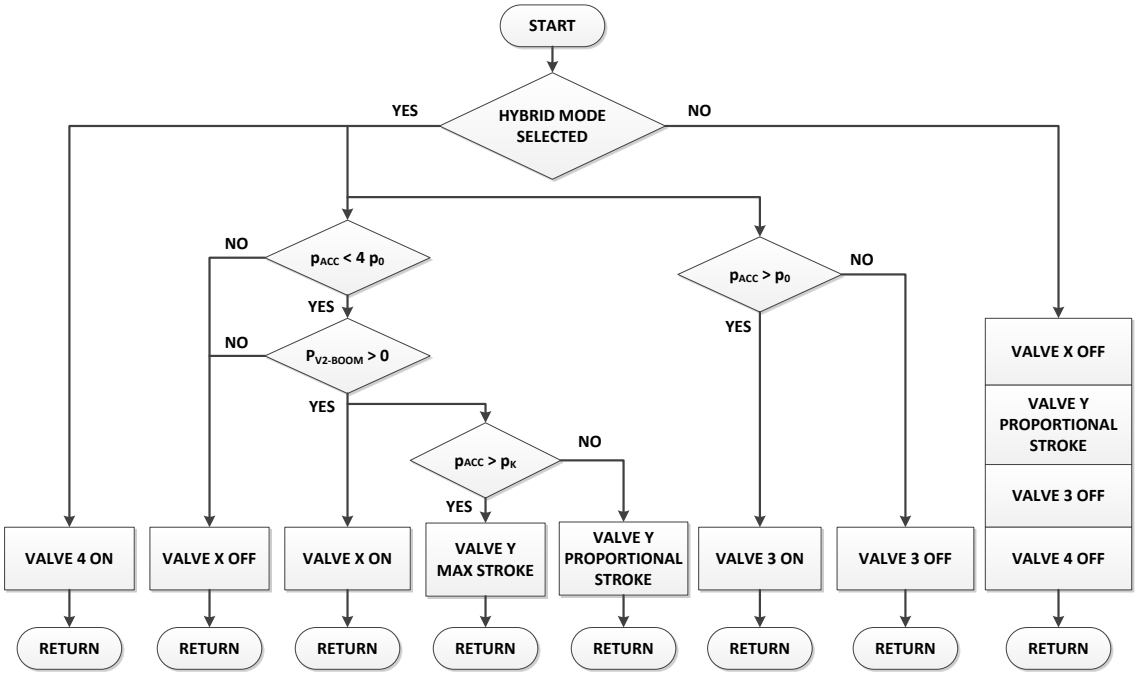

Figure 6.24: Control Strategy Logic Scheme.

As previously stated, the valve Y spool position is controlled to have the same position of the boom main spool during lowering phase.

During the recovery phase (valve X enabled), a further rule has been introduced in order to minimize the throttle losses in the valve Y when the accumulator pressure is sufficient ($p_{ACC} > p_K$) for balancing the front equipment weight. If ($p_{ACC} \leq p_K$) the valve Y opening is the same of the boom one, otherwise ($p_{ACC} > p_K$) the valve Y is fully opened. Moreover, suitable hysteresis were introduced in order to avoid frequent valves commutations.

6.4 Discussion

The optimal dimensioning of the proposed ERS has been presented in detail in this chapter.

The dimensioning methodology takes advantage of the DP algorithm, which has been deeply presented even through a large reported bibliography.

In order to exploit the DP algorithm the excavator mathematical model causality, presented in Chapter 2, has been reverted and the model validated. Then the ERS inverse causality model has been inserted in model and the optimization performed.

The obtained results pointed out the maximum achievable fuel saving percentage through the usage of the proposed ERS and its component optimal sizing and control strategy.

Finally the rule-based control strategy to be implemented in the ECU has been derived from the optimal one.

In the next chapter the realized ERS prototype mathematical model will be presented and validated on the basis of the experimental results (see Chapter 8).

Symbols

Symbol	Definition	Unit
A	Area	[m^2]
cd	Orifice Discharge Coefficient	[-]
d	Diameter	[m]
F	Force	[N]
F_C	Coulomb Friction Force	[N]
k_3	Valve 3 Pressure Drop Coefficient	[kg/m^7]
k_L	Hydraulic Line Pressure Drop Coefficient	[$Pa/(m^3/s)$]
k_T	Drag Torque Friction Coefficient	[(Nm)/(r/min)]
k_V	HLA Viscous Friction Coefficient	[(Ns)/m]
k_X	Valve X Pressure Drop Coefficient	[kg/m^7]
k_Y	Valve Y Pressure Drop Coefficient	[kg/m^3]
$k_{\Delta p}$	HLA Differential Pressure Friction Coefficient	[m^2]
$\dot{m}_f$	Fuel Mass Flow Rate	[kg/s]
n	Rotary Velocity	[r/min]
p	Pressure	[Pa]
Q	Volumetric Flow Rate	[m^3/s]
T	Torque	[N·m]
T_C	Coulomb Friction Torque	[N·m]
u	ECU Command	[-]

v	Velocity	[m/s]
V	Volume	[m^3]
Vd	Volumetric Displacement	[m^3/r]
Symbol	**Definition**	**Unit**
x	Spool Linear Position	[m]
γ	Politropic Index	[-]
η_{hm}	Hydraulic-mechanical Efficiency	[-]
η_V	Volumetric Efficiency	[-]
ρ	Fluid Density	[kg/m^3]
τ	Transmission Ratio	[-]
ω	Angular Velocity	[rad/s]
Subscripts	**Definition**	
A	Workport A	
ACC	Accumulator	
B	Workport B	
C	Counter	
EQ	Equivalent	
HLA	Hydraulic Linear Actuator	
HRA	Hydraulic Rotary Actuator	
HE	Heat Exchanger	
i	i-th	
ICE	Internal Combustion Engine	
IN	Inlet	
LS	Load Sensing	
MAX	Maximum	
MIN	Minimum	
MS	Main Spool	
OUT	Outlet	
P	Piston	
PIL	Pilot	
R	Rod	
SUC	Suction	
TANK	Reservoir	

References

6.1 *N. Kim, S. Cha, H. Peng. Optimal Control of Hybrid Electric Vehicles Based on Poyntryagin's Minimum Principle. IEEE Transactions on Control Systems Technology, vol. 19, no. 5, September 2011.*

6.2 *G. Paganelli, S. Delprat, T.M. Guerra, J. Rimaux, J.J. Santin. Equivalent Consumption Minimization Strategy for Parallel Hybrid Powertrains. Veh Technol Conf (VTC) 2002. 0-7803-7484-3/02/$17.00 02002 IEEE.*

6.3 *C. Musardo, G. Rizzoni, B. Staccia. A-ECMS: an Adaptive Algorithm for Hybrid Electric Vehicle Energy Management. Proceeding of the 44th IEEE Conference on Decision and Control, and the European Control Conference 2005. Seville, Spain. December 12-15 2005.*

6.4 *J. Gao, F. Sun, H. He, G.G. Zhu, E.G. Strangas. A Comparative Study of Supervisory Control Strategy for a Series Hybrid Electric Vehicle. Power Energy Eng Conf 2009:1-7. 978-1-4244-2487-0/09/$25.00 ©2009 IEEE.*

6.5 *M. Neuman, H. Sandberg, B. Wahlberg. Rule-Based Control of Series HEVs Derived from Deterministic Dynamic Programming.*

6.6 *R.E. Bellman. Dynamic Programming. Princeton – N.J.:Princeton University Press, 1957.*

6.7 *D. Bertsekas. Dynamic Programming and Optimal Control. 3rd Ed. Belmont. Massachusetts: Athena Scientific, 2005.*

6.8 *B.C. Chen, Y.Y. Wu, H.C. Tsai. Design and Analysis of Power Management Strategy for Range Extended Electric Vehicle using Dynamic Programming. Applied Energy 113 (2014) 1764-1774. http://dx.doi.org/10.1016/j.apenergy.2013.08.018.*

6.9 *T. Bleazard, H. Haria, M. Sprengel, M. Ivantysynova. Optimal Control and Performane Based Design of the Blended Hydraulic Hybrid. Proceedings of the ASME/BATH 2015 Symposium on Fluid Power and Motion Control FPMC2015. October 12-14, 2015, Chicago, Illinois, USA.*

6.10 *J. Peralez, P. Tona, M. Nadri, P. Dufour, A. Sciarretta. Optimal Control for an Organic Rankine Cycle on Board a Diesel-Electric Railcar. Journal of Process Control 33(2015)1-13. http://dx.xoi.org/10.1016/j.procont.2015.03.009.*

6.11 *O. Sundstrom, L. Guzzella. A Generic Dynamic Programming Matlab Function. Proceedings of the 18th IEEE International Conference on Control Applications, pp. 1625-1630, Saint Petersburg, Russia, 2009.*

Chapter 7: **Energy Recovery System Mathematical Modelling**

In this chapter the prototype of the proposed ERS studied and optimally dimensioned in the previous chapters will be presented in detail as well as its mathematical model.

The realized mathematical model will be inserted in the standard excavator in order to realize the hybrid excavator model, then exploited for the related energy analysis presented in Chapter 9.

7.1 Prototype of the Hybrid Control Valve

In Chapter 5 a novel ERS architecture for the energy recovery from the boom actuator during the implement lowering was proposed. In Chapter 6 the ERS components were optimally dimensioned with particularly focus on the hydraulic accumulator and the valve Y of the HCV. In this chapter the first prototype of the HCV will be presented and mathematically modelled.

Figure 7.1 reports the HCV ISO scheme of the studied ERS.

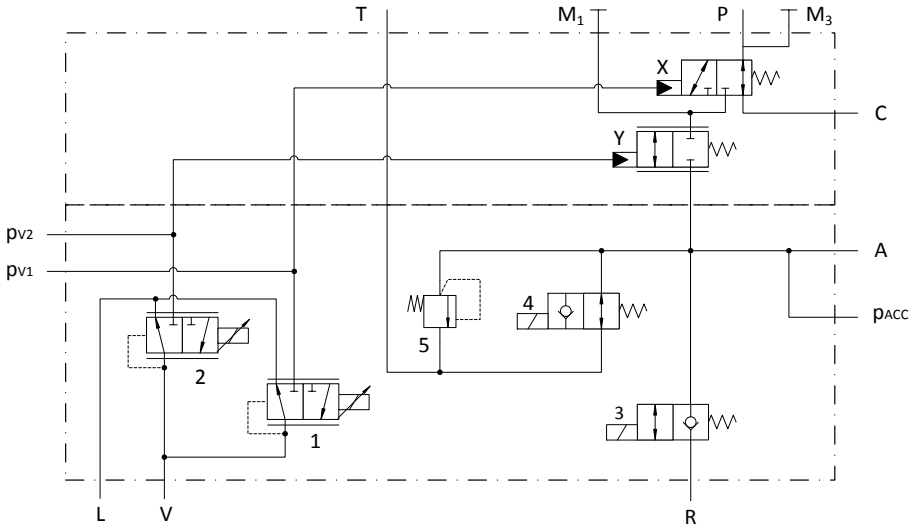

Figure 7.1: HCV ISO Scheme.

The HCV is composed of the valve X, Y, 3 and 4, which accordingly to the defined control strategy, see Chapter 6, enable the energy recovery and reuse phases.

The pressure relief valve 5, integrated within the HCV block, limits the maximum accumulator pressure in order to avoid pressure levels out of the accumulator safe working zone.

Valves 3 and 4 are electro-actuated through the usage of ON/OFF solenoids. On the contrary valves X and Y are electro-hydraulically actuated through the usage of two proportional pressure reduction valves.

Dedicated pressure sensing ports (M_1, M_3, p_{ACC}, p_{V1}, p_{V2}) have been included in the system in order to monitor the HCV functioning during the test bench characterization and validation tests (see Chapter 8) and to instrument the HCV with the sensors required for its control on the hybrid machinery.

Figure 7.2 depicts the HCV prototype CAD model. This prototype valve has been realized by Walvoil S.p.A.

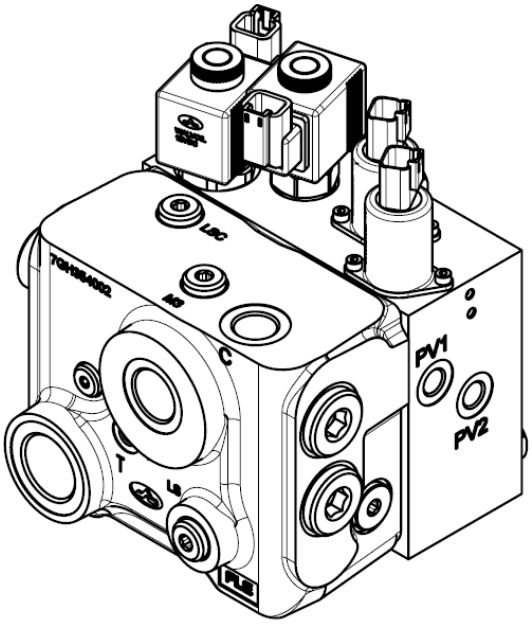

Figure 7.2: HCV Prototype CAD Model.

The complete ISO scheme of the hybrid excavator is reported in Appendix 6. The FGU exploited in this version of the machinery has been properly modified by Casappa S.p.A. accordingly to the specifics required for the functioning of the pilot pump with a pressurized suction line.

7.2 ERS Modelling

In this section the direct causality mathematical models of the ERS components will be described in detail.

7.2.1 Valve X

Figure 7.3 shows the valve X model causality. The model input are the enable signal (u_1), which is defined by the ECU according with the defined control strategy, defining the valve main spool position: if $u_1 = 0$ the spool is in the neutral position, i.e. the flow path available is from P to C (Fig.7.1), if $u_1 = 1$ the spool is in completely opened, i.e. the flow path available is from P to Y (Fig.7.1); the pressure of the A line of the boom between the HCV and the DFCV workport ($p_{A1'}$); the pressure of the XY chamber (p_{XY}), between the valve X and the valve Y, and the pressure of the line A of the boom between the HLA and the HCV (p_C).

The output of the model are the flow rates to and from the mentioned chambers ($Q_{A1'}$, Q_X, Q_{A-BOOM}).

The following assumptions were done for the modelling: the dynamic of the valve spool has been considered through a first order lag and no internal leakages have been considered.

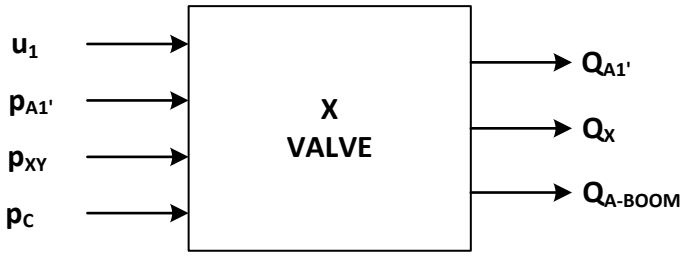

Figure 7.3: Valve X Causality.

The model output are defined by (*Eq.7.1*) and (*Eq.7.2*).

$$\begin{cases} u_1 = 0 \\ \Delta p_{AC} = p_C - p_{A1'} \\ Q_{A1'} = f(\Delta p_{AC}) \\ Q_{A-BOOM} = -Q_{A1'} \\ Q_X = 0 \end{cases} \tag{7.1}$$

$$\begin{cases} u_1 = 1 \\ \Delta p_{CX} = p_C - p_{XY} \\ Q_X = f(\Delta p_{CX}) \\ Q_{A-BOOM} = -Q_X \\ Q_{A1'} = 0 \end{cases} \quad (7.2)$$

The pressure inside the chambers XY, A1′ are evaluated through (*Eq.2.66*) while $f(\Delta p_{AC})$ and $f(\Delta p_{CX})$ are the experimentally defined correlation between the differential pressure and the flow rate of valve X (see Chapter 8).

7.2.2 Valve Y

Valve Y model causality is represented in Fig.7.4. The model input are the pilot pressure (p_{V2-HCV}), defined by the ECU and proportional to the boom ($p_{V2-BOOM}$), which control the boom main spool position ($x_{MS-BOOM}$) (Chapter 2) during the user lowering phase, the pressure of the XY chamber (p_{XY}), between the valve X and the valve Y, and the pressure of the hydraulic accumulator (p_{ACC}).

The output of the model is the flow rate (Q_Y) to the accumulator line A.

The flow forces have been neglected in the modelling.

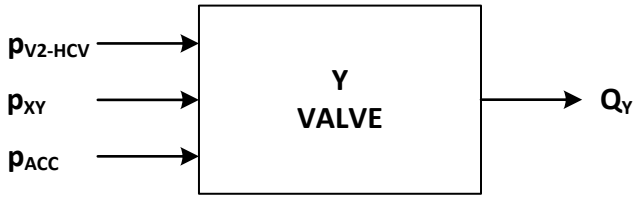

Figure 7.4: Valve Y Causality.

The flow rate to the accumulator line is evaluated through (Eq.7.3).

$$Q_Y = cd_Y \cdot A_Y(x_Y) \cdot \sqrt{\frac{2 \cdot |p_{XY} - p_{ACC}|}{\rho}} \quad (7.3)$$

The discharge coefficient (cd_Y) has been calibrated with the aid of the experimental results obtained during the test bench characterization activity on the HCV (see Chapter 8). The accumulator pressure (p_{ACC}) is calculated through (*Eq.6.29*).

The valve Y spool position is defined by (*Eq.7.4*).

$$\ddot{x}_Y \cdot m_Y + \dot{x}_Y \cdot c_Y + (x_Y + x_{0-Y}) \cdot k_Y + F_{C-Y} = p_{V2-HCV} \cdot (\frac{\pi \cdot {d_Y}^2}{4}) \quad (7.4)$$

The parameters (m_Y, x_{0-Y}, k_Y, d_Y) are known by the valve OEM, the viscous friction coefficient (c_Y) and the Coulomb friction force (F_{C-Y}) have been evaluated through the experimental activity.

Once defined the valve Y spool position (x_Y) the orifice flow area is defined through the correlation reported in Fig.7.5.

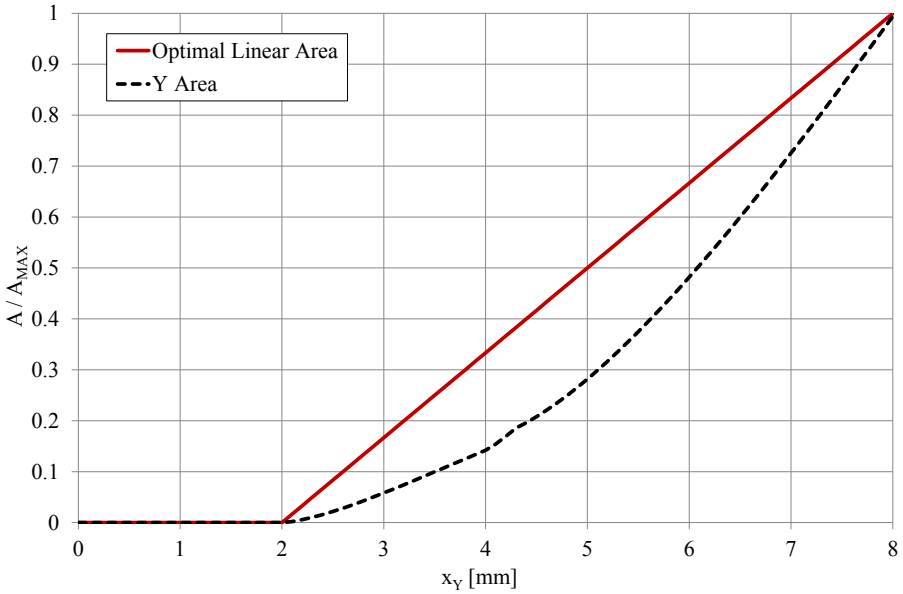

Figure 7.5: Valve Y Areas.

The two curves reported in Fig.7.5 represent the optimal linear area (continuous red line), defined in Chapter 6, and the actual area (dashed black line) respectively.

In the realized prototype of the HCV the valve Y area has been defined starting by the linear optimal one, but in the first part of the stroke the area has been reduced in order to be confident of avoiding cavitation even in the not considered possible operating conditions.

7.2.3 Valve 3

Figure 7.6 shows the valve 3 model causality. The model input are the enable signal (u_2), which is defined by the ECU according with the defined control strategy, thus defining the valve main spool position: if $u_2 = 0$ the spool is in the neutral position, i.e. the available flow area in zero, if $u_2 = 1$ the spool is in completely opened, i.e. the A to R flow path is available to

the flow rate (Fig.7.1); the pressure of the hydraulic accumulator (p_{ACC}); the pressure of the suction line chamber ($p_{SUC-LINE}$), between the valve 3 and the suction port of the pilot pump.

The output of the model is the flow rate to and from the accumulator line and the suction line (Q_3).

The following assumptions were done for the modelling: the dynamic of the valve spool has been considered through a first order lag and no internal leakages have been considered.

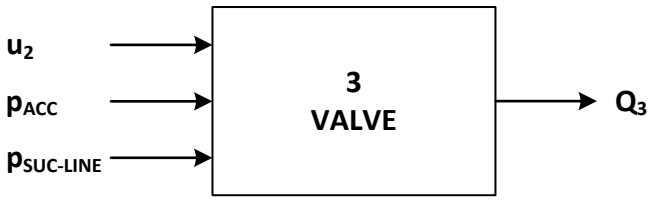

Figure 7.6: Valve 3 Causality.

The model output are defined by (*Eq.7.5*) and (*Eq.7.6*).

$$\begin{cases} u_2 = 0 \\ Q_3 = 0 \end{cases} \tag{7.5}$$

$$\begin{cases} u_2 = 1 \\ \Delta p_3 = p_{ACC} - p_{SUC-LINE} \\ Q_3 = f(\Delta p_3) \end{cases} \tag{7.6}$$

The $f(\Delta p_3)$ is a correlation between the flow rate and the differential pressure of the valve 3, when fully opened, experimentally defined (see Chapter 8).

7.2.4 Pressure Relief Valve 5 and Valve 4

The pressure relief valve 5 and the valve 4 (Fig.7.1) define the related outlet flow rates from the hydraulic accumulator during certain operating conditions of the ERS.

If the ERS is enabled valve 4 is closed thus the related flow rate is zero. On the contrary if the ERS is disabled valve 4 is completely opened and the accumulator will be discharged. This valve has been modelled as a simple orifice.

The pressure relief valve 5 limits the maximum accumulator pressure. If the accumulator pressure exceed the valve setting pressure part of the flow rate incoming from valve Y, entering into the accumulator, is discharged by valve 5 according to (*Eq.7.7*).

$$\begin{cases} if\ p_{ACC} \geq p_{SET-5} \\ \Delta p_5 = p_{ACC} - p_{SET-5} \\ Q_{LIM} = k_5 \cdot \Delta p_5 \end{cases} \quad (7.7)$$

The gradient (k_5) has been defined according to the experimental results.

7.3 Discussion

In this chapter the mathematical model of the proposed ERS has been presented, focusing on the sub-systems causality and models description.

Appendix 7 reports the hybrid excavator mathematical model global causality.

The developed model has been calibrated and validated on the basis of dedicated experimental activities (see Chapter 8).

The hybrid excavator mathematical model has been utilized to perform a complete energy analysis of the system in order to establish its overall efficiency and fuel saving capabilities (see Chapter 9).

Symbols

Symbol	Definition	Unit
A	Area	[m^2]
c	Viscous Friction Coefficient	[N/(m/s)]
cd	Orifice Discharge Coefficient	[-]
d	Diameter	[m]
F_C	Coulomb Friction Force	[N]
k	Spring Stiffness	[N/m]
m	Mass	[kg]
p	Pressure	[Pa]
Q	Volumetric Flow Rate	[m^3/s]
u	ECU Command	[-]
x	Linear Position	[m]
x_0	Spring Initial Position	[m]
ρ	Fluid Density	[kg/m^3]
Subscripts	**Definition**	
ACC	Accumulator	
C	Counter	
LIM	Pressure Relief Valve	
SET	Setting	
SUC	Suction	
XY	XY Chamber	

Chapter 8: **Hybrid Excavator - Experimental Activity and Model Validation**

This chapter deals with the experimental activity carried out on the proposed ERS and on the hybrid excavator.

The experimental activity is divided in test bench and on the field activities. The firsts have the aim of characterizing the HCV components and validating the ERS mathematical models. The seconds have both the purpose of validating the hybrid excavator mathematical model on the basis of the experimental fuel consumption results.

8.1 Test Bench Experimental Activities

The experimental tests described in this section refer to the HCV characterization and model validation. The tests were carried out with the aid of the test rig available at the Walvoil Test Department.

The characterization tests were performed for the valves X, Y and 3, Fig.5.25, while the validation test was carried out for the HCV model, see Chapter 7.

8.1.1 Valve X Characterization

The valve X, as described in the previous chapters, is ON/OFF actuated in order to connect port P of the HCV with port C or valve Y during the non-recovery phases or the recovery phases respectively. Therefore the characterization of both the orifices was performed.

P → C Orifice

Figure 8.1 reports the test bench ISO scheme configuration during the experiment.

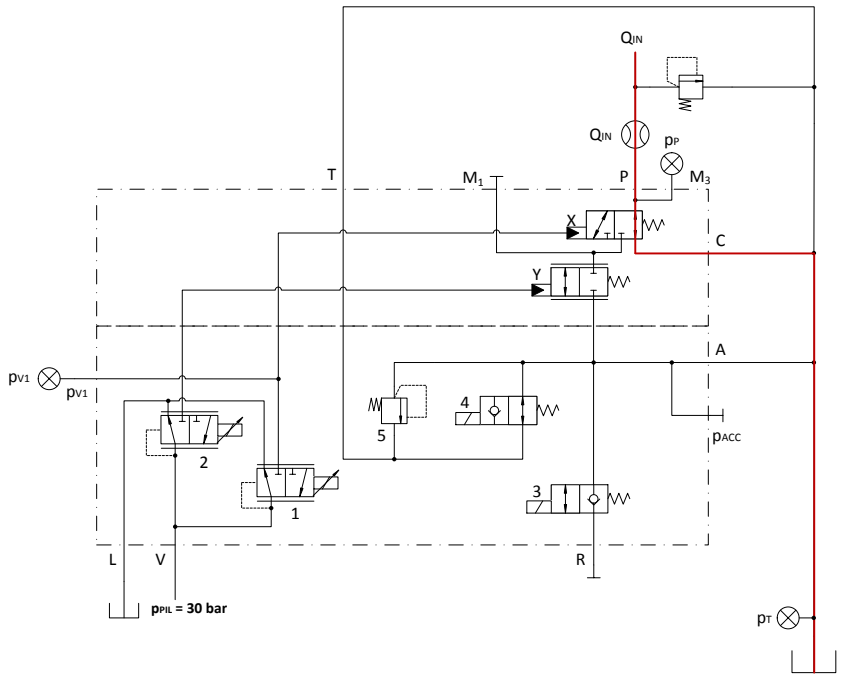

Figure 8.1: Valve X – P→C Orifice Characterization ISO Scheme.

Maintaining valve X in the neutral position (enabling the flow path from port P to port C) a flow rate ramp was imposed, exploiting the test bench internal pump, from zero to the maximum user[30] flow rate. The red line defines the path available to the flow.

During the test, the inlet flow rate (Q_{IN}) and the pressures (p_P) and (p_T), correspondent to port P and C respectively, were measured through the usage of flow rate and pressure transducers, whose mean features are reported in Tab.8.1.

Table 8.1: Transducer Main Features Valve X P→C Test.		
Symbol	Transducer Type	Main Features
Q_{IN}	VSE® Flow Meter	300 l/min ±0.2% FS
p_T, p_P	TRAFAG® Pressure Transducer	0 – 60 bar ±0.1% FS

The experimental $Q - \Delta p$ characteristic of valve X P→C orifice was defined and inserted in the mathematical model.

The same operating condition of the performed test were imposed to the model in order to verify the valve P→C orifice.

Figure 8.2 reports the comparison between the experimental (black dashed curve) and numerical (red curve) valve $Q - \Delta p$ characteristics.

The good match of the reported curves validates the mathematical model.

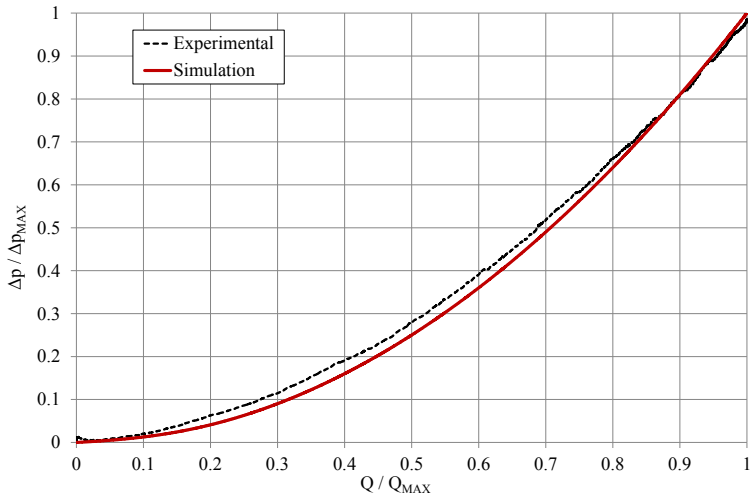

Figure 8.2: Valve X – Experimental and Simulation $(Q - \Delta p)_{PC}$ Characteristic Comparison.

[30] Equal to the boom maximum flow rate defined during the hydraulic system design.

P → Y Orifice

A similar procedure was performed for the P→Y orifice. Figure 8.3 reports the test bench ISO scheme configuration during this test.

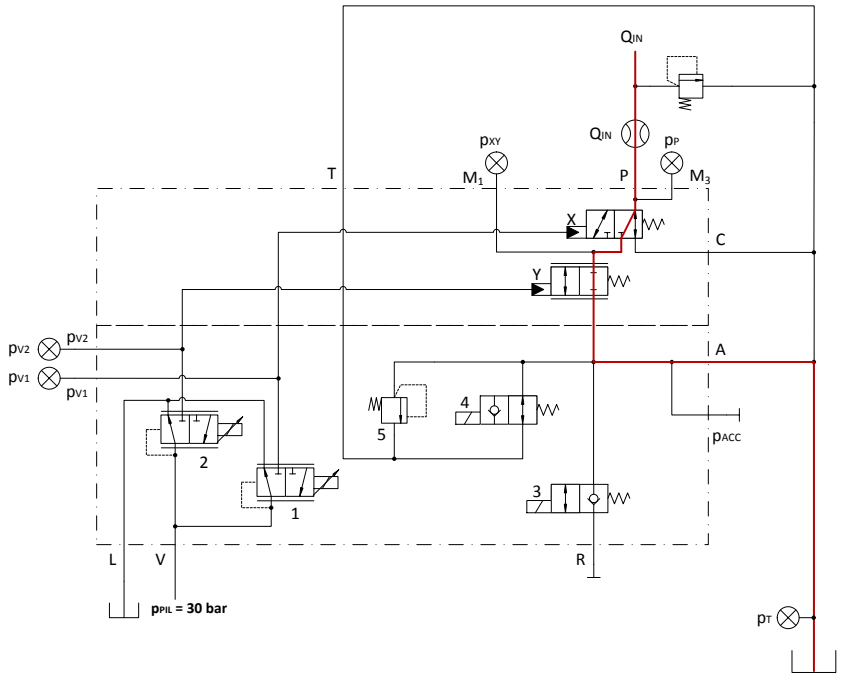

Figure 8.3: Valve X – P→Y Orifice Characterization ISO Scheme.

Valve X was set in the P→Y position and valve Y spool was displaced to the maximum position enabling the flow path represented by the red line.

A flow rate ramp was imposed from zero to the maximum user flow rate. The inlet flow rate (Q_{IN}) and the pressures (p_P) and (p_{XY}), correspondent to port P and the line XY (between valve X and Y) respectively, were measured through the usage of flow rate and pressure transducers, whose mean features are reported in Tab.8.2.

Table 8.2: Transducer Main Features Valve X P→Y Test.		
Symbol	Transducer Type	Main Features
Q_{IN}	VSE® Flow Meter	300 l/min ±0.2% FS
p_P, p_{XY}	TRAFAG® Pressure Transducer	0 – 60 bar ±0.1% FS

The experimental $Q - \Delta p$ characteristic of valve X P→Y orifice was defined and exploited in the mathematical model.

The same operating condition of the performed test were imposed to the model in order to verify the valve P→Y orifice.

Figure 8.4 reports the comparison between the experimental (black dashed curve) and numerical (red curve) valve $Q - \Delta p$ characteristics. The good match of the reported curves validates the model.

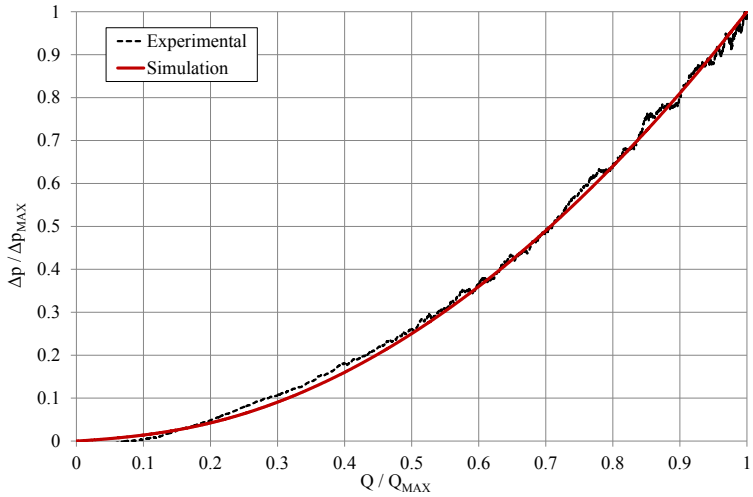

Figure 8.4: Valve X – Experimental and Simulation $(Q - \Delta p)_{PY}$ Characteristic Comparison.

8.1.2 Valve 3 Characterization

Valve 3 is a ON/OFF flow control valve which enable the connection between the hydraulic accumulator line A and the pilot pump suction line R.

Figure 8.5 depicts the test bench ISO scheme configuration during its characterization test.

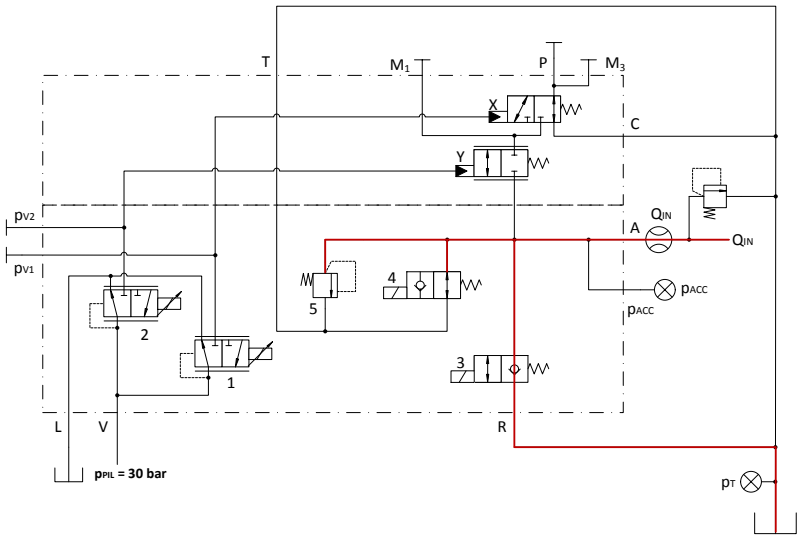

Figure 8.5: Valve 3 – A→R Orifice Characterization ISO Scheme.

During this test valves X and Y were maintained in the neutral position (avoiding the connection between line A and line P) while valve 4 and valve 3 were activated (avoiding the connection between line A and the tank and enabling the connection between line A and R) defining the flow path highlighted in red.

A flow rate ramp was imposed from zero to double the maximum pilot pump flow rate. The inlet flow rate (Q_{IN}) and the pressures (p_{ACC}) and (p_T), correspondent to port A and the line R respectively, were measured through the usage of flow rate and pressure transducers, whose mean features are reported in Tab.8.3.

Table 8.3: Transducer Main Features Valve 3 A→R Test.

Symbol	Transducer Type	Main Features
Q_{IN}	VSE® Flow Meter	300 l/min ±0.2% FS
P_{ACC}, p_T	TRAFAG® Pressure Transducer	0 – 60 bar ±0.1% FS

The experimental $Q - \Delta p$ characteristic of valve 3 was defined and exploited in the mathematical model.

The same operating condition were imposed to the mathematical model and Fig.8.4 reports the comparison between the experimental (black dashed curve) and numerical (red curve) valve $Q - \Delta p$ characteristics. The good match of the reported curves validates the defined parameter.

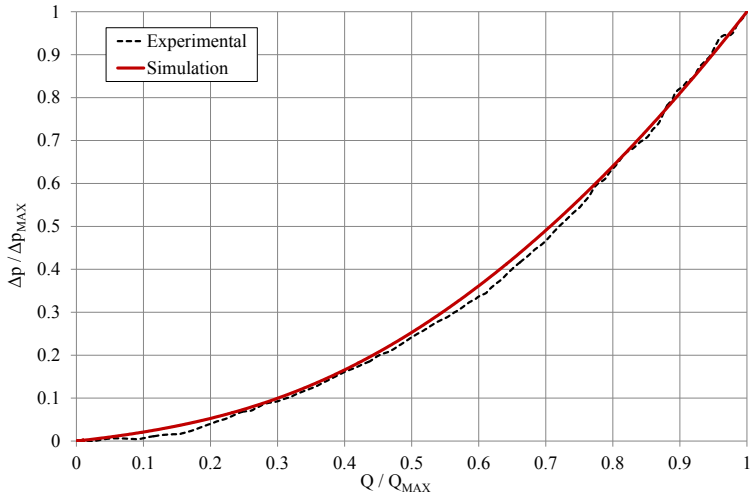

Figure 8.6: Valve 3 – Experimental and Simulation $(Q - \Delta p)_{AR}$ Characteristic Comparison.

8.1.3 Valve Y Characterization

Valve Y is a proportional flow control valve which defines the port P pressure in order to avoid cavitation in the rod chamber during the boom lowering, being the actuator velocity controlled by the meter-IN orifice.

Figure 8.7 represents the test bench ISO scheme configuration during its characterization test.

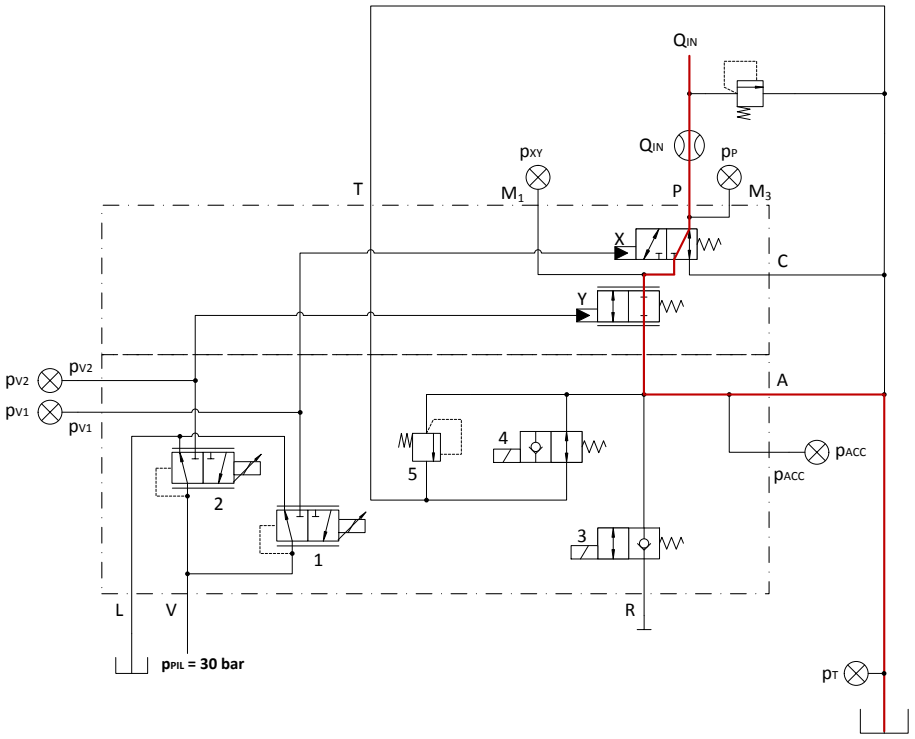

Figure 8.7: Valve Y Characterization ISO Scheme.

During this test the valve 3 was maintained in the neutral position (avoiding the connection between line A and line R), valve 4 was enabled (avoiding the connection between line A and the tank) and valve X was set to the P→Y position (i.e. fully displaced).

Initially valve Y was maintained in the neutral position and a constant flow rate was imposed, by the test bench internal pump, into line P.

Being the flow path, defined by the red line in Fig.8.7, initially closed by the valve Y the P line pressure rises to the pressure relief valve setting pressure.

A proportional quasi-steady opening of the valve Y was imposed, controlling the pilot pressure (p_{V2-HCV}) through the pressure reducing valve 2, opening the flow path to the fluid reaching the maximum area.

During the test the inlet flow rate (Q_{IN}) and the pressures (p_P), (p_{XY}), (p_{ACC}) and (p_{V2-HCV}) were measured. The adopted transducers main features are reported in Tab.8.4.

Table 8.4: Transducer Main Features Valve 3 A→R Test.		
Symbol	Transducer Type	Main Features
Q_{IN}	VSE® Flow Meter	300 l/min ±0.2% FS
p_P, p_{XY}	TRAFAG® Pressure Transducer	0 – 400 bar ±0.1% FS
p_{ACC}, $p_{V2\text{-}HCV}$	TRAFAG® Pressure Transducer	0 – 60 bar ±0.1% FS

Valve Y area, defined in Chapter 7, is known as well as the other geometrical and mechanical characteristics (e.g. mass, spring stiffness and initial force, spool external and rod diameters, etc.), thus recreating the same conditions of this experimental test in the simulation the valve discharge coefficient (c_d) and the friction forces (both viscous and Coulomb) were defined.

The input for the model, according with the causality defined in Chapter 7, were the pilot pressure (p_{V2-HCV}) and the valve differential pressure ($p_{XY} - p_{ACC}$), while its output was the flow rate (Q_Y), correspondent to (Q_{IN}) for this test.

Figure 8.8 reports the comparison between the experimental (black dashed curve) and the simulation (red curve) valve flow rates in function of the valve pilot pressure, i.e. the valve opening. The very good match between the curves validates the valve Y mathematical model.

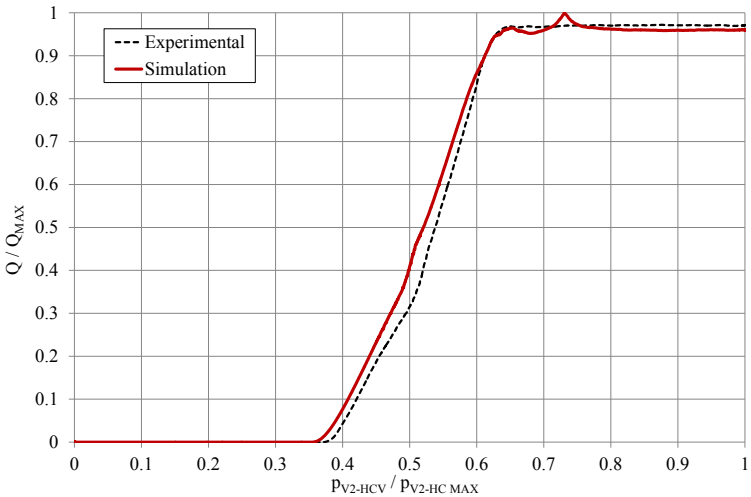

Figure 8.8: Valve Y – Experimental and Simulation $(Q - p_{V2-HCV})_Y$ Characteristic Comparison.

8.1.4 Recovery – Reuse Test Simulation

The experimental test described in this section is the simulation of the energy recovery and reuse operating condition (described in Chapter 5), performed on the test bench.

Figure 8.9 represents the bench configuration and the transducers, whose main features are reported in Tab.8.5, exploited during the test, while Fig.8.10 reports the photograph of the configuration.

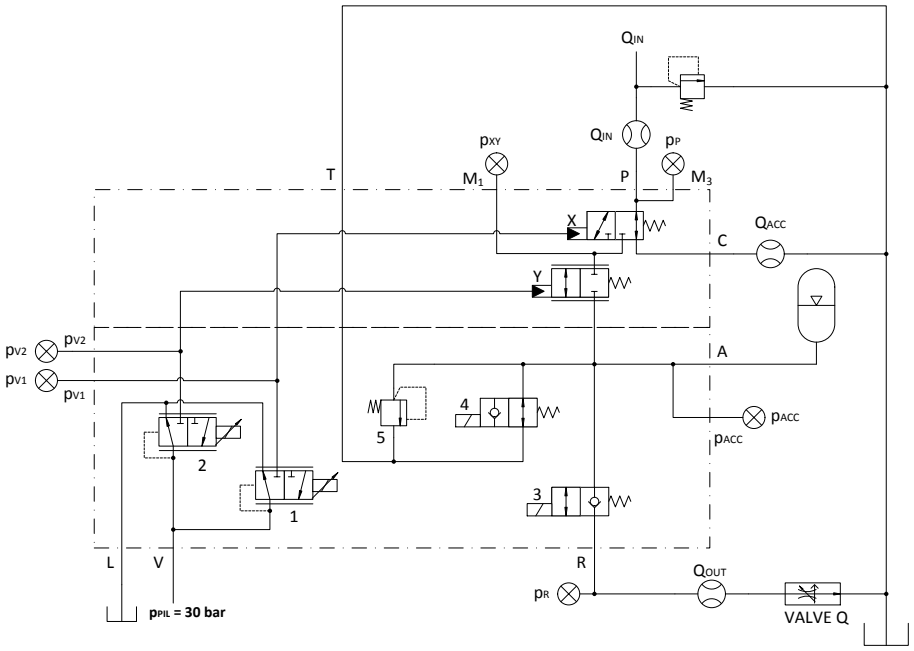

Figure 8.9: HCV Recovery – Reuse Simulation Test ISO Scheme.

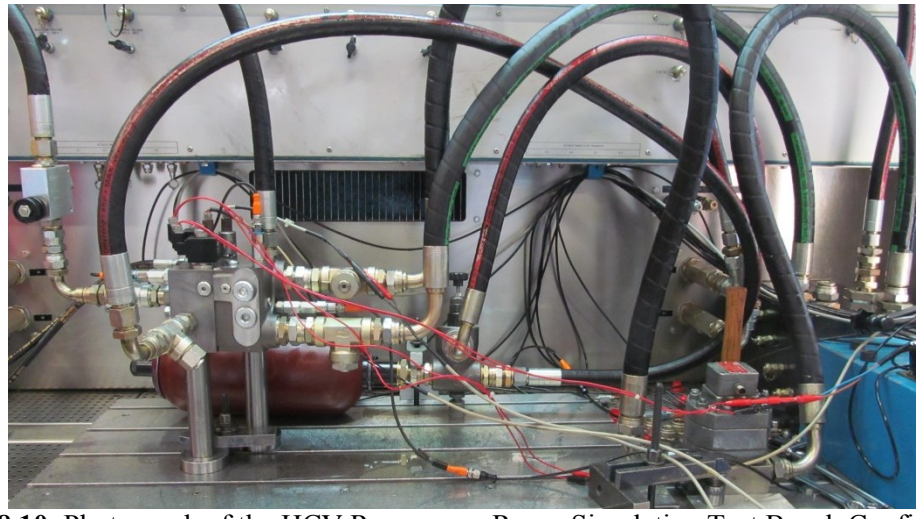

Figure 8.10: Photograph of the HCV Recovery – Reuse Simulation Test Bench Configuration.

Table 8.5: Transducer Main Features Valve 3 A→R Test.		
Symbol	Transducer Type	Main Features
Q_{IN}, Q_C	VSE® Flow Meter	300 l/min ±0.2% FS
Q_{OUT}	VSE® Flow Meter	80 l/min ±0.2% FS
p_P, p_{XY}, p_{ACC}	TRAFAG® Pressure Transducer	0 – 400 bar ±0.1% FS
$p_{V1\text{-}HCV}$ $p_{V2\text{-}HCV}$ p_R	TRAFAG® Pressure Transducer	0 – 60 bar ±0.1% FS

During this test the hydraulic accumulator was connected to the HCV port A, the boom actuator outlet flow rate was recreated exploiting the test bench internal pump and the pilot pump suction flow rate was recreated adopting a flow regulator valve (Valve Q).

Valve 4 was activated for all the test duration in order to avoid the connection between line A and the tank.

Initially valves X, Y and 3 were maintained in the neutral position while a constant flow rate was imposed in the line P. The flow path available to the flow is defined by the red line in Fig.8.11, i.e. it flows through the valve X P→C orifice. Thus the P line pressure is due to this orifice $Q - \Delta p$ characteristic.

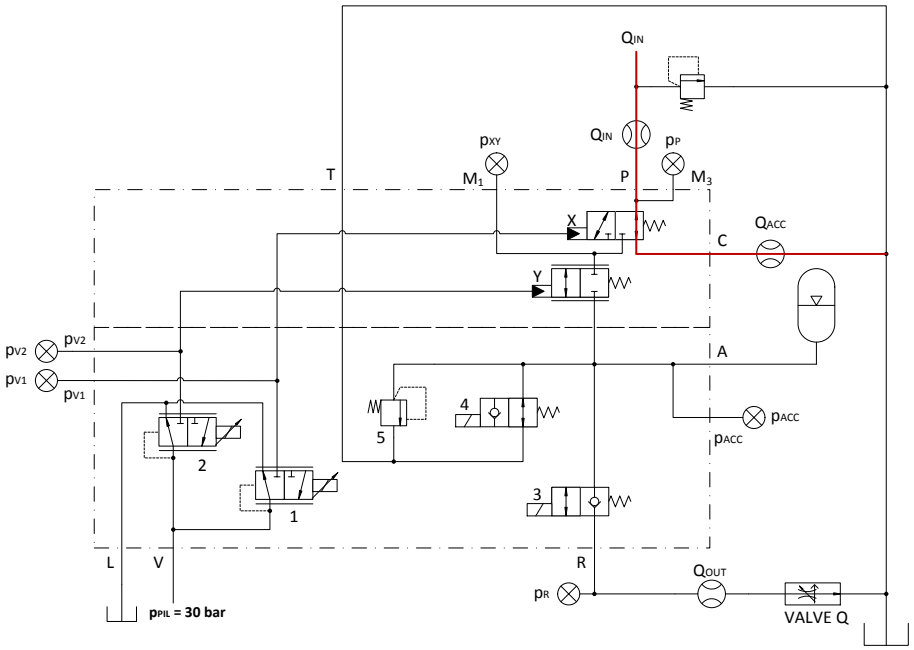

Figure 8.11: HCV Recovery – Reuse Simulation Test ISO Scheme – Initial Phase.

After this initial phase, valve X was set to the P→Y orifice meanwhile valve Y was opened through a ramp, controlling both the (p_{V1-HCV}) and (p_{V2-HCV}) respectively. Once the hydraulic accumulator pressure exceeded the defined minimum pressure level (p_0), defined in

the optimization procedure (Chapter 6), valve 3 was enabled connecting the accumulator line A to the recovery line R. The flow path available for the fluid during this phase, the recovery – reuse phase, is highlighted in red in Fig.8.12.

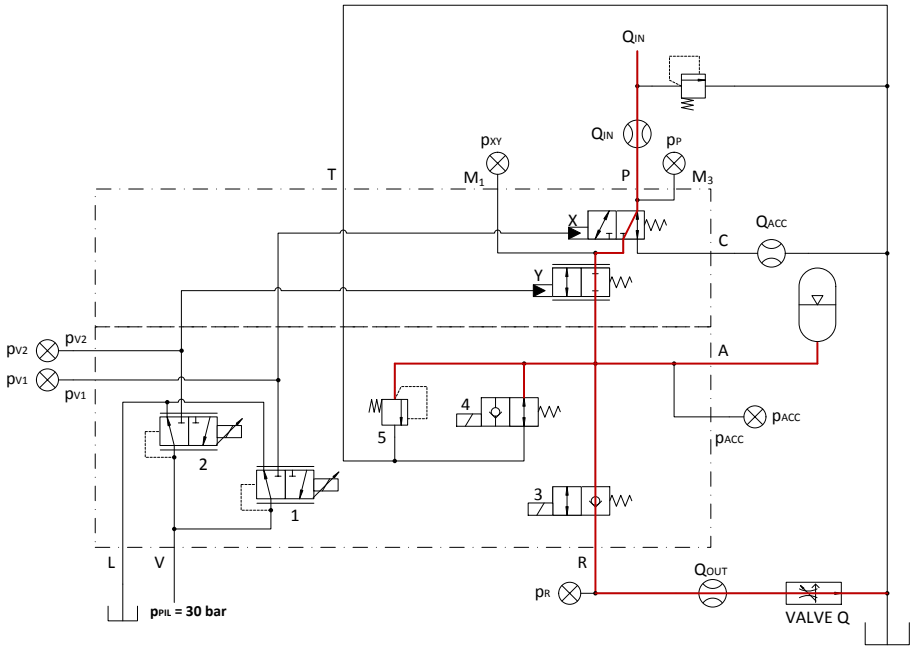

Figure 8.12: HCV Recovery – Reuse Simulation Test ISO Scheme – Recovery – Reuse Phase.

Finally the last performed testing condition concerned the reuse phase only, where valves X and Y were instantaneously set to the neutral position and valve 3 was kept enabled, Fig.8.13. During this phase the accumulator is discharged reusing the storage energy.

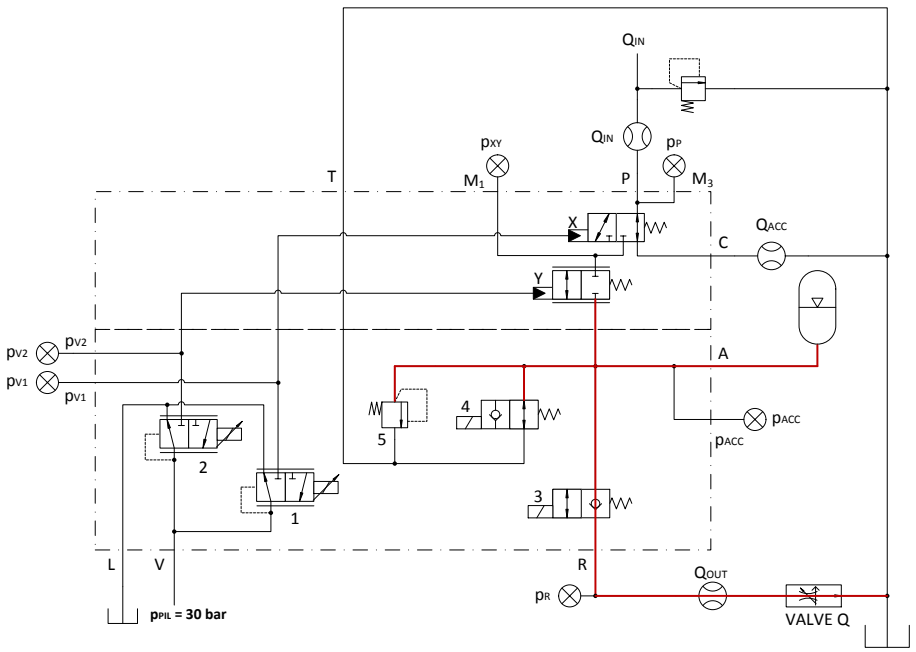

Figure 8.13: HCV Recovery – Reuse Simulation Test ISO Scheme –Reuse Phase.

During the testing phases the inlet flow rates (Q_{IN}), (Q_C), (Q_{OUT}) and the pressures (p_P), (p_{XY}), (p_{ACC}), (p_R), (p_{V1-HCV}) and (p_{V2-HCV}) were measured.

The same operating condition were imposed to the mathematical model of the HCV and accumulator assembly, Fig.8.14, in order to validate the HCV model previously characterized.

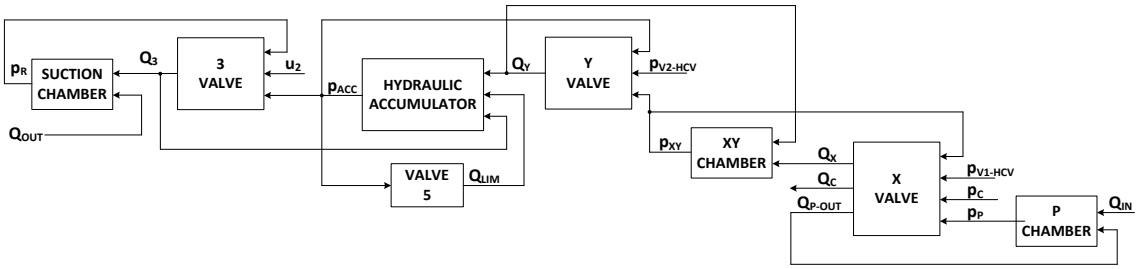

Figure 8.14: Hydraulic accumulator and HCV Assembly Causality Scheme.

The input for the model were the pilot pressures (p_{V1-HCV}) and (p_{V2-HCV}), the inlet and outlet flow rates, (Q_{IN}) and (Q_{OUT}), and the valve 3 command (u_3).

Figure 8.15, Fig.8.16 and Fig.8.17 report the comparison between the experimental (black dashed curve) and the simulation (red curve) of the inlet pressure (p_P), the net accumulator flow rate (Q_{ACC}), defined according (*Eq.8.1*), and the accumulator pressure (p_{ACC}) respectively.

$$Q_{ACC} = Q_{IN} - Q_C - Q_{OUT} \qquad (8.1)$$

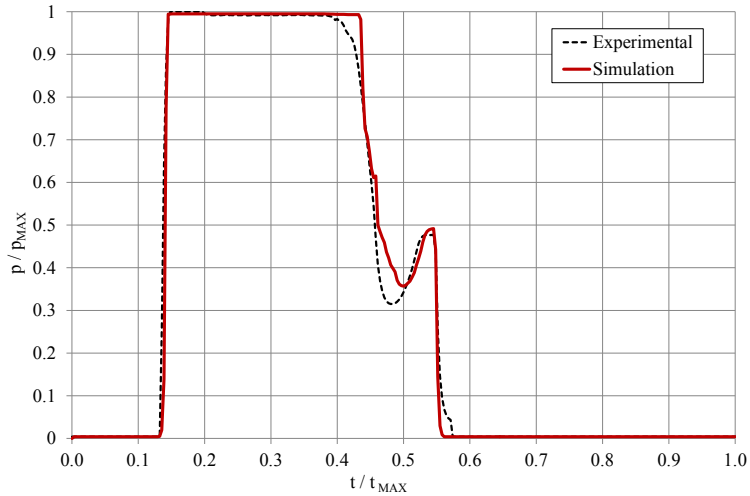

Figure 8.15: Inlet pressure (p_P) Experimental and Numerical Comparison.

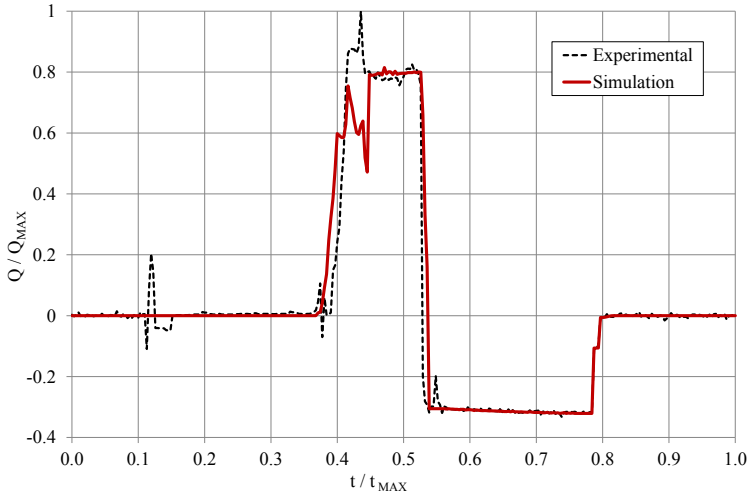

Figure 8.16: Accumulator Net Flow Rate (Q_{ACC}) Experimental and Numerical Comparison.

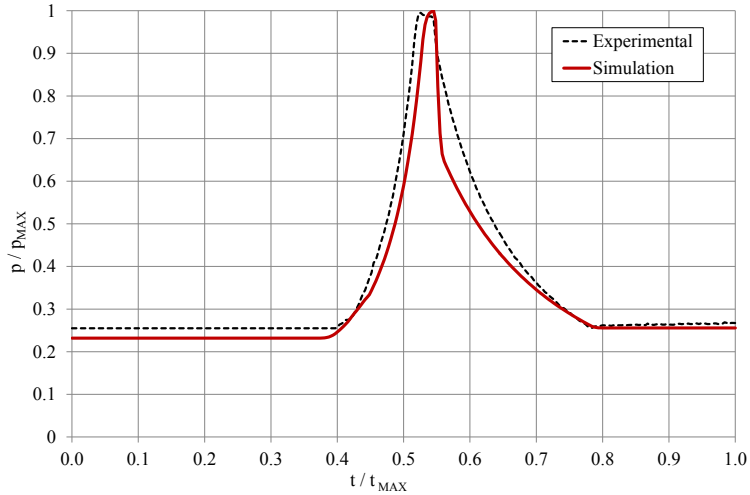

Figure 8.17: Accumulator Pressure (p_{ACC}) Experimental and Numerical Comparison.

The comparison of the results points out that the developed mathematical model of the HCV is able to replicate both the actual functioning of the valve assembly, defining correctly the accumulator net flow rate (Q_{ACC}), and its influence on the hydraulic system, i.e. defining the pressure resistance on the flow (p_P).

8.2 Hybrid Excavator Experimental Activities

In this section the experimental activities carried out on the hybrid excavator are presented and described.

The performed activities are aimed to the validation of the mathematical model of the hybrid excavator, Appendix 7. The validation was focused on both the hydraulic system and the fuel consumption prediction capability. Therefore for the hydraulic system validation the boom down-up cycle was carried out, while the JCMAS working cycle [*3.2*] was performed for the fuel consumption validation.

The excavator hydraulic system was already instrumented as reported in Fig.3.22 in order to acquire the required variables for the mathematical model characterization (Chapter 3) and validation (Chapter 4). Therefore the hybrid excavator was already instrumented too, Fig.8.18.

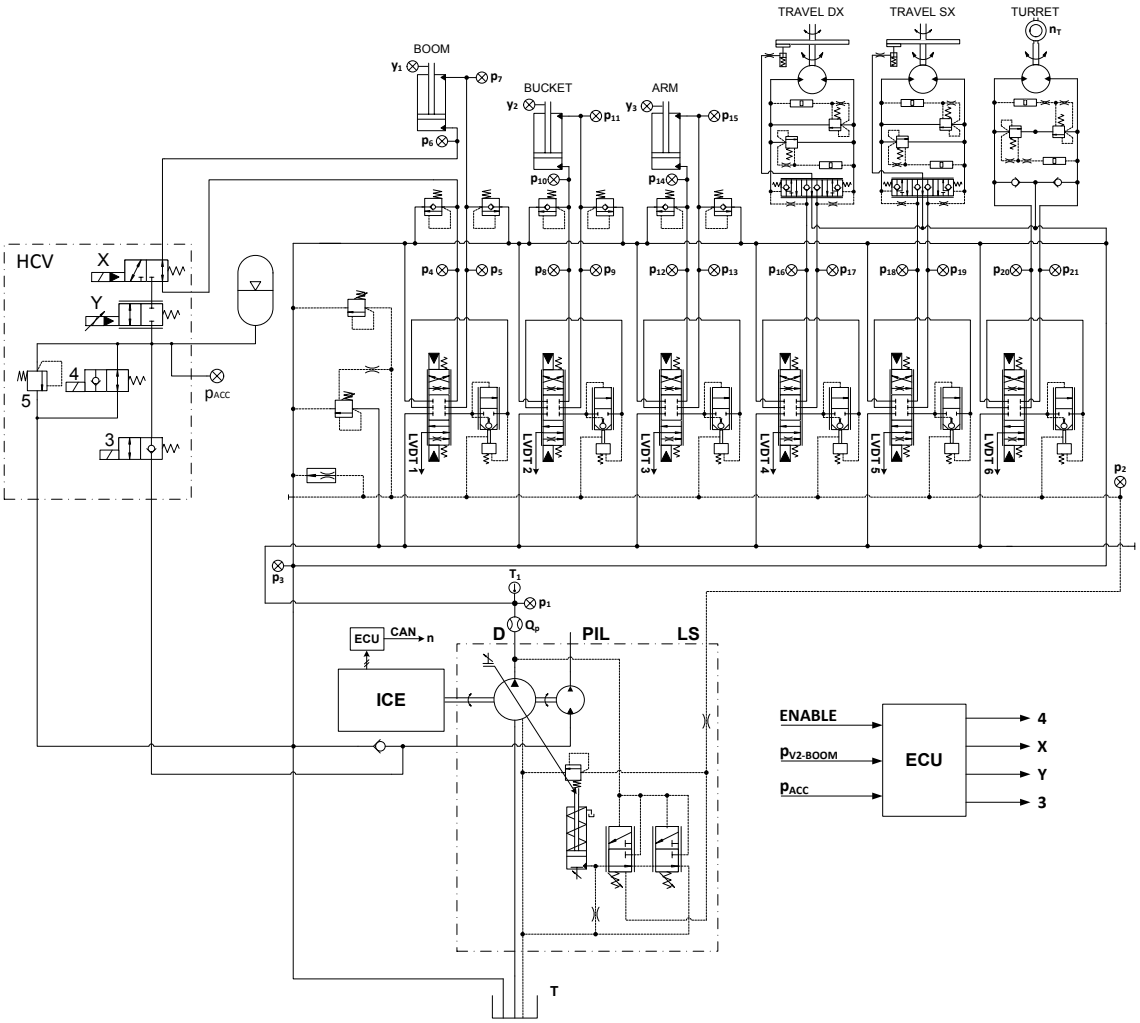

Figure 8.18: Hybrid Excavator System Experimental Setup ISO Scheme.

Figure 8.19 and Fig.8.20 report the photograph of the prototype of the hybrid excavator under investigation.

Figure 8.19: Photograph of the Hybrid Excavator Prototype – Accumulator Side.

Figure 8.20: Photograph of the Hybrid Excavator Prototype – HCV Side.

The same operating conditions of the experimental test were recreated during the simulations, i.e. the same initial position of the front excavation tool, ICE speed and boom main spool displacement were imposed. The control strategy, governing the ERS, was the algorithm defined through the optimization methodology (Chapter 6).

Figure 8.21 reports the comparison between the experimental and the numerical boom actuator linear displacement during the performed boom down-up movements, composed of two movements repetitions, while Fig.8.22 depicts the comparison related to the accumulator experimental and numerical pressures.

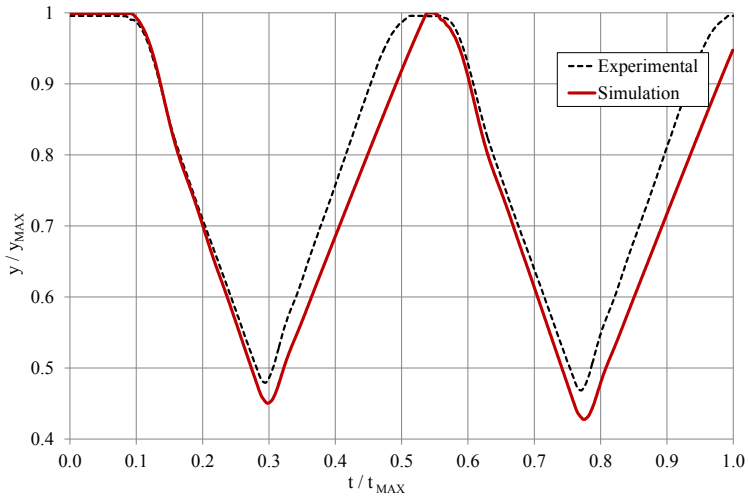

Figure 8.21: Boom Actuator Linear Displacement Experimental and Numerical Comparison – Boom Down-Up.

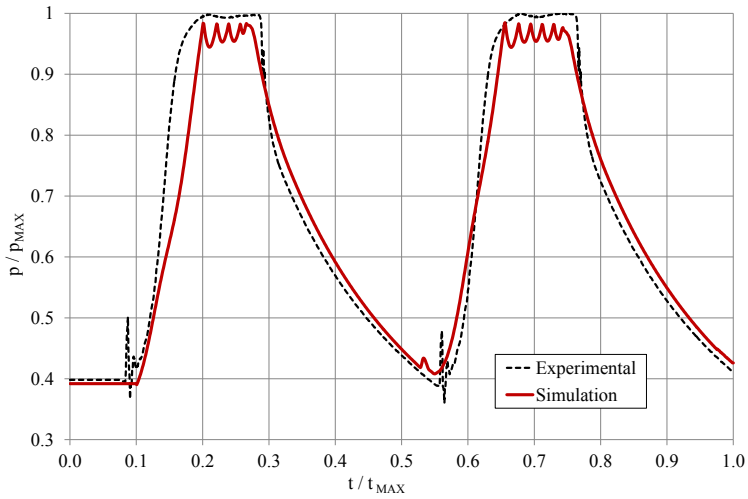

Figure 8.22: Accumulator Pressure (p_{ACC}) Experimental and Numerical Comparison – Boom Down-Up.

From the reported results comparisons, the hybrid excavator mathematical model results match in a very satisfying manner the experimental data validating the model developed for the hybrid version of the machinery for estimation of the hydraulic and mechanical variables.

Concerning the fuel consumption prediction capability of the hybrid model, the comparison between the experimental and the numerical fuel consumption results are reported in Tab.8.6.

Table 8.6: Experimental and Numerical Fuel Consumption Results Hybrid Excavator.				
Symbol	Experimental	U_{95} [%]	Numerical	$\frac{mf_{SIM}-mf_{EXP}}{mf_{EXP}}$ [%]
$\overline{mf_{DIGGING}}$	31.78 [g/cycle]	± 4.63	31.82 [g/cycle]	+0.13
$\overline{mf_{GRADING}}$	10.11 [g/cycle]	± 4.71	10.13[g/cycle]	+0.19
$\overline{mf_{TRAVEL}}$	3.29 [g/m]	± 8.2	3.255 [g/m]	-1.06
$\overline{mf_{IDLING}}$	1331 [g/h]	± 6.2	1330 [g/h]	-0.08
$\overline{mf_{JCMAS}}$	8.35 [l/h]	± 2.88	8.36 [l/h]	+0.12

Being the percentage differences between numerical and experimental fuel consumption ($\frac{mf_{SIM}-mf_{EXP}}{mf_{EXP}}$) always within the combined uncertainty limits experimentally defined for each operating mode, as for the standard machinery the hybrid excavator model fuel consumption prediction capability is confirmed.

8.3 Discussion

In this chapter the experimental activities of the hybrid excavator under investigation have been presented and described in detail.

In the first section the HCV model has been characterized and validated on the basis of experimental results obtained during test bench activities, while in the second section of this chapter the mathematical model of the complete excavator with the proposed ERS, i.e. the hybrid machinery, has been validated concerning both the hydraulic and mechanical variables calculation and the fuel consumption estimation.

The validated model of the hybrid excavator will be exploited to perform energy analyses of the system and evaluate other effective solution for fuel saving improvements.

Chapter 9: **Proposed Energy Saving Solutions Comparison**

In this chapter the proposed energy saving solutions for LS hydraulic systems (Chapter 5), applied to the excavator under investigation, will be analysed in detail taking into account the energy dissipations along the hydraulic systems and the fuel saving compared to the standard machinery layout. Afterwards, combining these solutions a novel hydraulic hybrid excavator architecture will be presented.

9.1 Energy Analysis of the Proposed Energy Saving Solutions

In Chapter 5 the detailed energy analyses of the standard hydraulic layout of the excavator under investigation have been conducted, for both the trench digging and the grading working cycles, in order to evaluate the energy dissipations and to propose some possible solutions to be adopted in order to improve the machinery efficiency.

In this section the energy analyses concerning the proposed solutions will be reported and discussed in detail pointing out their advantages and disadvantages in order to evaluate possible implementations.

9.1.1 Dual Pump LS System

In this sub-section are reported the energy analyses concerning the proposed dual pump LS system, Fig.5.17 (Chapter 5), for both the configuration exploiting two LS units having the same size of the original one, named 2LS, and the configuration mounting two LS units having a reduced size compared to the original according to the consideration reported in Chapter 5, named 2LSR.

Figure 9.1 and Fig.9.2 refer to the trench digging cycle and the grading cycle for the 2LS system configuration.

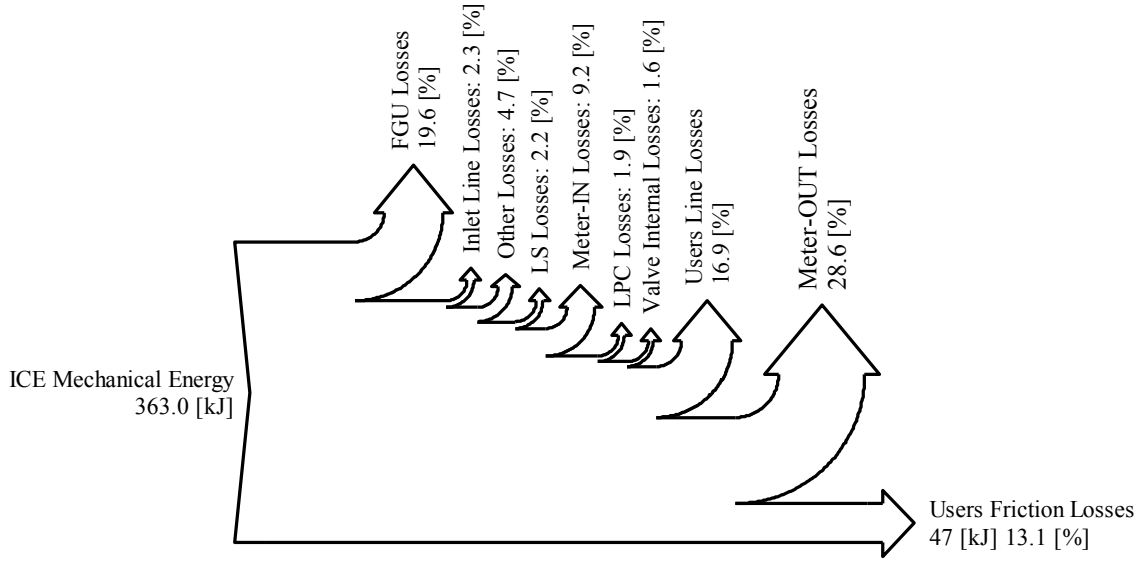

Figure 9.1: Sankey Diagram of the Trench Digging Cycle – 2LS Configuration.

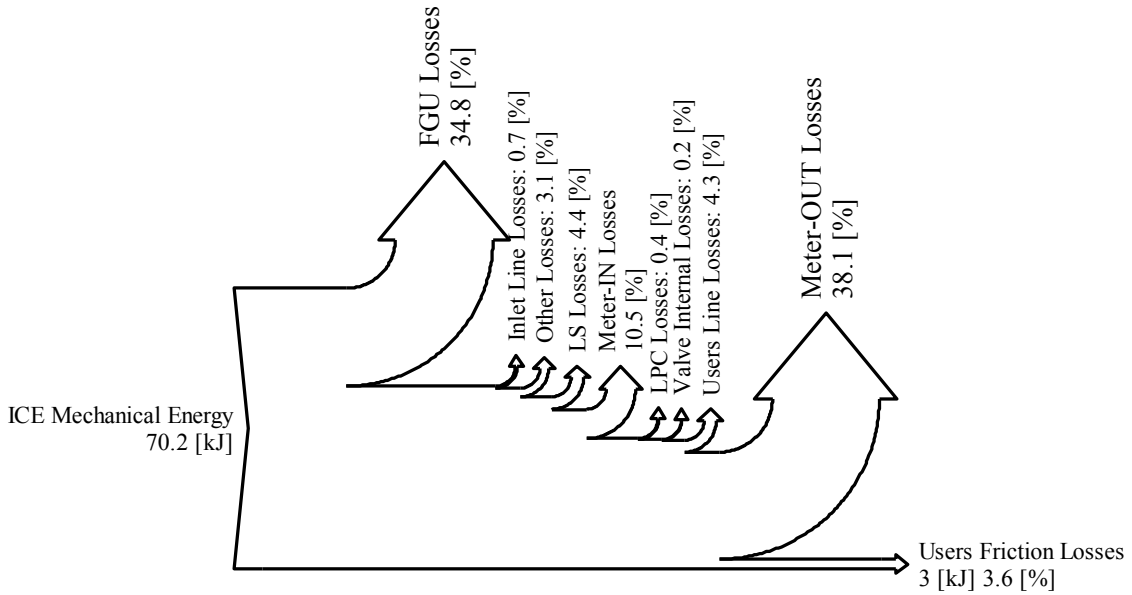

Figure 9.2: Sankey Diagram of the Grading Cycle – 2LS Configuration.

Referring to the reported energy flow diagrams, the 2LS system configuration on one hand reduces the energy dissipation in the LPCs: more than the 80% during the trench digging cycle and more than the 95% during the grading cycle compared to the standard system layout. On the other hand the energy dissipations related to the FGU increase of about 10% during the trench digging cycle and 20% during the grading cycle as a consequence of the usage of two LS pumps instead of only one. The others energy losses remain almost constant referring to the standard system layout.

Figure 9.3 and Fig.9.4 refer to the same cycles for the 2LSR system configuration.

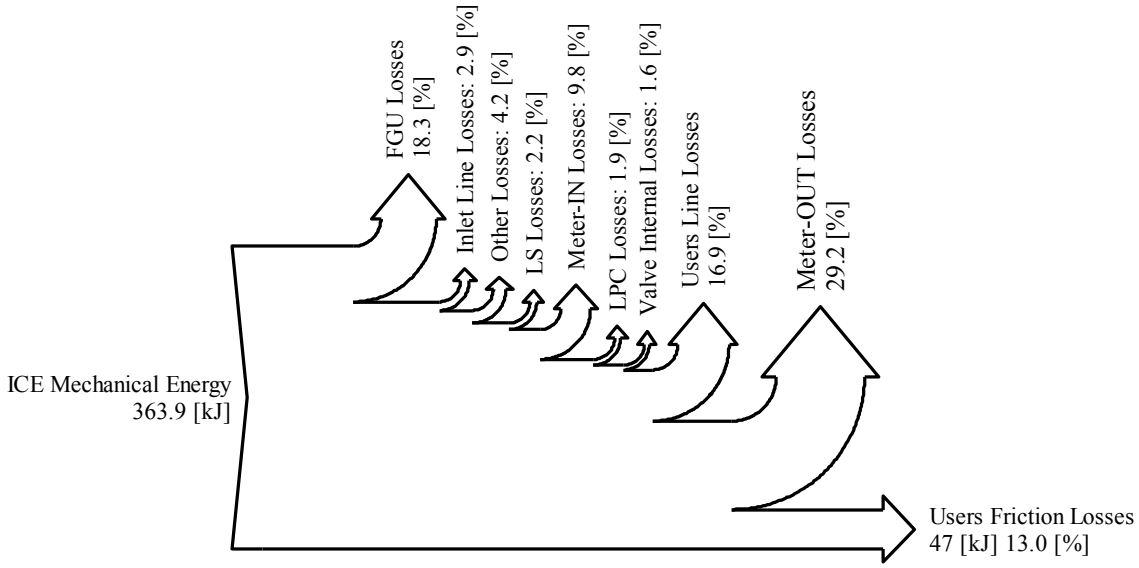

Figure 9.3: Sankey Diagram of the Trench Digging Cycle – 2LSR.

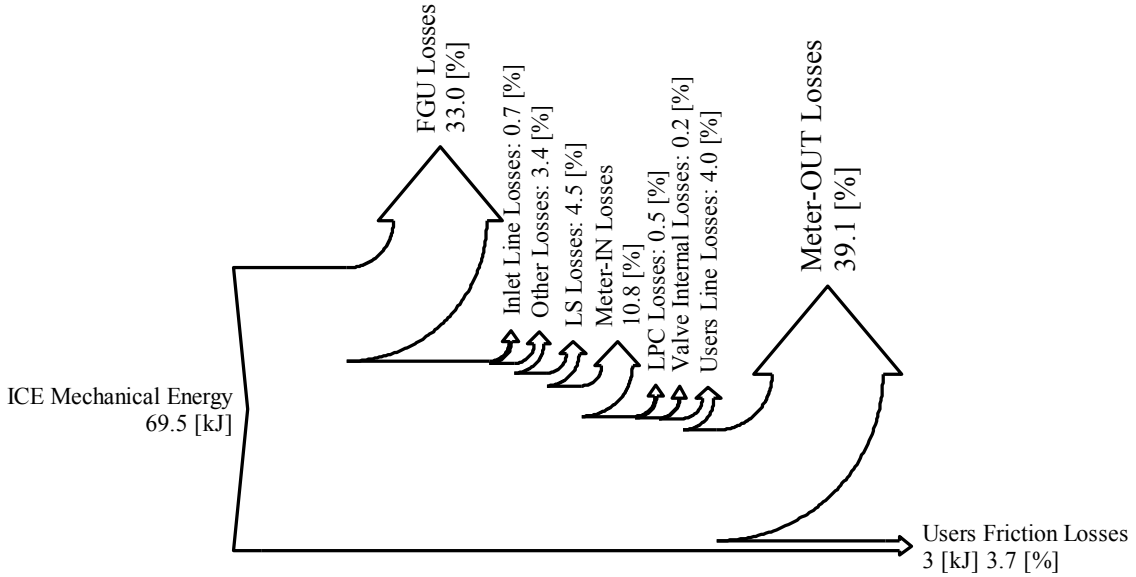

Figure 9.4: Sankey Diagram of the Levelling Cycle – 2LSR.

This configuration, as described in Chapter 5, takes advantage of two variable displacement units with a reduced size compared to the 2LS system configuration.

The analysis of the reported energy flow diagrams of the two configurations points out no further energy saving in terms of required mechanical energy, which remains almost the same during the cycles.

The energy dissipations related to the FGU decrease both during the trench digging cycle and the grading cycle, while the meter-OUT losses increases in the 2LSR configuration compared to the 2LS one, even if the performed working cycles are the same, as confirmed by the actuators position comparison reported in Fig.9.5.

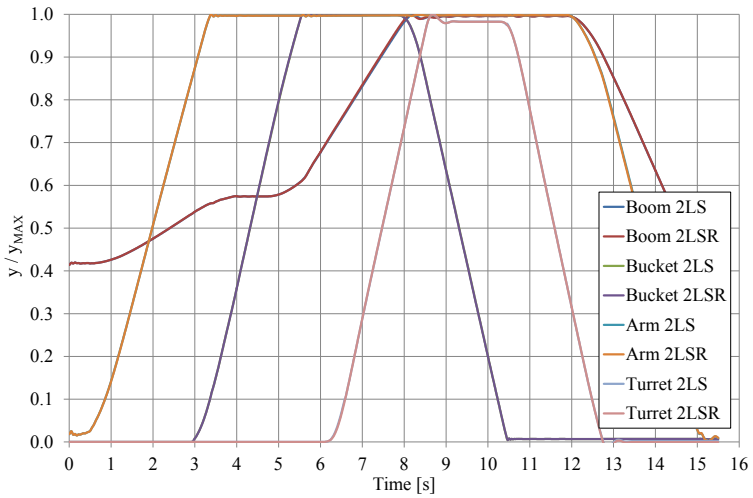

Figure 9.5: 2LS and 2LSR Actuators Positions Comparison – Trench Digging Cycle.

The justification is due to a higher meter-IN differential pressure (dp_{LS}) in the 2LSR system than the 2LS system, Fig.9.6, as a consequence in the usage of two pumps with a lower displacement which require a different TL setting[31]. Therefore in the 2LSR on one hand the main spools positions of the activated users are reduced in order to accomplish the required tasks, but on the other hand the meter-OUT losses are increased than in the 2LS system configuration.

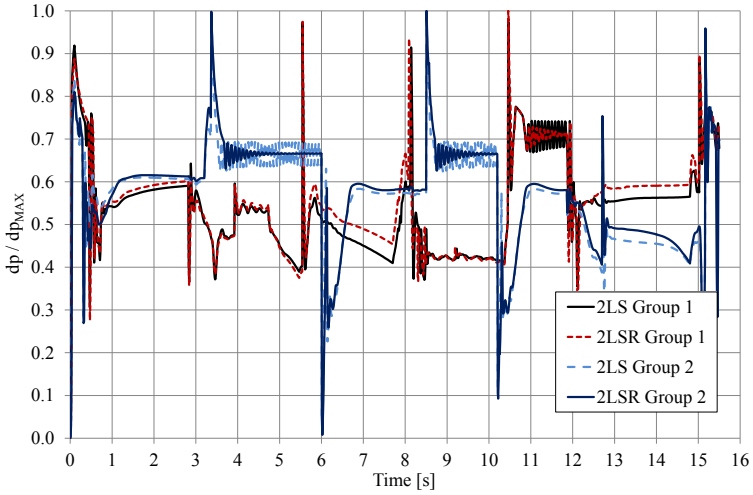

Figure 9.6: 2LS and 2LSR dp_{LS} Comparison – Trench Digging Cycle.

In conclusion, the 2LSR system layout has the same advantages of the 2LS configuration, regarding the hydraulic system users division in two users groups, thus reducing the LPCs energy losses. Moreover, utilizing two hydraulic pumps with a lower displacement additional advantages in terms of lower investment cost for the FGU can be achieved.

Table 9.1 and Tab.9.2 report the fuel saving percentage of the 2LS and 2LSR systems compared to the standard configuration.

Table 9.1: Numerical Fuel Consumption Reductions – 2LS System.

Cycle	Standard System	2LS System	$\frac{mf_{2LS}-mf_{STD}}{mf_{STD}}$ [%]
Trench Digging	34.12 [g/cycle]	31.87 [g/cycle]	-6.59
Grading	10.53 [g/cycle]	9.89[g/cycle]	-6.07
Travelling	3.26 [g/m]	3.37[g/m]	+3.37
Idling	1331.09 [g/h]	1348.12 [g/h]	+1.28
JCMAS	8.77 [l/h]	8.35 [l/h]	-4.78

[31] The two FGUs have not the same torque limiters settings even if the maximum FGU torque is the same.

Table 9.2: Numerical Fuel Consumption Reductions – 2LSR System.			
Cycle	Standard System	2LSR System	$\frac{mf_{2LSR}-mf_{STD}}{mf_{STD}}$ [%]
Trench Digging	34.12 [g/cycle]	31.88 [g/cycle]	-6.56
Grading	10.53 [g/cycle]	9.89[g/cycle]	-6.07
Travelling	3.26 [g/m]	3.47[g/m]	+6.44
Idling	1331.09 [g/h]	1347.8 [g/h]	+1.25
JCMAS	8.77 [l/h]	8.39 [l/h]	-4.33

9.1.2 Reduced Pump Margin LS System

Figure 9.7 and Fig.9.8 report the energy flow diagrams of the trench digging cycle and the grading cycle related to the reduced pump margin LS system configuration.

The energy saving advantages introduced by this configuration are related to the meter-IN and meter-OUT energy dissipations reduction.

In fact, the differential pressure, or margin pressure, (dp_{LS}), reduction on one hand reduces meter-IN losses (-25% in the trench digging cycle and -33% in the grading cycle), but on the other hand causes minor flow rates to the users[32].

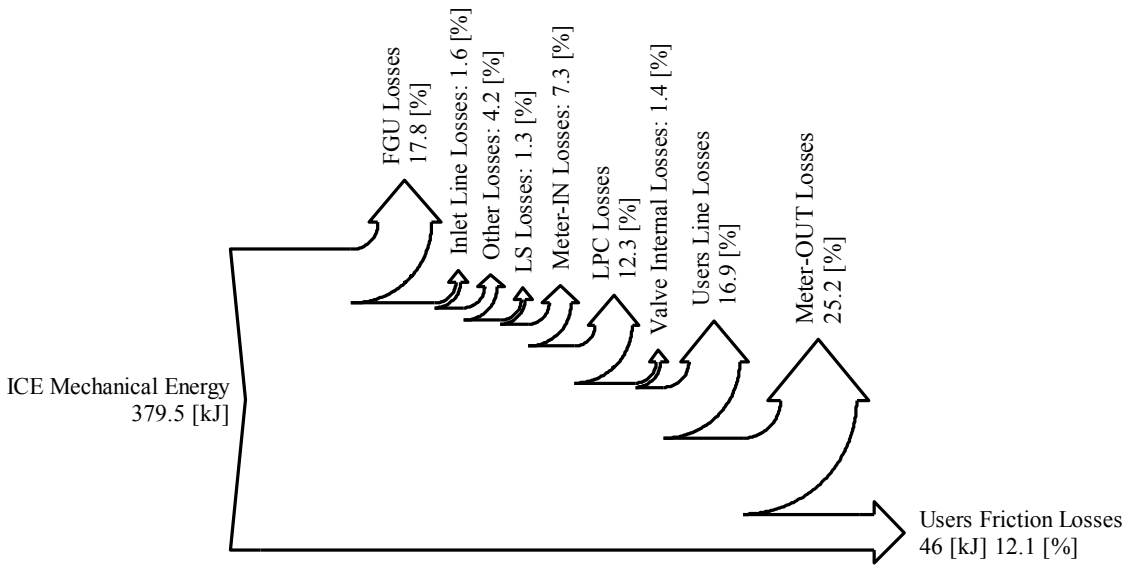

Figure 9.7: Sankey Diagram of the Trench Digging Cycle – Reduced LS.

[32] This statement is true only having the same flow area, i.e. the same spool position.

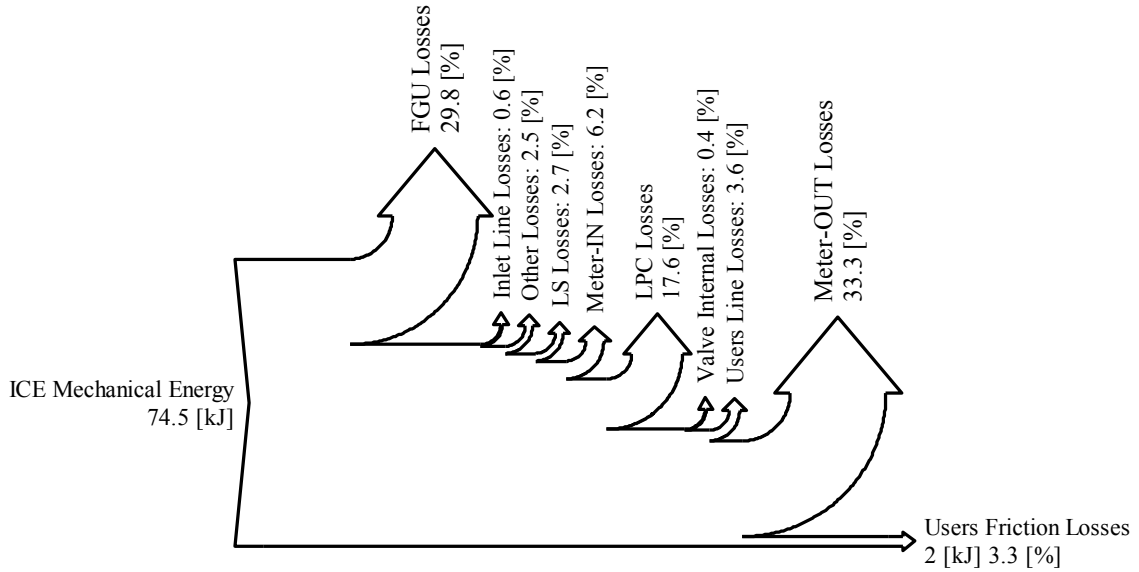

Figure 9.8: Sankey Diagram of the Levelling Cycle – Reduced LS.

Consequently, in order to respect the actuators positions in the simulated working cycles, the operator models define higher main spool strokes, thus increasing the flow rates to the users actuators and reducing the meter-OUT losses (-12% in the trench digging cycle and -11% in the grading cycle).

Table 9.3 reports the fuel saving percentage of the reduced LS system (RLS) compared to the standard configuration.

Table 9.3: Numerical Fuel Consumption Reductions – Reduced LS System.

Cycle	Standard System	RLS System	$\frac{mf_{RLS}-mf_{STD}}{mf_{STD}}$ [%]
Trench Digging	34.12 [g/cycle]	32.58 [g/cycle]	-4.51
Grading	10.53 [g/cycle]	10.07[g/cycle]	-4.37
Travelling	3.26 [g/m]	3.15 [g/m]	-3.37
JCMAS	8.77 [l/h]	8.40 [l/h]	-4.21

9.1.3 Optimized Flow Areas System

The energy flow diagrams of the optimized flow areas (OFA) system related to the trench digging and the grading cycles are reported in Fig.9.9 and Fig.9.10 respectively.

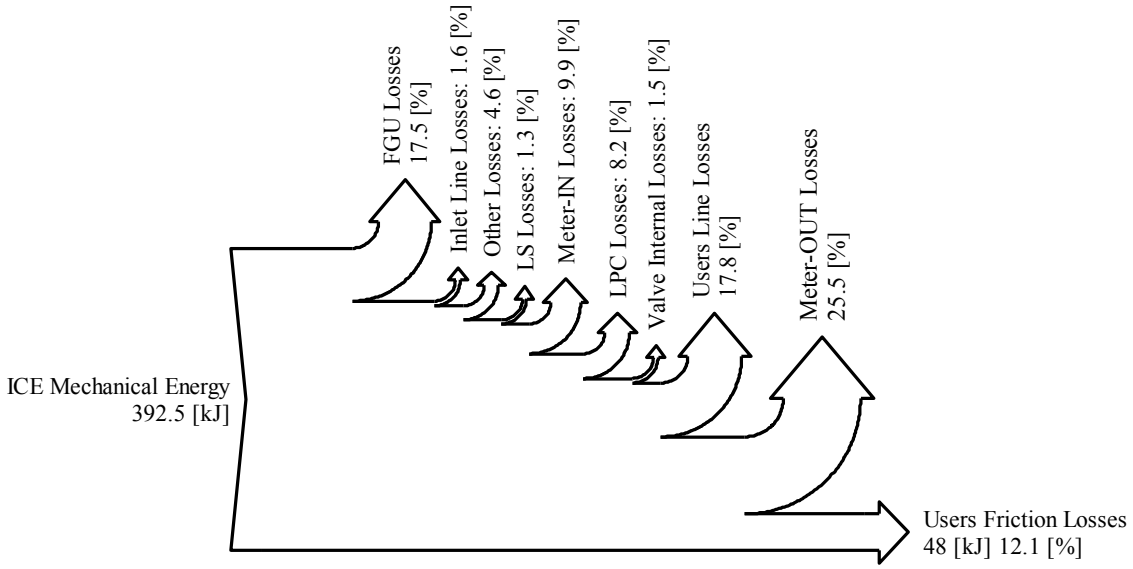

Figure 9.9: Sankey Diagram of the Trench Digging Cycle – OFA.

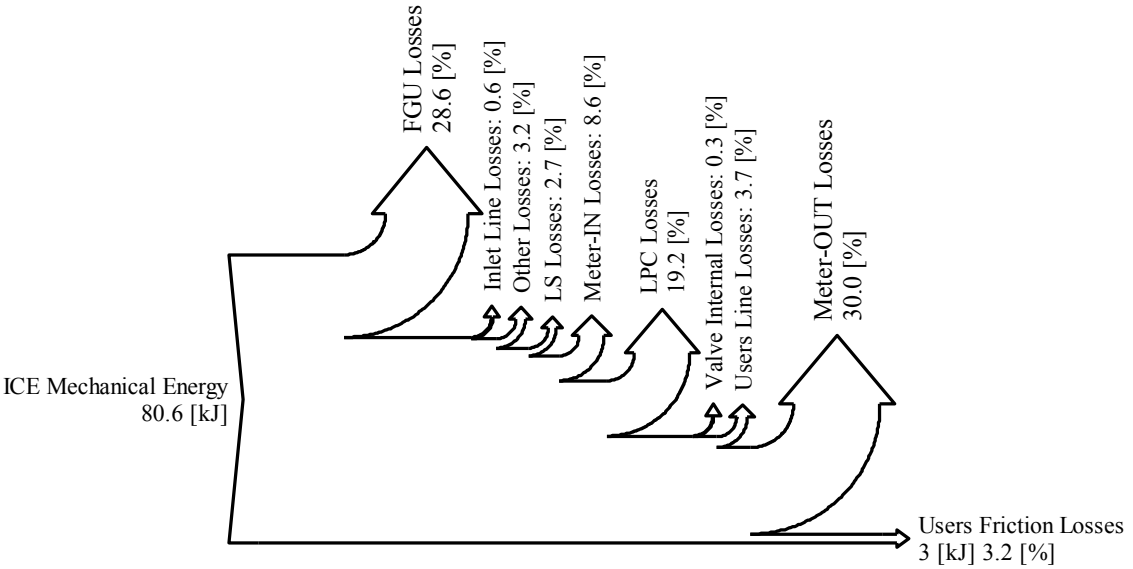

Figure 9.10: Sankey Diagram of the Levelling Cycle – OFA.

The optimization of the outlet orifices of the boom (during the connection P→A, B→T), arm (during the connection P→B, A→T) and bucket (during the connection P→B, A→T) introduces energy dissipation reduction in the meter-OUT and the LPCs. During the connections listed the loads acting on the hydraulic actuator are resistant.

Optimizing the meter-OUT flow areas the users pressures decrease as well as the energy dissipations (-9.5% in the trench digging cycle and -14% in the grading cycle), while the LPCs energy losses are reduced during parallel operations (-27.4% in the trench digging cycle while in the grading cycle no reduction).

Table 9.4 reports the fuel saving percentage of the optimized flow area system compared to the standard configuration.

Table 9.4: Numerical Fuel Consumption Reductions – Optimized Flow Area System.

Cycle	Standard System	OFA System	$\frac{mf_{OFA}-mf_{STD}}{mf_{STD}}$ [%]
Trench Digging	34.12 [g/cycle]	33.13 [g/cycle]	-2.90
Grading	10.53 [g/cycle]	10.26[g/cycle]	-2.56
JCMAS	8.77 [l/h]	8.58 [l/h]	-2.16

9.1.4 Boom Energy Recovery System

Figure 9.11 and Fig.9.12 represent the energy flow diagrams of the excavator with the boom ERS of the trench digging and the grading cycles respectively.

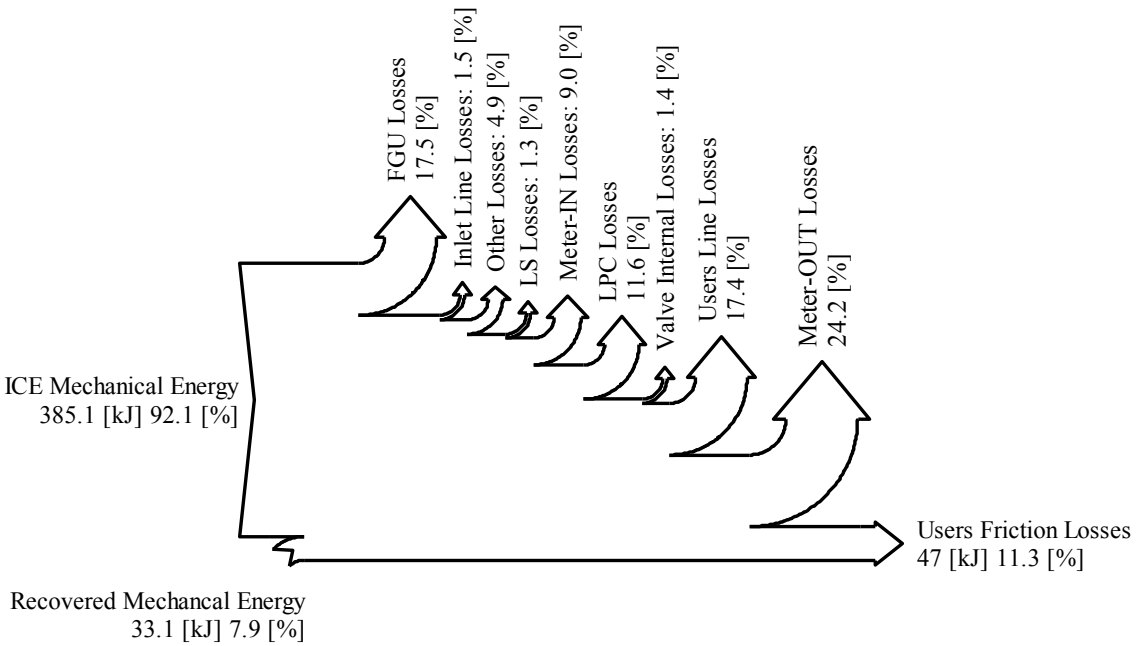

Figure 9.11: Sankey Diagram of the Trench Digging Cycle – Boom ERS.

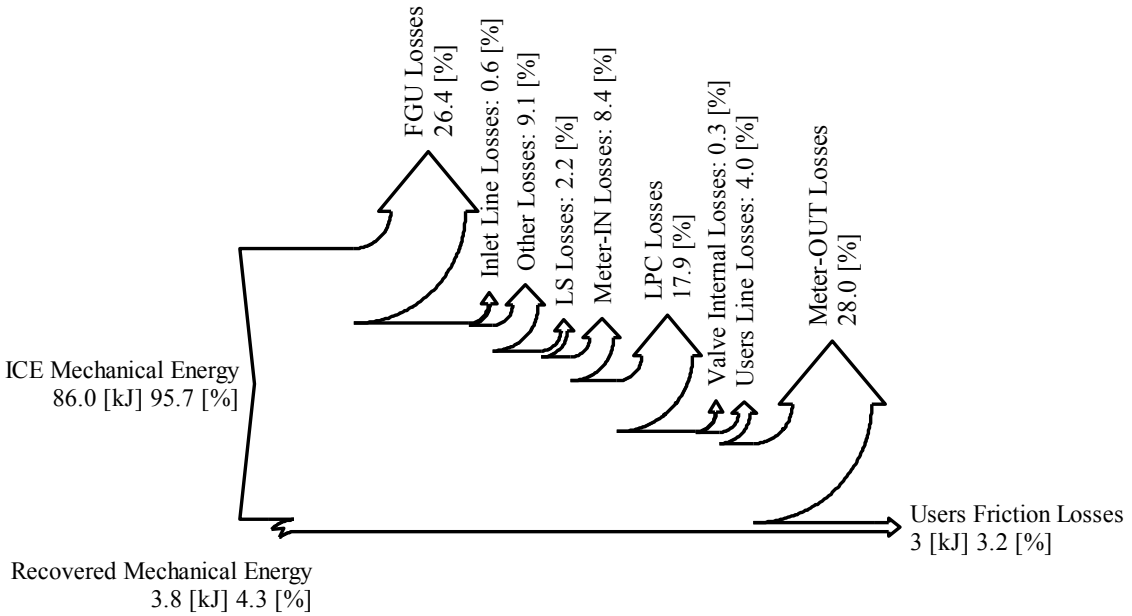

Figure 9.12: Sankey Diagram of the Levelling Cycle – Boom ERS.

The introduction of the proposed ERS in the standard hydraulic system allows both the energy recovery and reuse from the boom actuator during the lowering phase as well as its meter-OUT energy dissipations reduction (-8.5% in the trench digging cycle and -10.5% in the grading cycle) due to the lower outlet pressure imposed by the HCV in the first part of the actuator movement.

The advantages in the meter-OUT, in term of energy saving, are however countered by the increasing of the LPCs energy losses (+9% in the trench digging cycle and +4% in the grading cycle).

These considerations concerning the hydraulic system with the proposed ERS point out the advantage of combining the ERS solution with the other energy saving architectures and solutions in order to maximize the fuel saving.

Table 9.5 reports the fuel saving percentage of the excavator including the boom ERS compared to the standard layout.

Table 9.5: Numerical Fuel Consumption Reductions – ERS.

Cycle	Standard System	ERS	$\frac{mf_{ERS}-mf_{STD}}{mf_{STD}}$ [%]
Trench Digging	34.12 [g/cycle]	32.74 [g/cycle]	-4.04
Grading	10.53 [g/cycle]	10.24[g/cycle]	-2.75
JCMAS	8.77 [l/h]	8.52 [l/h]	-2.85

9.2 Hydraulic Hybrid Excavator

In this section the energy analyses concerning the proposed hydraulic hybrid excavator concept will be reported and discussed in detail.

The previous section pointed out the advantages and the disadvantages of the energy saving investigated solutions. Each solution has pointed out advantages in term of energy saving compared to the standard excavator system.

The dual pump systems (2LS and 2LSR) reduce considerably the LPCs energy dissipations while the reduced pump margin LS system the meter-IN ones. The meter-OUT energy losses are decreased by the optimized flow area system, the ERS and in part even from the other solutions.

The hydraulic system architecture of the proposed hydraulic hybrid excavator concept combines the 2LSR, the reduced pump margin, the optimized flow area and the ERS solutions in order to maximize the fuel saving. Figure 9.13 reports the simplified ISO scheme of the hybrid machine.

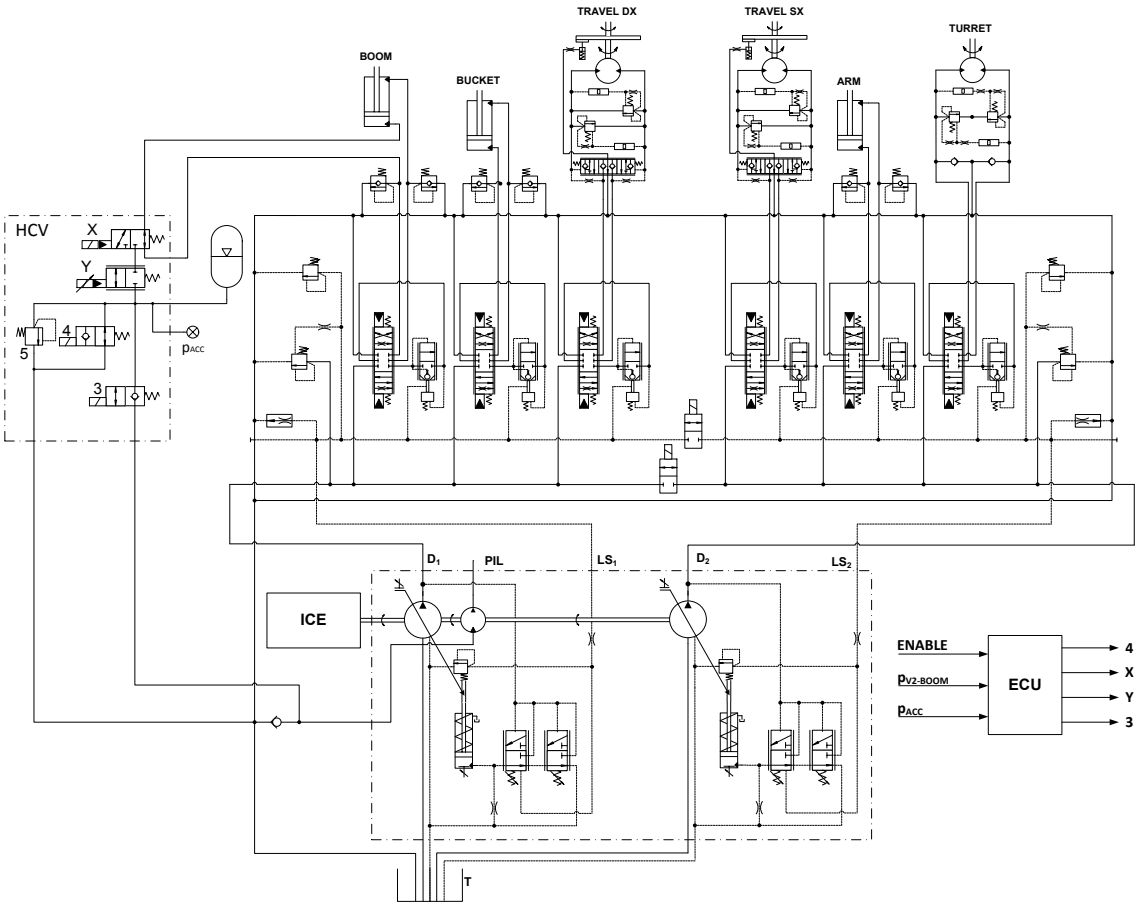

Figure 9.13: Hydraulic Hybrid Excavator Concept (ES85ZT-H) Simplified ISO Scheme.

Figure 9.14 and Fig.9.15 represent the hybrid excavator energy flow diagrams during both the trench digging and the grading cycles respectively.

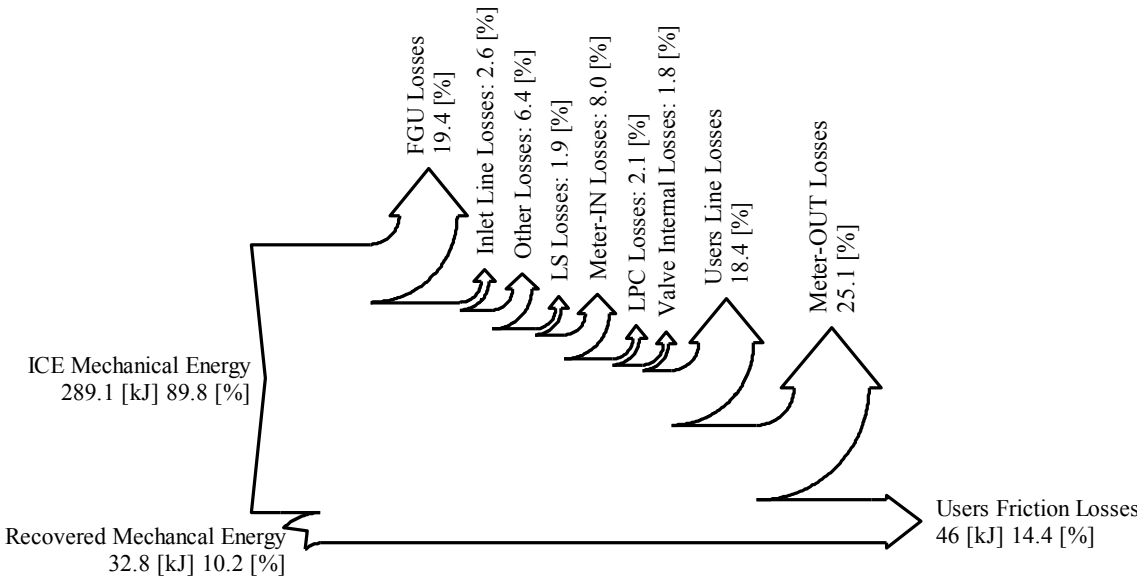

Figure 9.14: Sankey Diagram of the Trench Digging Cycle – ES85ZT-H.

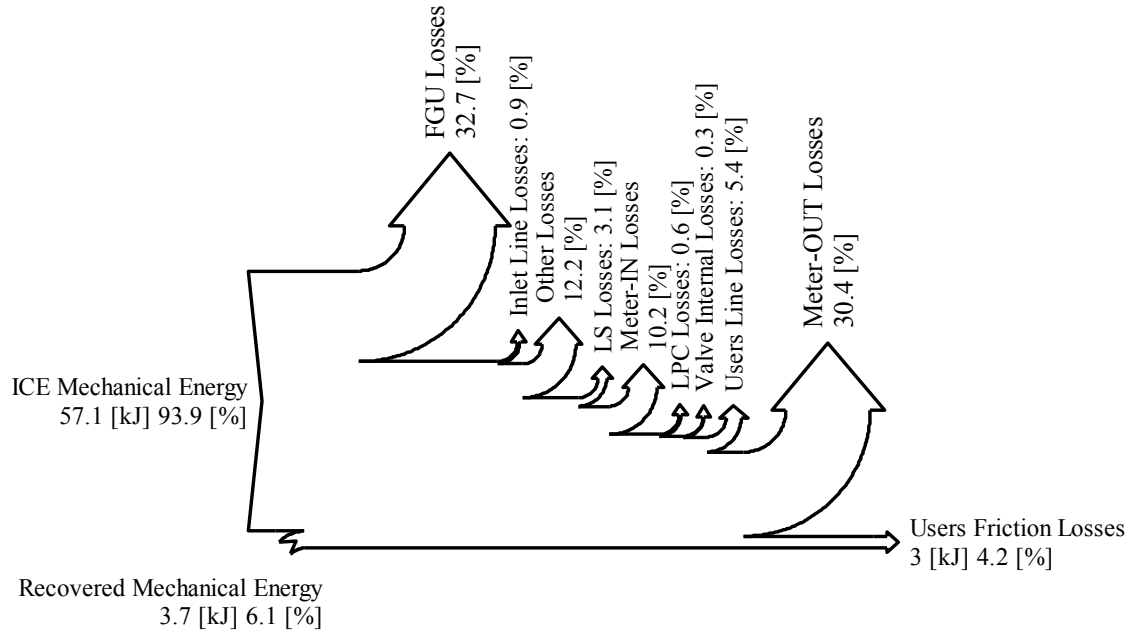

Figure 9.15: Sankey Diagram of the Levelling Cycle – ES85ZT-H.

The energy dissipations in the meter-IN, the LPC and the meter-OUT orifices have been reduced of the 30%, 85% and 27% during the trench digging and of the 10.4%, 97.6% and 34% during the grading cycles compared to the standard machinery.

Finally Tab.9.6 reports the fuel saving percentage of the hydraulic hybrid excavator concept (ES85ZT-H) compared to the standard configuration.

Table 9.6: Numerical Fuel Consumption Reductions – ES85ZT-H.

Cycle	Standard System ES85ZT	Hybrid System ES85ZT-H	$\frac{mf_{ES85ZT-H} - mf_{STD}}{mf_{STD}}$ [%]
Trench Digging	34.12 [g/cycle]	28.73 [g/cycle]	-15.79
Grading	10.53 [g/cycle]	9.35[g/cycle]	-11.21
Travelling	3.26 [g/m]	3.47[g/m]	+6.44
Idling	1331.09 [g/h]	1347.8 [g/h]	+1.25
JCMAS	8.77 [l/h]	7.81 [l/h]	-10.95

Conclusions

In this Ph.D. thesis a numerical and experimental study of energy saving solutions for mobile hydraulic machinery has been presented and described in detail.

A dedicated and detailed literature review (Chapter 1) has pointed out many different solutions for the energy saving in mobile hydraulic systems, from new controlling methods to novel system architectures.

A middle size excavator (9000 kg) has been selected as the case study for the research project. This kind of machinery is typically equipped with LS hydraulic system, especially in the European market. Therefore the conducted studies have been focused on energy saving solution for LS hydraulic systems.

In order to compare and evaluate the proposed energy saving solutions, the mathematical model of the machinery under investigation has been developed (Chapter 2) and validated (Chapter 4) on the basis of the experimental results obtained on both test bench and on the field activities (Chapter 3).

Once validated the mathematical model of the excavator, being confident of the simulations results, detailed energy analyses (Chapter 5) have been conducted, on the reference working cycles (JCMAS), in order to evaluate the energy dissipations in the hydraulic system and to propose energy saving solutions.

From the performed analysis on the LS system of the excavator under investigation some very promising energy saving solutions have been defined:

- the dual LS system (2LS);
- the reduced pump margin system (RLS);
- the optimization of the meter-OUT flow areas (OFA);
- the introduction of an energy recovery system (ERS).

Each of the proposed solution has pointed out advantages in term of energy saving as well as some related disadvantages, from a profound system architecture modification to dedicated control strategies definition.

In fact, considering ERSs their effectiveness, i.e. their energy saving capability, strongly depends on both their control, components dimensions and even to the system architecture.

For these reasons, a parameters optimization on the proposed ERS layout and the definition of the optimal control strategy have been performed taking advantages of the DP algorithm in order to maximise the energy saving percentage (Chapter 6).

A prototype of the ERS has been realized and inserted in the excavator (Chapter 7) and dedicated experimental activities both on test bench and on the field have been conducted (Chapter 8). The comparison between the standard machinery and the prototype with the ERS, on the JCMAS working cycle, pointed out a fuel saving of about -3% and up to -4.5% in the trench digging cycle, confirming the predicted percentage with the mathematical models.

The fuel saving related to the introduction of the ERS could be further increased modifying the system architecture in order to avoid LPC energy dissipation during parallel operations, which is the greatest disadvantage of the standard LS architectures.

From the energy analyses conducted with the aid of the mathematical models of the proposed energy saving solutions (Chapter 9) the following fuel saving percentage on the JCMAS cycle have been obtained:

- -4.8% with 2LS;
- -4.2% with RLS;
- -2.1% with OFA;
- -2.85% with ERS.

Combining the proposed solutions a novel hydraulic hybrid excavator architecture has been defined and a fuel saving up to 11% and 16% have been pointed out on the JCMAS and the trench digging cycle respectively.

In the future, the developed and validated mathematical models will be exploited for the definition of other ERS architectures, even of the electric type, and most sophisticated control strategies.

Dott. Eng. Luca Riccò

Appendix

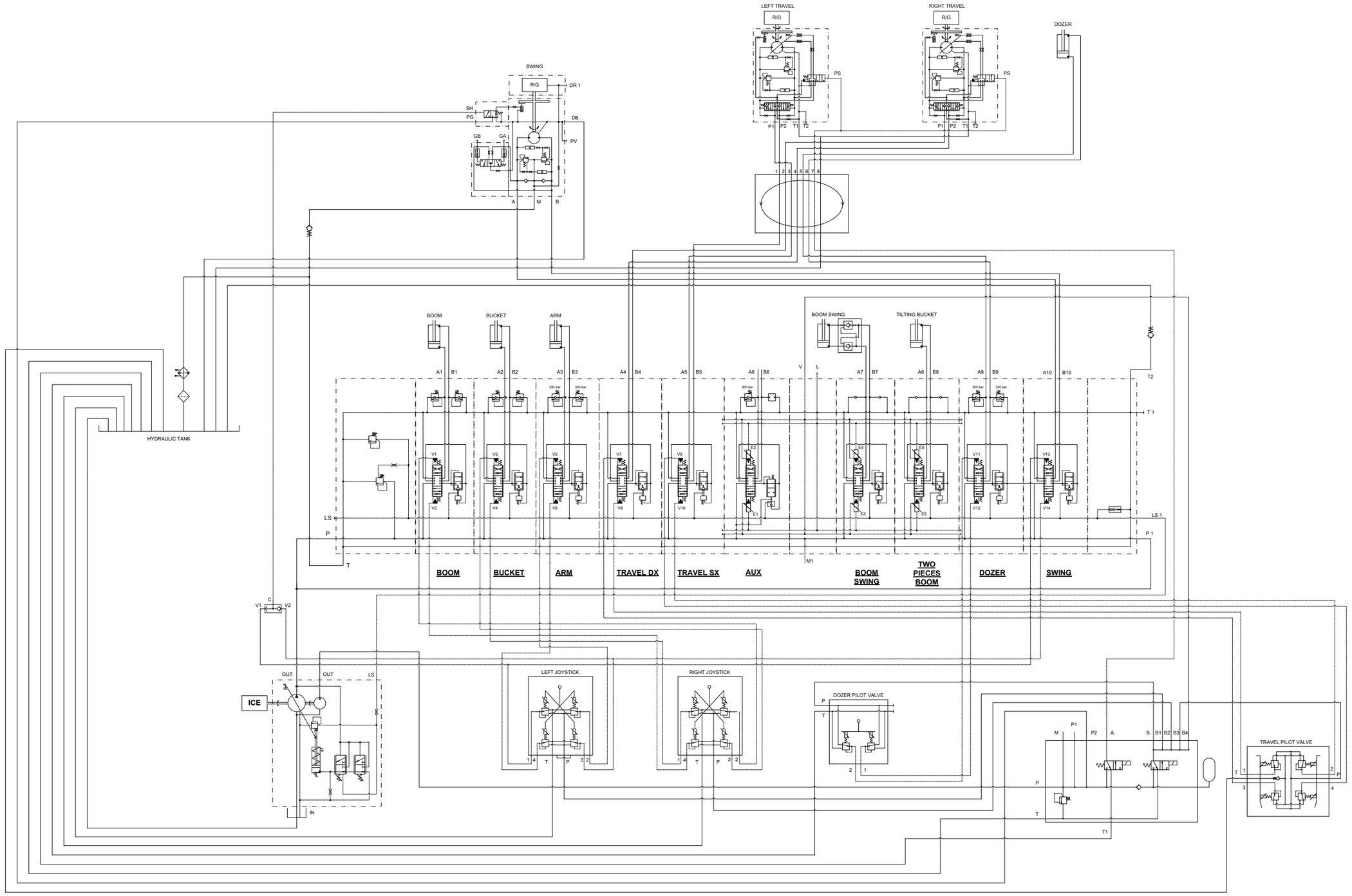

Appendix 1: ES85ZT Hydraulic System ISO Scheme.

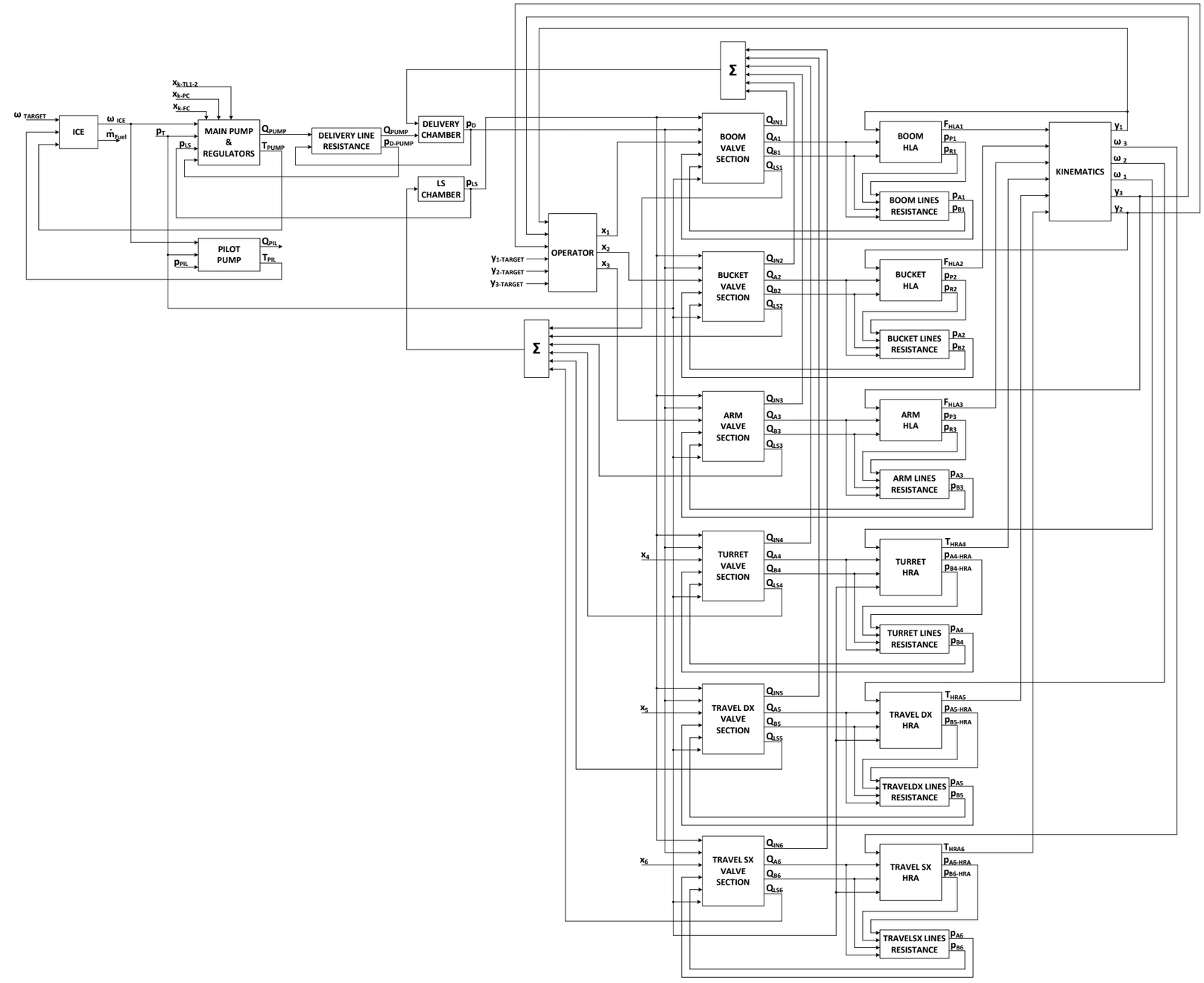

Appendix 2: ES85ZT Direct Causality Scheme.

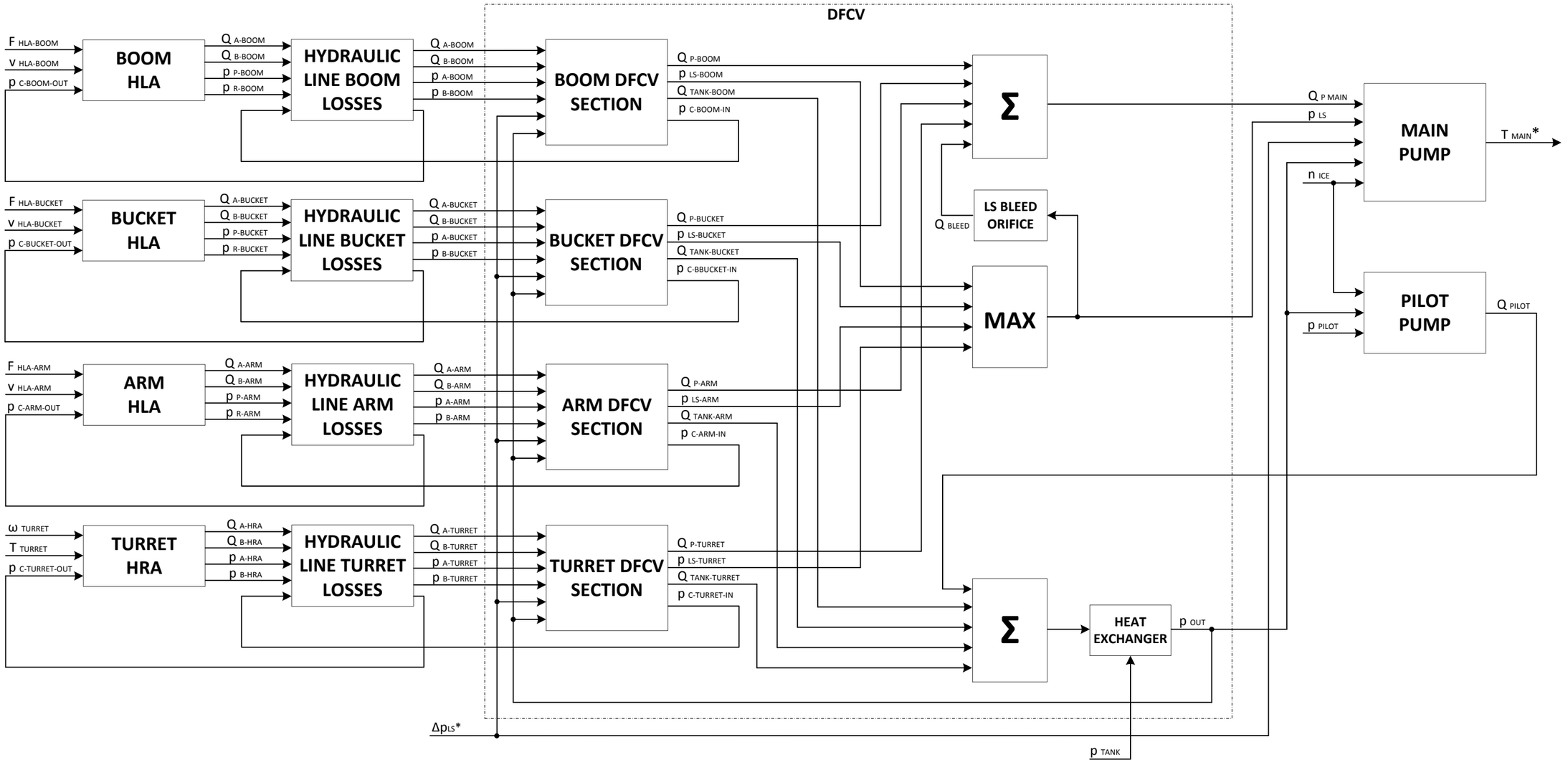

Appendix 3: Torque Limiter Inverse Causality Model Scheme.

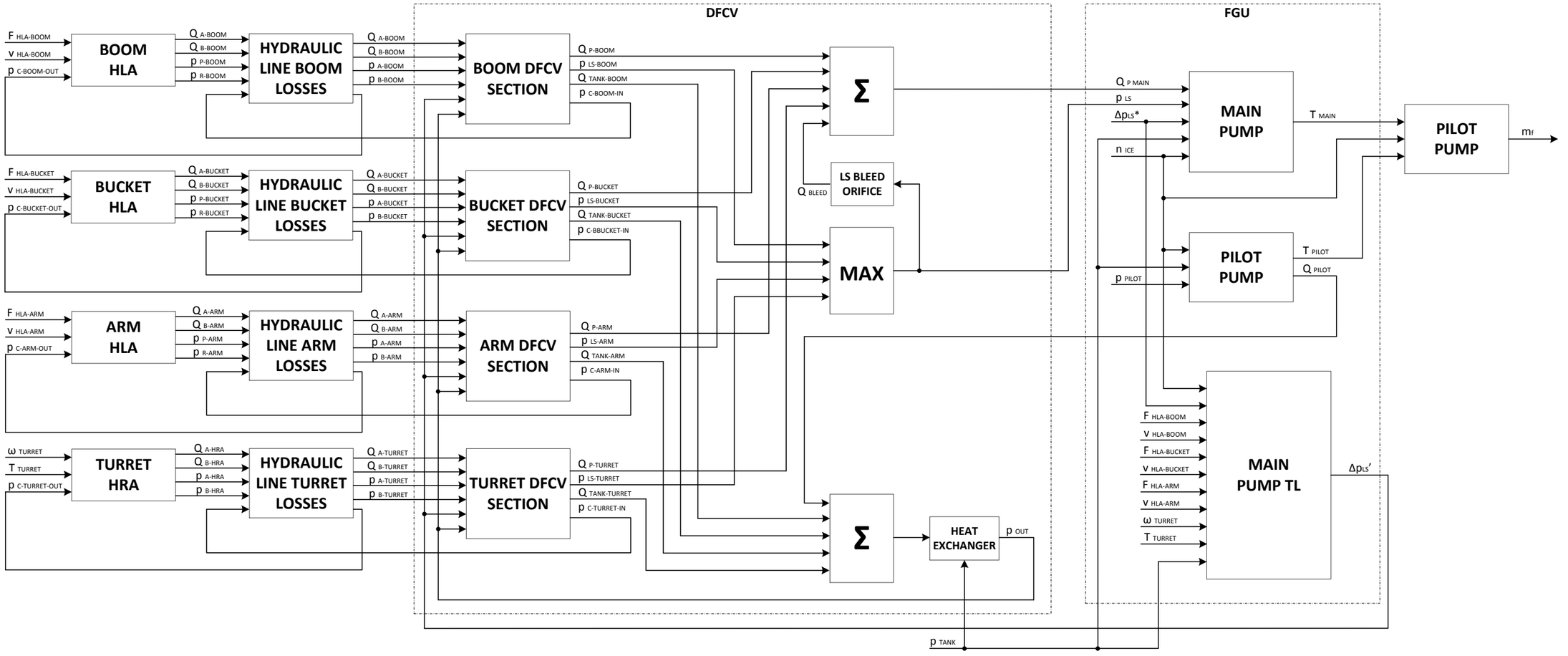

Appendix 4: ES85ZT Inverse Causality Model Scheme.

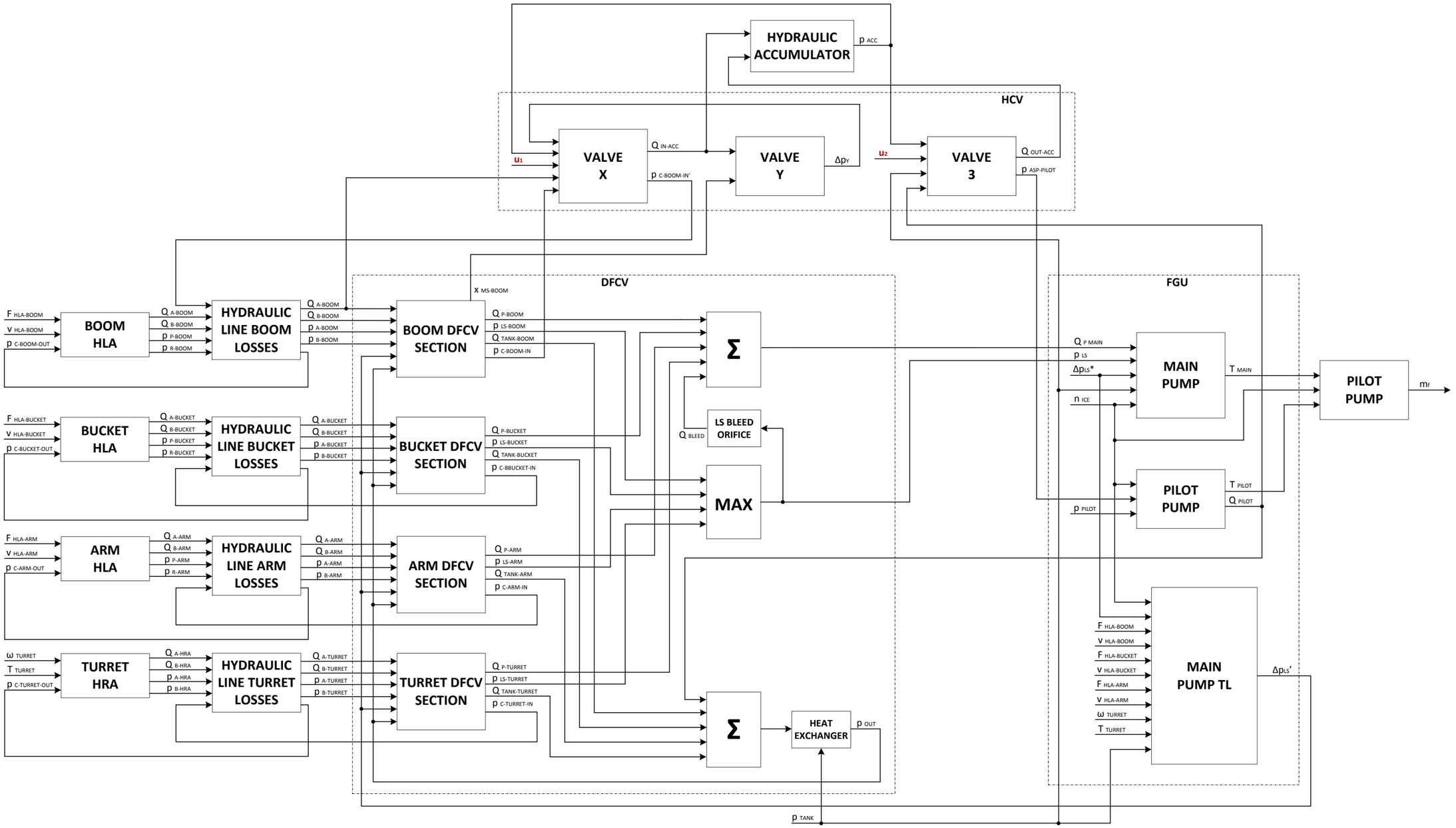

Appendix 5: Excavator with ERS Inverse Causality Model Scheme.

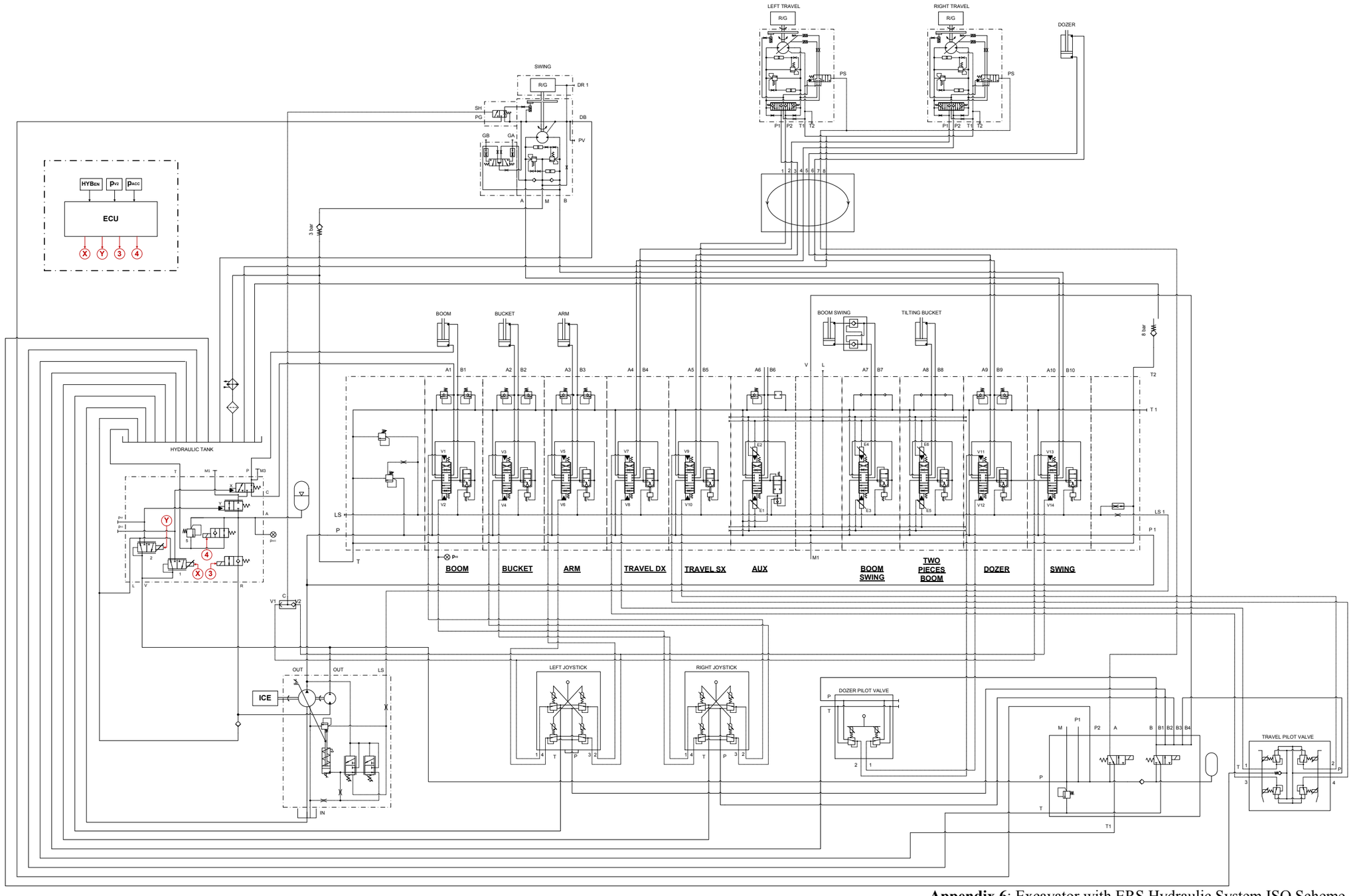

Appendix 6: Excavator with ERS Hydraulic System ISO Scheme.

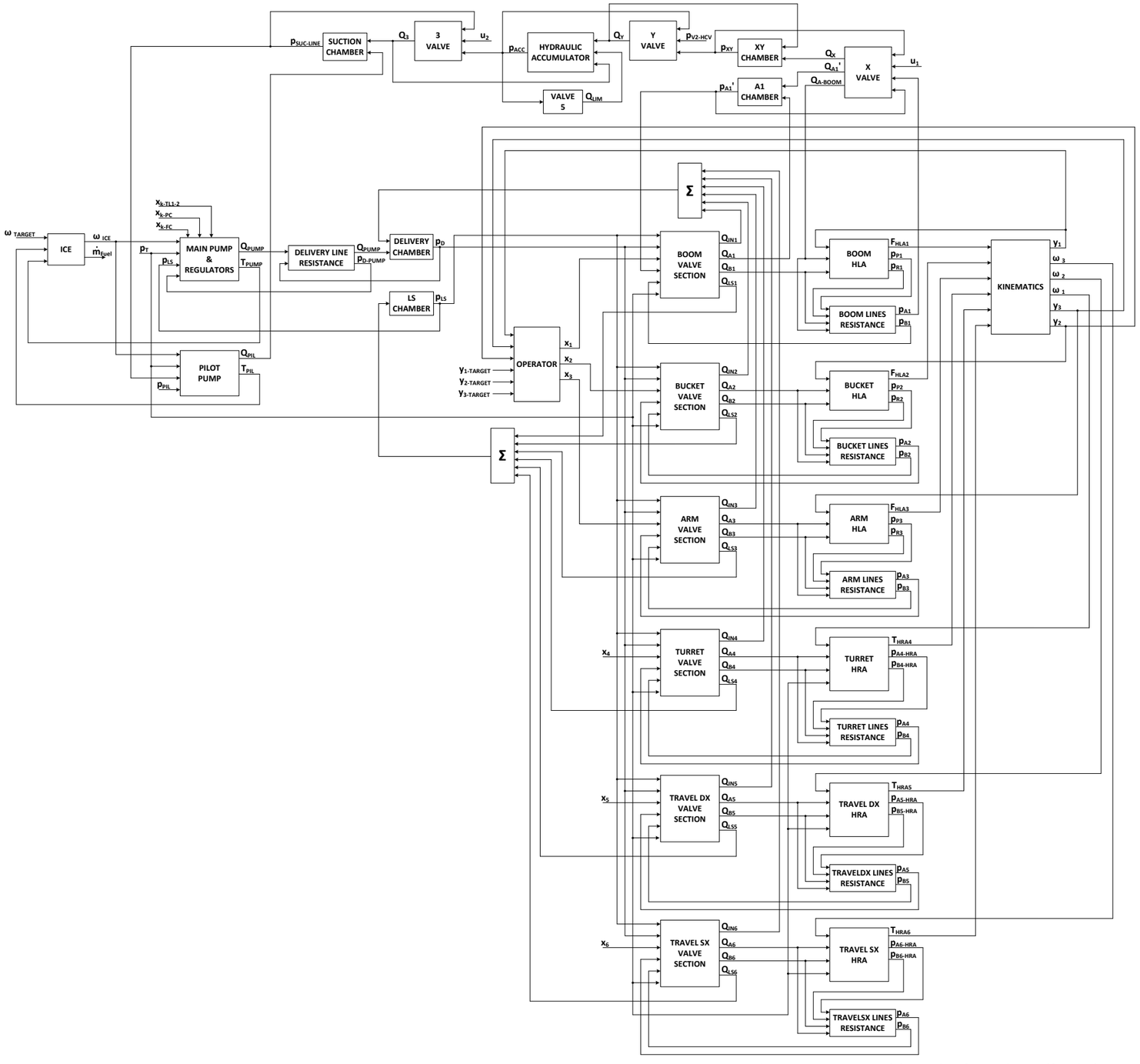

Appendix 7: Excavator with ERS Direct Causality Scheme.